Surface X-ray Diffraction Studies of Electrode/Vacuum and Electrode/Electrolyte Interfaces

By

Elizabeth M. Cocklin

Department of Physics

University of Liverpool

This thesis is submitted in accordance with the requirements of the University of Liverpool for the degree of Doctor of Philosophy

July 2017

Viva Voce Examination

14:00, 3rd May 2017

Surface Science Research Centre, University of Liverpool

Examiners

Dr Chris Nicklin

I07, Diamond Light Source

Dr Hem Raj Sharma

Department of Physics, University of Liverpool

PhD Supervisors

Primary: Dr David Martin

Secondary: Prof. Christopher A. Lucas

Declaration

I, Elizabeth Margaret Cocklin, declare this thesis is a presentation of my own work except where indicated in the text. It has not been previously submitted, in part or whole, to any university or institution for any degree, diploma, or other qualification.

Elizabeth Margaret Cocklin

3rd March 2016

Signed: *Original submitted copy signed: Elizabeth Cocklin*

Surface X-ray Diffraction Studies of the Electrode/Vacuum and

Electrode/Electrolyte Interface - Elizabeth Cocklin – March 2017

Abstract

This thesis presents in situ Surface X-ray Diffraction (SXRD) studies of surfaces and interfaces, in both Ultra High Vacuum (UHV) and an electrochemical environment. Primarily Crystal Truncation Rod (CTR) measurements are utilised to determine a model for the atomic structure at the interface.

A SXRD characterisation of the clean Ag(110) and Ag(111) surfaces in UHV were determined as a reference for the rest of the work in this thesis. Following this the growth conditions and structures of a silicene layer on Ag(111) were investigated, by Low Energy Electron Diffraction (LEED) and preliminary SRXD study of the interface structure is presented.

A comprehensive study of the Ag(*hkl*)/alkaline interface is presented. X-ray Voltammetry (XRV) measurements have been performed to determine the potential dependence of the system. CTR measurements have been used to determine the structure at both the electrode and electrolyte sides of the interface. The results reveal large structural changes on the electrolyte side of the interface, with the response of relaxation of the surface layers in the metal. The presence of specifically adsorbed OH on the surface stabilises cations in a compact double layer through non-covalent interactions. The studies were extended to determine the effects of saturating the electrolyte gases, CO and O_2 on the double layer structure. The results indicate that double layer structure is subtly perturbed, and hints at a change in the nature of bonding at the interface.

Time resolved SXRD measurements are utilised to determine the dynamics of the restructuring of the electrolyte layering at the Ag(111)/Alkaline interface. In order to gain a comprehensive picture of the structural dynamics, two other systems are studied; the Au(111) reconstruction to determine the timescale of the (1 x 1) ↔ $(p \times \sqrt{3})$ reconstruction, and the underpotential deposition of Ag on Au(111). The results indicate that the mass transport of ions through electrolyte is on a timescale comparable to the charge transfer, whereas the ordering of ions and surface metal atoms occurs on much longer timescales.

Acknowledgments

Firstly I would like to thank my supervisors, Dr. David Martin and Prof. Chris Lucas for giving me this opportunity, and for all their help and guidance throughout my PhD. Thank you to David for all the time spent in the lab teaching me UHV, and for being the most patient and calm person I know in academia. Thank you to Chris for his enthusiasm to science, endless stories, and most importantly introducing me to red wine.

Thanks to Dr. Yvonne Gründer for inviting me on all her synchrotron experiments, and for discussions about data. Thanks to Dr. Vin Dhanak for letting me use his UHV chamber, and to Dr. David Hesp and Tom Whittles for their valuable UHV expertise. Thanks to Naomi Sisson for being an excellent teacher during my first steps into electrochemistry and synchrotron experiments.

Thank you to Dr. Sarah Horswell for all the silver experiments, I valued the time learning from her in the lab and discussing the data. Thanks also for the good company at the beamline. Thanks to Dr. Ross Springell and the group from Bristol, for my favourite beamtime experiments (and some memorable photos).

I would like to say thank you to all the beamline staff that have helped me over the past few years. Thanks to everyone from XMaS, in particular Paul Thompson, for his help and the many nights in Grenoble. Thank you to everyone at I07, especially Matt Forster for keeping me sane during my lonely experimental prep times, and thanks for all the help with the silver and silicene experiments.

Thank you to Felix Schwarz for being a good friend and for introducing me to climbing, for that, I will always be grateful.

Thank you to everyone in the Stephenson, there was always someone there (day and night!) whenever I needed a chat. In particular thanks to Rob Treharne, for all the time spent listening, advising and supporting me – and giving me a nudge when I really needed it! Thank you for taking the time to read my thesis, and for the useful feedback, it is all much appreciated. Thanks to Josh Fogg for the beamtime company, the trips to the pub and the entertaining walks back to Ridgeway house. Karaoke one day, I promise! Thanks to Nikolas for the discussions about silicene, and the entertaining chats. Thanks to Paula for the encouragement, advice and tea breaks. Thanks to Iain for the many nights spent dancing in Hannah's Bar! And thanks to the original Stevie Gs, Jonathan and Petar.

I would like to say a big thank you to my favourite Yorkshireman, Gary Harlow, for the many cups of tea, gossip and support over the years. Thanks for providing the most entertaining stories and memories, it's a shame we never went on another beamtime together! Thank you for never letting me give up, and for always being there when I needed a friend. Thank you to Lisa Rhodes-Martin for picking up the pieces when Gary left, and for the numerous extended tea breaks. I look forward to finally seeing her outside of the Stephenson Institute again when this is all over.

Thank you to Lisa and Han for being so caring and supportive. And thanks for all the gin and wine!

A big thank you to my mum for always believing in me, even though the majority of the time I never believed in myself. Thank you for always supporting me and looking after me.

Most of all I would like to thank Jack. Thank you for everything. Thanks for looking after me, cooking for me, supporting me and always listening to me (even when I talked about CTRs!). Thanks for all the fun times we had when I actually left the Stephenson, I look forward to climbing, walking and actually spending time with you again!

Contents

List of figures

List of tables

List of Abbreviations

AFM	-	Atomic force microscopy
C.E.	-	Counter Electrode
CTR	-	Crystal truncation rod
CV	-	Cyclic voltammetry
DFT	-	Density functional theory
DLS	-	Diamond Light Source
DWF	-	Debye Waller factor
EAM	-	Embedded Atom Method
ESRF	-	European Synchrotron Radiation Facility
fcc	-	Face-centred cubic
FOR	-	Fractional order rods
FTIRS	-	Fourier transform infrared spectroscopy
FWHM	-	Full width at half maximum
GIXRD	-	Grazing incidence X-ray diffraction
hcp	-	Hexagonal close-packed
HOMO	-	Highest occupied molecular orbital
HOR	-	Hydrogen oxidation reaction
IHP	-	Inner Helmholtz plane
LEED	-	Low energy electron diffraction
LINAC	-	Linear accelerator
LUMO	-	Lowest unoccupied molecular orbital
ML	-	Monolayer
MuSST card	-	Multipurpose unit for synchronisation sequencing and triggering card

ORR	-	Oxygen reduction reaction
OHP	-	Outer Helmholtz plane
PEM	-	Proton exchange membrane
pzc	-	Potential of zero charge
RBS	-	Rutherford Back Scattering
R.E.	-	Reference Electrode
RHEED	-	Reflection high-energy electron diffraction
RHEPD	-	Reflection High-Energy Positron Diffraction
ROI	-	Regions of interest
rms	-	Root-mean-squared
SNIFTIRS	-	Subtractively normalised interfacial Fourier transform infrared spectroscopy
STM	-	Scanning tunneling microscopy
SXRD	-	Surface X-ray diffraction
TRSXRD	-	Time-resolved surface X-ray diffraction
UHV	-	Ultra high vacuum
UPD	-	Under potential deposition
W.E.	-	Working electrode
XPS	-	X-ray photoemission spectroscopy
XRV	-	X-ray voltammetry

1 Introduction

The study of surfaces and interfaces is of paramount importance to the development of new materials for a variety of technological areas such as nanotechnology, and renewable energy. The ability to understand the structure on an atomic level is important to be able to tailor new stable and efficient materials, and tune their properties. In order to do this it is important to understand simple model systems to determine the driving force behind structure formation and catalytic activity. Consequently there has been a wealth of research utilising single crystal electrodes; as they have well defined atomic arrangements with specific adsorption sites.

Over the years there have been a vast amount of techniques developed to characterise the atomic structure of single crystal surfaces, for example many early surface characterisation studies were carried out in Ultra High Vacuum (UHV)

utilising techniques such as Low Energy Electron Diffraction (LEED) and X-ray Photoemission Spectroscopy (XPS); which probe the electrode-gas interfaces. These techniques were later extended to probe the structure of electrochemical systems ex situ, where a sample would be transferred from an electrochemical cell to the UHV environment. Whilst a wealth of knowledge has been obtained from ex situ studies, one cannot be certain that the structural models obtained are a true representation of the electrochemical interface. Without potential control structures may not be stable, and weakly adsorbing ions in the double layer may be lost on emersion. To bridge the gap in the knowledge, it is essential to develop and exploit *in situ* structural techniques (where the system remains under potential control) to develop a dynamic picture of the electrochemical interface. Scanning Tunneling Microscopy (STM) and Surface X-ray Diffraction (SXRD) have been instrumental in this. The primary technique used in this thesis is SXRD. The disadvantage of using SXRD is the need for high intensity X-rays, as scattering from surface is very weak in comparison to the bulk; synchrotron radiation is therefore required.

Understanding the structure of clean surfaces is a vital starting place in which correlations between surface structure and adsorption can be made. When a crystal is terminated the properties of the atoms in the top few layers differ to that in the bulk; the coordination number at the surface is reduced and the electron distribution is modified. As a response the top atomic layers may reconstruct (in-plane symmetry is different to the bulk crystal lattice) or undergo relaxations (displacement from the bulk equilibrium position along the surface normal). In UHV only a few noble metals are known to reconstruct under specific preparation conditions (Pt, Au, Ir)[1], whilst nearly all metals experience vertical relaxations of the top metal layers [2]. The reconstructions and relaxations of a metal differ between the low index surfaces due

to the coordination number of the surface; for example for fcc metal surface the relaxation effect increases in the order (111)<(001)<(110) [2–4]. The addition of adsorbates on the surface can enhance, lift or even induce reconstruction of surfaces [5].

The majority of work presented in this thesis concerns the silver (Ag) low index surfaces. Silver is a noble metal which does not experience in-plane reconstruction without the addition of adsorbates, such as oxygen [6] or alkali metals [5]. Ag has been extensively studied in UHV, to determine the relaxations of the clean surface [7–15]. The adsorption of oxygen species on Ag surface is of particular interest due to the role of surface oxide in the catalytic gas phase reactions of organic molecules, such as; ethylene epoxidation and methanol oxidation [16]. Atomic resolution (STM) images of the oxygen-promoted restructuring of the Ag(111) surface [17] have been combined with density functional theory (DFT) calculations [18] in an attempt to understand the function of silver as an oxidation catalyst.

The adsorption of hydroxide and oxygen species onto metal surfaces is also vital to understand surface reactivity and catalytic behaviour at the electrochemical interface. Whilst the electrochemistry of silver has been widely studied in the oxide region, there have been considerably less studies in the underpotential oxide region, where hydroxide (OH^-) is specifically adsorbed. This region is of particular interest as important electrochemical reactions occur; such as the Oxygen Reduction Reaction (ORR), CO oxidation, amongst others. In 2010 it was proposed that non-specifically adsorbed cations (cations which retain their hydration shell), are stabilised in a compact double layer by non-covalent (van der Waal's) interactions with $OH_{ads,}$ and have been proven to play an important role in the kinetics of the ORR on Pt [19]. Depending upon the hydration energies of the cation the ORR can

be inhibited by cation-hydroxide clusters. An understanding of the electrolyte layering at the interface is obviously of paramount importance as the structure of the layering may be tuned in order to enhance or inhibit electrochemical reactions. Structural studies of Ag in electrochemical environments compared to other noble metals, such as Au and Pt, is severely lacking, which is likely due to the difficulty in preparing the surface and obtaining atomic-scale structural information from a reactive surface in the liquid environment. The majority of structural studies of Ag have been made ex situ, hydroxide adsorption on Ag(*hkl*) was investigated by Horswell *et al.* [19,20] which indicated evidence of an ordered (2×6), and $c(2 \times 2)$ at higher coverages on the Ag(110) surface, these structures are shown schematically in Figure 1.1. An early model of the Ag(111)/alkaline interface was proposed by Savinova [22], which identified the presence of cations in the interface structure. More recently Lucas *et al.* [23] investigated the structure of the

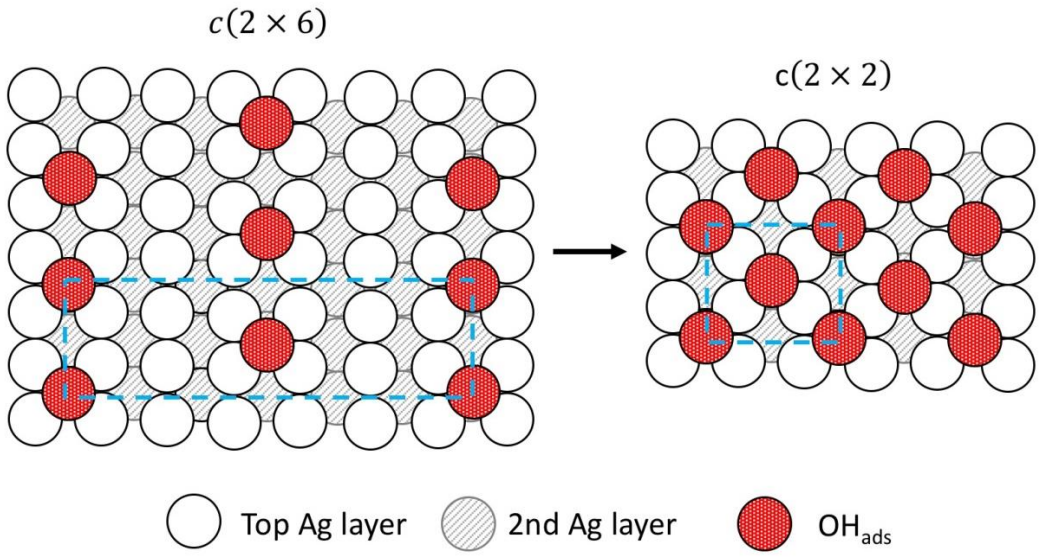

Figure 1.1 Proposed structures for the OH- adlayer at negative potentials. White circles, top row Ag atoms; grey circles, second row Ag atoms; red circles, adsorbed OH^-. The blue dashed rectangles indicate the unit cell of the hydroxide structure.

Ag(*hkl*)/alkaline interface by SXRD, and proposed which was consistent with analogous results obtained on Pt electrodes [19]; at positive potential cations are stabilised in a compact double layer by adsorbed OH through non-covalent interactions. In a similar study by Nakamura *et al*. [24], in 0.1 M CsBr + 0.05 M CsOH electrolyte, Cs^+ cations are found to interact with adsorbed Br through non-covalent interactions. It is essential to develop a detailed knowledge of the Ag(*hkl*)/Alkaline interface to develop a fundamental understanding of the driving forces behind important catalytic processes and the stability of the electrodes under reaction conditions.

In addition to its properties as an electrode, silver has gained renewed interest in the past 5 years as the primary substrate for growth of a new two-dimensional material, silicene; the silicon analogue of graphene which would have the advantage over graphene of being compatible with the established silicon electronics industry. Unlike graphene, silicene is not freestanding as it cannot be exfoliated from bulk silicon and thus requires a substrate to grow on.

The low tendency for alloy formation makes silver the ideal substrate, and consequently the majority of studies are on silver [25]. Silicon nanostructures have been formed on all three low index Ag surfaces. The majority of studies have focussed on Ag(111) with the aim to grow a honeycomb sheet of silicene. A preliminary SXRD investigation of silicene on Ag(111) is reported in Chapter 4 of this thesis.

An outline of the content in this thesis is as follows;

- **Chapter 2** discusses theoretical principles behind the work in this thesis. The

chapter begins with a discussion of the electrochemical interface and the models which have been developed in order to describe it. Following this the theoretical background to SXRD, and the principle behind LEED are described.

- **Chapter 3** describes the experimental details such as sample preparation, the different types of electrochemical cells used and experimental setup. A description of the data acquisition procedure, in addition consideration of the necessary correction factors and data fitting procedures are provided.

- **Chapter 4** As the majority of this thesis concerns silver single crystals, it is important to establish the clean electrode/vacuum structure as a reference in order to determine the effect of electrolyte and adsorbates on the structure of the electrode surface. Chapter four begins with an SXRD study of the Ag(111) and Ag(110) surfaces in UHV. There are currently no reported SXRD studies of the relaxations of clean Ag(110) surface. The surface has predominantly been studied by LEED [7–9,26] and Rutherford Back Scattering (RBS) [9,10], however there are large discrepancies between different studies, it is therefore important to determine the structure with SXRD to provide a useful comparison throughout this thesis.

- **Chapter 5** investigates the growth and structure of a silicene layer on Ag(111). The growth of silicene is challenging, with the temperature of the crystal during deposition, and the deposition rate, being key factors. Only a

narrow temperature range exists in which the growth takes place, thus, careful control over the growth conditions is necessary. These conditions were successfully optimised and are described in this chapter. The growth conditions and structures of silicene sheets on the Ag(111) surface were investigated by LEED, and preliminary structural SXRD analysis is also presented.

- **Chapter 6** presents a comprehensive *in situ* study of the Ag(*hkl*)/alkaline interface in the underpotential oxide region, i.e. the region where OH^- is reversibly adsorbed. X-ray Voltammetry (XRV) measurements were performed to highlight the potential dependent structural changes at the interface. A model for the interface structure was determined through analysis of Crystal Truncation Rod (CTR) data taken at fixed potentials, corresponding to the regions where the surface is free of adsorbates, and where OH is adsorbed. The study highlights the sensitivity of the electrolyte layering on the atomic geometry of the surface. The studies were extended to effects of saturating the electrolyte gases, CO and O_2 on the double layer structure.

- **Chapter 7** One of the most important aspects of electrochemistry is to determine the dynamics of structural rearrangement of the electrochemical interface. SXRD is ideally suited to probe the structural evolution of the interface in real time. In Chapter 7 time resolved SXRD measurements are utilised to determine the dynamics of the restructuring of the electrolyte layering at the Ag(111)/Alkaline interface. In order to gain a comprehensive

picture of the structural dynamics, two other systems are studied; the Au(111) reconstruction to determine the timescale of the $(1 \times 1) \leftrightarrow (p \times \sqrt{3})$ reconstruction, and the underpotential deposition of Ag on Au(111).

- **Chapter 8** Finally a conclusion of the main results and discussion of future work is presented, with a consideration for the study of the Ag(111)/silicene system in an electrochemical environment.

2 Theoretical Principles

2.1 Introduction

The experiments in this thesis probe the atomic structure of both the electrode/vacuum interface and the electrode/electrolyte interface primarily through Surface X-ray Diffraction (SXRD) measurements. The scattered intensity of an X-ray beam from the surface is far weaker, by ~10^6 , than scattering from the bulk and thus synchrotron radiation is required to probe the surface (~1-10 Å). In this chapter the theoretical principles behind X-ray diffraction are built up, and the principles behind Low Energy Electron Diffraction (LEED) are considered.

2.2 Electrochemistry

'*Electrochemistry is the study of structures and processes at the interface between an electronic conductor (the electrode) and an ionic conductor (the electrolyte) or at the interface between two electrolytes.'*

This definition of electrochemistry is taken from Schmickler and Santos [27]. In this section a basic description of the metal-electrolyte interface is presented, which will consider electrode reactions, and a discussion of the electrical double layer models. Following this cyclic voltammetry and adsorption phenomena will be considered. Further background can be found in the source material references [27–32].

2.2.1 Electrode Reactions

At the electrochemical interface electrode reactions occur when there is charge transfer between ions and the electrode, this is known as a Faradaic reaction - or redox reaction. When an electron is lost this is known as oxidation, and the reverse process of gaining an electron is known as reduction. In an electrochemical cell there are two half reactions where oxidation and reduction occurs. Oxidation occurs at the anode, and reduction at the cathode.

Oxidation:

$$R + ne^{-} = O \tag{2.1}$$

Reduction:

$$O - ne^{-} = R \tag{2.2}$$

where O is the oxidised species, R is the reduced species and n is the number of electrons exchanged between them.

Energy levels

When a metal is brought into contact with electrolyte their Fermi levels align, this is shown in Figure 2.1. When a potential is applied to a metal the energy of the Fermi level either increases or decreases, this is illustrated in Figure 2.2. When a metal comes into contact with a solution charge is transferred at the interface to

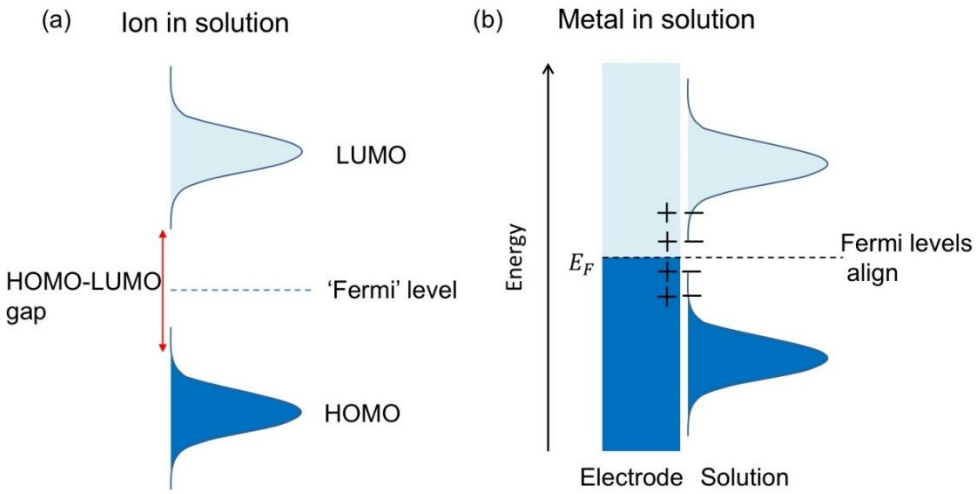

Figure 2.1 Energy levels (a) ion in solution (b) metal in solution - Fermi levels align.

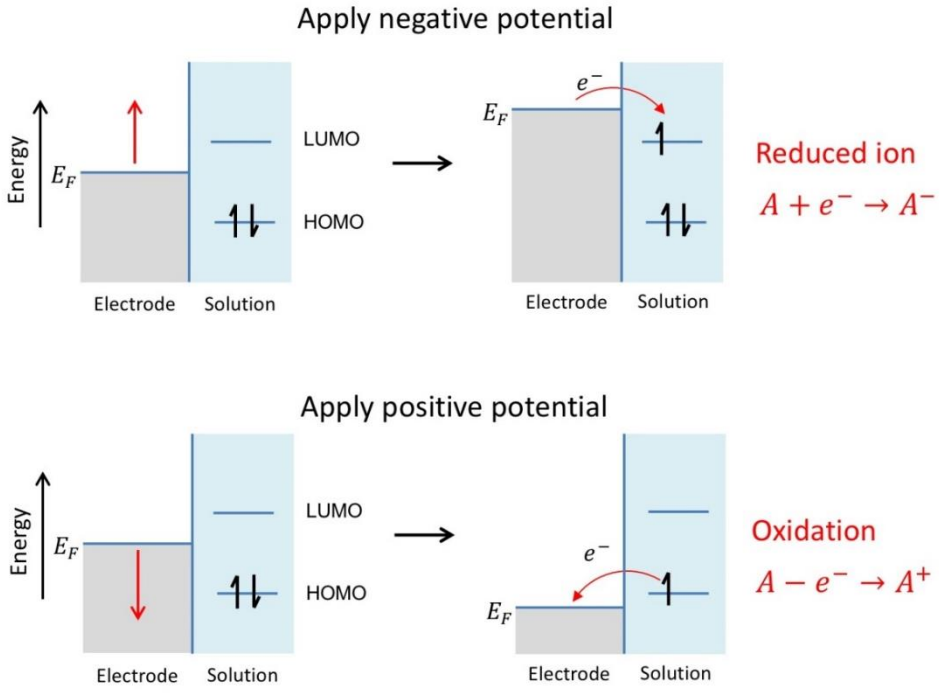

Figure 2.2 Effect of applied potential on the Fermi level in a metal. Applying a potential changes the energy of the Fermi level.

equilibrate the Fermi levels. When a negative potential is applied the Fermi level increases and electrons are transferred from the electrode to species in electrolyte. This occurs when the energy of the Fermi level is above the lowest unoccupied

molecular orbital (LUMO).When a positive potential is applied the energy of the Fermi level decreases below the highest occupied molecular orbital (HOMO), resulting in oxidation – electron transfer to the electrode.

We need to be able to measure and control the potential of the working electrode in order to control the electrochemistry at the interface. The electrode potential cannot be directly measured; instead it must be compared against a standard reference electrode. The cell potential is the sum of the standard potentials for each half reaction:

$$E_{cell}^{0} = E_{R}^{0} + E_{O}^{0} \quad (2.3)$$

The superscript '0' denotes that it is under standard conditions (i.e. T = 298 K).

The reaction in the cell has a change in Gibbs free energy, G, which can be related to the cell potential. Chemical energy (G) can be converted to electrical energy (E_{cell}) by:

$$\Delta G = -nFE_{cell} \quad (2.4)$$

Where n is the number of electrons transferred, and F is the Faraday constant.

If the reaction is under standard conditions then this becomes:

$$\Delta G^{0} = -nFE_{cell}^{0} \quad (2.5)$$

When E^0 is positive, the reaction is spontaneous and when E^o is negative, the reaction is non-spontaneous. From thermodynamics, the Gibbs energy change under non-standard conditions can be related to the Gibbs energy change under standard conditions via the following equation:

$$\Delta G = \Delta G^{0} + RT \ln \frac{[O]}{[\mathrm{R}]} \quad (2.6)$$

Where R is the gas constant (~8.3 J K^{-1}), T is the absolute temperature, $[O]$ and [R] are the concentration of the reductant and oxidant.

Substituting in for ΔG and ΔG^0:

$$-nFE = -nFE^0 + RT \ln \frac{[O]}{[R]} \tag{2.7}$$

Dividing both sides by $-nF$ gives:

$$\Delta E = \Delta E^0 - \left(\frac{RT}{nF}\right) \ln \frac{[O]}{[R]} \tag{2.8}$$

This is known as the Nernst equation. This equation indicates that the electrical potential of the cell depends on the concentration of electroactive species. During a redox reaction the concentration of the reductant and oxidant changes, which results in a decrease in cell potential until the reaction is at equilibrium where $\Delta G = 0$. In order to drive further reactions a potential must be applied.

2.2.2 Electric double layer models

When a metal electrode is brought into contact with electrolyte with different chemical potentials the charge of the surface is balanced by an excess charge in the electrolyte. The metal is an excellent conductor, which means its excess charge is restricted to a depth ~ 1 Å into the surface. Conversely, the conductivity of an electrolyte is several orders of magnitude less than that of a metal (it is dependent upon the concentration of ions), which results in an extended charge distribution over a larger region ~ 5 - 20 Å. The charge distribution at the interface is known as the electric double layer. In aqueous electrolyte the voltage drop across the interface is of the order of 1 V, this defines the electrochemical window. Outside the potential limits the solution decomposes, at positive potential oxygen evolution sets in and at negative potential hydrogen evolution sets in. The potential window is much wider in ionic liquid of the order of several volts. The following sections describe how the double layer region is modelled; a schematic is shown in Figure 2.3.

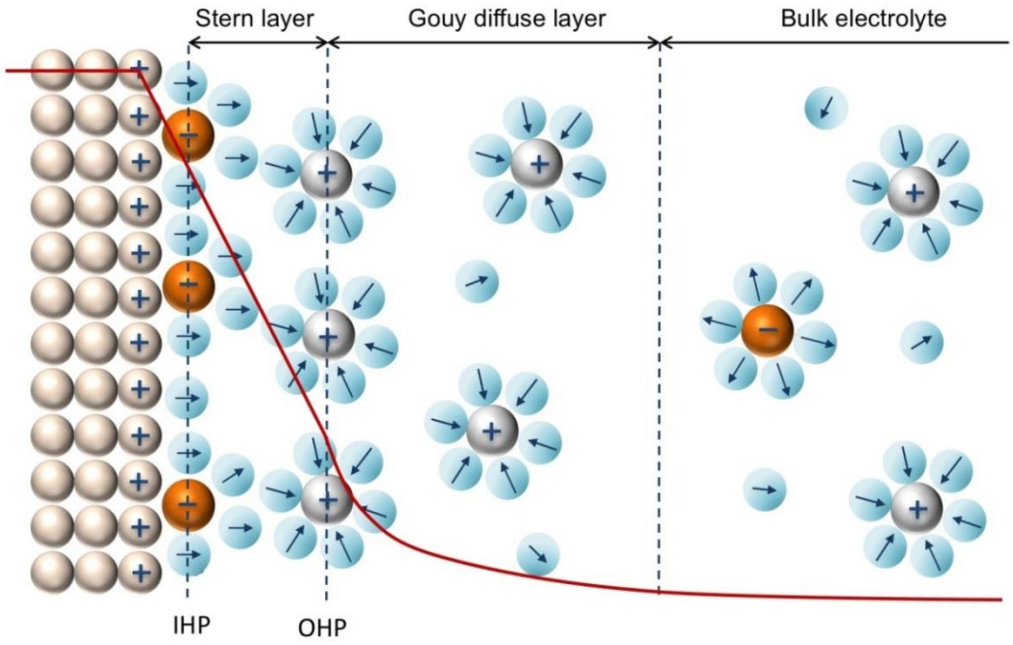

Figure 2.3 Schematic representation of electrical double layer models.

The Helmholtz model

In 1853, Helmholtz [34] proposed the first model of the electrode/electrolyte interface. This model assumes that there are no Faradaic processes occurring at the electrode surface, i.e there is no charge transfer occurring, and that the charge density at the electrode surface, q^m, arising from excess or deficiency at the surface is equalised by the redistribution of ions in solution q^s; maintaining charge neutrality on the electrode such that:

$$q^m = -q^s \tag{2.9}$$

In this model it is assumed that the solvation shell around the ions determines their closest approach, i.e. it prevents them from directly interacting with the surface. This is known as the Outer Helmholtz Plane (OHP). A resulting potential drop

occurs in the region between the electrode surface and the OHP, which was described by Helmholtz as the 'electrical double layer'. The double layer is analogous to an electrical capacitor:

$$C = \frac{\varepsilon}{4\pi d} \tag{2.10}$$

where ε is the electric permittivity of the medium, and d distance of the Helmholtz-plane from the electrode surface.

Gouy-Chapman model

Gouy [35] and Chapman [36] independently proposed that the charge was spread over a diffuse layer as opposed to being concentrated at the OHP later modified the Helmholtz model. This occurs due to Brownian motion opposing the electrostatic attraction and repulsions of ions from the electrode, thereby dispersing excess charge over a diffuse layer. The capacitance is given by:

$$C = \left(\frac{2z^2F^2\varepsilon c^*}{RT}\right)^{1/2} cosh\left(\frac{zF\phi}{2RT}\right) \tag{2.11}$$

where z is charge on the ion, and ϕ is the total potential drop across solution side of double layer

Stern model

In 1924 Stern [37] proposed a model, which combined the previous two. He assumed that there was a minimum distance of closest approach in the OHP where the majority of charge was concentrated, and that charge also extended into the diffuse layer.

The capacitance of this model behaves like two capacitors (the Helmholtz and Gouy-Chapman capacitance) in series:

$$\frac{1}{C} = \frac{1}{C_H} + \frac{1}{C_{GC}} \quad (2.12)$$

Grahame model

In 1947 Grahame [38] proposed that the ions could penetrate the OHP if they lost part or all of their solvation shell and come into direct contact with the electrode, these ions are said to be 'specifically adsorbed' on the surface. This closer plane of approach was termed the Inner Helmholtz Plane (IHP).

2.2.3 Potential of zero charge

The charge of an electrode can be controlled by an applied potential; it can be positively or negatively charged. Therefore, it must follow that there is some potential where there is zero charge. This is called the potential of zero charge, pzc. The pzc is a characteristic quantity which is different for all metals, and also differs for the different surface geometries of a metal. The pzc is related to the work function, Φ:

$$\phi_{pzc} = \Phi + C \quad (2.13)$$

Where C is a constant which depends on the scale on which the electrode potential is measured (the reference electrode). It is a useful quantity for comparing different surfaces.

2.2.4 Cyclic voltammetry

Cyclic voltammetry (CV) is an important technique for measuring the current as a function of potential. This is a simple method of characterising an electrochemical system. Features in the voltammogram can be attributed to electrochemical processes such as adsorption and desorption at the interface, and surface reconstruction. As cyclic voltammetry is a measure of electron transfer,

peaks in the voltammetry can be integrated to give the charge transfer for a particular process. The simplest way of measuring the current is to use a two electrode set up. This consists of a working electrode, where the reaction of interest is taking place, and a stable reference electrode that the potential at the working can be measured against. The potential difference between the working electrode and reference electrode is given by:

$$E_{cell} = (\phi_m - \phi_s) + (\phi_s + \phi_{ref}) + iR \quad (2.14)$$

The first term in equation (2.14) $(\phi_m - \phi_s)$ represents a voltage drop at the electrode/electrolyte interface, the second $(\phi_s + \phi_{ref})$ is the voltage drop at the reference electrode interface and the final term iR represents the potential drop between the two electrodes (solution resistance). For this to work, the iR term needs to be negligible so that the reference electrode is in equilibrium to have its standard value, a large current through the reference electrode can cause it's chemical composition to break down. This set up works perfectly well for measurements where only a small current is passed, such as for microelectrodes, however, for larger electrodes, as used throughout this thesis (Area = 0.79 cm^2), a larger current is passed. This is avoided by using a three-electrode set up shown in Figure 2.4. In addition to the working and reference electrode there is a third 'counter' electrode; this is chosen to be a material that does not produce any substances that may affect the behaviour of the working electrode. In this configuration the voltage is measured between the working electrode and the reference electrode, a high input impedance restricts current being drawn from the reference electrode.

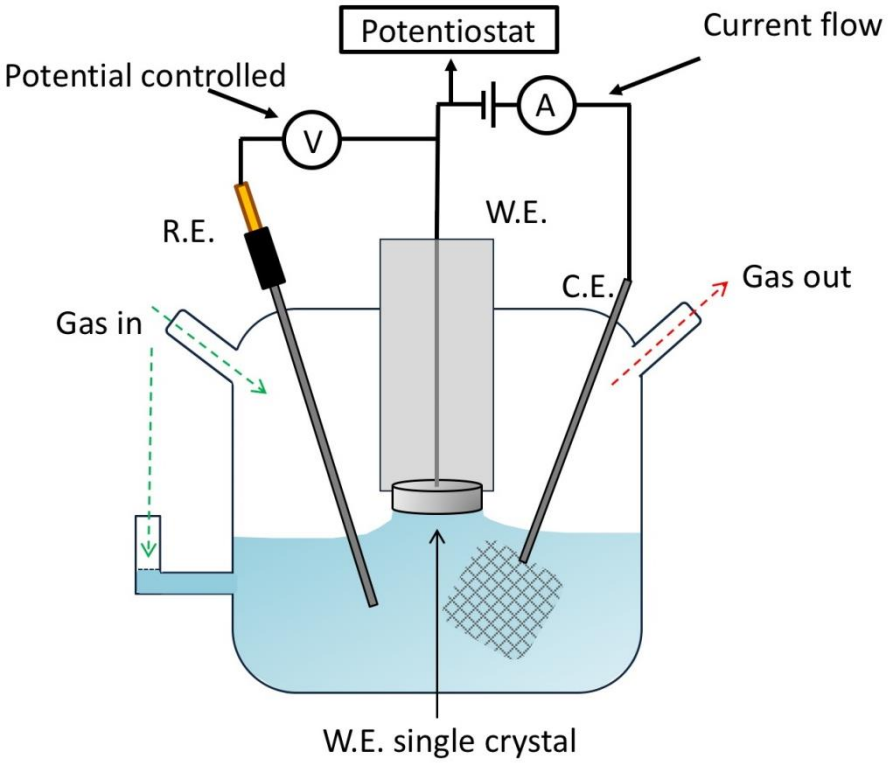

Figure 2.4 Schematic of 3 electrode electrochemical cell. W.E. working electrode, C.E. counter electrode, R.E. reference electrode. The potential is controlled between the working and reference electrodes, and the current flows between the working and counter electrodes.

In this configuration the voltage is measured between the working electrode and the reference electrode, a high input impedance restricts current being drawn from the reference electrode.

The current is measured whilst the potential of the working electrode, with respect to the reference electrode, is swept linearly between the cathodic (negative) and anodic (positive) limits, E_1 and E_2 respectively, at a constant sweep rate seen in Figure 2.5. The shape of the forward and reverse scans should be similar; however it depends on the reversibility of the A/B redox couple. The cycle starts from E_1 and scans linearly at to E_2, oxidising species B to species A, which is then reduced on the reverse negative sweep.

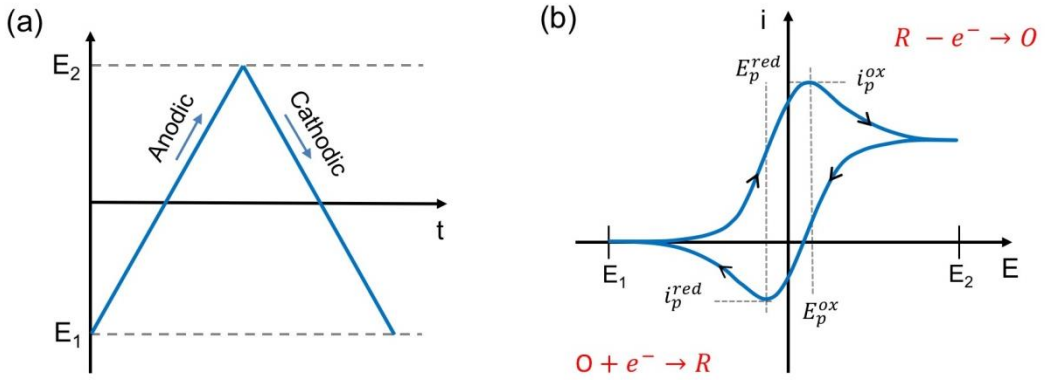

Figure 2.5 Schematic of cyclic voltammetry measurements (a) the variation of potential with time (b) the current response of the system.

In Figure 2.5 (b) an increase in current corresponds to an oxidation or redox reaction, where:

i_p^{ox} – peak current in oxidation process

E_p^{ox} – electrode potential corresponding to the oxidation process

i_p^{red} – peak current for in reduction process

E_p^{red} – electrode potential corresponding to the reduction process

Initially no current is passed as the potential is not great enough in order to drive a reaction. Once the current is sufficiently positive enough the current begins to increase, corresponding with the oxidation of the reduced species. The current increases to a peak current i_p^{ox}. The current gradually decreases until all of species A is converted to B. The shape of a CV can also be influenced by external factors such as scan rate, this is illustrated in Figure 2.6; features become much sharper at a slower scan rate, and with higher concentration of ions in electrolyte more current flows giving a larger CV shape.

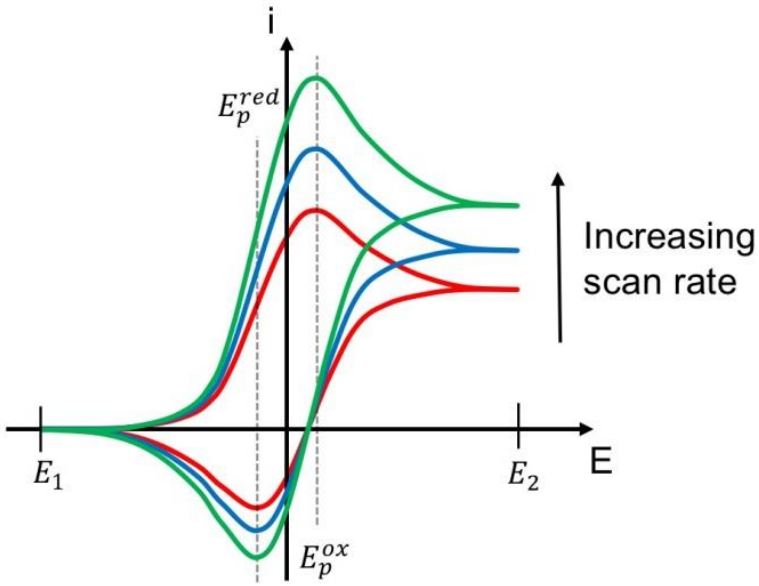

Figure 2.6 Effect of increasing scan rate on CV.

Although this is a quick method to perform in the lab, it is purely based on electron transfer it lacks structural information of the interface; for this we need to combine cyclic voltammetry with a structural technique *in situ* such as Scanning Tunneling Microscopy (STM), or SXRD. SXRD is discussed at length in section 2.4.

2.2.5 Adsorption phenomena

As discussed in the double layer models, adsorption processes can occur at the interface. The adsorption of ions falls into two categories:

1) **Chemisorption** – Occurs in the IHP and involves chemical interactions between the adsorbate and substrate. The bonding is either covalent (electrons are shared) or ionic (electrons are transferred).

2) **Physisorption –** occurs in the OHP, involves weak electrostatic interactions mainly via van der Waals forces.

2.2.6 Chronoamperometry

This technique is used to measure the current response during a potential step. The voltage is stepped from an initial potential, E_1, to a final potential E_2, and the current is measured as a function of time, the perturbation and response is shown in Figure 2.7. The shape of the resulting current evolution response, transients, gives an indication of the process under study, for example, the mechanism of an adsorption/desorption process. By fitting an appropriate lineshape to the current transient, of exponential form, the time constant for the charge transfer processes can be extracted.

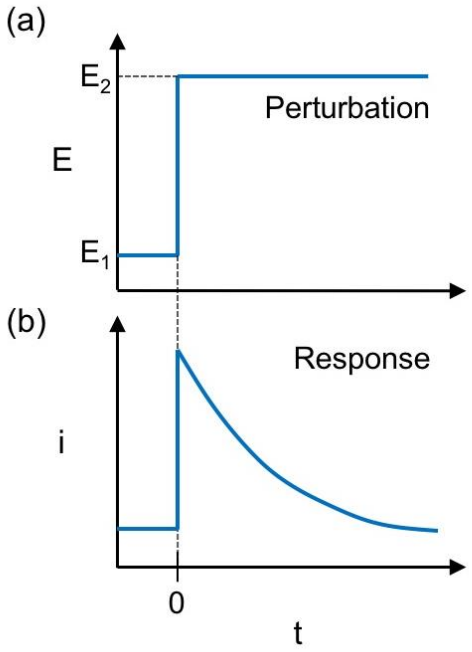

Figure 2.7 Potential step measurements (a) the change in potential – the potential is stepped between two limits, resulting in a square wave form, (b) the current evolution response.

2.3 Basic theory of diffraction

The structure of a crystal can be determined by the way in which incident waves interact with the sample. Diffraction occurs due to the interference effects produced by the phase difference between elastically scattered waves from different atoms in a crystal. The incident wave must have a wavelength comparable to the atomic spacing of a crystal for diffraction to occur, X-rays, neutrons and electrons satisfy this.

2.3.1 Crystallographic definitions

A crystal is a defined as a repeating basic with long-range order. The periodic array can be descrived by a space lattice with a group of atoms attached to each lattice point. The space lattice is defined by three vectors **a**, **b** and **c** such that any integer multiple of the vectors from any point in the lattice will locate a similar point. The unit cell is the parallelepiped defined by the sides **a**, **b** and **c** with $\alpha, \beta \; and \; \gamma$ are the angles between them. Figure 2.8 shows the face centred cubic (fcc) crystal structure, which is the structure of the single crystals used in this thesis.

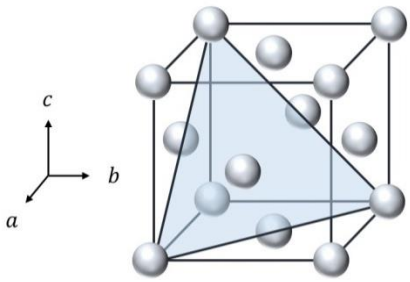

Figure 2.8 The face centred cubic fcc crystal structure. The (111) plane is highlighted.

The unit cell can be translated through space in all directions by:

$$\boldsymbol{R} = n_1\boldsymbol{a} + \mathrm{n}_2\boldsymbol{b} + n_3\boldsymbol{c} \tag{2.15}$$

where n_i is an integer, which builds up the crystal structure.

2.3.2 Crystal planes and Miller indices

There are an infinite number of 2D parallel planes in a 3D crystal structure. These planes have a specific arrangement of atoms and can be defined by its Miller indices (*hkl*). The Miller indices are determined by calculating the fraction of intercepts of the plane with the a, b and c axes and then taking the reciprocal. Directions are denoted [*hkl*] and are perpendicular to the (*hkl*) plane. This thesis focuses on the three low index fcc(*hkl*) surface planes which are depicted in Figure 2.9. Each set of parallel planes has an associated atomic arrangement, coordination number and interplanar spacing, d_{hkl}.

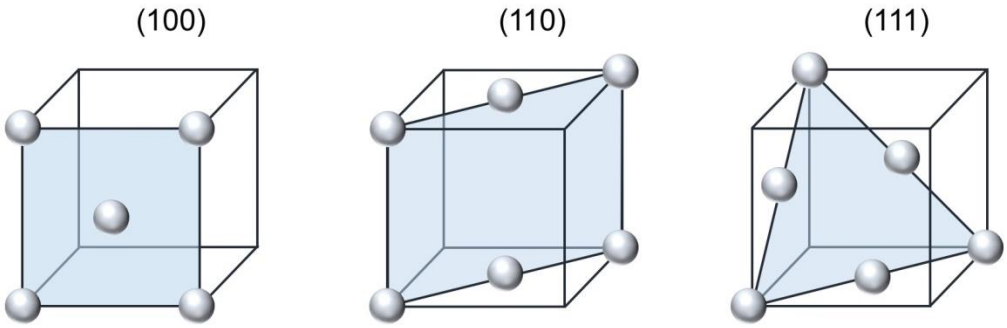

Figure 2.9 schematic representation of the fcc(*hkl*) low index planes.

The spacing between parallel planes is given by:

$$d_{hkl} = \frac{a_0}{\sqrt{H^2 + K^2 + \mathrm{L}^2}} \tag{2.16}$$

where a_0 is the lattice constant.

The scattering geometry from a set of parallel planes is shown in Figure 2.10, the planes are separated by a distance d_{hkl} (the interplanar spacing). When two parallel waves scatter from parallel planes their path difference (the additional distance travelled by the second wave to the lower plane) is given by 2dsinθ. Constructive interference occurs when the path difference is some integer number, n, of wavelength λ. This construction gives us, Bragg's law [39]:

$$n\lambda = 2d\sin\theta \tag{2.17}$$

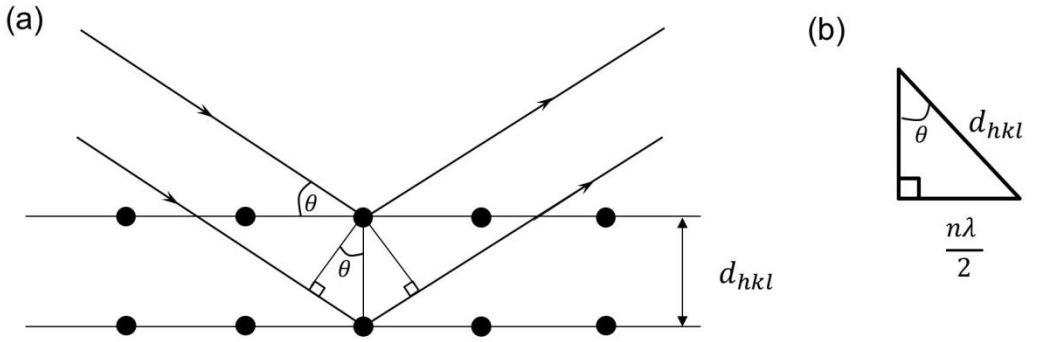

Figure 2.10 Geometric representation of Bragg's law considering scattering from two crystal planes.

Although Bragg's law determines the conditions for constructive interference, it does not consider the scattering power from the atoms in the crystal which one needs to determine structural analysis.

2.4 X-ray Diffraction

The scattering cross-section of X-rays is small, so the effects of multiple scattering can be neglected and a kinematic approach can be taken. Scattering arises from the electrons in an atom, this section will build up the theory of X-ray

diffraction starting from scattering from a single electron, to scattering from the bulk and surface layers of a crystal. The addition of adlayers and electrolyte layering will also be considered. The derivations in this chapter follow references [39–43], which can be referred to for a more rigorous explanation.

2.4.1 Momentum transfer

The important variable in X-ray diffraction is the momentum transfer **q**, which is defined in terms of the incident and diffracted X-ray wave vectors, $\mathbf{k_i}$ and $\mathbf{k_f}$ respectively:

$$\boldsymbol{q} = \boldsymbol{k_f} - \boldsymbol{k_i} \tag{2.18}$$

Where the magnitude of k_i:

$$|\boldsymbol{k_i}| = \left|\boldsymbol{k_f}\right| = |\boldsymbol{k}| = \frac{2\pi}{\lambda} \tag{2.19}$$

where λ is the X-ray wavelength. Using this Bragg's law can now be expressed in terms of the momentum transfer and wave vector(shown schematically in Figure 2.11):

$$|\boldsymbol{q}| = 2|\boldsymbol{k}|sin\theta = \ sin\left(\frac{2\theta}{2}\right) \tag{2.1}$$

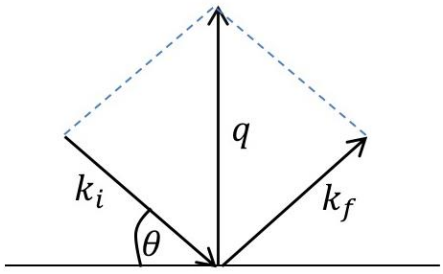

Figure 2.11 Schematic showing construction of momentum transfer q, conserved in in elastic scattering.

2.4.2 Scattering from an electron

When a photon is incident on an electron its electric field exerts a force on the electron causing it to oscillate and radiate a secondary wave with the same wavelength as the incident wave. The amplitude of the scattered wave can be described classically by the Thompson scattering formula which describes the amplitude of a scattered wave A_e from an electron at position r_e as a function of the incident wave A_i:

$$A_e e^{-i(\boldsymbol{k_f}\cdot\boldsymbol{r_e})} = A_i \frac{e^2}{4\pi\epsilon_0 mc^2}\frac{1}{R_0} e^{-i(\boldsymbol{k_i}\cdot\boldsymbol{r_e})} \tag{2.20}$$

The $\frac{1}{R_0}$ term arises from the spherical wave nature, and the prefactor term is the Thompson scattering length $r_0 = \frac{e^2}{4\pi\epsilon_0 mc^2}$. Equation (2.20) can be rewritten in the form:

$$A_e = A_i \frac{r_0}{R_0} e^{i(\boldsymbol{q}\cdot\boldsymbol{r_e})} \tag{2.21}$$

Which gives the amplitude of the scattered wave in terms of the momentum transfer $\boldsymbol{q}$ (where $\boldsymbol{q} = \boldsymbol{k_f} - \boldsymbol{k_i}$).

2.4.3 Scattering from a single atom

The scattering from an atom can be built up by considering its electron density. Scattering from an atom arises from the constructive interference of spherical waves from each electron in the atom. The electron density is $\rho(\boldsymbol{r'})$, where

$\boldsymbol{r}'$ is the position of the electron. The scattering from an atom is given by substituting the positon vector of the electron and summing over the all electrons in the atom. The scattering from an atom is given by:

$$A_a = A_i \frac{r_0}{R_0} \int_{-\infty}^{+\infty} \rho(\boldsymbol{r}')\, e^{-i\boldsymbol{q}\cdot(\boldsymbol{R_n}+\boldsymbol{r_j}+\boldsymbol{r}')} \boldsymbol{d^3 r}' \tag{2.22}$$

$$A_a = A_i \frac{r_0}{R_0} \rho(\boldsymbol{r}') e^{-i\boldsymbol{q}(\boldsymbol{R_n}+\boldsymbol{r_j})} \tag{2.23}$$

and $f(\boldsymbol{q})$ the atomic form factor, is given by:

$$f(q) = \int_{-\infty}^{+\infty} \rho(\boldsymbol{r}')\, e^{-i\boldsymbol{q}\cdot\boldsymbol{r}'} \boldsymbol{d^3 r}' \tag{2.24}$$

The atomic form factor gives a q dependence to the scattering power of each atom, when $\boldsymbol{q}$ =0 all electrons scatter in phase so $f(\boldsymbol{q})$=Z, as $\boldsymbol{q}$ increases electrons begin to scatter out of phase, the atomic form factors are tabulated for each element in the International Tables for Crystallography [45]. The form factor also needs to account for the resonant effect of photons at adsorption edges, the equation is modified by dispersion corrections f' and f'' which are energy dependent:

$$f(\boldsymbol{q}, E) = f(\boldsymbol{q}) + f'(E) + if''(E) \tag{2.25}$$

2.4.4 Scattering from a unit cell

To evaluate the scattering from a unit cell the calculation must sum over all the atoms in the unit cell. As the atoms in the unit cell may not be the same element, the corresponding form factor $f_j(\boldsymbol{q})$ must be included. $\boldsymbol{r_j}$ is the relative position of the *jth* atom in the unit cell:

$$A_u = A_i \frac{r_o}{R_0} \sum_{j=1}^{N} f_j(q) e^{(i\boldsymbol{q}\cdot(\boldsymbol{R_n}+\boldsymbol{r_j})} \tag{2.26}$$

$$A_u = A_i \frac{r_o}{R_0} F(\boldsymbol{q}) e^{(i\boldsymbol{q}\cdot\boldsymbol{R_n})} \tag{2.27}$$

where $F(\boldsymbol{q})$ is the structure factor, given by:

$$F(\boldsymbol{q}) = \sum_{j=1}^{N} f_j(\boldsymbol{q}) e^{i(\boldsymbol{q}\cdot\boldsymbol{r_j})} \tag{2.28}$$

The structure factor is the Fourier transform of the electron density, and dependent on the position of the atoms in the unit cell.

2.4.5 Scattering from a crystal

To determine the electron density of a crystal the atomic distribution must be considered. The next step is to sum the scattering over all the unit cells in the crystal, where the crystal is defined by N_1, N_2 and N_3 unit cells along the crystal axes. The position of each unit cell is given by:

$$R_n = n_1\boldsymbol{a} + n_2\boldsymbol{b} + \mathrm{n}_3\boldsymbol{c} \tag{2.29}$$

The scattered amplitude is thus:

$$A_c = A_i \frac{r_o}{R_0} F(\boldsymbol{q}) \sum_{n_1=0}^{N_1-1} \sum_{n_2=0}^{N_2-1} \sum_{n_3=0}^{N_3-1} e^{iq(n_1\boldsymbol{a}+n_2\boldsymbol{b}+n_3\boldsymbol{c})} \tag{2.30}$$

2.4.6 The scattered intensity

Experimentally it is the scattered intensity which is measured, the amplitude is related to the scattered intensity by $I(\boldsymbol{q}) \propto |A_c|^2$. Consider one term which is the sum of a geometric progression written in the form:

$$S_{N_1}(\boldsymbol{q}\cdot\boldsymbol{a}) = \sum_{n_1=0}^{N_1-1} e^{i\boldsymbol{q}\cdot(n_1\boldsymbol{a})} = \frac{1-e^{iN_1\boldsymbol{q}\cdot\boldsymbol{a}}}{1-e^{i\boldsymbol{q}\cdot\boldsymbol{a}}} \tag{2.31}$$

Applying Euler's formula $e^{i\theta} = cos\theta + isin\theta$, and multiplying the equation by its complex conjugate, it becomes:

$$\left|S_{N_1}(\boldsymbol{q}\cdot\boldsymbol{a})\right|^2 = \frac{sin^2(N_1\boldsymbol{q}\cdot\boldsymbol{a}/2)}{sin^2(\boldsymbol{q}\cdot\boldsymbol{a}/2)} \tag{2.32}$$

This is analogous to the N-slit interference function. The interference function reflects the periodic array of atoms in the crystal, which gives rise to diffraction spots, Bragg reflections, in reciprocal space. The equations gives maxima when $\boldsymbol{q}\cdot\boldsymbol{a} = 2\pi n$ where n is an integer.

The scattered intensity is defined as:

$$\mathrm{I}(\boldsymbol{q}) = I_i\left(\frac{r_0}{R0}\right)^2 |F(\boldsymbol{q})|^2 \frac{sin^2\left(\frac{1}{2}N_1\boldsymbol{q}\cdot\boldsymbol{a}\right)}{sin^2(\frac{1}{2}\boldsymbol{q}\cdot\boldsymbol{a})}\frac{sin^2\left(\frac{1}{2}N_2\boldsymbol{q}\cdot\boldsymbol{b}\right)}{sin^2(\frac{1}{2}\boldsymbol{q}\cdot\boldsymbol{b})}\frac{sin^2\left(\frac{1}{2}N_3\boldsymbol{q}\cdot\boldsymbol{c}\right)}{sin^2(\frac{1}{2}\boldsymbol{q}\cdot\boldsymbol{c})} \tag{2.33}$$

were I_i is the intensity of incident photon. When the following conditions are met, the above equation produces maxima. These are the Laue conditions for diffraction:

$$\boldsymbol{q}\cdot\boldsymbol{a} = 2\pi H$$

$$\boldsymbol{q} \cdot \boldsymbol{b} = 2\pi K$$

$$\boldsymbol{q} \cdot \boldsymbol{c} = 2\pi L \tag{2.34}$$

which satisfy the vector $\boldsymbol{q} = H\boldsymbol{a}^* + K\boldsymbol{b}^* + L\boldsymbol{c}^*$ where the reciprocal space vectors are related to real-space vectors by:

$$\boldsymbol{a}^* = 2\pi \frac{\boldsymbol{b} \times \boldsymbol{c}}{\boldsymbol{a} \cdot (\boldsymbol{b} \times \boldsymbol{c})} \tag{2.35}$$

$$\boldsymbol{b}^* = 2\pi \frac{\boldsymbol{c} \times \boldsymbol{a}}{\boldsymbol{b} \cdot (\boldsymbol{c} \times \boldsymbol{a})} \tag{2.36}$$

$$\boldsymbol{c}^* = 2\pi \frac{\boldsymbol{a} \times \boldsymbol{b}}{\boldsymbol{c} \cdot (\boldsymbol{a} \times \boldsymbol{b})} \tag{2.37}$$

When h, k and l are integer values they form a 3D lattice satisfying the Laue conditions and can also be described by the Bragg condition.

The intensity at a particular **q** value is given by:

$$I_{hkl} = I_i \left(\frac{r_0}{R_0}\right)^2 |f(\boldsymbol{q})|^2 N_1^2 N_2^2 N_3^2 \tag{2.38}$$

2.5 Surface X-ray Diffraction

2.5.1 Scattering from a surface

So far the calculations have assumed scattering from a crystal which is infinite in all directions. We are interested in the surface structure, and therefore we must modify the equations to consider scattering from the surface. When the crystal is terminated at the surface the Laue condition for the c direction is no longer valid, as the crystal is semi-infinite along the c axis. This reduces equation (2.38) to:

$$I_{CTR} = I_0 \left(\frac{r_0}{R_0}\right)^2 |f(\boldsymbol{q})|^2 N_1^2 N_2^2 \frac{1}{2sin^2\left({}^1/_2\, \boldsymbol{q} \cdot \boldsymbol{c}\right)} \tag{2.39}$$

This equation produces sharp peaks in intensity for values where L is an integer, in equation 2.40, which corresponds to Bragg peaks due to scattering from the bulk. In between the Bragg peaks the intensity is modulated along the surface normal, L, direction Figure 2.13. These streaks of intensity have been termed as Crystal Truncation Rods (CTRs) by Robinson [40].

2.5.2 Modelling surface structure

The equation above assumes a perfectly terminated crystal. This is not usually the case. Factors such as surface roughness, σ, surface relaxations, ε, and occupation, θ, modify the shape of the CTR profile.

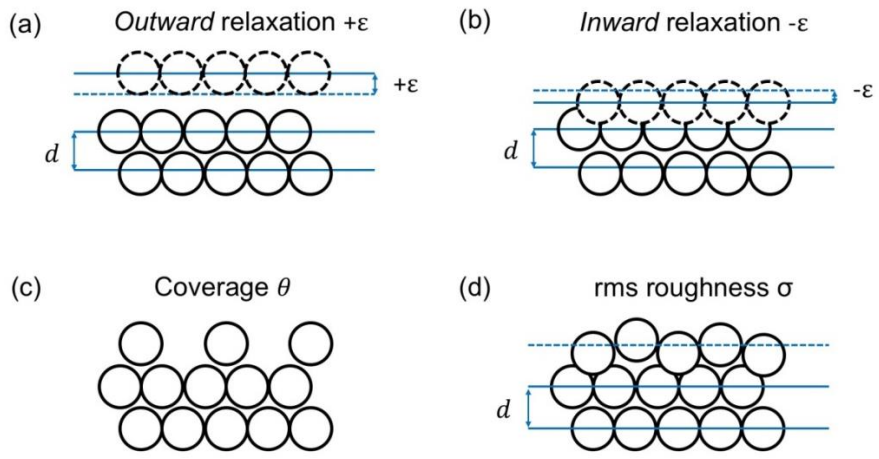

Figure 2.12 Schematic representation of the structural parameters used to model the surface. Side view of a crystal (a) Top metal layer undergoes an outward relaxation, where the layer relaxes away from the bulk (into vacuum, or electrolyte) – increasing the d-spacing. (b) Top metal layer undergoes an inward relaxation; where the layer relaxes towards the bulk – decreasing the d-spacing. (c) Change in coverage; given in a fractional form of the bulk-terminated surface. (d) rms roughness – average displacement of atoms.

The physical representation of these parameters is shown in Figure 2.12. The effects of these parameters are illustrated in Figure 2.13. When surface undergoes a relaxation (*inwards* or *outwards*) this causes an asymmetry around the Bragg peaks (Bragg peaks where intensity is a maximum). Reduced surface occupation causes a decrease in intensity between the Bragg peaks, which is most noticeable at the anti-Bragg position which is half way between two Bragg peaks, the position most sensitive to the termination of the surface . An increased surface roughness has a similar effect, however, the decrease in intensity at the anti-Bragg position which becomes greater with increasing L. By careful modelling of the CTR data it is possible to extract structural information such as the coverage, surface roughness, and relaxations of the crystal surface and of any adsorbed structures.

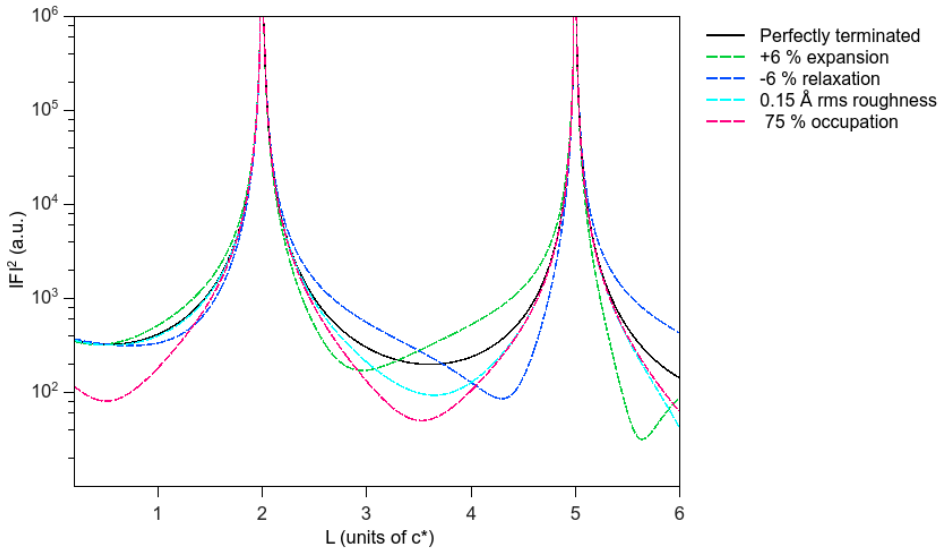

Figure 2.13 Demonstration of how changing different structural parameter modify the CTR profile. The in-plane CTR for a Ag(111) surface was simulated by a python program. The solid black line indicates the perfectly terminated surface.

The specular CTR

The **q** vector is entirely along the surface normal direction. It is unique in that there is no momentum transfer (component of **q**) in the surface plane.

Non-specular CTRs

Non-specular CTRs have an additional in-plane momentum transfer, which is sensitive to the in-plane structure of the surface layers.

Fractional Order Rods FORs

If the termination of the surface reconstructs, or there are ordered adsorbed structures on the surface with a different symmetry to the bulk crystal lattice, then the scattering becomes separate from the bulk. The structure gives rise to additional rods of scattering termed fractional order rods (FORs) or superstructure rods.

In this thesis all three fcc(*hkl*) low index surfaces have been studied. In following sections, each surface will be treated in turn to determine the layering and structure of the surface.

2.5.3 The (111) surface

The (111) surface is the most close packed of the three low index fcc surfaces. The layer stacking is ABC with layer B in the fcc hollow sites and layer C in the hcp hollow sites.

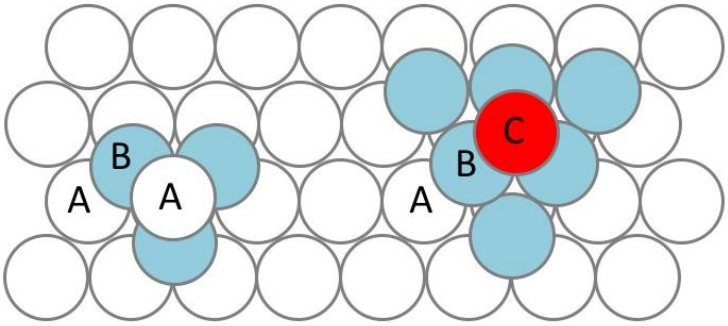

Figure 2.14 Schematic of hcp (left) and fcc (right) stacking. Atoms are arranged in a hexagonal pattern in layer A, the second layer, B, is shifted so that the atoms fill the hollow sites of layer A. In for hcp stacking the next layer lies directly above A – giving ABA stacking, or it is shifted with respect to both A and B, and lies in the hollow sites of layer B – giving ABC stacking.

The layer stacking defines the c lattice parameter as shown in Figure 2.15 (a). The layer stacking defines the separation of Bragg peaks in reciprocal space, in this case the unit cell is repeated every 3 layers, thus the Bragg peaks are separated by 3 in *L*, as seen in Figure 2.15 (c).

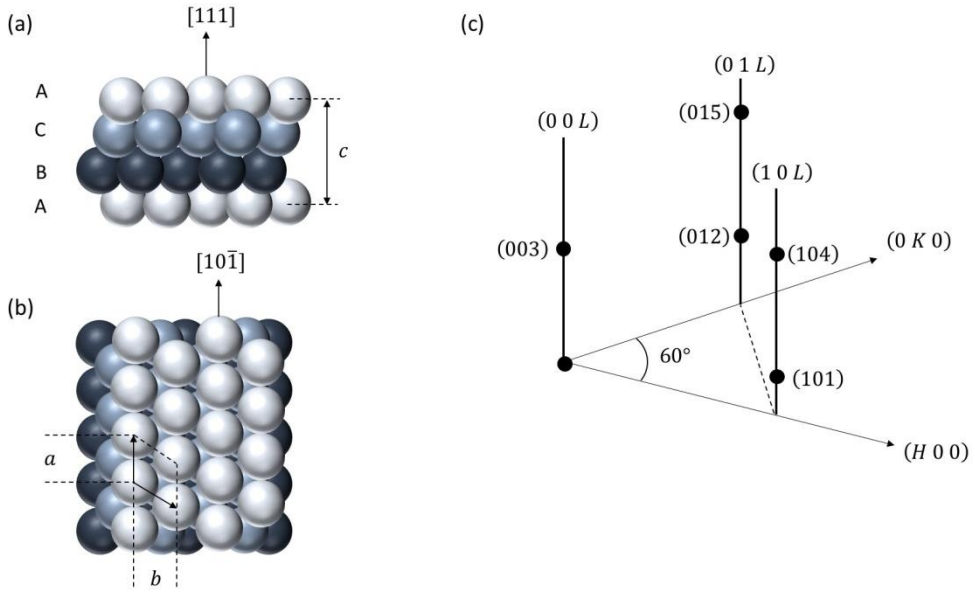

Figure 2.15 Schematic of fcc(111) (a) side-view real space structure (b) top view real space structure (c) corresponding Bragg reflections in the reciprocal space lattice.

The directions are defined such that H and K vectors, $[H\ 0\ 0]_{hex}$ and $[0\ K\ 0]_{hex}$, lie in the surface plane and subtend an angle of 60° and L is defined along the surface normal $[0\ 0\ K]_{hex}$ direction. The units of H, K and L are defined as:

$$\boldsymbol{a}^* = \boldsymbol{b}^* = \frac{4\pi}{\sqrt{3}a_{NN}} \text{ and } \boldsymbol{c}^* = \frac{2\pi}{\sqrt{6}a_{NN}} \tag{2.41}$$

Where a_{NN} is defined as the near-neighbour distance.

The cubic unit cell is related to the surface unit cell by the following transformations:

$$\begin{aligned} H_{cubic} &= \frac{2}{3}H_s - \frac{2}{3}K_s + \frac{2}{3}L_s \\ K_{cubic} &= \frac{2}{3}H_s + \frac{4}{3}K_s + \frac{1}{3}L_s \\ L_{cubic} &= -\frac{4}{3}H_s - \frac{2}{3}K_s + \frac{2}{3}L_s \end{aligned} \tag{2.42}$$

To determine the scattering from the CTR the bulk structure factor must be considered first. As the crystal is semi-infinite the equation is summed from z = 0 to z = -∞. The phase difference between layers must be considered, as previously mentioned, the (111) unit cell repeats every 3 layers thus the phase difference is given by $e^{2\pi i\left(-\frac{\boldsymbol{H}}{3}+\frac{K}{3}+\frac{L}{3}\right)}$, the coordinates of the atoms in the first layer situated at (0, 0, 0), 2nd (-1/3, 1/3, 1/3) and 3rd at (-2/3, 2/3, 2/3):

$$F_{Bulk} = f(\boldsymbol{q})f_{DWF}\sum_{j=0}^{-\infty} e^{2\pi i\left(-\frac{H}{3}+\frac{K}{3}+\frac{L}{3}\right)j} = \frac{f(\boldsymbol{q})f_{DWF}}{1 - e^{2\pi i\left(\frac{H}{3}+\frac{K}{3}+\frac{L}{3}\right)}} \tag{2.43}$$

where $f(\boldsymbol{q})$ is the atomic form factor and f_{DWF} is the bulk Debye-Waller factor which accounts for the thermal disorder of the atoms in the bulk. The disorder of atoms has the effect of decreasing the peak diffracted intensity. The Debye-Waller factor is related to the root-mean-squared (rms) displacement of atoms about their equilibrium position σ. The Bulk Debye-Waller factor is given by:

$$f_{DWF} = e^{-\frac{1}{2}\boldsymbol{q}^2\langle {\sigma_{\boldsymbol{q}}}^2\rangle} \tag{2.44}$$

Where $\langle {\sigma_{\boldsymbol{q}}}^2\rangle$ is the average atomic displacements:

$$\langle {\sigma_{\boldsymbol{q}}}^2\rangle = \frac{B}{8\pi^2} \tag{2.45}$$

Where the B-factor (units $Å^2$) of an element can be found as a function of temperature is tabulated in the international tables of crystallography. The units of σ are in angstroms.

When a surface is terminated the properties of the surface layers differ from that of the bulk and this difference can extend several layers into the bulk. To account for the differences the surface is modelled separately from the bulk, usually only the top 3 layers are considered in the modelling for systems concerned in the thesis. The structure factor of the surface layers is given by:

$$F_{Surf} = \sum_{j=1}^{j=3} f(\boldsymbol{q}) f_{DWF(j)} \theta_j e^{2\pi i\left(-\frac{1}{3}H+\frac{1}{3}K+\left(\frac{1}{3}+\varepsilon_j\right)L\right)j} \tag{2.46}$$

A number of additional terms are included in the calculation for the surface layers. The Debye-Waller factor of each layer is considered separately by the term $f_{DWF(j)}$ as it can differ from the bulk due to the difference in interatomic bond strengths. It is

usually modelled as the bulk Debye-Waller factor multiplied by an individual component for each layer, along the surface normal:

$$f_{DWF(j)} = e^{-\frac{1}{2}\langle q\sigma\rangle^2} \cdot e^{-\frac{1}{2}\langle q_z\sigma_j\rangle^2} \tag{2.47}$$

θ_j is the occupation of the surface layers which is a percentage of a complete monolayer, and ε_j accounts for the displacement of the layers away from their equilibrium position. The effect of these parameters is discussed later in the chapter in section 2.5.2.

The total scattered intensity is given by:

$$I_{Tot} = |F_{Tot}|^2 = \left|F_{Bulk} + F_{Surf}\right|^2 \tag{2.48}$$

2.5.4 The (001) surface

The (001) surface has a square unit cell, which is more open than the (111) surface. It has ABAB stacking where layer B sits in the four-fold hollow sites of layer A. The structure is shown schematically in Figure 2.16.

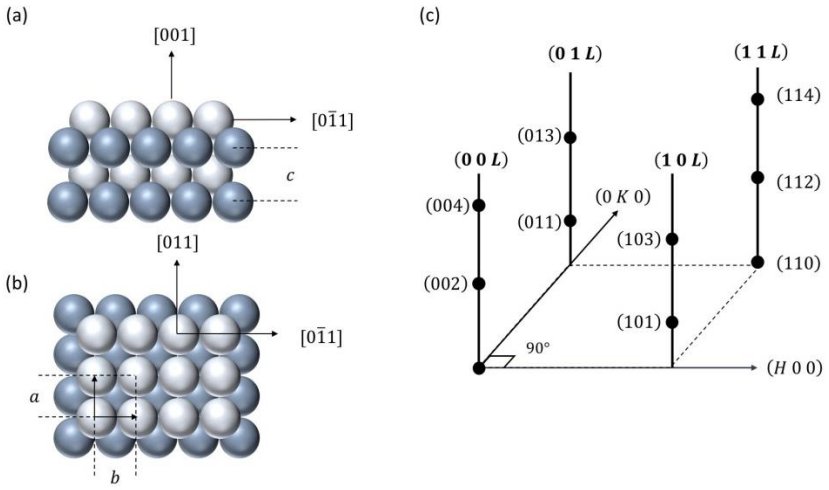

Figure 2.16 Schematic of fcc(001) (a) side view real-space surface structure (b) top view real-space surface structure (c) corresponding Bragg reflections in the reciprocal space lattice.

For SXRD experiments the (001) surface is indexed to a surface tetragonal unit cell. This can be related to the bulk cubic unit cell by the following transformations:

$$H_c = H_s + K_s \tag{2.49}$$

$$K_c = H_s - K_s \tag{2.50}$$

$$L_c = L_s \tag{2.51}$$

The units of H, K and L are given by:

$$\boldsymbol{a}^* = \boldsymbol{b}^* = \frac{2\pi}{a_{NN}} \;\; and \;\; \boldsymbol{c}^* = \frac{4\pi}{\sqrt{2}a_{NN}} \tag{2.52}$$

The phase factor for the (001) surface is $e^{2\pi i\left(\frac{H}{2}+\frac{K}{2}+\frac{L}{2}\right)}$. Similarly to the (111) the CTRs can be described by considering the bulk and surface layers separately. The bulk structure factor is given by:

$$F_{Bulk} = \frac{f(\boldsymbol{q})f_{DWF}}{1 - e^{2\pi i\left(\frac{H}{2}+\frac{K}{2}+\frac{L}{2}\right)}} \tag{2.53}$$

and the scattering from the top 3 layers is:

$$F_{Surf} = \sum_{j=1}^{j=3} f(\boldsymbol{q})f_{DWF(j)}\theta_j e^{2\pi i\left(\frac{1}{2}H+\frac{1}{2}K+\left(\frac{1}{2}+\varepsilon_j\right)L\right)j} \tag{2.54}$$

2.5.5 The (110) surface

The (110) is the most open of the three low index surfaces, with a rectangular unit cell shown in Figure 2.17. The surface is defined such that *H* is along the $[1\ \bar{1}\ 0]$ direction, *K* along $[0\ 1\ 0]$ and *L* is defined along the surface normal $[1\ 1\ 0]$ with ABAB layer stacking. The Bragg peaks of the (110) surface are spaced much further apart than the other two surfaces, this is because the layer spacing is so small.

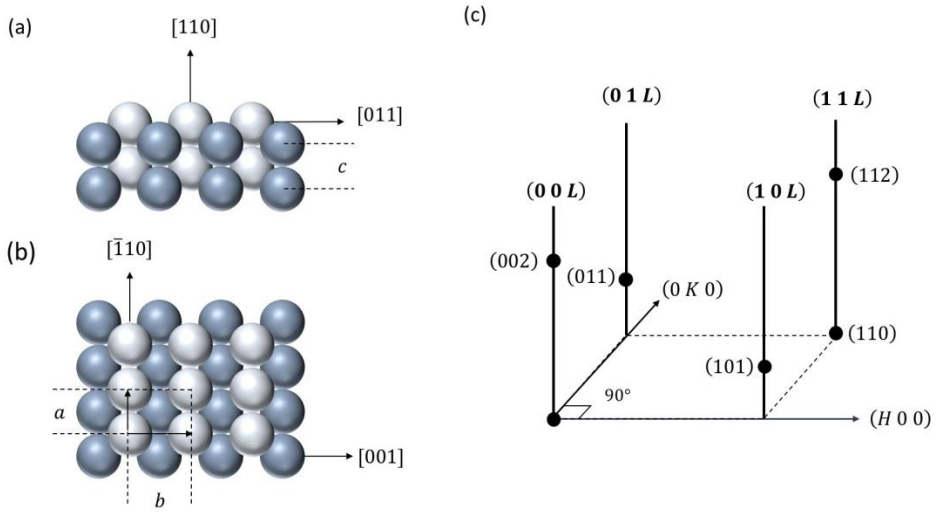

Figure 2.17 Schematic of (110) (a) side view real-space surface structure (b) top view real-space surface structure (c) corresponding Bragg reflections in the reciprocal space lattice.

$$\boldsymbol{a}^* = \boldsymbol{b}^* = \frac{2\pi}{a_{NN}} \;\; and \;\; \boldsymbol{c}^* = \frac{4\pi}{\sqrt{2}a_{NN}} \tag{2.55}$$

The surface cell is related to the bulk cubic unit cell by the following transformations:

$$H_c = K_s + L_s \tag{2.56}$$

$$K_c = -H_s + K_s \tag{2.57}$$

$$L_c = K_s \tag{2.58}$$

As with the previous surfaces, the CTRs can be described by separate bulk and surface terms. Like the (001) surface, the (110) also has ABAB stacking, giving a phase difference of $e^{2\pi i\left(\frac{H}{2}+\frac{K}{2}+\frac{L}{2}\right)}$. The scattering from the bulk is given by

$$F_{Bulk} = \frac{f(\boldsymbol{q})f_{DWF}}{1 - e^{2\pi i\left(\frac{H}{2}+\frac{K}{2}+\frac{L}{2}\right)}} \tag{2.59}$$

with scattering from the top three surface layers.

$$F_{Surf} = \sum_{j=1}^{j=3} f(\boldsymbol{q}) f_{DWF(j)} \theta_j e^{2\pi i\left(\frac{1}{2}H+\frac{1}{2}K+\left(\frac{1}{2}+\varepsilon_j\right)L\right)j} \tag{2.60}$$

2.6 Modelling surface structures and the electrode/electrolyte interface

Up to this point only the bulk terminated surface structure has been considered in the structure factor, however, it is possible to modify the equations to include scattering from other surface structures, ordered electrolyte layering and scattering from the bulk electrolyte. Adlayer structures can be commensurate, which have registry with the surface structure or incommensurate and the equation must be modified accordingly.

The total form factor would then be:

$$|F_{Tot}|^2 = \left|F_{Bulk} + F_{Surf} + F_{Com} + F_{incom}\right|^2 \tag{2.61}$$

2.6.1 Commensurate adlayers

Under certain conditions in UHV and in the electrochemical environment species can adsorb on the electrode surface. Depending upon the electrode surface, adsorbed species and growth conditions ordered structures can form. As the structures have in-plane ordering they can have a dramatic effect on the non-specular CTR profile, see Figure 2.18, and the therefore the structure must be considered in the calculation.

In order to model this equation (2.46) must be modified to account for the different element, the form factor, and the structure. For example, consider a commensurate Ag layer on an Au(111) electrode surface, adsorbed in the 3-fold hollow sites.

Then equation (2.46) then becomes:

$$F_{Surf} = f(\boldsymbol{q})_{Ag}\theta_{Ag}f_{DWF(Ag)}\theta_j e^{2\pi i\left(-\frac{1}{3}H+\frac{1}{3}K+\left(\frac{1}{3}+\varepsilon_{Ag}\right)L\right)Ag} \tag{2.62}$$

For other commensurate structures, the *H*,*K*,*L* positions are changed.

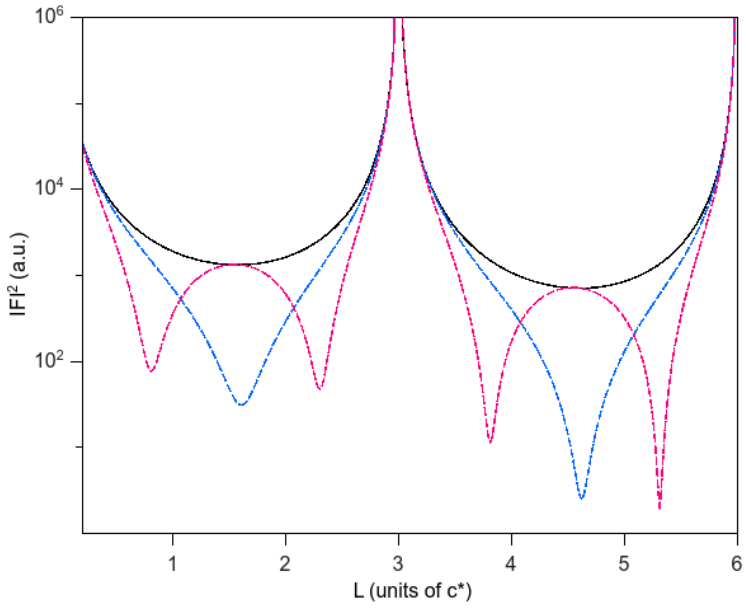

Figure 2.18 CTR profiles calculated from a python program. The solid black line is the CTR profile for a perfectly terminated Au(111) surface, a commensurate monolayer of Ag (the blue dashed line), a commensurate bilayer Ag (dashed pink line).

The addition of commensurate layers of an element different to the bulk causes the CTR profile to change dramatically, this can be seen in Figure 2.18. The addition of one commensurate layer causes a decrease of intensity between the Bragg peaks with a minimum intensity at the anti-Bragg position. The addition of a commensurate

bilayer manifests as an oscillation between the Bragg peaks with two minima. The profile of the CTR is thus dependent upon the number of commensurate layers

2.6.2 Incommensurate adlayers

An incommensurate adlayer has no in-plane registry with the underlying crystalline lattice, and is therefore only effects the specular CTR, for which the momentum transfer is entirely along the surface normal. An incommensurate layer can be modelled using the following equation, which is only dependent on *L*.

$$F_{incom} = f(\boldsymbol{q})_{ad}\theta_{ad}f_{dwf_{ad}}e^{2\pi il(\mathrm{H})}$$

where H_{ad} is the height of the adlayer.

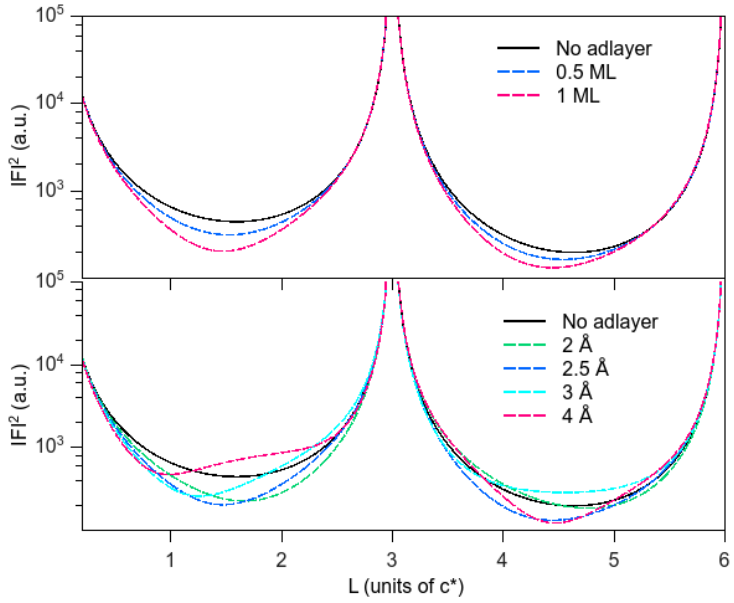

Figure 2.19 Specular CTR of an Au(111) surface calculated using a python program to simulate the structure. The effect of adlayer coverage and interlayer spacing on the profile of the CTR is demonstrated. In the top panel an incommensurate adlayer was included into the model at a height of 2.5 Å above the top metal layer. In the bottom panel the coverage of the adlayer is fixed at 1 ML and the height of the adlayer is changed.

Figure 2.19 shows the effect of an adlayer on the specular CTR. The top panel shows how increasing adlayer coverage decreases intensity at the anti-Bragg. Changing the height of the layer affects the asymmetry around the Bragg peaks.

2.6.3 Modelling electrolyte

At the electrode/electrolyte interface layering of water molecules, and ions can occur. These layers are often disordered in-plane and can be modelled as an incommensurate adlayer. This is usually sufficient to model the structure at the interface, however, there are small contributions from the bulk electrolyte which should be added to the model for completeness.

An error function is used to model the bulk electrolyte, this is a smooth function which starts from the top surface layer and saturates at a distance where the composition of the electrolyte becomes that of bulk electrolyte. An alternative approach is to use a layered profile function. Both models are discussed in reference [46] and the electron density profiles are shown in Figure 2.20.

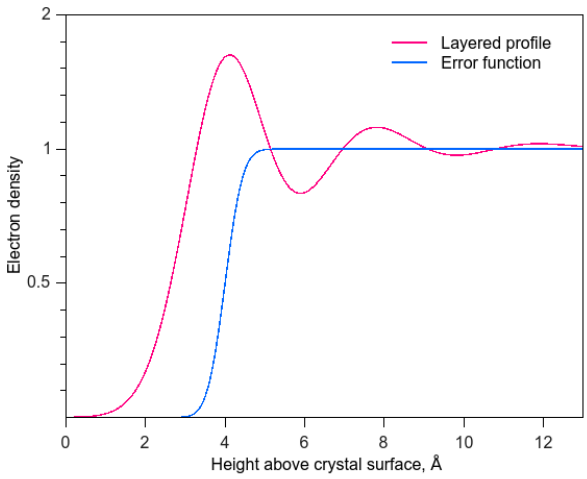

Figure 2.20 Electron density profiles from the top of a crystal surface of the error function and a layered model. Profiles were simulated using a python program.

2.7 Conventions used throughout thesis

Surface layers

Throughout this thesis usually the top three layers of a metal are modelled as the 'surface layers', and as such they are modelled independently of the bulk. The layers are defined such that layer 1 is at the vacuum/electrolyte interface and layer 3 is closest to the bulk. The interlayer distance d_{12} is defined as the distance between layers 1 and 2, this is shown schematically in Figure 2.21

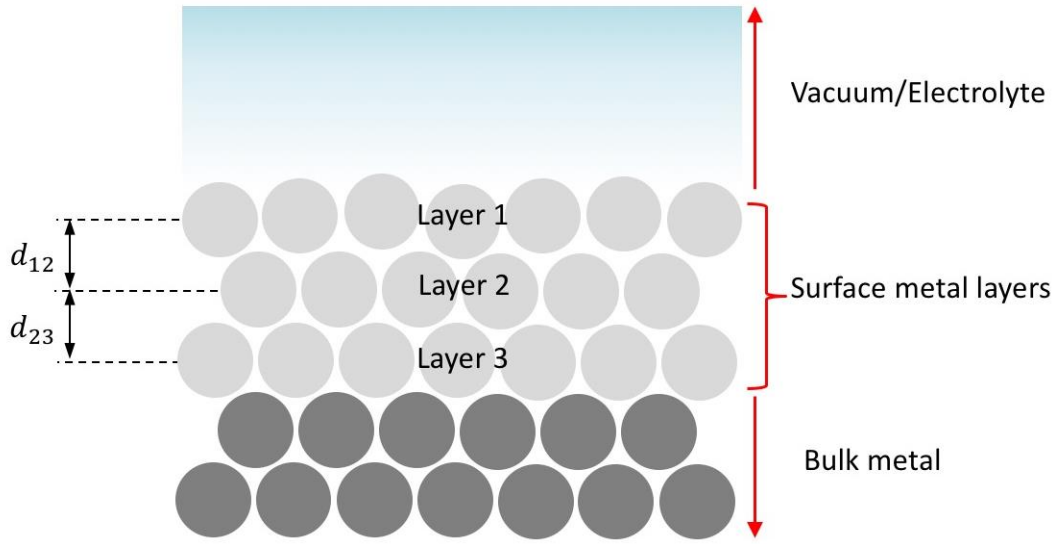

Figure 2.21 Metal interface structure. Metal layer 1 is defined as the layer at the metal/ vacuum(or electrolyte) interface. The top 3 metal layers are modelled as the 'surface', bulk metal is modelled separately.

Adlayers

The height of additional adlayers, or liquid layers, are measured at a distance from the top metal layer, this is shown schematically in Figure 2.22.

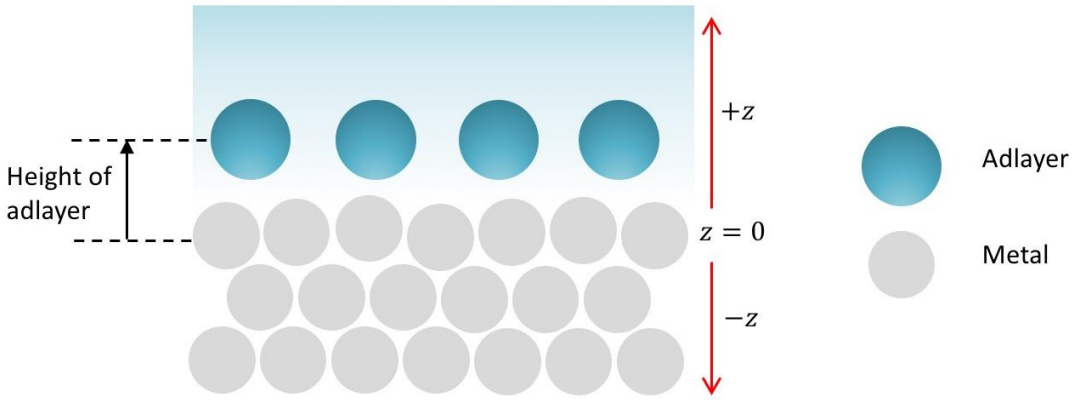

Figure 2.22 Height of adlayer measured above equilibrium position of the top surface metal layer.

2.8 X-ray voltammetry

X-ray voltammetry (XRV) is a technique which combines X-ray diffraction with cyclic voltammetry. This is an extremely powerful technique whereby the structural changes can be dynamically linked to the change in potential, these can be correlated to the current response in the cyclic voltammetry measurements. The X-ray intensity is measured as a function of potential at a fixed point in reciprocal space. The point in reciprocal space is chosen for its sensitivity to a particular surface property, such as relaxation of the surface, commensurate adlayer adsorption or the fact that new scattering arises due to the formation of a superstructure. In an experiment the surface is usually characterized by XRV to evaluate the potential ranges over which stable interface structures are formed. The system can then be studied in detail (CTR measurements) at the relevant applied potentials.

2.9 Low Energy Electron Diffraction, LEED

Low energy electrons have a have a short mean free path which means they can only probe the first few layers of a crystal, rendering them highly surface

sensitive. Low Energy Electron Diffraction (LEED) is dependent upon the wave nature of electrons. The wavelength of an electron beam is given by the non-relativistic De Broglie relation:

$$\lambda_i = \frac{h}{mv} = \frac{h}{p} \tag{2.63}$$

where, h is Planck's constant, m is the mass of an electron and p is the momentum.

A beam of electrons of a well-defined energy (usually 20-300 eV) is fired at a normal to the sample surface. A typical LEED setup is shown in Figure 2.23. Electrons are emitted from a filament and accelerated into a drift tube before hitting the surface. Electrons are back-scattered from the surface according to Bragg diffraction conditions (see equation 2.64) onto a series of grids, this is shown schematically in Figure 2.23. The sample must be well ordered, to give rise to a LEED pattern. Elastically scattered electrons are accelerated towards the fluorescent screen and contribute to the LEED pattern. Inelastically scattered electrons contribute to a bright background light across the screen. By applying a voltage to the other grids the inelastically scattered electrons can be suppressed, thereby reducing the diffuse background.

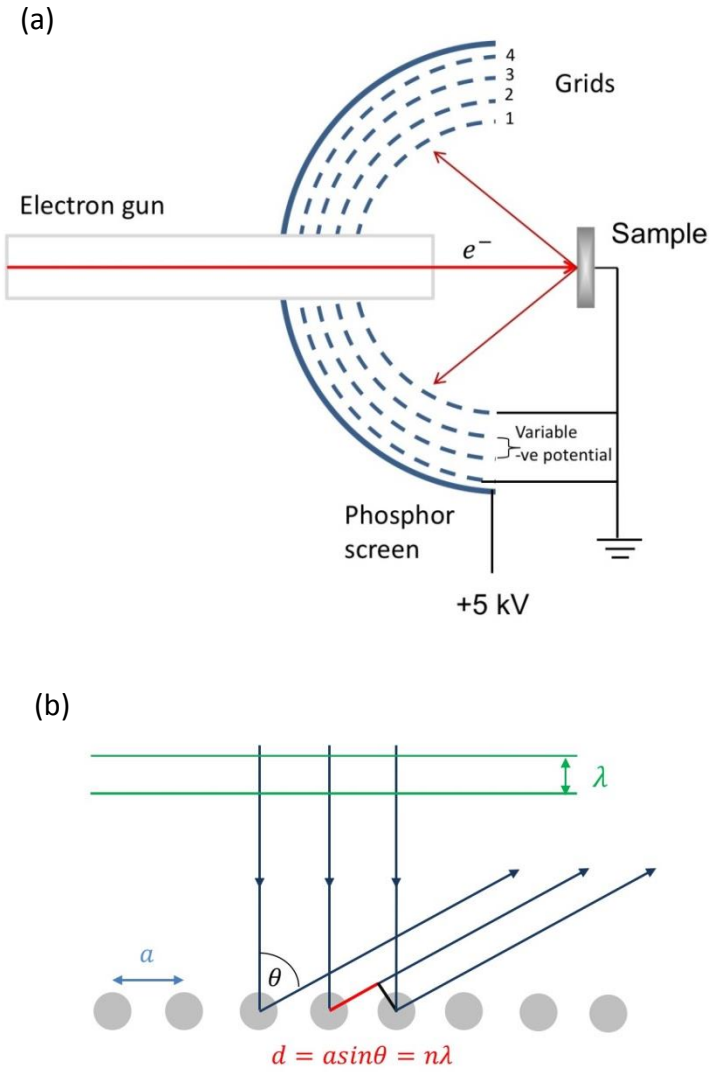

Figure 2.23 Schematic of (a) LEED optic (b) Schematic representation of the backscattered electrons from a one dimensional array of atoms with a regular lattice spacing, a. The wavelength of incoming electrons is represented by the green lines, and the path difference, d, between the scattered waves is indicated in red.

Diffraction spots occur over a range of energies, dependent on whether the rod is within the Ewald sphere. The energy of the incident electron beam is given by:

$$E = \left(\frac{\hbar^2}{2m}\right)\boldsymbol{k^2} \tag{2.65}$$

Where $\boldsymbol{k} = \frac{2\pi}{\lambda}$. By varying the energy of the incident beam the radius of the Ewald sphere $\boldsymbol{k_i}$, changes. The Ewald Sphere is a geometric construction of the interference condition. Higher energies allow access to a larger area of reciprocal space as the Ewald sphere cuts more rods which manifests as an increase in the number of diffraction spots in the LEED pattern, this is shown schematically in Figure 2.24. LEED is often used to determine the cleanliness and quality of a surface. A LEED pattern which has sharp bright spots with a low background is considered to be a well ordered clean surface. However, this is not always the case, a sample which has a good LEED pattern can appear rough with SXRD or to imaging techniques, such as STM. Despite this, LEED gives a good indication as to the surface structure of the electrode surface; from the diffraction pattern the unit cell of the surface can be determined. LEED can also be used to determine the structure of adsorbed overlayers, and their registry to the electrode surface.

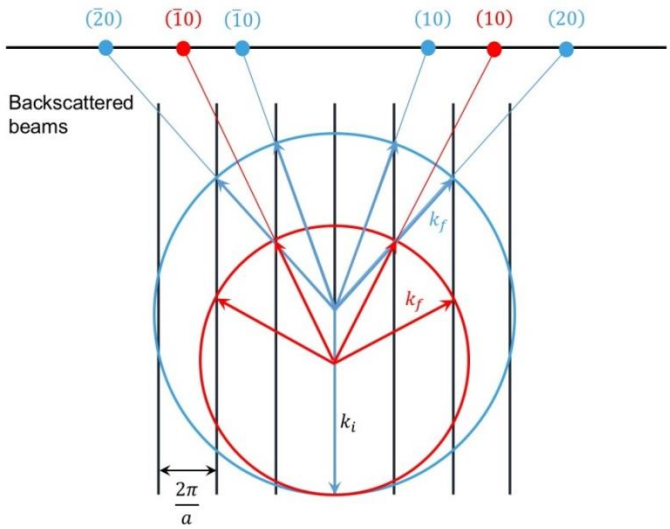

Figure 2.24 Ewald sphere construction for an electron beam incident normal to the surface. The blue Ewald sphere has greater energy than the red, which increases the radius of the sphere and the diffraction spots appear closer on the screen.

2.10 X-ray photoemission spectroscopy XPS

XPS is used to determine the cleanliness of the electrode surface. The working principle of XPS is based on the photoelectric effect. XPS measures the kinetic energy of electrons emitted after a sample is radiated with X-rays. The kinetic energy of the electrons can be determined from the following relationship:

$$E_k = E_p - (E_b + \phi) \tag{3.2}$$

Where E_k is the kinetic energy of the electrons, E_b is the binding energy of the electrons, E_p is the energy of the photons, and ϕ is the work function of the surface. An XPS spectrum consists of a plot of the number of counts against the binding energy. Peaks in the spectrum can be associated with a particular element – spectra for the elements are tabulated in literature [47]. XPS can be used to identify additional peaks that arise from contamination, such as oxygen or carbon. Once the XPS spectra are free from additional peaks, the sample is determined to be clean.

2.11 Why surface X-ray diffraction?

The primary technique used in this thesis is surface X-ray diffraction. As previously highlighted SXRD is very surface sensitive and it is also highly versatile, as it can be used *in situ* in a variety of environments – meaning it is an ideal technique in order to probe the solid/liquid interface. Although electrochemical STM has been used to probe the structure of the solid/liquid interface [48–50] there are limitations to this technique – the STM tip can interfere with the with the interface structure [51] and cannot probe electrolyte layering. These limitations can be

overcome by using SXRD, as the probe does not interfere with the measurement (although there are particular circumstances were a beam effect does come into play [52]). By measuring the specular CTR, which has momentum transfer completely in the surface normal rendering it sensitive to changes in electron density about the surface normal, electrolyte layering can be probed [23,53,54].

Although LEED-IV is routinely performed for studies in vacuum, data analysis can be timely as a dynamic (multiple scattering effects must be considered) approach must be used. Use of SXRD can dramatically reduce the analysis time as a kinematic (single scattering) approach can be applied.

There are, of course, disadvantages to SXRD such as the need for a high intensity X-ray beam in order to resolve small scattering signal of the interface structure from background scattering, and the ability to penetrate through electrolyte. For this a synchrotron is required. This can be a problem in itself, as there is limited access time to a synchrotron source. One must submit a proposal applying for beamtime - gaining beamtime is very competitive.

Although there are some disadvantages of SXRD, the advantages far outweigh these, and confirm SXRD as a powerful, versatile technique. Access to beamtime is incredibly valuable and the experiments can deliver a wealth of information. More recently it is has been possible to perform time resolved measurements [55–60] which can probe structural changes of a dynamic interface in order to determine structural kinetics.

3 Experimental methods

3.1 Introduction

The previous chapter built up the theoretical considerations behind SXRD experiments in UHV and in an electrochemical environment. The outcome of such experiments is crucially dependent upon the sample and environmental preparations prior to the measurements. This chapter outlines the methods used to prepare and characterise single crystals, and the electrochemical and diffraction setup. Beyond this there is a discussion of the synchrotron beamline; how to start an experiment through to how to process and analyse the data.

3.2 Sample preparation and characterisation

The preparation of a clean highly ordered crystal is of vital importance in both UHV and electrochemical environment. Changes to the surface can affect the interface structures and alter the electrochemical response. For this reason, a lot of

care and time was taken to prepare clean and atomically well-defined samples. Samples used for electrochemical measurements were bought from Material-Technologie & Kristalle GmbH, Mateck, Germany, and were circular, with 10 mm diameter and 3 mm thick, aligned to within <0.1° miscut. Samples for UHV experiments were bought from Surface Preparation Laboratory, SPL, in the Netherlands, aligned to within <0.1° miscut. The samples had a groove around the sides which was used to hold tantalum strips for mounting to a plate in UHV, see Figure 3.1. After receiving the crystals further preparation was required to ensure the crystals had a clean highly ordered surface before experiments. To do this the crystals were prepared and characterised in UHV.

Figure 3.1 Gold and silver crystals mounted on plates in UHV.

3.2.1 UHV sample preparation

The samples were cleaned through several sputter and anneal cycles. The surface is 'sputtered' by bombarding with Ar^+ ions at 10^{-6}mbar, 1kV for 15-20 minutes; this removes contamination from the surface. The sample is subsequently annealed; a current is passed through a filament, which is in thermal contact with the sample. Samples are usually annealed for 15-20 minutes, although sometimes it is

necessary to do a long anneal (1 hour) in order to improve the surface quality. Annealing the sample orders the surface, however, it can also bring up any impurities from the bulk, especially when preparing a new crystal, which is why repeat cycles and careful monitoring of the surface condition is required. Monitoring is done by X-ray Photoemission Spectroscopy (XPS), and LEED. The majority of work in this thesis is on silver single crystals. Silver requires UHV preparation before every experiment. There are electrochemical methods for cleaning silver; however, they can roughen the surface over time. Silver samples were treated with great care; annealing was kept under 500 ℃ as above this temperature the surface can lose long range order [61] and appear cloudy by the eye. As the Ag surface can easily oxidise in air, the transfer to the electrochemical cell is a delicate process requiring the load lock of the UHV chamber to be surrounded by a glove bag filled with inert gas, such as Argon. The sample is then transferred out into the inert atmosphere and inserted into an acid cleaned beaker of ultrapure Milli-Q water. Great care must then be given to transfer the crystal into the electrochemical cell, keeping the surface covered with electrolyte at all times.

3.2.2 Flame Annealing

After preparation in UHV gold crystals can be easily reprepared through a flame annealing technique, which has been shown to produce highly ordered surfaces [2-3]. The technique involves annealing the gold crystal using a butane torch until the surface is glowing orange (see Figure 3.2); the surface is kept at temperature for several seconds before being allowed to cool slightly with the flame still circling close around the crystal this is repeated over several minutes. The sample is then

allowed to cool in air before being covered with a drop of ultra-pure water prior to the transfer into the electrochemical cell. Quenching of the sample with water should only be done once the sample has cooled sufficiently, too soon and the thermal shock can induce a poor surface quality and damage to the bulk [1]. The quality of the surface can be inferred from cyclic voltammetry, for example broad peaks can indicate the surface is rough, and extra peaks can be an indication as to steps on the surface.

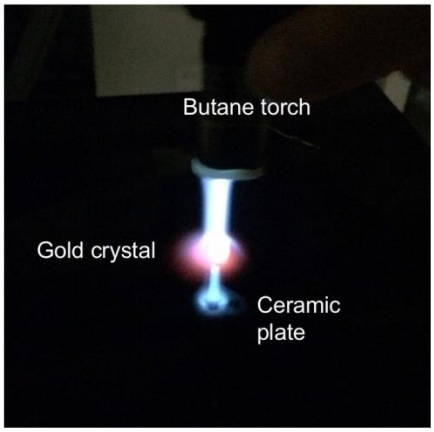

Figure 3.2 A gold crystal prepared by the flame annealing technique.

3.3 Cleaning of electrochemical equipment

Prior to assembling the cell all parts must be thoroughly cleaned. The cell, fittings, tubing and reservoir and any glassware are soaked overnight in a concentrated acid mix; 1:1 sulfuric H_2SO_4 and nitric HNO_3; this removes any contamination. After soaking, the parts are rinsed 10 times in ultra-pure (Milli-Q) water and subsequently boiled and rinsed in ultrapure water 3 times. Ultra-pure water is defined by the level of resistivity. The resistivity of the ultra-pure water used in this thesis was 18.2 MΩ·cm. This is achieved through filtration and ionization steps. The system monitors the ion concentration by measuring the electrical resistivity of

the water.

3.4 Potentiostat

A potentiostat is used to control the applied potential between the working electrode and the reference electrode, such that the potential drop between them is equal to the desired voltage. The reference electrode is connected with high input impedance and is ideally current free. The current in the electrochemical cell is passed through the working electrode and the counter electrode. A schematic of a potentiostat is shown in Figure 3.3. The current measured is a direct measure of the flow of electrons at the electrochemical interface. The potentiostat used in this thesis is the Versastat 4 from Princeton Applied Research. For in-situ X-ray experiments the potentiostat was located in the experimental hutch and interfaced to GDA (DLS) [63] or SPEC (ESRF) [64] (software used for instrument control and data acquisition), which could be controlled via computer in the control room.

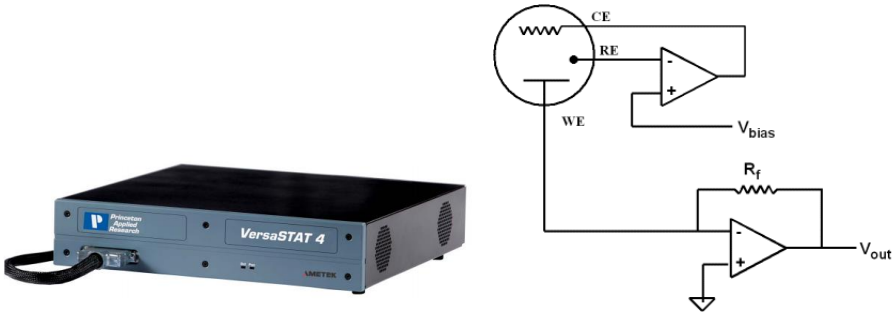

Figure 3.3 (a) photo of the Princeton Applied Research Versastat potentiostat. (b) simplified schematic of a potentiostat circuit.

3.5 The X-ray electrochemical cells

3.5.1 The X-ray electrochemical thin layer cell

This cell differs from the conventional hanging meniscus set up (discussed in section 2.2.4), a 'thin-layer' configuration is required for *in situ* use as to minimise

the attenuation of X-rays due to the liquid. A schematic of the thin-layer cell is shown in Figure 3.4 and a photo of the cell can be seen in Figure 3.5 (a). The main body of the cell is constructed from Kel-F, a material that can be machined to the required specifications and is chemically inert. Fittings to the cell are made from teflon or PEEK. The crystal is held in a collet which is designed to tighten around the sides of the crystal when it is screwed in place; keeping the crystal in a fixed position at the center of rotation in the cell throughout the experiment. The collet sits slightly above the level of the cell, and the crystal surface is again higher above this so that it sits at the highest point in the cell; this is to ensure that the X-rays can access the whole surface and are not clipped by anything in the way. The crystal sits on top of a coiled wire, which forms a contact to the outside of the cell. Electrolyte inlet and outlet holes allow electrolyte to be exchanged during the experiment.

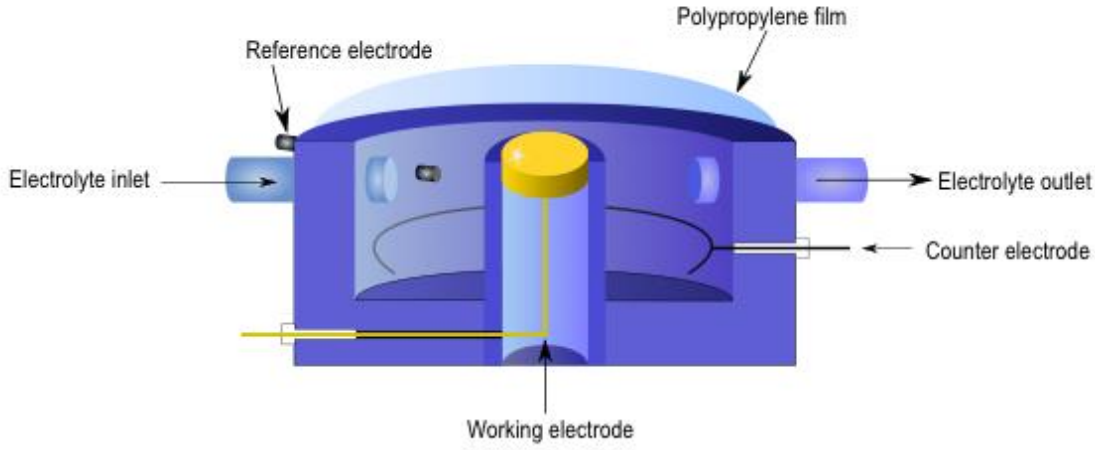

Figure 3.4 Schematic representation of the electrochemical thin layer cell. The crystal is held in the centre of the cell, the cell is filled with electrolyte through the inlet tube and is enclosed by a polypropylene film – transparent to X-rays.

(a)

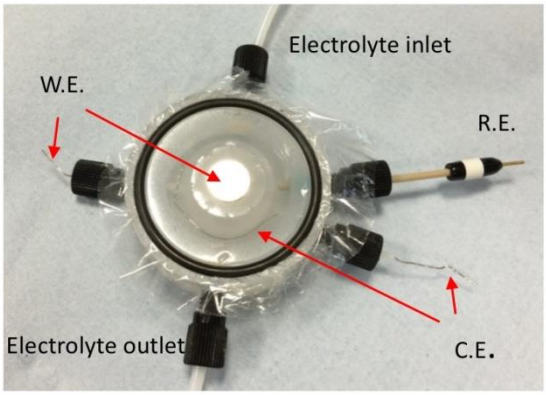

(b)

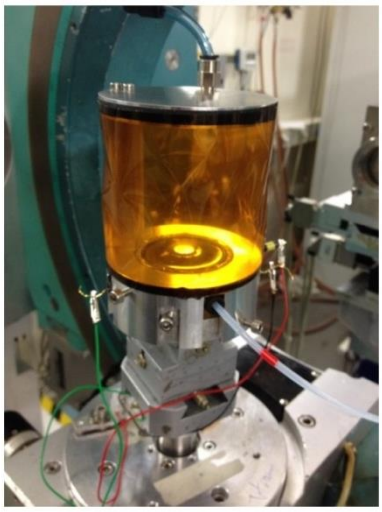

Figure 3.5 (a) Thin-layer electrochemical cell (b) thin-layer cell set up with the outer hood on the diffractometer at XMaS beamline, ESRF.

The inlet is connected to an electrolyte reservoir by teflon tubing, and the outlet to a syringe, forming a closed system. A non-permeable polypropylene film (12 μm thick) purchased from Chemplex is used as a window on the top of the cell as it is transparent to X-rays, and is sealed in place by a rubber o-ring. The film traps a thin layer of electrolyte on top of the surface. The polypropylene films are naturally hydrophobic, however, exposing polypropylene to heat causes chain degradation [65]. Oxidation occurs forming a free radical which reacts further with oxygen, followed by chain scission yielding aldehydes and carboxylic acids, which are hydrophilic. As such, the films are boiled before use to make the films hydrophilic. As the SXRD measurements require long acquisition times two films are used to minimize beam damage, which can cause the films to split and the cell to fill with air; which would result in repreparing the cell (and crystal) and a loss of beam time. The electrochemical cell is enclosed in an outer metal frame chamber, shown in Figure 3.5 (b), which is sealed with a kapton window, this is filled with nitrogen to keep the cell protected – free from O_2.

Au, Ag, and Pt wires for the counter and contact to the working electrode are dipped in the cleaning acid, rinsed in ultra-pure water and flame annealed. Silver wires are dipped in weak Nitric acid or Ammonia Hydroxide/ Hydrogen peroxide mix until shiny and rinsed thoroughly. Once the cell is assembled it is leak tested with the film pulled down. Once prepared, the working electrode is transferred to the cell with drop of ultra-pure water covering the surface, it is then tightened into place in the collet and the cell is filled to form a meniscus over the crystal before covering with the polypropelene film. Fresh electrolyte purged with N_2 (or saturated with O_2 or CO depending on the experiment) is pulled through and any bubbles are removed from the cell. The film can be inflated, or deflated, when deflated the film traps a thin layer of electrolyte on the surface ~ $10\mu m$ which allows the transmission of X-rays whilst also maintaining potential control of the system. One of the constraints with this set up is that, unlike the conventional hanging meniscus set up, the voltammetry is not specifically due to the ordered surface, but also has a contribution from the polycrystalline sides and back of the crystal (as the whole crystal is contact with electrolyte). However, this is not a problem for the X-ray measurements and the voltammetry can be correlated to preliminary measurements with the hanging meniscus cell. For certain X-ray measurements, such as time resolved studies, this set up is not suitable and a different set up is required which is discussed in the following section.

3.5.2 Droplet Cell

In the previously discussed X-ray cell the thin layer of electrolyte has a high resistance, i.e. a high RC constant; which is not suitable for fast kinetic measurements such as the time dependent measurements discussed in chapter 6.

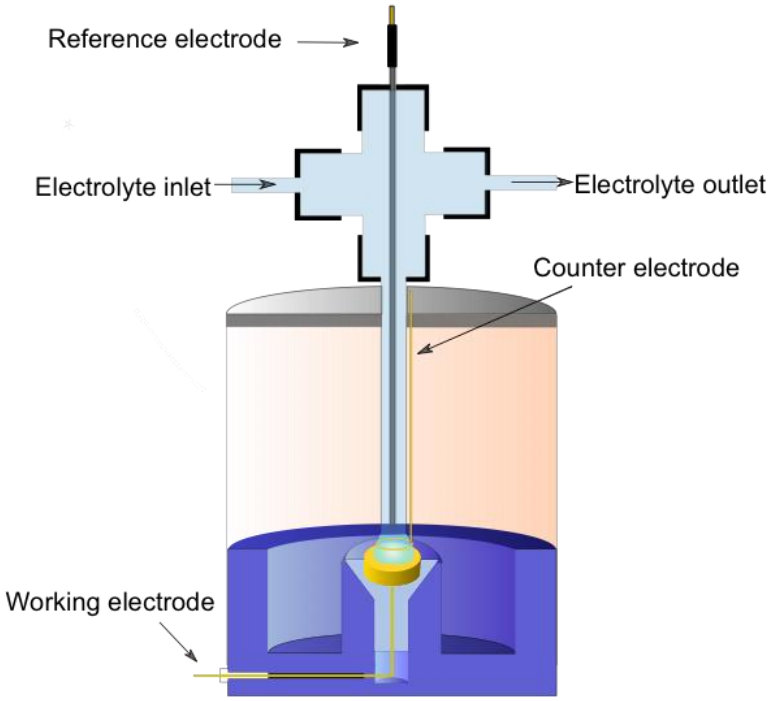

Figure 3.6 Schematic of the electrochemical X-ray droplet cell. Counter electrode and reference electrode are in close proximity to the working electrode; thereby reducing the RC constant of the cell.

Instead, a droplet cell is used, which minimizes the electrolyte resistance by placing all of the electrodes in close proximity, a schematic of the cell is shown in Figure 3.6. The sample is held in the same way as with the thin layer cell, however, unlike the thin layer cell, the electrolyte is only in contact with the single crystal surface. A glass or Teflon crosspiece is held above the sample, attached to a glass or quartz capillary, which is filled with electrolyte. A droplet of electrolyte is suspended from the end of the capillary making contact with the crystal. To minimize the RC drop, the counter electrode forms a ring around the droplet; this also acts to stabilize the droplet, and a long $Ag/AgCl^-$ 'flex-ref' (World Precision Instruments) is held in place above the working electrode in the capillary. The size of the droplet is

controlled with the electrolyte inlet and outlet. Similarly, with the thin layer cell, the cell is surrounded by an outer chamber, which can be filled with inert gas. There are however limitations with this geometry; the droplet is only stable when the cell is flat or has a very small incident angle, and it requires the use of higher energy >15 KeV as the X-rays are attenuated by the liquid droplet.

3.6 Synchrotrons

Synchrotrons are machines in which charged particles, electrons or positrons, are accelerated at relativistic speeds on a curved path, through a magnetic field, resulting in the emission of synchrotron radiation. Over the years the brilliance of synchrotron sources has drastically improved (the brilliance determines the quality of the beam, it is a combined measure of the flux, the beam divergence, coherence, and

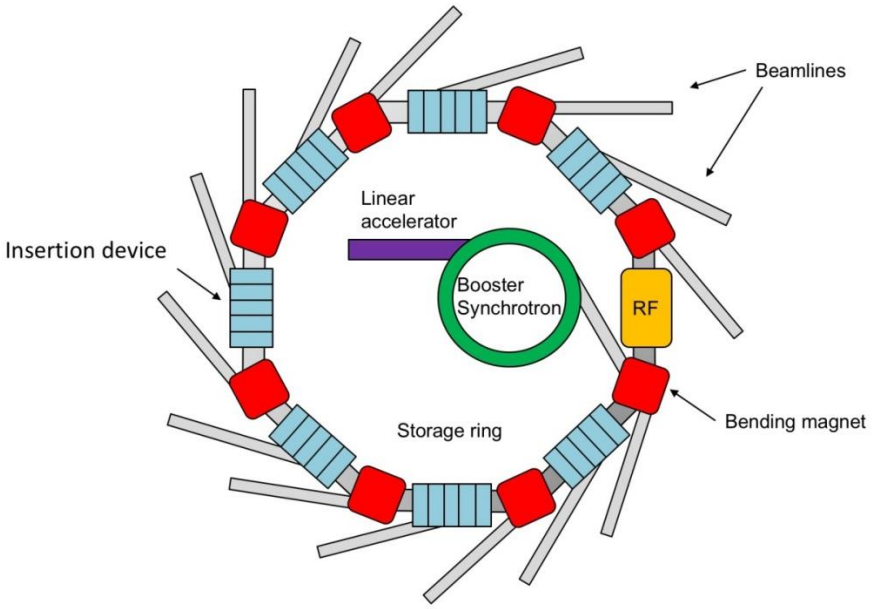

Figure 3.7 Schematic representation of a 3rd generation synchrotron.

the source size) and todays' 3rd generation synchrotrons have a many orders of magnitude greater than lab based rotating anode sources. This makes synchrotron radiation crucial for determining the structure of interfaces, where scattering due to surface structures is low in comparison to the bulk; it is essential to use high energy X-rays to resolve the weak signal and electrochemical studies require high X-ray energies in order to penetrate the electrolyte layer. The first generation synchrotrons had a major advancement with the introduction of electron storage rings. This consists of a ring where the beam is continuously circulated. This development brought beam stability and higher fluxes of radiation. A schematic of a typical 3rd generation synchrotron is shown in Figure 3.7. Electrons are accelerated in a linear accelerator (LINAC) and into a booster synchrotron up to GeV energy range before being transferred to the storage ring. The storage ring consists of straight sections and bending magnets, in order to control the path of the electron beam. As the electron beam circulates around the storage ring it will lose energy, there are Radio Frequency (RF) cavities which boost the electrons to account for the energy lost. Tangential to the storage ring are many beamlines. Some utilise radiation from the bending magnets, and others use radiation from insertion devices. The insertion devices are situated in the straight sections of the ring and produce high intensity X-rays. Insertion devices consist of magnets with alternating polarity which forces electrons to oscillate in the horizontal plane [44]. There are two types of insertion devices:

1. **Wigglers** – are a series of magnets with alternating polarity. The electrons path through a wiggler can be considered a series of small arcs like a bending magnet which deflects the beam oscillating the electrons in

the horizontal plane causing the emission of synchrotron radiation and leading to enhanced intensity.

2. **Undulators** – similar to a wiggler but the arrangement of magnets in an undulator cause the emitted radiation to be in phase with the rest, adding together constructively, which produces a highly collimated beam over a narrow energy range.

3.7 Beamline and Diffractometer

Figure 3.8 shows a schematic of the optics configuration of a beamline. In the optics hutch there are a series of monochromators, mirrors and slits in order to define and focus the beam. The energy of the beamline can range as according to the specifications of the beamline. Before an experiment begins a specific energy is defined using a monochromator. The monochromator consists of two Si(111) crystals which exploit Bragg's law to give the desired beam energy. The second crystal is held on a translational stage, which maintains the outgoing beam at a constant exit height. The translational stage can be moved to change the angle to select the wavelength of the beam. Mirrors are used to focus the beam size to a small spot on the sample. Additional slits are used to reduce the size of the beam vertically and horizontally. To protect the detector when aligning with the main beam and when scanning close to intense Bragg peaks, attenuators can be inserted. A monitor such as an ion chamber is usually placed after the attenuators, before the sample, which is used to monitor fluctuations in beam which can be normalised out of the data in the analysis stage. The beam then hits the sample at the centre of rotation which is described in the following section. To measure the diffracted intensity a

detector is used. The majority of experiments in this thesis used an area detector (Pilatus). Slits are used in front of the detector to optimise the signal to noise ratio. The method for data extraction for Pilatus images is discussed later on in section 3.9. There are several types of diffractometers that can be used. The data in chapters 4-6 was obtained from beamline I07, Diamond Light Source, DLS. Data in chapter 7 was measured on beamline ID03 in ESRF, Grenoble. I07 and ID03 have a similar set up,

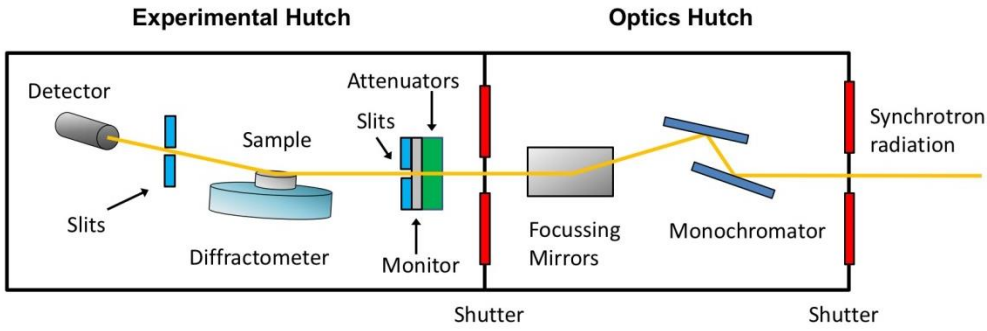

Figure 3.8 Simplified schematic of the optics of a beamline

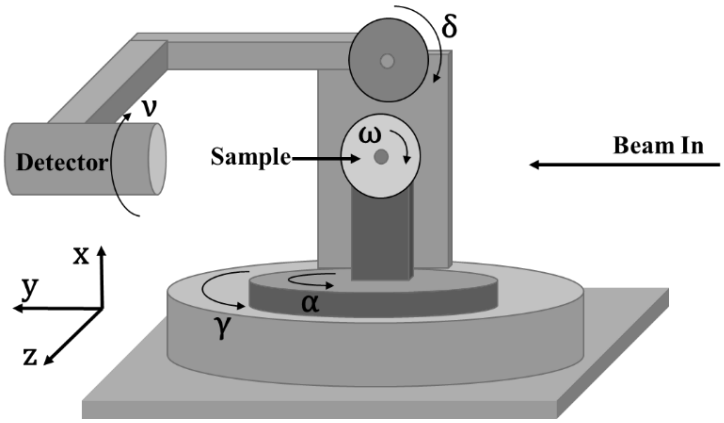

Figure 3.9 Schematic of 2+3 Circle diffractometer in vertical mode. Laboratory frame of reference and sense of rotations are indicated. Figure reprinted from reference [66] with permission.

they have a Huber (2+3) diffractometer [67] which can be set up in vertical or horizontal scattering geometry shown in Figure 3.9. A hexapod is mounted to the diffractometer to allow for adjusting the height of the sample and rotation required for alignment. The incident angle of the sample and azimuth are given by α and ω, respectively, in vertical scattering mode (which was used for the experiments in chapters 4-6) or χ and θ in horizontal scattering mode (used in chapter 7). The detector arm allows movement in δ (vertical movement) and γ (horizontal movement); ν determines the post slit sample rotation. Experimental set up of the I07 beamline allows for both UHV and electrochemical measurements to be made. The beamline houses two experimental hutches EH1 and EH2 [68], both can be seen in Figure 3.10. In EH1 the sample is enclosed in the electrochemical set up mounted on a goniometer which is attached to the hexapod stage Figure 3.10 (c). A flight tube can be installed in EH1 to produce a beam path into EH2. EH2 is set up for *in situ* UHV measurements; the entire UHV system is mounted on the diffractometer. The UHV chamber has a 'buffer chamber' where samples are prepared by sputter anneal and can be characterised by LEED and STM. The X-ray beam is focussed in the analysis chamber, through a Beryllium window 20 mm x 120 mm which allows incident angles up for 30°. A larger exit window enables the detector to access angles of 120° vertically by 30° horizontally.

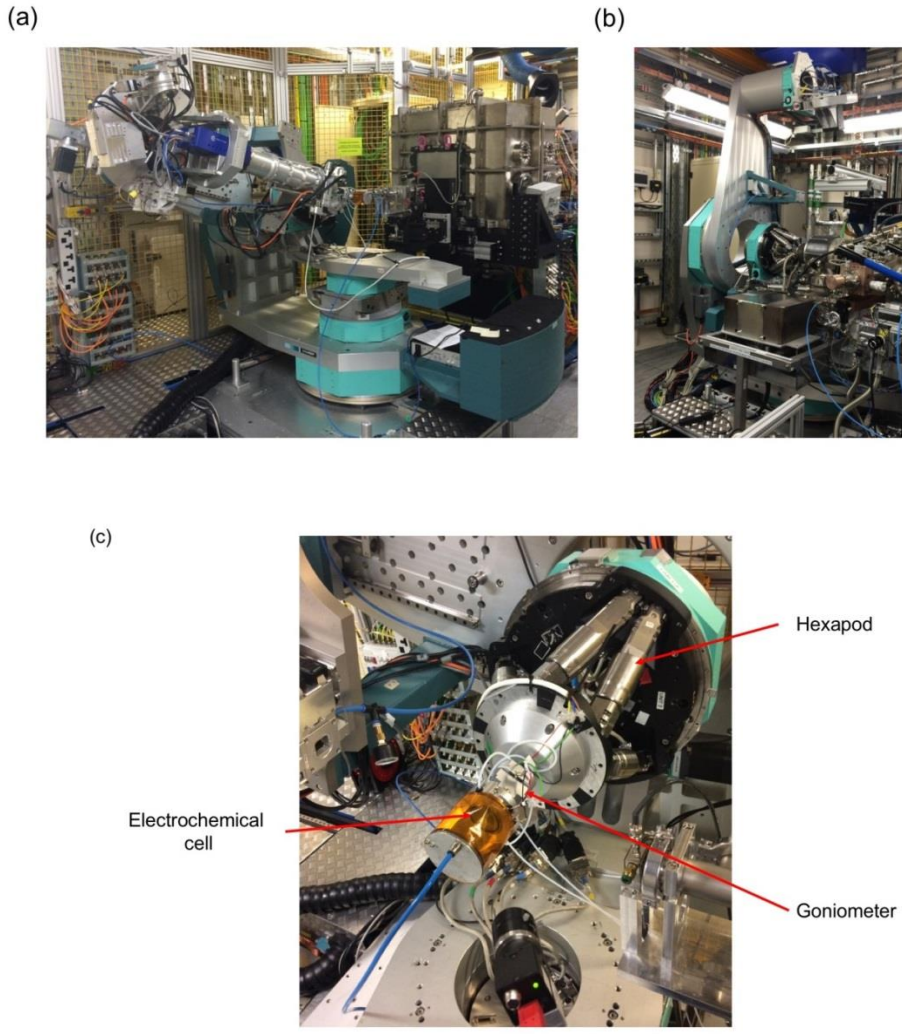

Figure 3.10 Experimental hutches on I07 beamline, Diamond light source (a) EH1 - *in situ* electrochemical experiments (b) EH2 - UHV experiments and sample preparation.

3.8 Alignment procedure

Once the beamline is set up with the correct configuration, and the sample is mounted on the diffractometer the first step of the experiment is to align the sample. Initially, all angles of the diffractometer are set to zero and the sample is mounted. To ensure the sample is flat and in the center of rotation, the sample can be laser aligned; this consists of reflecting a laser beam from the sample surface on to a wall.

The tilts of the goniometer can be adjusted so the beam does not move with the rotation of omega (or phi). A similar procedure can be done with the hexapod, a camera is set up with a cross hair and the sample is rotated and adjusted so that the centre of the crosshair stays in the centre of the crystal. The first scan with the X-rays is to check the height of the sample, the intensity is monitored as the sample is moved vertically through the beam, the height is adjusted to where the sample 'half cuts' the beam. The next step is to set up a UB matrix in order to maneuver in reciprocal space; it relates the Miller indices of the reciprocal vector (HKL) with its' real space coordinates (xyz) by:

$$Xyz = UB\ HKL \tag{3.3}$$

The UB matrix is composed of two sub-matrices, U and B. U describes the orientation of the crystal axes with respect to the lab reference system, and B defines a set of orthogonal axes based on the crystal axes which only depends on the unit cell parameters. The UB matrix requires real space angles for two or more reciprocal space positions. The first Bragg peak to find is often the specular (0, 0, L) which is easiest to find as it is independent of omega. Once the peak is found in alpha it makes is easier to find a non-specular reflection. The position of the Bragg peak is optimised in gamma and delta. Usually two non-specular Bragg peaks are identified and one of them is swapped as the primary instead of the specular Bragg peak as it is dependent upon more than one angle (it is more accurate to use to calculate the UB matrix). Once the alignment is complete the experiment can start. The first thing to check is the anti-Bragg position to ensure is there is a strong signal. The anti-Bragg position is due to scattering from the surface, and is therefore a good indication as to

the quality of the surface. Subsequently an L scan is performed to determine the 'cut-off' in L where total external reflection occurs giving a limit in L for the experiment.

3.9 Scans and Data extraction

Rocking scans

The sample is rotated whilst the detector remains stationary. A rocking scan is used to measure points in reciprocal space along a CTR. A Lorentzian line shape is fit to the rocking scan, with a straight line for the background and it is the integrated intensity that is calculated; as it is the integrated intensity which is directly related to the structure factor. Rocking scans are made at positions (in L) along the CTR, or are measured at certain points in reciprocal space to monitor a specific structural feature.

Stationary Scans

If an area detector is being used, then the whole width of the CTR can be integrated at once. This means that there is no need to use rocking scans (unless measuring Fractional Order Rods where scattering is weak); which makes the data capture time much quicker. This method increases the counting statistics with the benefit of decreasing the data collection time. 'Regions of interest' (ROI) are set up to capture the signal of the CTR, and background regions an example can be seen in Figure 3.11. The ROIs contain the sum of the signal. Regions are set up during the

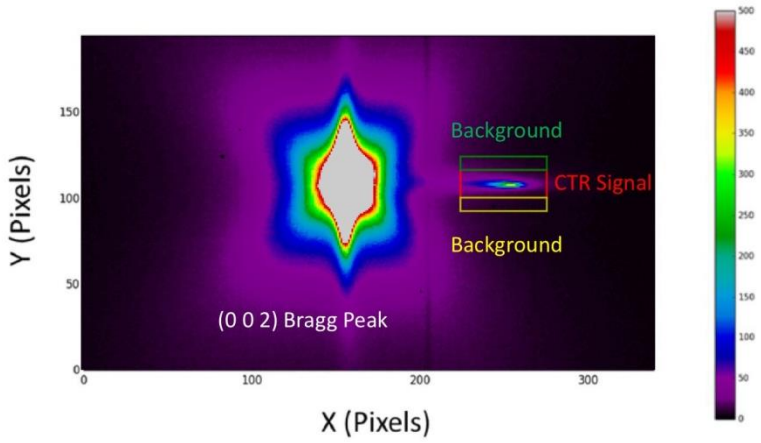

Figure 3.11 Detector image (cropped) of stationary scan taken on the (0, 0, L) CTR. ROI regions are set up to define the signal from the CTR, and background regions.

experiment, and the intensity is saved in the data file. However, it is important to check through the images to ensure that the sample alignment is correct for the chosen regions of interest. This is another benefit of using a 2D detector, the regions of interest can be changed or defined after the experiment and it gives more information than a point detector can as features such as powder lines, can be seen in the images.

Reciprocal space scan

In a direct reciprocal space scan, the diffractometer scans hk along a diffraction (normally at a fixed q_z value) in reciprocal space. This allows structures with a different periodicity (such as a reconstruction) to be investigated.

3.10 Geometric Correction factors

Before the data can be analysed there are a number of corrections which need to be made to the data to account for the diffractometer geometry, sample size,

detector slit and beam size which all have an effect on the measured intensity. Corrections for the (2 + 3) diffractometer are given in [67].

Lorentz factor

Accounts for the change in integration volume as it is converted from real space angle to reciprocal space.

2 + 3 circle

$$L = \frac{1}{sin\delta cos\gamma} \tag{3.4}$$

Polarisation factor

The vertical magnetic field of an undulator causes electrons to deflect horizontally, emitting radiation which is polarised horizontally. The polarisation factor accounts for changes in intensity due to the polarisation of the beam. A (2 + 3) geometry can move the detector in both horizontal and vertical planes,

$$P = p_h P_{hor} + (1 - p_h) P_{ver} \tag{3.5}$$

where

$$P_{hor} = 1 - (cos\delta sin\gamma)^2 \tag{3.6}$$

and

$$P_{ver} = p_h P_{hor} + (1 - p_h) P_{ver} \tag{3.7}$$

Where p_h is the horizontal polarisation, P_{hor} is the horizontal polarisation component and P_{ver} is the vertical polarisation component.

Rod interception

This is to account for the angle which the detector makes with the rod. For measurements where the angle is small the interception is almost perpendicular, for measurements at higher L the beam is no longer perpendicular to the rod

$$R = cos\beta_{out} \tag{3.8}$$

Active area correction

Accounts for the overlap of beam footprint and detector footprint with changing incident angle on the sample, it depends on the beam defined slits, detector slits and sample geometry. This correction ignores the beam footprint and sample size.

$$A = \frac{cos\beta_{out}}{sin\delta} \tag{3.9}$$

3.11 Data Analysis

Once the correction factors have been applied the CTR data can then be fit. The data is fit to a model as described in chapter 2 using a non-linear least squares algorithm, using a python program written by C. A. Lucas and developed by G. Harlow and Y. Gründer. The structural parameters of the top metal layers and any adlayers are varied to minimise the χ^2 value given by:

$$\chi^2 = \sum \frac{(M-T)^2}{\sigma^2} \tag{3.10}$$

Where M is the measured value, T the theoretical value and σ^2 is the variance of the data. This is divided by the number of degrees of freedom to determine the reduced

χ^2 value. The statistical error on each CTR data point is given by $\sqrt{n}$. Systematic errors which are determined from comparing symmetry equivalent reflections, and are usually in the range 5-10 %.

To obtain the best structural model to the data a systematic approach is required. To begin with the simplest model is considered; a clean bulk terminated surface, at this point only the scale factor parameter is optimised. The complexity of the model is increased in order to obtain the lowest reduced χ^2 and best structural model to the data, by varying structural parameters such as occupation of the metal layers (θ_n), relaxation (ε_n) and root mean squared (rms) roughness (σ). Usually only the top three metal layers are considered in the model. Similarly adlayers can be included into the model, depending upon the system. The exact fitting procedures are discussed within the results chapters. In the case of the electrochemical data the non-specular CTR data are usually fit first. The non-specular CTRs have in plane momentum transfer as well as out of plane and are used to obtain a good fit to the metal structure. Once a good fit has been obtained the parameters are fixed. The specular CTR is sensitive to vertical ordering from incommensurate adlayers and electrolyte layering at the interface. If the fit to the non-specular CTRs does not model the specular CTR data then additional adlayers or electrolyte layering is included in the fit. Sometimes changes between electrochemical systems are small, and to highlight the structural differences between them it is advantageous to simultaneously fit the data sets together, and a fit to the ratio of the data. This fitting procedure was utilised to fit the data in chapter 6.

4 Ag/UHV interface

4.1 Introduction

Understanding the atomic structure of an electrode surface is essential for determining adsorbate and reaction phenomena at an interface. When a crystal is terminated, the properties of its surface layers can greatly differ from the bulk. The termination changes the atomic coordination of atoms at the surface, and the conduction electron distribution, as a consequence the atoms rearrange and displaces to a structure which minimises the surface free energy. This is done through reconstruction of the surface atoms in-plane (which modifies the symmetry of the surface) and/or through relaxation (displacement of atomic layers in the surface normal) – this is discussed in section 2.5.2. Depending upon the nature of the electrode the forces which induce rearrangement of atoms can be felt over varying degrees. Semiconductors, for example, this can be felt a large distance [69] into the

surface, whereas for metals the effects are not as pronounced and only the top few layers are effected due to the nature of the bonding [2,3].

For surfaces that do not reconstruct, UHV studies have shown most surfaces undergo an *inward* relaxation at room temperature [26], where the layer spacing between the top two layers is reduced compared to the bulk spacing, whilst at higher temperatures the layer spacing is expanded [5,6].

Surface relaxation can be explained by the Smoluchowski effect [60], in which the corrugation of the surface leads to a corrugation of electronic charge, this is shown in Figure 4.1. The charge gradient at the surface leads to an increase in kinetic energy, and as a result (in order to lower the kinetic energy) the charge undergoes 'smoothening'. This has the effect of relaxation of the surface layers.

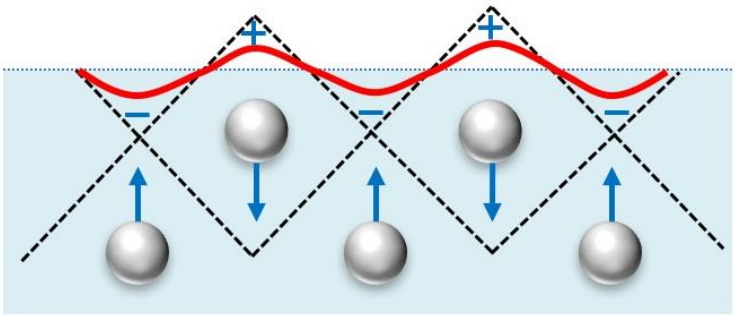

Figure 4.1 Schematic of the Smoluchowski smoothing effect. Charge distribution is shown along the Wigner-Seitz cells.

The effect of charge smoothening is stronger the 'rougher' or more open a surface is. The resulting effect lowers the work function of the surface.

Early theoretical work of the relaxation of surfaces only considered the effect of coordination number on the relaxation of the surface and predicted the spacing between the top two atomic layers should be expanded in relation to the bulk spacing [7–11]; contradictory to experimental studies. The problem was addressed by the

heuristic model determined by Finnis and Heine [77]. The model considers the redistribution of electron density caused by the truncation of the surface. The redistribution of charge causes an electrostatic force on the top atomic layer which results in an *inwards* relaxation of the layer as a response. The extent of the relaxation is dependent upon the structure of the surface, the less packed a surface is, the greater the surface relaxation will be. Much of the early investigations of surface relaxation only considered the relaxation of the top metal layer until the effect of multilayer relaxations was considered in an electrostatic model by Landman *et al.* [2]. The model proposed the relaxation can perturb several layers into the bulk of the crystal and often the response of the layers is oscillatory relaxations i.e. a change in sign of the relaxation of the top atomic layers which is damped with increasing

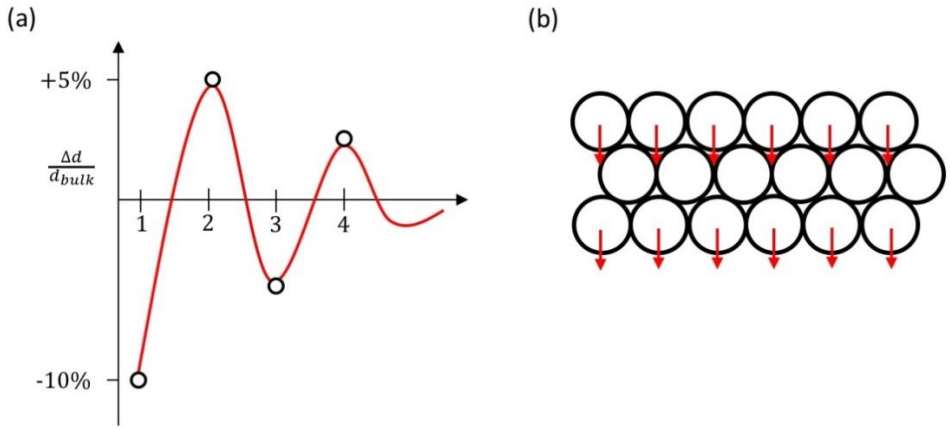

Figure 4.2 Oscillatory surface layer relaxations. (a) damped oscillatory relaxations with increasing layer distance towards the bulk, (b) schematic representation of surface relaxation – alternating relaxation. Figure is reproduced from [78].

distance towards the bulk, this is shown in Figure 4.2. This was confirmed by LEED studies on Al(110) [79] and Cu(110) [14,15]. If relaxation of the electrode surface is not sufficient to minimise the surface free energy then the surface can reconstruct, this occurs with Au, Pt and Ir surfaces [1].

Understanding the clean electrode surface is clearly an important preliminary measure for obtaining the correct model when adsorbates and electrolyte are introduced. The Ag(*hkl*) surfaces do not reconstruct unless induced by adsorbates such as oxygen [6] or alkali metals [82]. Early studies of the Ag(110) surface proposed a large *inwards* relaxation of the top metal layer of between 7-10% [7,15,71,72], although only the relaxation of the top layer was considered in modelling the surface. The multilayer model was applied to subsequent studies of Ag(110), by numerous LEED and ion scattering studies (summarised in Table 4.4.1), which confirmed the oscillatory model proposed by Landman *et al.* [2], however the magnitude of the relaxations varied between studies and techniques. For Ag(111) the relaxations of the top metal layers are determined to be very small in comparison to Ag(110), with either no small *inwards* relaxations of the top two atomic layers [12,13], or no relaxation at all [14].

The work in this thesis is primarily on Ag low index surfaces of single crystals. As the results in literature vary between techniques, it is therefore important to determine the structure of the clean Ag surfaces in UHV in order to compare them to systems throughout this thesis, as there are no reported SXRD studies of the clean Ag(110) surface. This chapter presents the structure of the clean Ag(110) and Ag(111) in UHV as studied by SXRD. The Ag(001) surface was not studied in UHV, however, the studies in literature will be discussed in comparison with the other surfaces.

4.2 Experimental

The silver single crystals were obtained from SPL in the Netherlands and oriented to within less than 0.1°. Samples were prepared in UHV by several cycles of

Ar^+ sputtering and annealing at 480℃. The temperature of the sample did not exceed 500℃ degrees as above this temperature the silver surface can roughen and lose long range order which causes the surface to appear cloudy [85]. The quality of the sample was determined by LEED, repeated sputter-anneal cycles were performed until a sharp a (1×1) pattern, with low background was obtained and checked for contamination with XPS. The measurements were carried out at room temperature on the I07 beamline at the Diamond Light Source using focused incident X-rays of energy 20 keV. A 2+3 circle diffractometer with a PILATUS 100k (Dectris) detector was used to record the X-ray measurements. The Ag(110) reciprocal surface unit cell (*H, K, L*) was indexed using the LEED convention such that *H* is along [1 -1 0], *K* along [0 1 0] and *L* is along the [1 1 0] surface normal. The units for *H, K* and *L* are $a^* = c^* = 2\pi/a_{NN}$ and $b = 4\pi/\sqrt{2}a_{NN}$ where $a_{NN} = 2.888$ Å is the nearest-neighbor distance in the crystal. The Ag(111) surface was indexed to a conventional hexagonal unit cell for *fcc*(111) surface that is defined such that the surface normal is along the $(0, 0, L)_{hex}$ direction and the $(H, 0, 0)_{hex}$ and $(0, L, 0)_{hex}$ vectors lie in the plane of the surface and subtend 60°. The units for *H, K* and *L* are a* = b* = $4\pi/\sqrt{3}a_{NN}$ and c* = $2\pi/\sqrt{6}a_{NN}$.

4.3 Results and discussion

4.3.1 Ag(110)/Vacuum interface

Due to the geometry of the Ag(110) surface, the closely spaced layers mean that the Bragg peaks are spaced far apart in reciprocal space. As a result, a limited range in L can be accessed than with (111) and (001) surfaces as the intensity falls off into the background, signal away from the Bragg peaks with increasing L. To obtain a

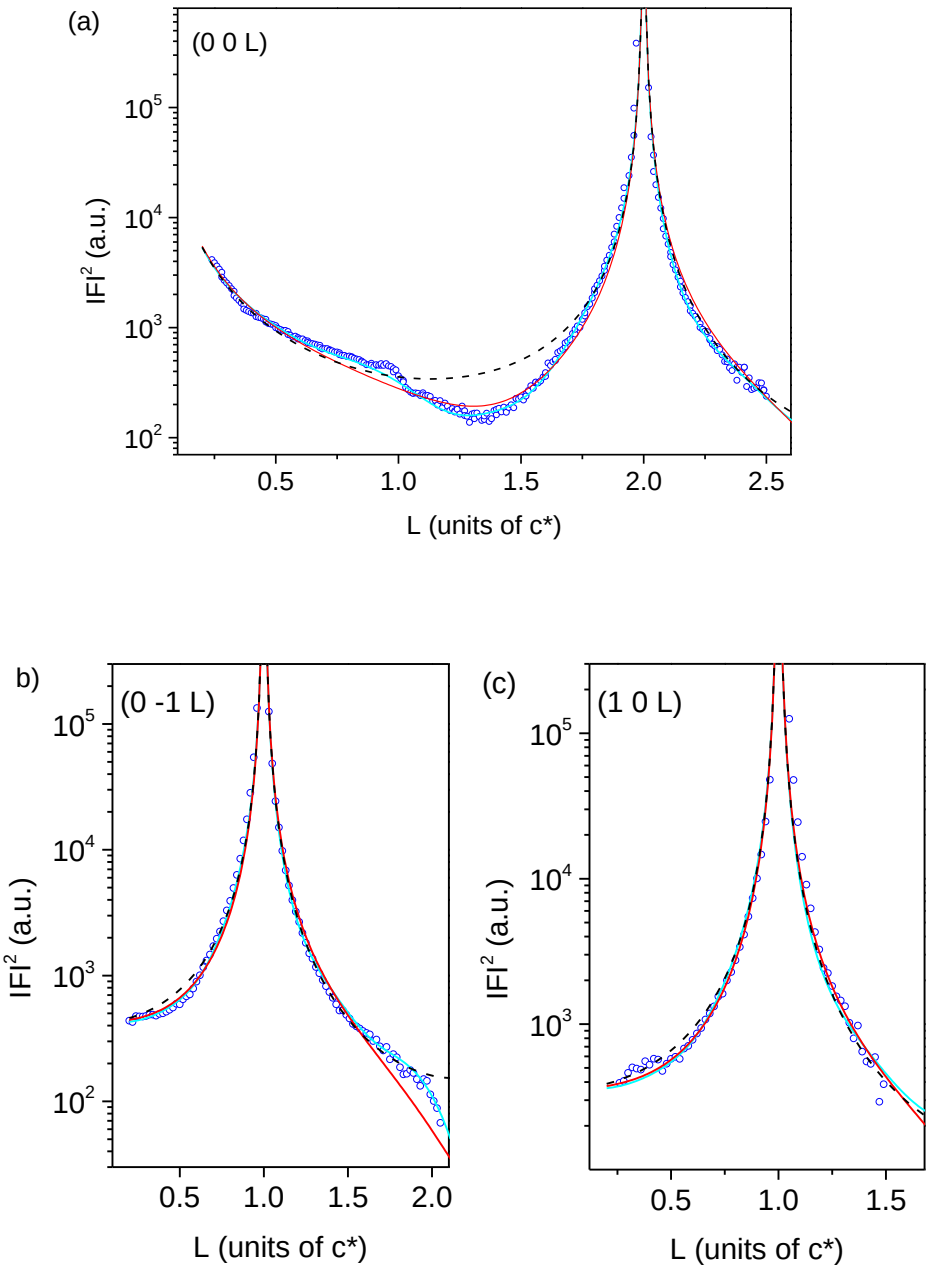

Figure 4.3 The measured X-ray intensity along specular CTR (a) (0, 0, L) and first order non-specular CTRs (b) (0, -1, L) and (c) (1, 0, L). The dashed line is the calculated intensity for a perfectly terminated (110) surface with no relaxation. The solid lines are the calculated fits to the data; the red line represents the fit to the data by varying only the top layer relaxation and rms roughness, and cyan is the best fit which incorporates relaxations of the top four atomic layers, and rms roughness of the top two.

Method	Δ_{12} (%)	Δ_{23} (%)	Δ_{34} (%)	Ref.
Experimental				
SXRD	-6.5	+2.0	-0.6	This work
LEED	-5.7	+2.2	-	[26]
LEED	-7	+1	-2	[8]
RBS	-7.8 $\pm$ 2.5	+4.3 $\pm$ 2.2	-	[10]
RBS	-9.5 $\pm$ 2.0	+6.0 $\pm$ 2.5	-	[86]
Theoretical results				
EAM	-6.87	+2.19	-1.04	[4]
EAM	-5.9	+0.5	-0.3	[87]
EAM	-5	+0.3		[88]
Tight binding	-6.2	+0.7	<0.7	[89]
Perturbation theory A	-6.36	+5.03	-1.33	[71]
Perturbation theory A	-6.12	+2.73	-3.39	[71]

Table 4.4.1 Comparison of percentage variations of the interlayer spacing with experimental and theoretical results. EAM is embedded atom method, RBS is Rutherford Back Scattering.

structural model for the surface CTR measurements were made on the specular CTR, (0, 0, L) and two first order non-specular CTRs, (1, 0, L) and (0, -1, L) and were fit simultaneously. The CTR data and calculated fits are shown in Figure 4.3, the black dashed line represents the calculation of a perfectly terminated surface; with layer spacing of the surface layers equal to the bulk spacing ($d_{(110)}$ = 1.445 Å). It is apparent that there must be some relaxations of the surface layers as the experimental data deviates from the calculated perfect termination of a (110) surface – the intensity is reduced asymmetrically around the Bragg peaks (as discussed in section 2.5.2). The occupation of the metal layers was fixed at unity, as the clean Ag(110) surface is not known to reconstruct in UHV, and the LEED pattern indicated a (1 × 1) terminated surface. This is justified as varying the occupation of the top metal layer did not improve the fit. As a starting point, a simple two parameter

model was explored. The vertical displacement, ε, and the rms roughness, σ, of the top metal layer were varied. The calculated fit (represented by the red line) gave an *inwards* relaxation of -0.051 ± 0.002 Å (corresponding to a reduced layer spacing of d_{12}=1.393 Å, -3.5 % contraction relative to the bulk spacing 1.444 Å) and a large rms roughness of 0.235 ± 0.005 Å (the bulk Debye-Waller factor is 0.096 Å) this gave a reduced χ^2 of 5.84 which does not give a good fit to the data. As the Ag(110) surface is known to undergo multilayer relaxations at the surface, the relaxations of further layers was considered in the model. The best fit to the data was obtained by varying the vertical displacement of the top 4 metal layers and the rms roughness of the top two which gave a reduced χ^2 of 2.48. Including the rms roughnesss of the 3rd and 4th layers did not lead to any significant improvement of the reduced χ^2, therefore they were not included in the model. It is interesting to notice that there is a small oscillation in the specular CTR just before L=1 which the model could not replicate. Removing these data points did not change the fit parameters, and no unusual features could be seen in the individual image files. The sharpness of the feature (in

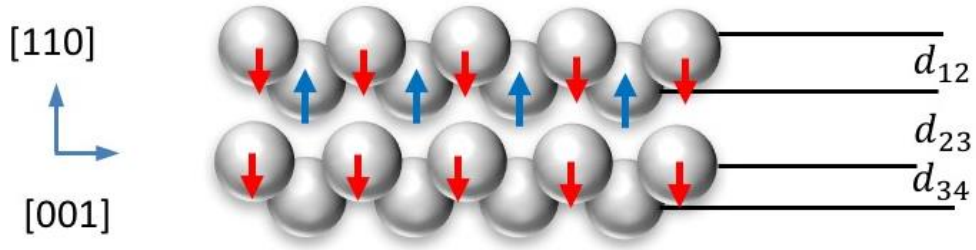

Figure 4.4 Schematic representation of the Ag(110) oscillatory surface relaxations.

L) implies that it is due to a three dimensional structure rather than the surface. At present we are not certain of the origin of this scattering feature. The model indicates the layer spacings of d_{12} = 1.350 Å, d_{23} = 1.473 Å and d_{34} = 1.435 Å and 1st and 2nd

layer rms roughnesss of $\sigma_1 = 0.22 \pm 0.01$ Å and $\sigma_2 = 0.07 \pm 0.02$ Å respectively. The surface layer rms roughnesss, was relatively large compared to the bulk thermal roughness of 0.096 Å. This is in agreement with the multilayer Rutherford Back Scattering (RBS) study by Holub-Krappe *et al.* [86] which identified an increased thermal vibration in the top two atomic layers ($\sigma_1 = 0.14$ Å and $\sigma_2 = 0.09$ Å). This large roughness in the surface layers is not unusual for *fcc*(110) surfaces; due to the geometry of the surface it is more prone to roughening and silver is sensitive to a roughening transition [47,48]. Comparing the interlayer distances to the bulk value of 1.445 Å, the relaxations correspond to an oscillatory variation of $\Delta_{12} = -6.5$ %, $\Delta_{23} = +2.0$ % and $\Delta_{34} = -0.6$ % (where a positive or negative value corresponds to an *outwards* or *inwards* relaxation of the layer spacing, respectively). The oscillatory multilayer relaxations are in good agreement with all previous experimental data and theoretical models, which are summarised in Table 4.4.1, and consistent with the model that the oscillatory nature damps with increasing depth towards the bulk [2,3,34]. Despite agreement on the oscillatory behaviour of the surface, there are discrepancies between the magnitudes of the relaxations. Previous studies have focussed on LEED and ion scattering techniques, and this is the first reported SXRD study of the Ag(110) surface. The SXRD study is in remarkably close agreement with the theory calculations determined by the Embedded Atom Method (EAM)[4]. The values determined by SXRD are close to the LEED study by Davis and Noonan [26] and Lindroos *et al*. [8]; although only the first two interlayer spacings were considered in the LEED analysis. Interestingly the Rutherford Back Scattering (RBS) studies indicate significantly larger first and second interlayer distances which is not in agreement with other experimental findings or the distances predicted by theory calculations. A possible explanation for the differences arising from LEED and RBS,

put forward by M. Lindroos *et al.* [8] is due to the differences in sampling techniques. LEED is sensitive to well-ordered areas of the crystal, in comparison to RBS which samples the entire geometric area the beam is incident.

Another possible explanation for the discrepancies between studies could be due to the preparation of the surface. The characteristics of the Ag(110) surface are known to be sensitive to the history of the sample preparation [91]. Early studies by Zanazzi *et al*. [83] and Maglietta *et al.* [15] identified the importance of a well prepared Ag(110) surface for determining the surface relaxation, their differences between theory and LEED experimental measurements were reportedly due to a rough crystal, with a new freshly prepared crystal the relaxation of the surface was in closer agreement with their theory. The sample used in this work was oriented to within 0.1^{o} of the (110) plane, which is an order of magnitude greater than the sample used in the LEED study by Lindroos *et al.* [8], (other studies do not state the accuracy) which could also account for the differences in magnitude of the relaxations.

4.3.2 Ag(111)/vacuum interface

To determine a structural model for the Ag(111) surface measurements of the specular CTR, (0, 0, L) were made and the data is presented in Figure 4.5. As a greater range of L can be measured (compared with the Ag(110) surface), and no in-plane reconstruction is present, the specular CTR should be sufficient to determine the interlayer spacing of the Ag(111) surface. The black dashed line in Figure 4.5

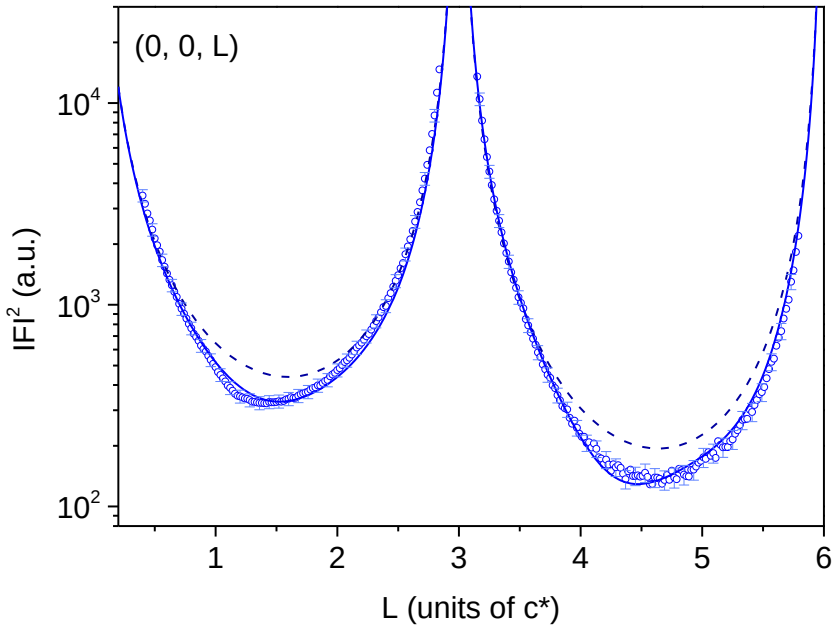

Figure 4.5 Specular CTR of the Ag(111) clean surface in UHV. Black dashed line represents the calculated fit for a perfectly terminated. The blue line represents the calculated best fit to the data using the model described in the text.

is a calculation of the Ag(111) surface with bulk termination (without any relaxations or surface roughness). This does not give a good fit to the measured data. The measured data has a slight asymmetry around the Bragg peaks which indicates that there is some relaxation of the surface. The intensity is also lower at the anti- Bragg positions, which suggests that the surface is perhaps quite rough. The CTRs were measured after cleaning the surface from a previous deposition of silicon on the surface; it is quite possible that the surface required more cleaning cycles to obtain a better quality surface. The Ag(111) electrode was fit with a simple model of allowing the top metal layer to relax and the rms roughness to vary. This however did not represent the data sufficiently; varying relaxations in the 2nd and 3rd metal layer still did not represent the data. It was possible to obtain a better fit to the data by using a structural model in which the coverage of the top metal layer was allowed to vary;

this gave a reduced occupancy of θ_{Ag} = 0.936 $\pm$ 0.003 monolayers, (ML). The reduced surface occupancy has not been noted before in UHV studies, however, the X-ray beam is averaging over a large part of the crystal surface (which is determined by the footprint of the incident beam), and hence it is not unusual to observe surface coverage below unity. This result has been found in an electrochemical environment by Lucas *et al.* [23] with a reduced occupancy of 0.94 ML. The top two layers have a small inwards relaxation of ε_1 = -0.007 $\pm$ 0.001 Å and ε_2 = -0.013 $\pm$ 0.001 Å and a top layer rms roughness of σ_1 = 0.053 $\pm$ 0.004 Å, which gives a reduced χ^2 of 1.23. The inclusion of a third layer relaxation did not improve the fit. The 2nd layer relaxation is slightly larger than the first, which is unusual; normally the magnitude of the relaxations is damped further into the bulk. This result could be explained by the reduced occupancy and rms roughness accounting for the relaxation of the top surface layer. The results are in accordance with the Landman model which predicts small relaxations for *fcc*(111) surfaces. Experimental UHV studies of the clean surface yield different results for the relaxations. Some authors say there is a small *inward* relaxation in the top two metal layers [12] whilst a LEED study by Soares *et al.* [14] finds that the surface is bulk like with no surface relaxations.

The results indicate the importance of a well prepared crystal. The Ag(111) surface may not be the best quality surface, however, the data was taken in between measurements of a silicon deposition experiment (discussed in chapter 5) which allows direct comparison between the two systems.

4.4 Conclusions

The results are a good indication as to the clean structure of Ag(111) and Ag(110) which is useful to know to compare to how the surface changes when it is in

contact with electrolyte or with silicon deposited. The Ag(110) surface was modelled by multilayer relaxations which identified an oscillatory nature of the surface relaxations in agreement with previous experimental data and theoretical models. The Ag(111) surface showed much smaller relaxations and only changes to the top two metal layers were required to fit the data. The Ag(001) surface was not studied in UHV in this thesis, however, previous studies have found that small *inwards* relaxation of the surface or no relaxations at all [11]. The strength of the relaxation is of the order Ag(111)<Ag(001)<Ag(110). The findings for Ag(111) and Ag(110) are consistent with this sequence. The relaxations of the surface increase with the coordination number of the surface. For an fcc metal the coordination number is 12, but at a surface this is reduced to 9 for (111), 8 for (001) and 7 for (110). The atoms try to increase their electron density by relaxing towards the bulk. The (111) surface is the most stable, whilst the (110) surface is much more open with the lowest coordination number and is more prone to relaxation to reduce surface energy consistent with the magnitude of the relaxations determined in this chapter.

5 Silicene Structures on Ag(111)

5.1 Introduction

The discovery of graphene [92] and its compelling electronic properties has fuelled research into other 2-dimensional materials. In particular, other group-IV elements have received significant attention (Si, Ge, Sn) [80,81]. 2-dimensional forms of Si and Ge were actually predicted in 1994 by Takeda and Shiraishi [95] prior to the emergence of graphene. They were predicted theoretically to exist in a free-standing form with a low corrugated hexagonal structure – 'buckled honeycomb' - rather than the planar structure of graphene, this is shown in Figure 5.1. Later termed 'silicene' [96], the silicon based analogue of graphene is now an

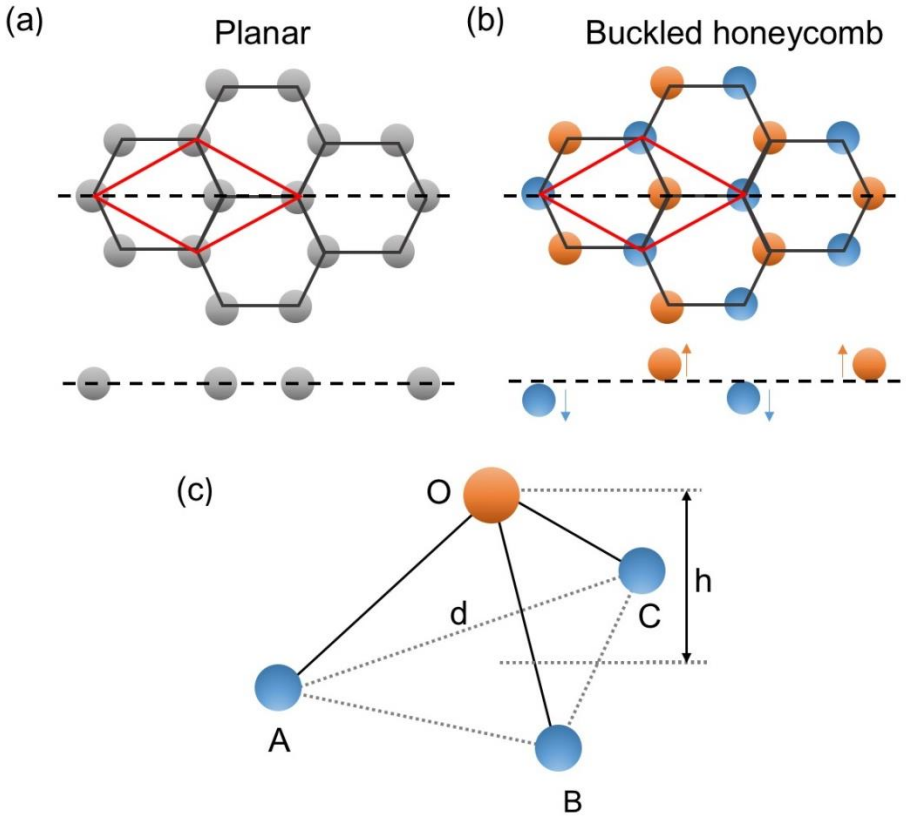

Figure 5.1 Schematics of (a) planar lattice, where grey circles represent atoms, and (b) buckled honeycomb lattice, where the blue circles represent atoms in the bottom plane and the orange circles represent atoms in the top plane. (c) Pyramid consisting of four Si atoms, *h* is the height of the top plane above the bottom – giving a measure of the buckling. Image reproduced with permission from [97] Copyright (2015) Progress in Surface Science.

emerging new material, and is proposed to have similar novel electronic and chemical properties as graphene, but with the advantage of being more easily integrated into the silicon based electronics industry. Unlike Graphene, silicene is much more difficult to produce as the hexagonal structure does not exist naturally in a free-standing state, and cannot be exfoliated from the bulk material as Si has a diamond structure. This is due to the difference in hybridisation between Si and C. Carbon is easily sp and sp^2 hybridised, whereas silicon undergoes sp^3 hybridisation which makes a three-dimensional tetrahedral configuration, shown in Figure 5.1 (c).

In its lowest energy state silicene is slightly buckled and its Si-Si bond length is much larger compared to the C-C bond in graphene. This prevents full sp^2 hybridisation of the structure, the buckling enables larger overlapping of orbitals forming a mixed sp^2 and sp^3 hybridisation [98]. Free-standing silicene is predicted theoretically to be a gapless semiconductor with Dirac cones at the K points of the Brillouin zone like graphene [93]. However, the buckled nature of silicene may allow potential to tune the band gap, by applying an electric field to silicene may open up the bandgap [99]. This introduces the potential for logic applications and topological insulators [100].

The immense potential of silicene has created a surge in its research within the past few years and understanding the atomic structure of silicene is of vital importance to tune its electronic properties [101]. As silicene does not occur naturally, a substrate is required in order to grow it. Silicene has been reported to grow on ZrB2(0001) [102], Ir(111) [103] and MoS_2 [104]. The most promising and, as a result, the most widely studied substrate is silver. Silver and silicon have a low tendency to alloy [91-92]. Ag/Si phase diagram shows no miscibility in the solid phases, and the reverse system Ag on Silicon is known to make a sharp interface [107] which makes it an ideal substrate to study, as, for silicene to be truly 'free-standing' it must have little or no interaction with the substrate. The similar electronegativity of Ag and Si should lead to only a small charge transfer [108] however, the extent of this interaction is still under debate [51].

The first experimental report of silicene was on Ag(111), an STM study, by Lalmi *et al.* [109], however, the results have never been reproduced and this is now widely disregarded. Reports have followed of silicene structures on the Ag(110) surface in the form of nanoribbons [110]. In 2012 the first sheets of silicene on

Ag(111) were reported independently by Vogt *et al.* [111] and Lin *et al.* [112].

The growth of silicene is extremely sensitive to the Ag substrate temperature and the Si deposition rate. Depending on these parameters a wealth of different structures can be obtained (4×4) [83,89,93,96–103], $\left(\sqrt{13} \times \sqrt{13}\right)R19.9°$ [83,94,99,102,104-105], $\left(2\sqrt{3} \times 2\sqrt{3}\right)R30°$ [95,105–107], $(3.5 \times 3.5)R26°$ [115] and $\left(\sqrt{7} \times \sqrt{7}\right)R19.1°$ [117] structures are often found to coexist. All of the structures are understood to be a single silicon layer, with a honeycomb lattice arrangement. The amount of buckling in the layer varies between the orientations of the honeycomb lattice [97], as the density of the unit cell varies between structures. Upon further deposition of Si, beyond the monolayer, a $4/\sqrt{3} \times 4/\sqrt{3}$ [113] structure is formed which is proposed to be 'multilayer silicene' [122].

Despite the wealth of silicene structures the best candidate for free-standing silicene is the (4×4) structure, which is predicted theoretically, and shown experimentally to have a low buckled state [94,109]. As such, the (4×4) structure is the most widely investigated structure. In order to determine the atomic structure, surface sensitive techniques have been utilised. STM and AFM have been used to identify the atomic arrangement of Si, however, information relating to the substrate is lacking. For this, diffraction techniques such as LEED and RHEED are required as they are far more powerful and reliable for the determination of atomic structure.

There have been several models proposed for the (4×4) structure with varying densities of Si atoms in the unit cell. The model which is currently accepted was first proposed by Lin [112] (STM, LEED) and Vogt [111] (STM, LEED) , with 18 Si atoms in the unit cell, 12 in the lower plane and 6 buckled in a higher plane. This model was later backed up more detailed investigations by LEED-IV [123] and Reflection High-Energy Positron Diffraction RHEPD [118], which also proposed Si

buckling parameters of 0.74-0.78Å and 0.8 Å respectively. The differences in models indicate that further investigations are still required in order to confirm the correct structural model for the Si/Ag(111) system. The analysis of dynamical diffraction based techniques, such as LEED and RHEPD, is complex due to multiple scattering effects. The cell coordinates of all atoms in the surface region must be determined simultaneously, which leads to parameter coupling. These techniques are also primarily sensitive to the top few atomic planes and thus the precision of the relaxations may be low. SXRD, however, is an ideal technique which can overcome these uncertainties as it is sensitive to the both the surface layers and the bulk, and a kinematic approximation can be applied making the analysis much simpler.

In this chapter the growth of silicene structures on Ag(111) has been investigated by LEED and SXRD. A preliminary structural model of the surface normal structure of Ag(111)/Silicene interface is proposed.

5.2 Experimental

SXRD experiments were carried out at I07 beamline at Diamond Light Source, with an X-ray beam of energy 20 KeV. Silicon was evaporated from a Si rod using an Omicron electron bombardment evaporator with an integrated flux monitor. This was used to maintain a constant deposition rate. Silicene was synthesised in UHV and characterised *in situ* through SXRD. The SXRD experiment followed standard procedures for the collection of structure factor data to enable structure analysis. This involved measurement of a large set of symmetry-independent structure factors due to the (4×4) ordered silicene phase and the CTRs from the underlying Ag(111) substrate. A specular CTR analysis of the interface structure is given in this chapter. The specular CTR offers valuable information about the coverage of the silicon layer

and the Ag-Si layer spacings, which can be used as a starting point for the complete structural analysis. A full structural analysis is currently being performed, but is outside the scope of this thesis. The growth parameters and LEED images presented in section 5.3.1 were taken in the nanomaterials characterisation laboratory in the Stephenson Institute for Renewable Energy in University of Liverpool by the author of this thesis and David Martin. The initial SXRD experiment at Diamond Light Source was not optimised and as a result the experiment was repeated at a later time by David Martin, Chris Lucas, and Nikolas Antonatos from University of Liverpool and Matthew Forster, and Jonathan Rawle from I07, Diamond Light Source; this LEED and SXRD data is presented in section 5.3.2. The SXRD data presented in this chapter was processed and fit by the author of this thesis.

5.3 Results and discussion

5.3.1 LEED

For optimising the growth conditions LEED was an essential technique used to identify the type of silicene structure on the surface. Determining the conditions for silicene growth was a very difficult process of trial and error to even obtain an ordered structure. The growth of silicene structures depends critically on the temperature of the substrate and the rate of deposition. The structure of Si on Ag(111) was investigated at different temperatures. The temperature was measured with a static pyrometer, Land Infrared System 4, (emissivity 0.2), from Landmark. To gain a temperature reading of the surface the pyrometer was positioned next to a viewing port on the UHV chamber and focused on the surface of the crystal. The substrate spots were orders of magnitude brighter than the superstructure spots, which drowned out the intensity from the silicene. In order to obtain clear images of

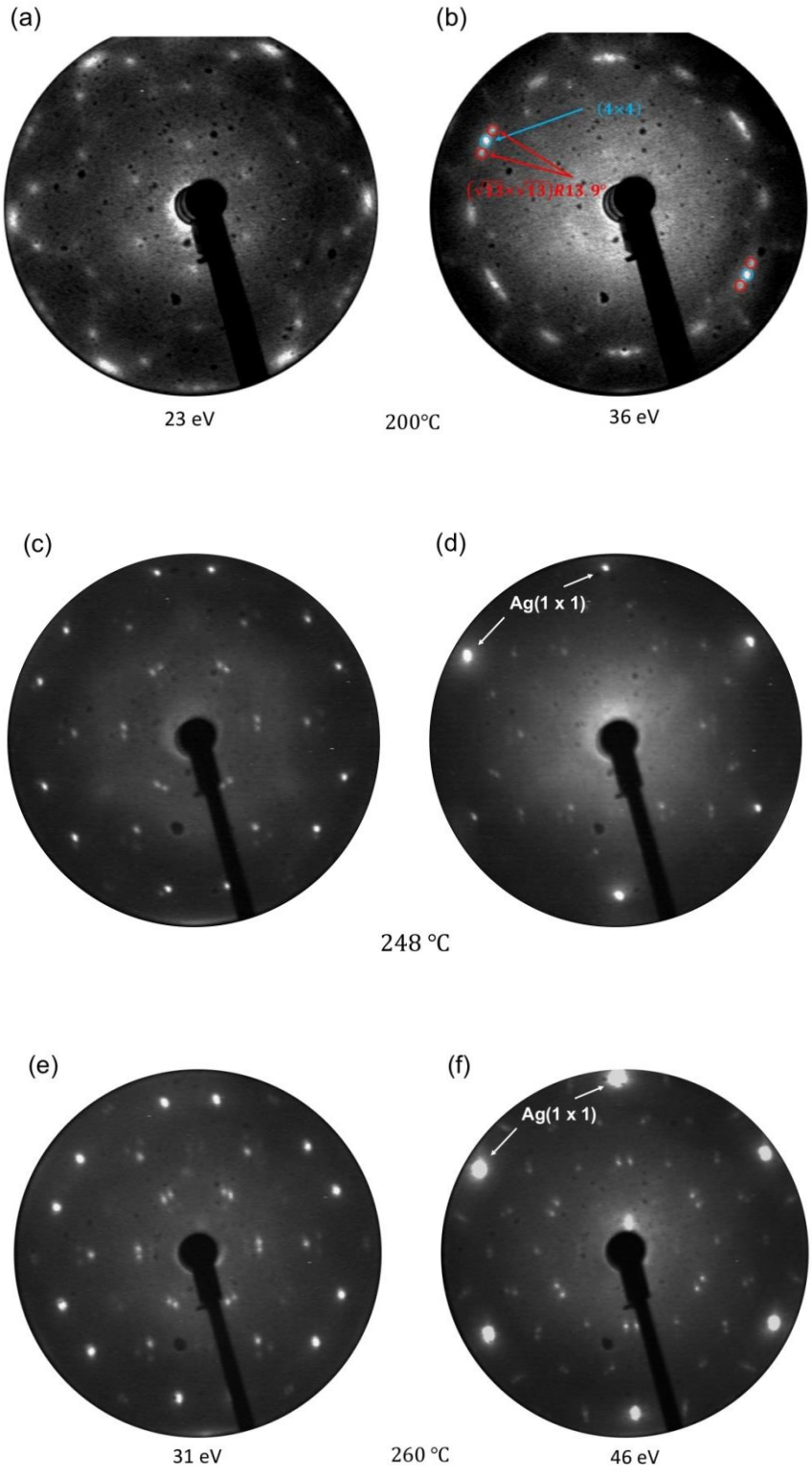

Figure 5.2 LEED images obtained after depositing Si at various temperatures. Images were taken at energies (a) 23 e V(b) 36 eV, at 248º C taken at energies (c) 33 eV (d) 61 eV and at temperature 260º C at energies of (e) 31 eV and (f) 46 eV.

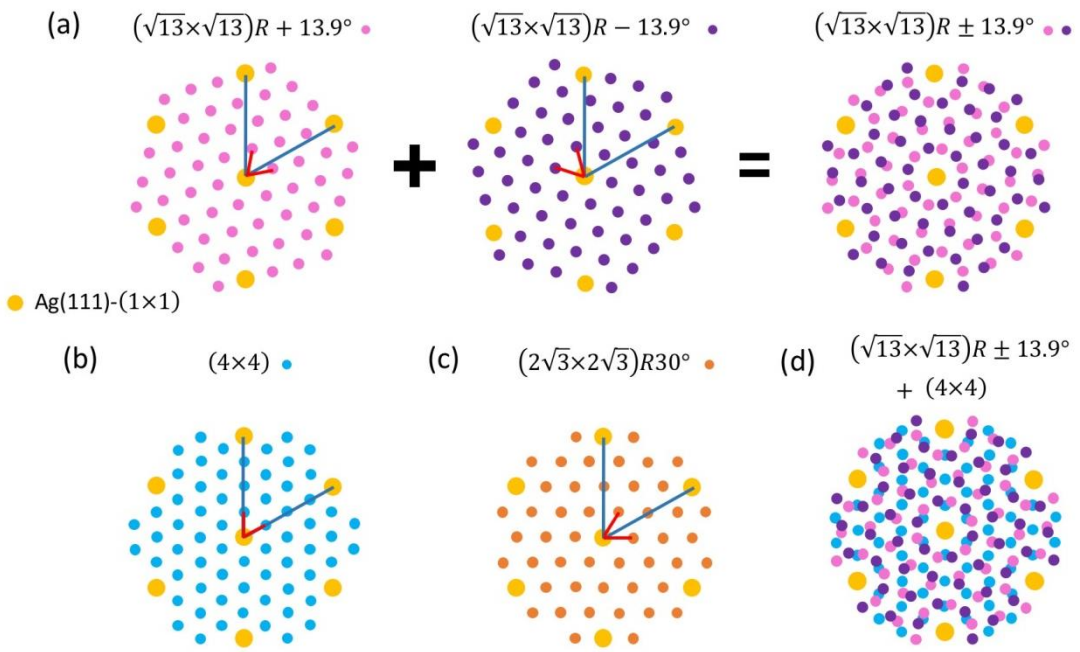

Figure 5.3 Simulated LEED images using LEEDpat and reproduced for presentation. The Ag(111) (1×1) substrate spots are indicated by the open yellow circles. The unit cell of Ag(111) is indicated by blue line, the bases for the superstructures are indicated by the red lines. (a) The two rotations of the $(\sqrt{13}\times\sqrt{13})R\pm13.9°$ structure are shown - two domains are overlayed in the image on the right where pink circles indicate the positive rotation and purple circles indicate the negative rotation. (b) (4×4) structure (blue circles) (c) $(2\sqrt{3}\times2\sqrt{3})R30°$ structure (orange circles) additional domains (as observed in the measured LEED pattern) cannot be simulated. (d) mix of $(\sqrt{13}\times\sqrt{13})R\pm13.9°$ and (4×4) as seen in measured LEED images.

the superstructure spots, the frames per second of the image capture was changed between images as the substrate spots came further in view – in order to reduce the intensity so that the superstructure spots were still in view. As the intensity was not relative between the images meaningful LEED-IV curves could not be extracted, despite this the LEED images contained enough information to determine the structures using image analysis software, ImageSXM written by Dr Steve D. Barrett (University of Liverpool). Figure 5.2 summarises the different LEED patterns that

were observed, and figure Figure 5.3 gives shows a simulated LEED pattern for the structures – for clarity. At low temperature (200℃) the coexistence of the (4×4) phase and $\left(\sqrt{13} \times \sqrt{13}\right)R13.9°$ can be observed. With increased temperature, at 248℃ only the $\left(2\sqrt{3} \times 2\sqrt{3}\right)R30°$ phase is visible, there is no pattern from the (4×4) structure. The spot splitting that can be seen is attributed to the coexistence of different domains of the $\left(2\sqrt{3} \times 2\sqrt{3}\right)R30°$ phase, which is more prominent with higher temperature as seen in Figure 5.2 (e) and (f). These results are in agreement with previous publications, which have shown that at lower temperatures the (4×4) structure coexists with the $\left(\sqrt{13} \times \sqrt{13}\right)R13.9°$ structure [100,101,105]. The $\left(2\sqrt{3} \times 2\sqrt{3}\right)R30°$ structure is found at higher temperatures and has been found to occur in a single phase [121]. The structure of this phase has been of great debate [106,111], LEED patterns showing additional spots have also been observed by various groups. Arafune *et al.* [115], Moras *et al.* [119] interpret the LEED patterns as a mixture of structures such as $\left(\sqrt{19} \times \sqrt{19}\right)R23.4°$ and $(3.5 \times 3.5)R26°$. More recently Jamgotchian *et al.* [120] and Rahman *et al.* [125] associate the extra spots to a large $\left(\sqrt{133} \times \sqrt{133}\right)R4.3°$ superstructure. It is obvious from the LEED images that this structure is a complex mix of phases. For this reason, and to limit the complexity of analysis, the low temperature phase of the Ag(111)/Si interface was probed by SXRD.

5.3.2 Characterisation by Surface X-ray Diffraction

A detailed description of the atomic structure of the Ag(111)/Silicene interface can be determined by SXRD. Scattering from specific silicene structures can be separated from the scattering due to the underlying substrate. As the (4×4)

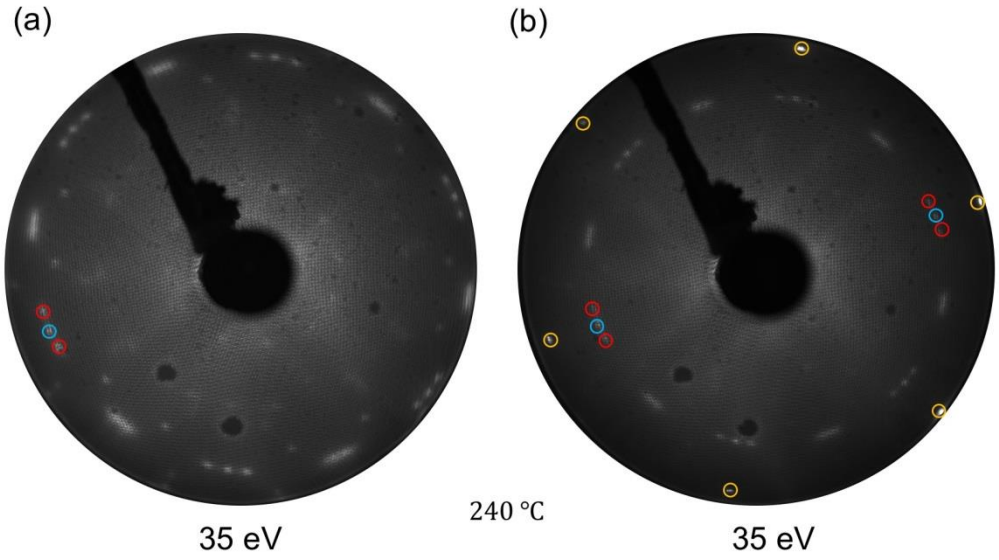

Figure 5.4 LEED images of Ag(111) surface after 60 minute Si deposition. The Ag(111) substrate spots are highlighted by yellow circles, Si (4×4) blue circles and $\left(\sqrt{13} \times \sqrt{13}\right)R13.9°$ red circles taken at (a) 35 eV and (b) 55 eV.

structure is the most studied surface it was the focus of the SXRD measurements in this section. The silicene structures were grown *in situ* in the UHV system on I07 at the Diamond light source. Si was deposited for 60 minutes at 1.5 nA flux with the substrate held at 360 ℃. The temperature was read by a thermocouple, between the sample and filament, which over reads the value of the substrate temperature. The actual reading is estimated as 2/3 of the measured value, this was obtained by measuring a sample with a well-known phase transition (this was previously determined by other users of the beamline). This would give an actual temperature reading of about 240 ℃. SXRD measurements were taken in the controlled atmosphere of the UHV chamber. These conditions resulted in a LEED pattern as seen in Figure 5.4. The LEED shows a mix of co-existing structures, (4×4) and $\left(\sqrt{13} \times \sqrt{13}\right)R13.9°$. Although there is a mix of structures, the scattering specific to

the (4×4) structure can be isolated due to the high resolution of the diffraction measurements.

In-plane structure

The in-plane directions were scanned to identify any scattering peaks occurring from the silicene structures. Figure 5.5 (a) shows an in-plane scan along the K-direction of both the clean Ag(111) surface and Si-covered surface. The intensity of the diffraction peaks of the Ag(111) surface dominates the measured signal. Since the scattering power of Si is considerably smaller than that of Ag, any peaks that arise due to scattering will be relatively small. Figure 5.5 (b) shows the data over a limited K range to highlight the peaks that arise due to the presence of the silicene layer. In addition to the data shown in Figure 5.5 scans along the symmetry equivalent directions, (H, 0), (H, K), (-H, K), and (-H, -K) were also measured.

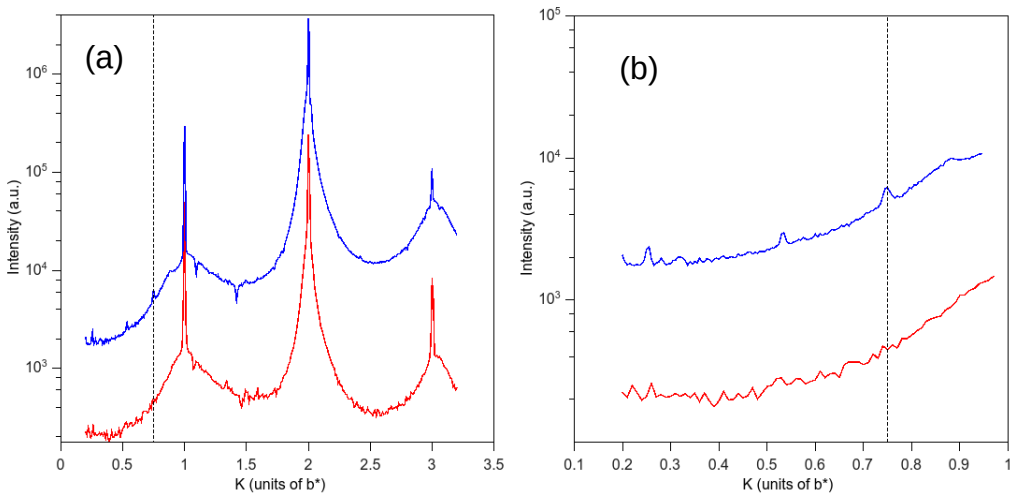

Figure 5.5 In-plane scan (H=0) along the K direction of the clean Ag(111) surface (red) and the Ag(111)/Si surface (blue). (b) smaller scale to identify (4 x 4) structure peak. Measured at L= 0.8.

Peaks due to scattering from the silicene layer were observed at (0.75, 0), (0, 0.75), and (0.75, 0.75). There are other peaks of a similar magnitude to the one at L=0.75 which can be seen in Figure 5.5, these peaks are not present in other symmetry equivalent directions – indicating that they are not due to ordered structures and are due to power peaks which can be seen in the image files.

Rocking scans

Rocking scans were performed at the superstructure peak position. The peak is located at H= 0.748 which corresponds to an in-plane lattice constant of a = 3.866 Å, this is in agreement with theory models for free-standing silicene [95]. The rocking scans through the (0.748, 0.748, 0.8) position are shown in Figure 5.6. The data were fit to a Lorentzian lineshape and gave a full width at half maximum (FWHM) of 0.44º respectively. The domain size can be determined by using

$$domain\ size = \frac{2}{\boldsymbol{q}\Delta\theta} \tag{5.11}$$

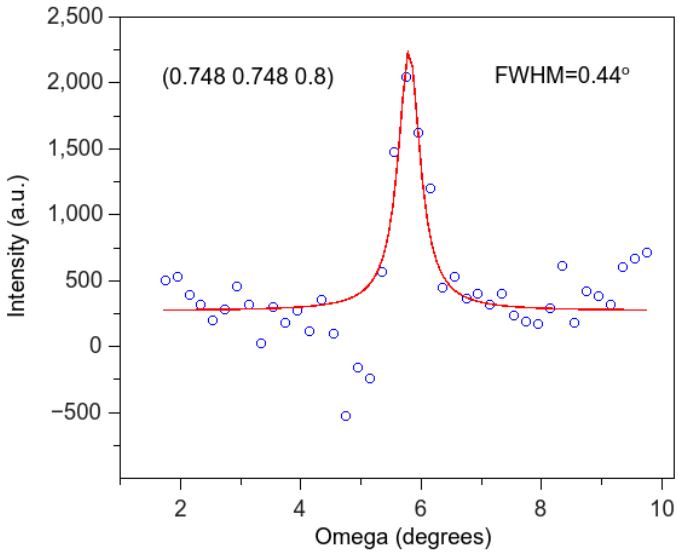

Figure 5.6 Rocking scan through the (4×4) structure peak (0.748, 0.748, 0.8).

where q is the momentum transfer and θ is the FWHM in radians. This gives an ordered domain size in the range 77-78 Å. The rocking scan of the (4×4) superstructure peak was measured in a study by Curella *et al*. [108] at substrate temperatures of 520 K and 570 K. At the lower temperature the peak 2.5 times broader (no values given for FWHM) and the integral was 2.4 times larger; which suggests that although the domains of the structure are smaller at the lower temperature, they cover a larger proportion of the surface.

L dependence

The X-ray measurements focused on the diffracted intensity from the (4×4) structure. A number of CTRs and symmetry equivalent Fractional Order Rods, FORs, were measured. A detailed analysis of these rods is beyond the scope of this thesis, however, a similar study has very recently been published (2016) by Curcella *et al.* [108], which determined the atomic structure of the (4×4) silicene phase through grazing incidence X-ray diffraction measurements (GIXRD) and DFT calculations data. They analysed a number of FORs arising from scattering from the (4×4) structure (calculated from rocking scans performed along the FORs), no CTRs were included in the analysis as they would contain information relating to other silicene orientations. The analysis from the GIXRD experiment indicates that the silicene unit cell consists of 18 atoms, with 6 atoms lying above the plane of the other 12 atoms, consistent with previous works [123]. Curcella *et al.* determine the distance between the two planes corresponds to a buckling of 0.76 Å and a buckling of the top two Ag metal layers which is consistent with a previous LEED study [123], the structural model determined by Curcella is shown in Figure 5.8. The form

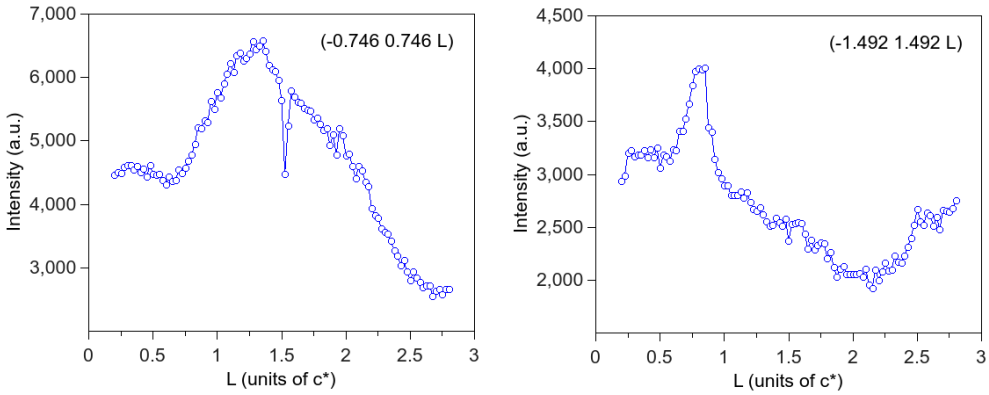

Figure 5.7 L scans along the first and second order superstructure rods, (-0.746, 0.746, L) and (-1.492, 1.492, L) respectively.

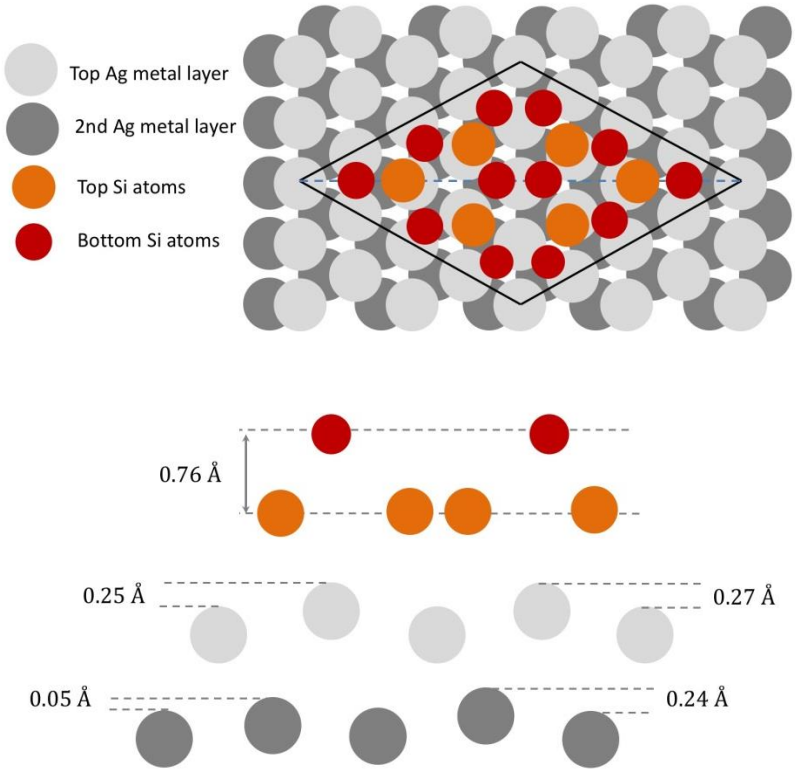

Figure 5.8 Top and side view of the (4 x 4) reconstruction of silicene on Ag(111), showing the unit cell, the top layer Si atoms (red), bottom layer Si atoms (orange), top Ag metal layer (dark grey) second layer Ag (light grey). Reprinted with permission from Curcella *et al*. [108] Copyright (2016) American Physical Society.

of the FORs in Figure 5.7 is very similar to those presented by Curcella which suggests that the structure would be very similar. The structural analysis presented by Curcella *et al.* does not include the CTRs, which are important to reference the structure to the substrate. It is not clear whether the CTRs were initially considered in the analysis, and determined to be too complicated; as the CTRs will have contributions from the other silicene structures on the surface.

Specular CTR analysis

A simpler analysis is to focus on the structure along the surface normal by analysing the specular CTR. The specular CTR is not sensitive to the in-plane atomic

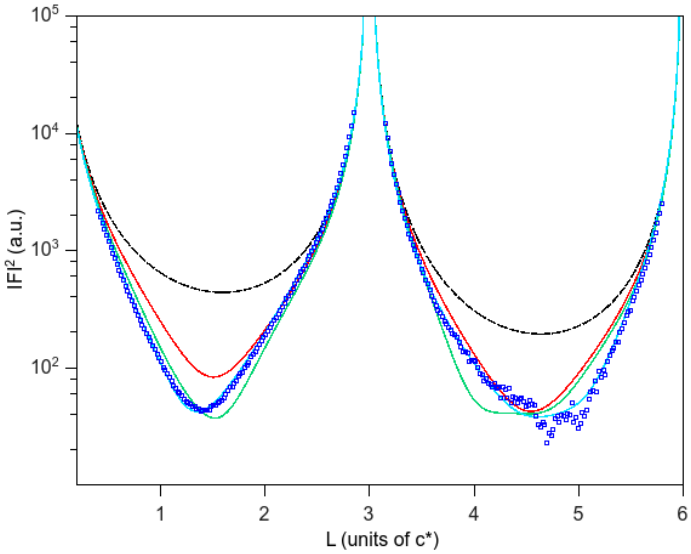

Figure 5.9 Specular CTR data of Si on Ag(111). The dashed black line is the calculated perfectly terminated Ag(111) surface with no silicon. The red line is the calculated CTR of a perfect monolayer of Si on the Ag(111) surface (with layer spacing fixed at bulk Ag value $d_{(111)}$ = 2.36 Å). The green line is the fit with 1 adlayer of silicon, and the blue line is the fit with two Si adlayers which gave the best fit to the data.

positions and is thus not specific to the (4×4) structure, but a sum over all of the silicene structures and the average in-plane Ag positions. The specular CTR and calculated fits can be seen in Figure 5.9. The shape of the CTR is dramatically different from the bulk terminated Ag(111) surface, represented by the black dashed line. The profile of the CTR is consistent with there being one monolayer of silicon on the surface as the intensity has a minima at the anti-Bragg position. A calculation according to a model with 1 monolayer (ML) of silicon (height of layer fixed at the d spacing of Ag(111) $d_{(111)}$ = 2.36 Å) on an unrelaxed Ag(111) surface is shown in Figure 5.9 as a comparison (red line). This does not give a good fit to the data, however, the form is very similar, suggesting a monolayer of Si on the surface. To model the data the vertical displacement of the top two metal layers, and the rms roughness of the top layer was allowed to vary, the silicon was incorporated into the fit as an adlayer, and the coverage and height of the layer was also varied. This gave

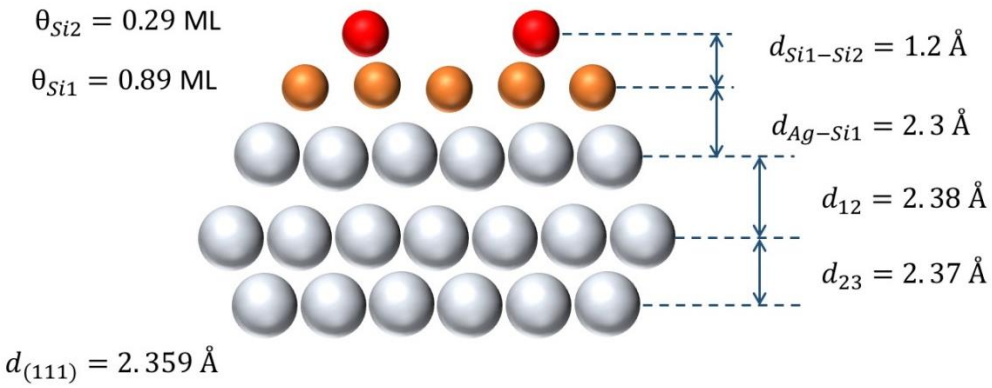

Figure 5.10 Schematic representation of the structural model of the Ag(111)/Si interface as determined by the model described in the text. The silver coloured balls represent the top 3 Ag surface metal layers. The orange circles represent the Si layer closest to the surface, and the red circles represent the top lying silicon atoms.

the poor fit represented by the green line with a reduced χ^2 of 15.36. This indicates there was something missing from the model. To improve the fit to the data it was necessary to incorporate a second silicon layer into the model. The best fit indicated the silver layers undergo a small *outwards* relaxation; top metal layer was expanded by 0.033 ± 0.001 Å, and had a rms roughness of σ=0.124 ± 0.004, second atomic layer relaxation of 0.012 ± 0.001 Å. The first silicon layer is located at 2.307 ± 0.005 Å above the top Ag metal layer, with coverage of 0.894 ± 0.007 ML and the second silicon layer is 3.50 ± 0.02 Å above the top metal layer with a coverage of 0.293 ± 0.008 ML, the rms roughnesss of the Si layers were fixed just above the value determined for Ag, at 0.15 Å, as this parameter can couple with the coverage during the fitting procedure. This fit gave a reduced χ^2 = 1.62, Figure 5.10 shows a schematic representation of the structural model. With silicon deposited, the *inwards* relaxations determined for the clean Ag(111) (in chapter 4) become an *outward* relaxations. This finding is consistent with the structural model determined by Curcella [108], which indicates a buckling in the top two silver layers. The specular CTR is not sensitive to in-plane positions and thus gives an average of the displacement of the layer as a whole. As the interlayer spacing between the two Si layers is small 1.19 ± 0.02 Å it is associated with the the buckling of the Si layer, rather than due to a bilayer of silicene. The buckling obtained for the Si layer is far greater than 0.76 Å previously determined for the (4×4) structure [108], however, it is not an unreasonable result considering the specular CTR accounts for the whole surface with scattering contributions from all of the silicene phases. It is possible that the (4×4) structure is not the most dominant phase on the surface. Theoretical models have predicted the $\left(\sqrt{13} \times \sqrt{13}\right)R13.9°$ and $\left(2\sqrt{3} \times 2\sqrt{3}\right)R30°$ are more strongly bucked ~1-1.2 Å [126], however; no experimental out of plane atomic

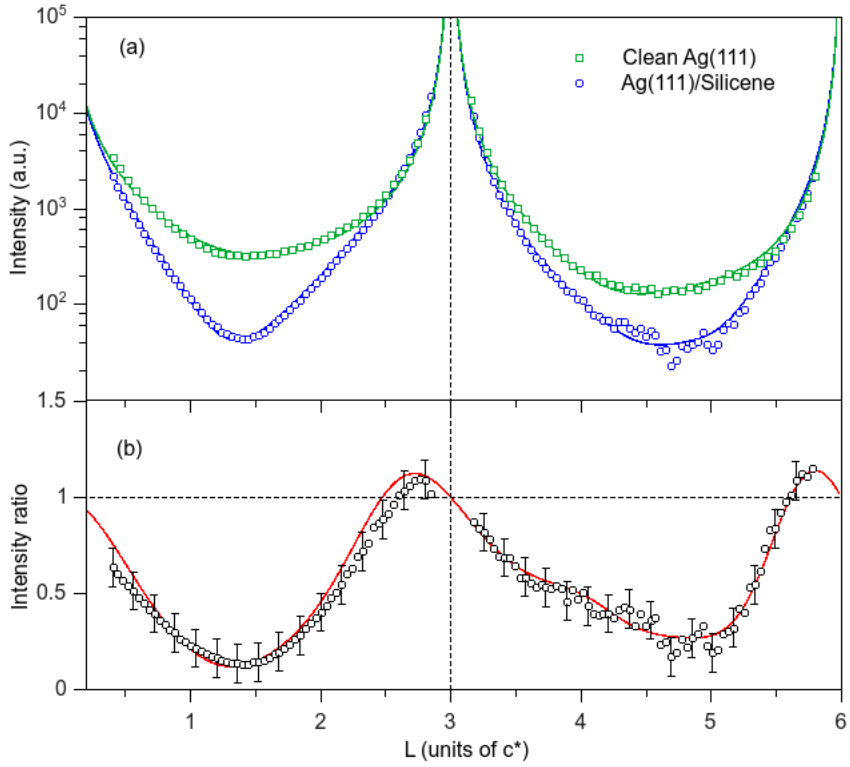

Figure 5.11 (a) Specular CTRs of the clean Ag(111) (green) and Si/Ag(111) (blue), (b) Si/Ag(111) normalised to the clean Ag(111) data (black circles) and ratio of the calculated fits (red line.)

structure of the interface has been determined for these phases. The increased buckling is attributed to the increased density of the structure.

In Figure 5.11 the data of the silicene covered Ag(111) surface is compared to the clean Ag(111) (which was presented in chapter 4). The ratio of the two datasets highlights the differences between the two systems and removes systematic errors. The solid line is the ratio of the two models used to fit the CTR data. The CTRs were modelled independently and a good fit to the ratio of the data indicates that any differences between the CTRs are well modelled. Although this is a simple model, it is a useful starting point to determine the structure of the Ag(111)/Silicene interface. As the specular CTR is an average over all the structures it also gives the

first experimental indication to buckling in the $(\sqrt{13} \times \sqrt{13})R13.9°$ structure. In order to establish the in-plane structure a comprehensive study of CTRs fractional order reflections is still required. This will be similar to the publication by Curcella, in addition, by including the CTRs in the analysis the silicene structure can be directly related to the bulk silver crystal. This would make for a more complex analysis as there would be scattering contribution from the $(\sqrt{13} \times \sqrt{13})R13.9°$ structure.

Deposition time

In this section the effect of Si deposition time on the (4×4) structure is determined. Silicon was deposited with a flux of 1.60 nA and the substrate was held at temperature ~238º throughout the measurements. The intensity was measured along the H direction through the (0.75, 0, 0.8) peak, (which occurs due to scattering from the (4×4) with increasing deposition time, this is shown in Figure 5.12 (a). The peak intensity increases with increasing deposition time until it levels off at 70 minutes (no LEED pattern was taken at this point – although LEED images were taken at 65 mins, Figure 5.4, and 75 mins, Figure 5.13). The increase in intensity at this position is attributed to the increasing coverage of the (4×4) structure. The point where the intensity levels off indicates the completion of a silicene monolayer. Figure 5.12 (b) shows the change in peak intensity with increasing deposition time and indicates a linear uptake of Si on the surface.

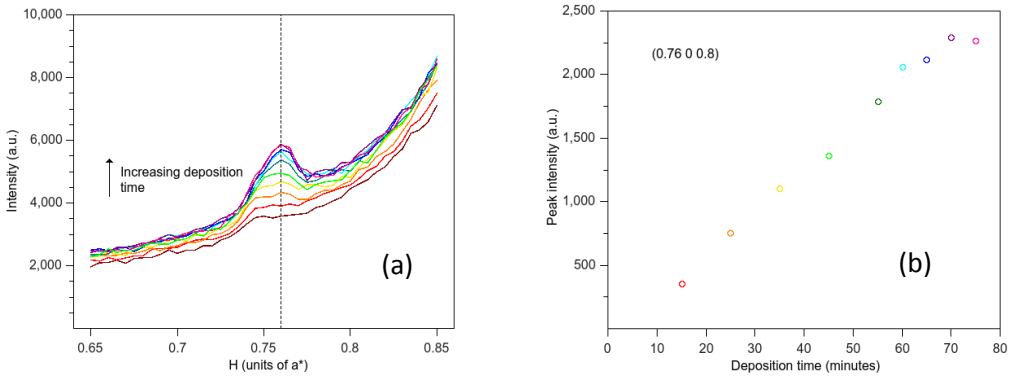

Figure 5.12 (a) Scans measured through the (H, 0, 0.8) direction for increasing deposition time of Si, (b) Intensity of the (0.76, 0, 0.8) peak with increasing deposition time of Si.

As the intensity saturated at 1 ML and took approximately 70 minutes the deposition rate could be calculated; 0.014 ML/min. The linear deposition rate is consistent with the study by Vogt *et al.* [111] which found slow deposition rates produce a better quality silicene structure. The deposition rate used by Vogt *et al.* was 0.016 ML/min and yielded a (4×4) LEED pattern, with no indication of other structures present on the surface. Although the structure presented in this chapter was grown at a similar deposition rate, a single (4×4) structure could not be obtained; this shows the difficulty and sensitivity of the growth of silicene. This is consistent with the LEED images, Figure 5.13, taken after 75 minutes of Si deposition. The LEED pattern is similar to that taken for 60 minutes; however, there is an appearance of extra spots which can be attributed to the $\left(4/\sqrt{3} \times 4/\sqrt{3}\right)$ which is consistent with studies in the high coverage regime where this structure appears [127]. The structure appears as part of a halo structure in the LEED images, which indicates that there are various rotational domains. The $\left(4/\sqrt{3} \times 4/\sqrt{3}\right)$ structure has been attributed to a bilayer of silicene by Arafune *et al* [127]. Padova *et al.* [128] have suggested that the structure is multilayer silicene, formed by islands of the $\left(4/\sqrt{3} \times 4/\sqrt{3}\right)$ structure.

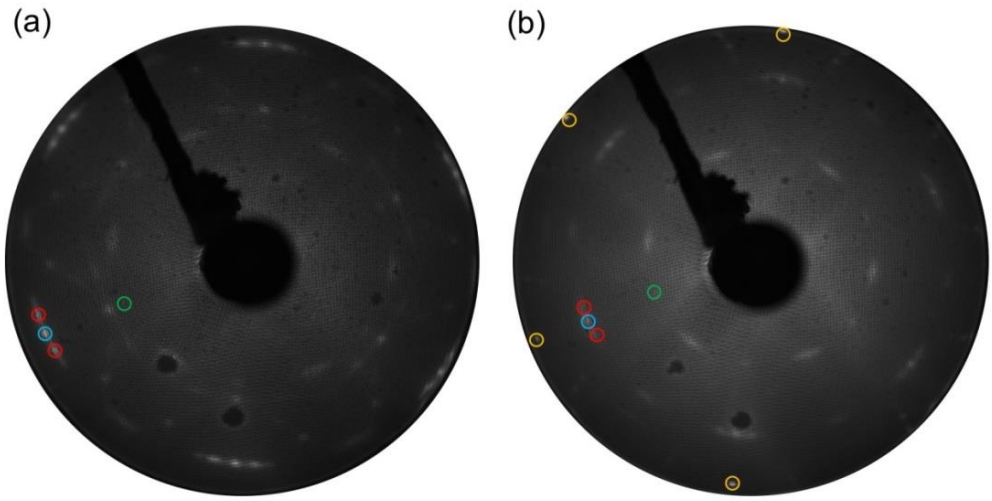

Figure 5.13 LEED images after 75 minute Si deposition Ag(111) substrate spots indicated by yellow circles, (4×4) blue circles and $\left(\sqrt{13} \times \sqrt{13}\right)R13.9°$, green $\left(4/\sqrt{3} \times 4/\sqrt{3}\right)$ taken at (a) 31 eV and (b) 48eV.

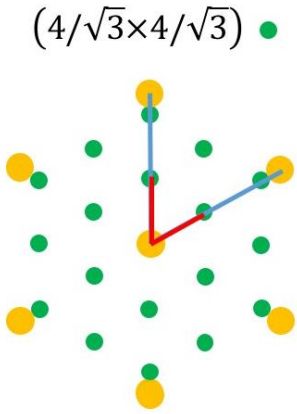

Figure 5.14 Simulated $\left(4/\sqrt{3} \times 4/\sqrt{3}\right)$ LEED pattern by LEEDpat and reproduced for presentation. The Ag(111) (1 x 1) substrate spots are indicated by the yellow circles, spots arising from the silicene structures are indicated by the green circles. The unit cell of Ag(111) is indicated by blue line, the bases for the $\left(4/\sqrt{3} \times 4/\sqrt{3}\right)$ are indicated by the red lines.

The model of this structure is still under debate as a structure similar to the Si (111) $(\sqrt{3} \times \sqrt{3})$ –Ag structure has been also been proposed [122].

A set of CTR and FOR measurements were taken after 75 minutes deposition. In Figure 5.15 the specular CTR is compared with the data from the 60 minute deposition and the clean Ag(111) surface. A model to this data has not yet been determined due to time constraints. As the interface structure is complex, it has proven difficult and time consuming to reproduce at fit to the data. However the form on the CTR is still of importance to and supports conclusions drawn from analysis of the LEED images.

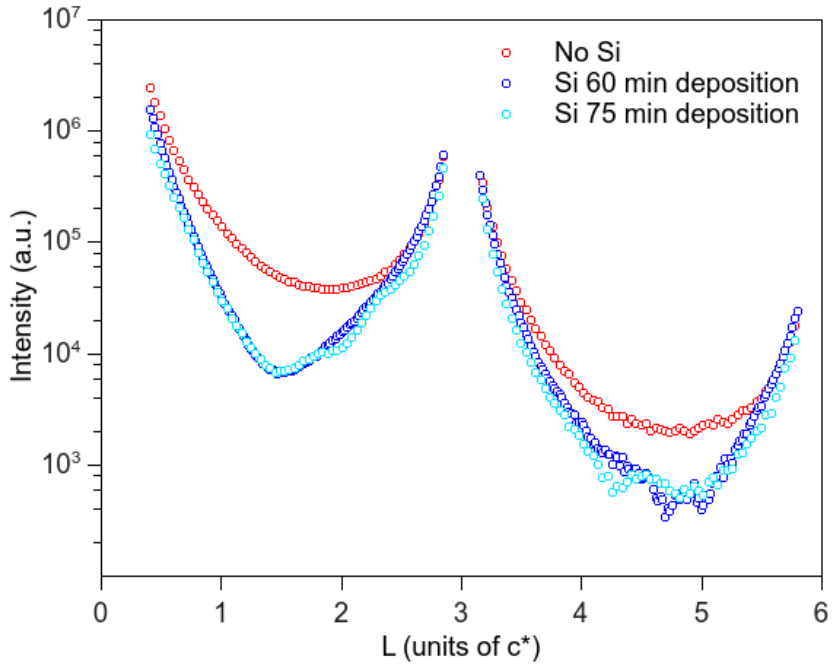

Figure 5.15 Specular CTR data of the clean Ag(111) surface, red, 60 minute Si deposition, blue, 75 minute Si deposition, cyan.

The shape of the 75 minute deposition is similar to that of the 60 minute deposition; however there are oscillations along the profile. The oscillations indicate that there are areas of several layers of silicene on the surface. From the LEED and

specular CTR measurements it is possible to assume that there are islands of $(4/\sqrt{3} \times 4/\sqrt{3})$ multilayer silicene coexisting with patches of monolayer silicene, as the (4×4) and $(\sqrt{13} \times \sqrt{13})R13.9°$ structures are still visible in the LEED pattern. Full CTR analysis would vital to help elucidate this structure.

5.4 Summary and conclusions

Silicene structures were successfully grown on the Ag(111) substrate. The Si/Ag(111) forms an exotic mix of structures and it is has proven difficult to form a single phase on the surface. SXRD is therefore the ideal technique in order to probe individual structures as the scattering from these structures can be separated in reciprocal space and a detailed analysis can be obtained.

The first specular CTR study of the interface structure has been presented, from this the average structure of the Si/Ag(111) interface has been determined. The analysis indicates interesting differences to the study by Curcella *et al.* [108], which only considered scattering from the FORs for the (4×4) silicene structure. The overall buckling of the surface was much greater than the value determined for the (4×4) structure indicating that this may not have been the most dominant structure on the surface under study. The specular CTR will have a contribution from the $(\sqrt{13} \times \sqrt{13})R13.9°$ structure as it is not sensitive to in-plane ordering. The result is interesting as it hints at a larger buckling, likely due to the $(\sqrt{13} \times \sqrt{13})R13.9°$ – which has only been theoretically predicted.

It is clear, that in order to obtain a complete analysis of the Ag(111)/Silicene interface the structure of the other silicene orientations needs to be addressed. The deposition of Si undoubtedly has an effect on the surface Ag(111) surface as it

undergoes small, but non-negligible changes which results in the expansion of the top two surface metal layers. The interaction of Si with the Ag(111) surface could be probed further by resonant surface X-ray diffraction which could determine the charge transfer at the interface [129].

6 Ag(*hkl*)/Alkaline electrolyte interface

6.1 Introduction

The development of new materials for clean energy conversion and storage is of vital importance towards the advancement of renewable energy technologies. A fundamental understanding of the structure at the electrochemical interface is central to this. Both the nature of the electrode material and the structure of the electrochemical double layer (as discussed in chapter 2) govern the mechanisms of important electrochemical processes, such as the Oxygen Reduction Reaction, (ORR), Hydrogen Oxidation Reaction, (HOR) and CO oxidation amongst others. Despite this, the focus of studies is predominantly on the metal side of the interface, and information about the double layer is severely lacking. Knowledge of the double

layer structure and how its architecture affects the kinetics of reactions allows for specific tailoring of the electrochemical interface.

Two types of interaction at the electrochemical interface have typically been considered:

1) Direct covalent bonding between adsorbates and the substrate - chemisorption. This occurs in the inner Helmholtz plane (IHP) where ions lose their solvation shell and become specifically adsorbed on the electrode surface.

2) Weak electrostatic, van der Waals, forces. This occurs in the outer Helmholtz plane (OHP) and affects ions near to the electrode surface, but does not involve any direct bonding – ions retain their solvation shell.

There have been a vast amount of studies of the structure of adsorbed species in the IHP, but an understanding of the OHP is lacking due to the limitations of *in situ* structural techniques. In recent years there has been a growing number of studies focussing on the structure of the electrolyte side of the interface where there is no specific adsorption [19, 51,131–138] most of these studies use SXRD. SXRD is the ideal technique to probe the structures in the electrolyte as X-rays do not interfere with the interface structure, unlike STM [138]. By combining specular crystal truncation rod (CTR) measurements (where the momentum transfer, **Q**, is entirely along the surface normal direction) with non-specular CTR results (where **Q** has an additional in-plane component) it is possible to probe both the surface metal layers and ordering above the interface, i.e. in the electric double layer, where the species are usually incommensurate with the underlying crystal lattice. Toney *et al.* [53] have used this technique to probe the structure of water molecules at the Ag(111)/alkaline interface. A non-adsorbing electrolyte of 0.1 M NaF was used in

order to solely observe the effect of the water molecules. They proposed a dense ice-like water structure at the interface, and the flipping of water molecules dependent upon the applied potential.

Strmcnik *et al*. [139] indicated cations are not specifically adsorbed on the electrode surface, but are located within the double layer and have a significant influence on the electrocatalytic trends in the ORR, HOR and oxidation of methanol on platinum. This was subsequently confirmed through SXRD results [132] which proposed at positive potentials adsorbed OH^- stabilised partially hydrated cations through non-covalent electrostatic forces. The non-covalent interactions between the cations and the adsorbed OH were found to increase in accordance with the hydration energies of the cations ($Li^+ >> Na^+ > K^+ > Cs^+$) which also corresponded to the coverage of clusters on the surface. These trends were found to be inversely proportional to the activities of the ORR and HOR. It was deduced that the coverage of spectator species (such as cations) has a major effect on the ORR in alkaline electrolytes as the presence of OH-cation clusters in the double layer blocks adsorption sites for reactants and therefore it is vitally important to understand their structure. Interestingly, Strmcnik *et al.* [132] compared the results to those obtained on nanoparticle systems which indicated an exact correlation. This stresses the importance of studies of model single crystal systems.

The studies have been extended by other groups to investigate silver single crystal surfaces. Nakamura *et al.* [24, 134] studied the Ag(001)/alkaline electrolyte interface in which hydrated Cs-water clusters were located above a c(2 x 2)-Br structure on the Ag(001) surface. The coverage and distance of Cs^+ layer within the OHP varied with potential. The Ag(111)/0.1 M KOH interface was investigated by Lucas *et al.* [23], it was proposed that at negative potential there is no adsorbed

species, but there is a presence of a hydrated cation at 4.1 Å, above the surface stabilised in the OHP by an electrostatic field effect (induced by the applied potential). At positive potential specifically adsorbed OH stabilises the hydrated cations at a distance of 3.6 Å above the surface through non-covalent (van der Waal's) interaction forming a compact double layer.

There have been numerous studies of surface oxidation of silver due to the role that the oxide plays in the catalytic gas phase reactions of ethylene epoxidation and methanol oxidation [16]. Despite this, a detailed knowledge of the Ag/alkaline interface, and a fundamental understanding of the electrocatalytic properties is lacking. There has been considerably less study of the underpotential region of oxidation, despite the fact that this is the potential region of the oxygen and hydrogen peroxide reduction reaction. This is mainly due to the difficulty in obtaining atomic-scale structural information from a reactive surface in the liquid environment. This chapter aims to give a comprehensive study of the structure of the Ag(*hkl*)/alkaline interface in the underpotential oxide region. Potentiodynamic X-ray Voltammetry (XRV) measurements, which involves monitoring the X-ray intensity of a structural feature as the potential is cycled, have been performed to determine the potential dependent structural changes at the interface. In addition to this the surface structure has been characterized at fixed potentials of interest by CTR analysis to resolve any changes highlighted by the XRV data. These studies have been extended to investigate the effects of the ORR and CO adsorption and oxidation on the double layer structure.

Cyclic voltammetry of the Ag(*hkl*) surfaces

The adsorption of oxygen and hydroxide species onto metal surfaces is key to understanding surface reactivity and catalytic behaviour both in the high pressure gas environment and at the electrochemical interface Figure 6.1 represents the cyclic voltammetry (CV) of the three low index Ag(*hkl*) surfaces in 0.09 M NaF + 0.01 M NaOH electrolyte over the potential region for OH^- adsorption [140]. In this electrolyte fluoride (F^-) and hydroxide (OH^-) are known to coadsorb, the extent to which they adsorb is dependent upon the pH of the electrolyte. There is a crossover between OH- dominated (highly alkaline solutions) to F- dominated adsorption (neutral and acidic solutions). For the purpose of this work, an alkaline pH was used to favour OH- adsorption. In Figure 6.1 (a) all CV datasets have two sets of broad anodic and cathodic current peaks, which are found to be pH-dependent [140]. The first peak is attributed to the specific adsorption o hydroxide (OH_{ads}). The second set of peaks at more positive potential is attributed to the discharge of OH followed by the formation of a submonolayer surface oxide, Ag_2O. In Figure 6.1 (b) the CVs of the three faces are compared using the potential of zero charge (pzc) scale. Comparing the faces indicates that the onset of both sets of peaks occur at the same potential relative to the pzc. This indicates that the difference in peak positions is due to the work function of the surface.

Over this electrochemical potential region the processes are reversible; indicated by the symmetry of the CV around the x-axis. Previous studies have found the adsorption of OH^- is a precursor to irreversible oxide formation on Ag surfaces at more positive potentials [132–134] The formation of a Ag_2O surface oxide phase changes the structure of the metal surfaces irreversibly, which affects the

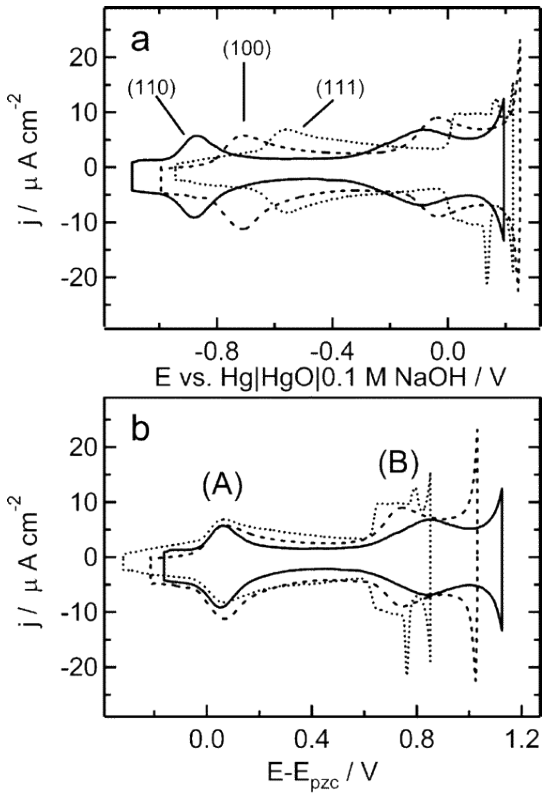

Figure 6.1 Ag(*hkl*) Cyclic voltammetry of Ag(111) (dotted line), Ag(110) (solid line), and Ag(100) (dashed line) in contact with 0.09 M NaF + 0.01 M NaOH: (a) potential referred to Hg/HgO/0.1 M NaOH; (b) potential referred to the respective pzc's. Reprinted with permission from [140] Copyright (2004) American Chemical Society.

electrochemical response. For the CTR measurements presented in this chapter the electrochemical window was restricted to within -1.0 V and -0.2 V (vs Ag/AgCl) - the region for reversible adsorption – in order to study the changes in the electric double layer structure.Ag(*hkl*) in 0.1 M NaOH + 0.09 M NaF: Potential effects

6.1.1 Ag(111)

To characterise the system, XRV measurements were performed at several structure-sensitive positions along the CTRs seen in Figure 6.2 at (a) (0, 0, 1.6) an anti-Bragg position on the specular which is sensitive to any layered electrolyte ordering at the interface (b) (1, 0, 3.7) a position on the (1, 0, L) CTR which is

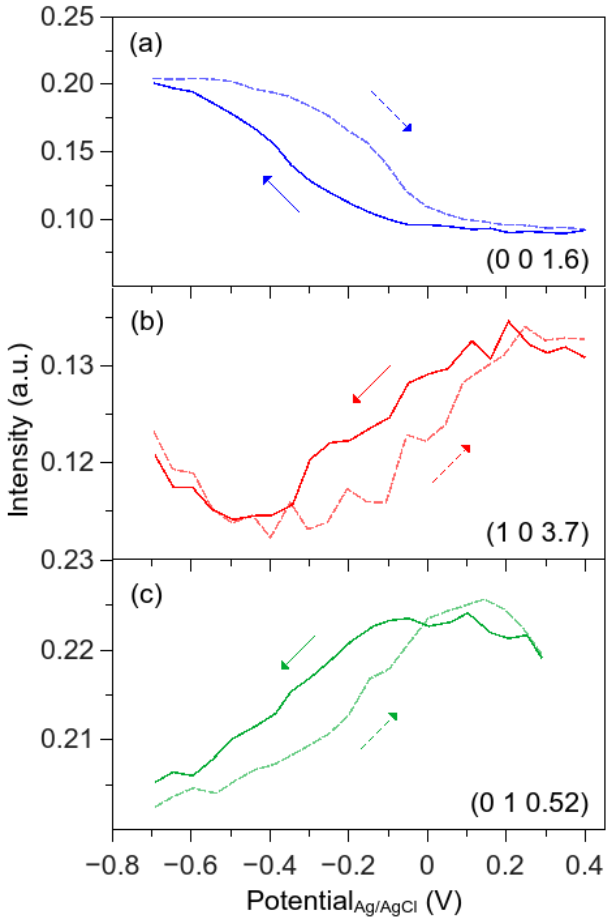

Figure 6.2 X-ray voltammetry (XRV) measured at (a) (0, 0, 1.6), (b) (1, 0, 3.7) and (d) (0, 1, 0.51). Sweep rate 20 mV/s.

sensitive to surface relaxation. (c) (0, 1, 0.52) an anti-Bragg position on the (0, 1, L) CTR sensitive to atomic positions which are commensurate with the Ag surface. The reversibility of all XRVs between these potential limits indicates that the processes occurring are fully reversible. The changes to the non-specular CTR positions are very small which indicate that there are only subtle effects occurring to the metal side of the interface; the intensity is proportional to the change in relaxation at the (1, 0, 3.7) position. Conversely, the changes at the specular CTR, are relatively large (~50% change in scattered intensity as seen in Figure 6.2). As there are only small surface relaxations in the metal, and there is no reconstruction, changes to the

specular CTR can be attributed primarily to the electrolyte side of the interface; the large change in intensity indicates the electrolyte must undergo significant restructuring between the potential limits. The change in scattered intensity at the (0, 0, 1.6) position is linked with the adsorption of OH^-, the increasing coverage of OH_{ads} on the positive scan causes a decrease in scattered intensity, and an increase on the negative sweep corresponding to the desorption of OH^-. The XRVs are used to evaluate the potential ranges over which stable interface structures are formed.

The system can then be studied in detail (via CTR measurements) at the relevant applied potentials to identify a structural model for the system. The CTR data was measured at E= -1.0 V, the negative potential limit corresponding to a region where there is no specific adsorption, and at E= -0.2 V, the positive potential limit corresponding to the region where OH is specifically adsorbed on the electrode surface. By modelling the CTR data a structural model for the system can be determined. To begin with the non-specular CTRs are fit separately to model the structure of the metal. Once a good fit is obtained the parameters are fixed, and the specular CTR is included in the fit to model any ordering in the electrolyte. After a good fit to the specular is obtained, then the parameters from non-specular CTRs and specular CTR are varied together in order to optimise the fit. In addition to this data taken at two different potentials can be fit simultaneously by modelling the ratio of the data sets. The ratio of the datasets highlights the changes between the systems, by modelling the ratio the systematic error is removed and a good fit to the ratio indicates differences between the datasets have been well modelled. The CTR fits or

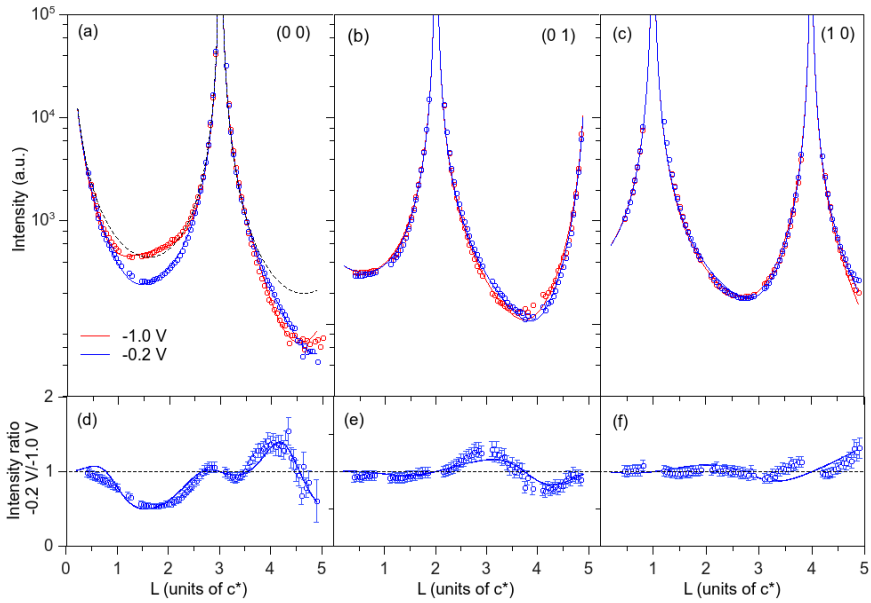

Figure 6.3 Crystal Truncation Rod (CTR) data of the Ag(111)/0.09 M NaF + 0.01 M NaOH interface measured at −1.0 V (red), and −0.2 V (blue) versus Ag/AgCl (a) the specular CTR, (0, 0, L) and (b) (c) the non-specular CTRs, (0, 1, L) and (1, 0, L) respectively. The CTR data measured at −0.2 V was normalized to the data measured at −1.0 V (d) (0, 0, L), (e) (0, 1, L) and (f) (1, 0, L). The solid lines are fits to the data according to the structural model described in the text. The dashed line in (a) is a calculation of the specular CTR without inclusion of any ordering in the electrolyte.

ratio fits can be weighted in the program. This method is especially important for fitting data where there are only small changes between datasets. Unless stated otherwise, this fitting method was used for the rest of the data in this chapter. The data and calculated fits can be seen in Figure 6.3 and parameters are summarised in Table 6.1. Parameters without an associated error were not varied. This is justified as many of the parameters are coupled, and varying them all together does not always give sensible values, or errors, for some parameters. The best fit was obtained by varying the vertical displacement of the top surface layer, ε, and the root-mean-squared (rms) surface roughness (σ_{Ag}). The occupation (θ) of the layer was fixed at 1, varying the parameter did not indicate reduced occupancy and did not improve the

parameter		-1.0 V	-0.2 V
Metal layer	ε_1(Å)	-0.021(1)	-0.0417(1)
	σ_{Ag1} (Å)	0.124(2)	0.117(2)
Oxygen layer	θ	0.22(3)	0.78(2)
	$d_{Ag\text{-}O}$ (Å)	2.74(8)	2.51(2)
	σ_O (Å)	0.15	0.15
Na^+ layer	θ	0.42(2)	0.14(2)
	$d_{Ag\text{-}Na}$ (Å)	4.06(1)	3.57(2)
	σ_{Na} (Å)	0.15	0.15
	Reduced χ^2	1.75	1.40

Table 6.1 Parameters giving the best fits to the data. The metal layers and adlayer parameters were varied simultaneously to obtain the final fit to the data.

fit. The best fit to the non-specular CTRs indicates that the top surface layer undergoes a small *inward* relaxation ~ 0.9 % of the Ag(111) layer spacing (d=2.36 Å), this is consistent with a previous study of Ag(111) in an alkaline electrochemical environment where a 0.7 % contraction of the top metal layer is determined, and consistent with UHV studies which identify a small *inward* relaxation of the clean surface at room temperature. Although this model gives a good fit to the (1, 0, L) and (0, 1, L) CTRs, it does not give a good fit to the specular CTR. As the specular CTR is sensitive to scattering from the electrolyte side of the interface, it was important to include electrolyte layering into the model; which was modelled by incommensurate adlayers. The rms roughness of adlayers was fixed at σ =0.15, slightly above the value determined for the top metal layer. The best fit to the data gave two adlayers located at 2.74 Å and 4.06 Å. As there is no specific

adsorption at negative potential the adlayer at 4.06 Å is attributed to a layer of Na^+ cations in the outer part of the double layer. This is appropriate as although the ionic radius of Na^+ is 0.95 Å, Na^+ is expected to be hydrated and the hydration radius of Na^+ is large much larger 1.8 Å indicating that the distance to the Na^+ cations should be relatively large This is consistent with the K^+ cation layer in the study by Lucas *et al.* [23] where it is situated 4.1 Å above the electrode surface. The adlayer closer to the surface is attributed to an ordered water layer above the electrode surface in the IHP, which was modelled as an oxygen layer with coverage $\theta = 0.22 \pm 0.03$ ML. This differs slightly from the model by Lucas *et al.* [23] which was fit with only a K^+ layer, however, water molecules are known to order at an electrode surface when a charge is applied to the electrode[53], [54] as the electric field at the interface orientates the water molecules near to the surface.

Scanning the potential to -0.2 V dramatically changes the specular CTR. The ratio of the -0.2 V and -1.0 V data are seen in Figure 6.3. The ratio highlights the systematic differences between the two data sets which are consistent with the changes seen in the XRV. The best fit to the non-specular data indicated that the *inward* expansion of the top layer increased to 1.7 % at positive potential. The increase in relaxation is induced by the specific adsorption of OH^- and is again consistent with the study by Lucas *et al.* To obtain the best fit to the specular data, the inclusion of two adlayers was necessary. The distance of both adlayers to the metal surface significantly decreases from negative potential to $d_{Ag\text{-}O}$=2.51 Å and $d_{Ag\text{-}Na}$=3.57 Å. As OH^- adsorption is known to occur at this potential the first adlayer is attributed to specifically adsorbed OH. The Ag-O layer spacing is much larger than that determined 2.2 Å by Lucas *et al.*. The difference between the bond length

could be due to the interaction of different cations in solution. As the scattering factor from H is small, OH was modelled as an oxygen layer. The second layer is assigned to a Na^+ cation layer which is in close proximity to the electrode surface. The spacing between the Na^+ cation adlayer and the Ag(111) surface is consistent with previous similar studies of K^+ adsorbed on Ag(111) [23] and Ba^{2+} cations adsorbed on Pt(111) [132], the metal-solvated cation spacings found were 3.6 Å and 3.4 Å respectively. As the non-hydrated ionic radius of Na^+ is 0.9 Å, the cation cannot be specifically adsorbed as the layer spacing is too large, which suggests that the Na^+ cations are hydrated. Strmcnik *et al.* [132] proposed that Ba^{2+} cations become partially hydrated whilst non-covalently interacting with the OH_{ads}. The model is plausible for this system, however, it is not certain and further investigations would be needed in order to determine any partial charge transfer at the interface.

6.1.2 Ag(110)

Although there have been a few *in situ* studies of the Ag(111) underpotential oxidation, there have been no structural studies of the Ag(110) electrode surface in an electrochemical environment. There have, however, been ex-situ LEED/RHEED measurements reported. Horswell *et al.* [21], [140] studied hydroxide adsorption on Ag(110) in alkaline electrolyte. The sample was emersed at a range of potentials and studied with LEED. The results indicated that the structure of OH was potential dependent; at low coverage of OH_{ads} a c(2 x 6) LEED pattern was observed, at more positive potentials OH fills in the troughs and forms a c(2 x 2) pattern. With the onset of surface oxide formation the observed LEED pattern was (1 x 1), however, the pattern had faint spots with a high background, which could be due to a disordered adlayer or due to electrolyte deposition as a result of wet emersion.

The potential dependent structure was monitored by XRV measurements. These were made at three structurally sensitive positions in shown in Figure 6.4 (a) (0, 0, 1.02), an anti-Bragg position on the specular CTR sensitive to any layered ordering at the interface, (b) (1, 0, 0.2) an anti-Bragg position on the (1, 0, L) non specular CTR sensitive to relaxation (c) (0, 1, 0.3) an anti-Bragg on the (0, 1, L) non-specular CTR sensitive to relaxation. The (0.5, 1.5, 0.2) fractional order position was also monitored which is sensitive to the (2 x 2) structure, however, no scattering above the background level was observed at any applied potential which indicated that there was no in-plane ordering which could be identified. As the potential is cycled from -1.0 V to -0.2 V there is a decrease in the intensity is observed at (1, 0, 0.2) which is consistent with a change in the relaxation of the Ag surface. The

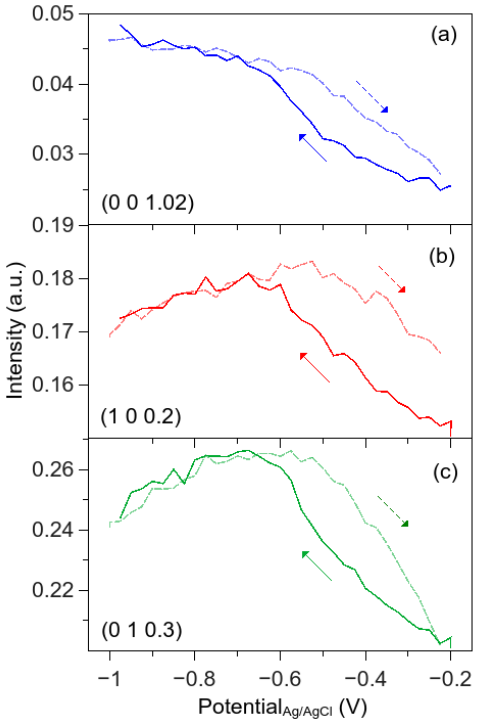

Figure 6.4 X-ray voltammetry (XRV) measured at (a) (0, 0, 1.02), (b) (1, 0, 0.2) and (c) (0, 1, 0.3).

onset of the decrease in intensity coincides with the adsorption of OH (as determined by voltammetry measurements [21,23]).

The changes to the intensity at the specular CTR position are relatively large (~50% change in scattered intensity), and is attributed to the increased OH^- coverage. To derive a structural model, of the surface CTR data was taken at fixed potentials (-1.0 V and -0.2 V), the specular CTR, which is sensitive to ordering in the surface normal including ordering in the electrolyte, and two non-specular CTRs (0, 1, L) and the (1, 0, L) sensitive to changes in the metal. If indeed there are ordered structures on the surface then scattering from them will make a contribution to the non-specular CTRs and must therefore be included in the model. The data and calculated fits are shown in Figure 6.5, and the corresponding structural parameters are summarised in Table 6.2. The calculated bulk terminated surface is indicated by the dashed lines in Figure 6.5, at both potentials and there are large differences in the

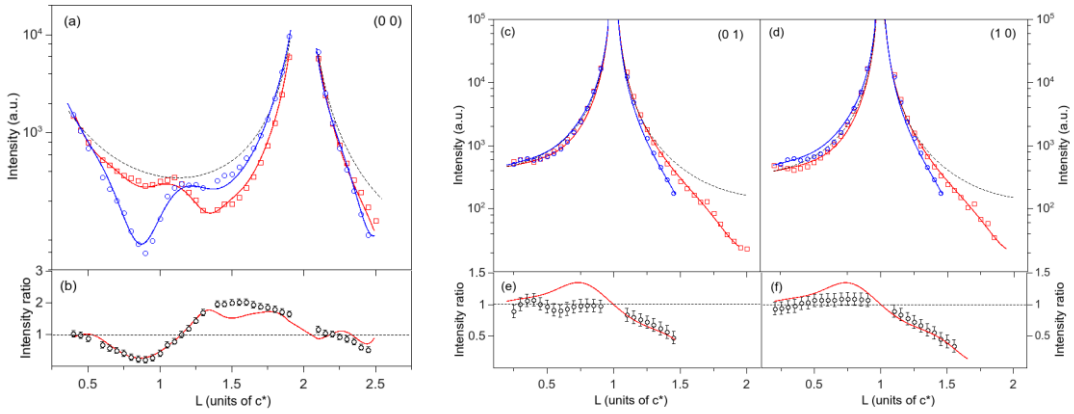

Figure 6.5 CTR data at -1.0 V (red) and -0.2 V, black dashed line indicates the calculated bulk terminated surface (a) Specular CTR data (b) ratio -0.2V/-1 V (c) (d) non specular CTRs (0, 1, L) and (1, 0, L) respectively (e)(f) ratio -0.2 V/-1.0V. Solid lines are fits to the data.

Parameter		-1.0 V	-0.2 V
Metal layers	ε_3 (Å)	0.007(2)	0.020(5)
	σ_{Ag3} (Å)	0.122(7)	0
	ε_2(Å)	-0.023(2)	-0.038(5)
	σ_{Ag2} (Å)	0.193(7)	0.13(1)
	ε_1(Å)	-0.023(1)	0.086(2)
	σ_{Ag1} (Å)	0.328(4)	0.464(8)
Oxygen layer	θ_0	0.60(5)	0.81(6)
	$d_{Ag\text{-}O}$ (Å)	2.87(4)	2.20(4)
	σ_O (Å)	0.15	0.15
Oxygen layer	θ_0	-	0.58(6)
	$d_{Ag\text{-}O}$ (Å)	-	3.29(7)
	σ_O (Å)	-	0.15
Error Function	σ_E	0.5	0.5
	d_E	5.00(9)	5.15(1)
	Reduced χ^2	1.60	1.98

Table 6.2 Parameters giving the best fits to the Ag(110) CTR data at -1.0 V and -0.2 V. The metal layers and adlayer parameters were varied simultaneously to obtain the final fit to the data.

measured data. It was possible to obtain a reasonable fit to the first order non-specular CTRs (0, 1, L) and (1, 0, L) by varying the structural parameters of just the top metal layer. However, as was found with the UHV data in chapter 4, a good fit to

all of the CTR data could not be obtained without considering multilayer relaxations of the surface.

In order to obtain a good fit to the data, all 3 CTRs were fit simultaneously. At negative potential, -1.0 V, the first and second metal layers are both relaxed *inward* and the third layer has a small *outward* relaxation, resulting in an overall surface relaxation Δ_{13} = -2.08 %. Surface relaxations were not sufficient to fit the specular CTR, which is sensitive to ordering in the surface normal from surface metal layers and any ordered electrolyte layering. To obtain a good fit to the data the rms roughness of all 3 metal layers was included in the fit. The rms roughness of the top metal layer was relatively large 0.328 ± 0.004 Å indicating that the surface is quite rough in an electrochemical environment compared with 0.22 Å determined for a clean surface in UHV (chapter 4). The specular CTR data has an oscillation occurring at ~ L=1, which cannot be modelled by the fit to the data without inclusion of any electrolyte ordering in the structural model. The best fit to the data was obtained by modelling the electrolyte with an adlayer and an error function. An error function (as discussed in chapter 2) models the scattering contribution from the bulk electrolyte, it is modelled from zero to infinity in the surface normal direction and saturates at the bulk density of water. The best fit was obtained with an adlayer at a height of 2.8 Å above the surface and an error function saturating at around d_E = 5 Å. There is no OH_{ads}, thus the adlayer is attributed to a Na^+ layer. This distance seems relatively close to the surface in comparison to the Ag(111) surface, where the Na^+ layer was located at 4.06 Å, however, it is perfectly reasonable if the geometry of the surface is considered. As the Ag(110) surface is much more open than the Ag(111) surface then the Na^+ layer could be located closer to the surface. The distance of closest approach of the Na^+ cation can be calculated using the hard sphere model,

given the metallic radius of silver (1.45 Å) and the hydrated radius of Na^+ (taken to be 1.8 Å) then the height above the surface is 2.2 Å for the hollow sites.

At positive potential, -0.2 V, there are changes to the non-specular CTRs, indicating a change in surface relaxations which is consistent with the XRV in Figure 6.4. The metal was modelled by varying the displacements of the top three metal layers and the roughness. The best fit to the data indicated that the top metal layer has a large *outward* relaxation 0.086 Å; ~6 % of the interatomic layer spacing (1.444 Å), accompanied by a large rms roughness of 0.464 Å. The magnitude of the relaxations in the 2nd and 3rd layers is also greater at positive potential. The relaxations result in a larger layer spacing between layers 1 and 2 Δ_{12}= +8.53 % and a reduced layer spacing between layers 2 and 3 Δ_{23}= -4.0%. At this potential there is a dramatic change to the shape of the specular CTR where there is a large aysmmetric dip in intensity between L = 0.75 and L = 1.2. To obtain a good fit to the data the electrolyte was modelled with two adlayers and an error function. The layer closest to the surface is attributed to specifically adsorbed OH, without this layer the dip in intensity on the specular CTR cannot be replicated by the model. The Ag-OH layer spacing of 2.2 Å would suggest that OH is adsorbed on atop sites, from hard sphere model calculations. The cation moves away from the surface to allow OH^- adsorption but are stabilised by the OH_{ads} at a distance of 3.29 Å from the metal surface. The distribution of adlayers in this system is very similar to the structure found for the Ag(111) interface. The Na^+ cation layer is in close proximity to the OH_{ad} on the surface, suggesting the cation is stabilised by non-covalent interactions with OH_{ads}.

In contrast to the Ag(111) surface the Ag(110) surface undergoes a large *outward* expansion with the adsorption of OH^-, this is consistent with UHV studies where a large expansion (~7%) of the Ag(110) surface layer has been reported which is induced by the adsorption of oxygen on the surface [6]. In contrast to UHV where the surface undergoes a (2 x 1) reconstruction with oxygen adsorption, the surface does not appear to reconstruct with OH adsorption, but induces a further roughness to the surface.

Although the ratios of the fits indicate there is perhaps something missing from the structural model, including specific adsorption sites for the adlayers into the model did not improve the fit and there was no sign of ordering in the in-plane scans. It is likely that the OH^- occupies a mix of adsorption sites. It is possible that there could be buckling of the surface metal layers which could be considered to improve the fit of the non-specular CTR data.

6.1.3 Ag(001)

Hydroxide adsorption on Ag(001) in UHV has been reported to show a c(2 x 2) LEED pattern [144] and theoretical calculations determine the most favourable OH^- adsorption site is the 4-fold hollow [145]. Ex situ studies [140] only indicate a hint of ordering in Reflection High-Energy Electron Diffraction (RHEED) where there are streaks corresponding to a c(2 x 2) structure, however, the streaks are very faint and the c(2 x 2) was not observed with LEED which was possibly due to the lower coverage of OH in an electrochemical environment or due to the presence of coadsorbed anions (F^-) and cations (Na^+). To determine the potential dependence of the surface, XRV were measured at two reciprocal lattice positions, (0, 0, 1.02), as shown in Figure 6.6 an anti-Bragg position on the specular CTR, and (1, 1, 2.7) a

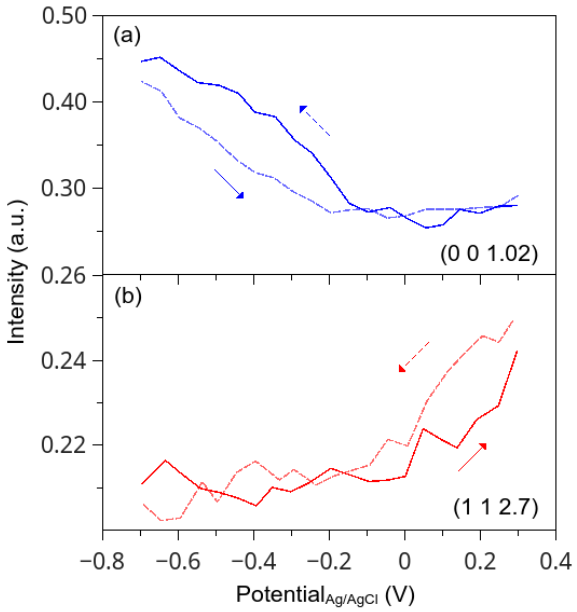

Figure 6.6 X-ray voltammetry (XRV) of Ag(001) measured at (a) (0, 0, 1.02) and (b) (1, 1, 2.7). The sweep rate for the XRV measurements was 20 mV/s.

position on the non-specular (1, 1, L) CTR sensitive to changes in relaxation of the metal surface. Differences in the XRV at both positions are observed as the applied potential is varied and OH^- is adsorbed. The change in the specular CTR is consistent with increasing OH^- adsorption. The intensity at the (1 1 2.7) increases with positive potential, indicating a relaxation of the metal layers. To determine a structural model, CTR data was measured at -0.8 V (corresponding to no adsorbed species) and -0.2 V (corresponding to OH adsorption). The non-specular CTRs were modelled independently of the specular CTR to determine the structure of the metal side of the interface. At -0.8 V varying the metal layer displacement (ε) and rms roughness (σ) was insufficient to fit the data which indicated that there could be some in-plane ordering which would need to be included into the model. To identify the layer spacing the specular CTR was modelled, which is not sensitive to in-plane ordering, and an adlayer was included to

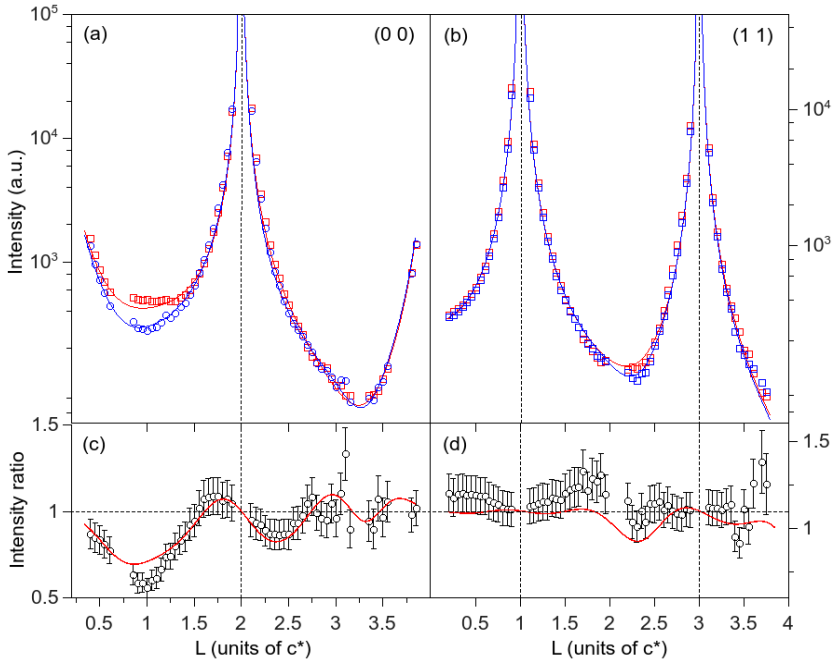

Figure 6.7 CTR data of the Ag(001) surface at -0.8 V (red) and -0.2 V (blue). (a) specular CTR (0, 0, L), (b) non-specular CTR (1, 1, L). Data measured at -0.2 V is normalised to data measured at -0.8 V and shown in (c) and (d). Solid lines are the fits to the data described by structural models in the text.

	Parameter	-0.8 V	-0.2 V
	ε_2(c.u.)	-	0.001(2)
	σ_{Ag2} (Å)	-	0.040(6)
	ε_1(Å)	-0.019(1)	-0.03(2)
	σ_{Ag1} (Å)	0.111(4)	0.13(1)
	θ	0.26(2)	0.83(6)
Adlayer	d(Å)	3.08(7)	1.65(3)
	σ(Å)	0.2	0.32(5)
	Reduced χ^2	1.76	1.82

Table 6.3 Best fit parameters to the Ag(001) CTR data at -0.8 V and -0.2 V.

model the electrolyte structure. The adlayer was positioned at ~ 3 Å above the metal layer. The coverage and vertical distance of the adlayer to the metal layer was fixed, and the layer was modelled in a range of specific adsorption sites; atop, bridge, 4-fold hollow. The best fit obtained was consistent with the on-top model. The displacement parameters and coverage were allowed to vary to obtain the best fit parameters for this model. At negative potential there is no OH^- adsorption, this layer is attributed to an ordered Na^+ layer at the interface including the scattering factor for Na^+ the coverage of the layer was θ_{Na} = 0.28 ML at a height of 3.08 Å above the top metal layer, the parameters are summarised in Table 6.3. As the Na^+ cations are not specifically adsorbed on the surface, i.e. the cation retains its solvation shell; its structure cannot be determined through ex situ measurements as the structure would likely be lost on emersion from the electrolyte. This study has demonstrated the importance of *in situ* structural techniques which can probe the double layer structure.

Clear systematic changes between the data measured at -0.8 V and 0.2 V can be seen in the ratio of the data sets. There is a small change in the non-specular CTR, indicating a change to the relaxation of the metal surface which is consistent with the XRV data. In addition, there is a large change in the specular CTR which suggests that there is a structural rearrangement within the electrolyte side of the interface. A fit to the non-specular data was obtained by varying the displacement of the top metal layer and the rms roughness, this did not give a good fit to the data. At -0.2 V the best fit to the non-specular data was given by varying the displacement and roughness of the top 2 metal layers. The best fit to the specular data was obtained by the inclusion of an adlayer, which is assigned to a specifically adsorbed OH layer. The Ag-OH layer spacing determined by the fit (1.65 Å) suggests that OH

is specifically adsorbed on bridge site from hard sphere model calculations. This is in contrast to the studies in UHV, where OH is adsorbed in the hollow sites. The difference in adsorption site could be explained by the presence of the cations in solution. The adsorption of OH induces a further *inward* relaxation of the top metal layer, and the second metal layer responds with an *outward* relaxation, reducing the interlayer spacing d_{12} by 1.5 %. The inclusion of a further adlayer did not improve the fit, which suggests that the cations are not ordered at the interface, or perhaps the coverage is too small to make a significant contribution to the scattering.

6.1.4 Discussion

The structure of the Ag(*hkl*)/alkaline interface shows a large potential dependence, with the effects felt on both sides of the metal/electrolyte interface. The main points to consider from the study are

1) Strong electrolyte layering effect on all three surfaces
2) Non-covalent interactions on Ag(111) and Ag(110)
3) Metal response – metal layer relaxations

A schematic representation of the interface structures are shown in Figure 6.8 and a summary of the parameters on all three surfaces is presented in Table 6.4. The changes to the interface are most prominent at the electrolyte side of the interface. At both potentials the ions redistribute to equalise the charge on the electrode. At negative potential this is done through a field effect; the positively charged cations are attracted to the negatively charged electrode, and equalise the charge forming an ordered layer (out of plane) in the outer part of the double layer. At this potential the

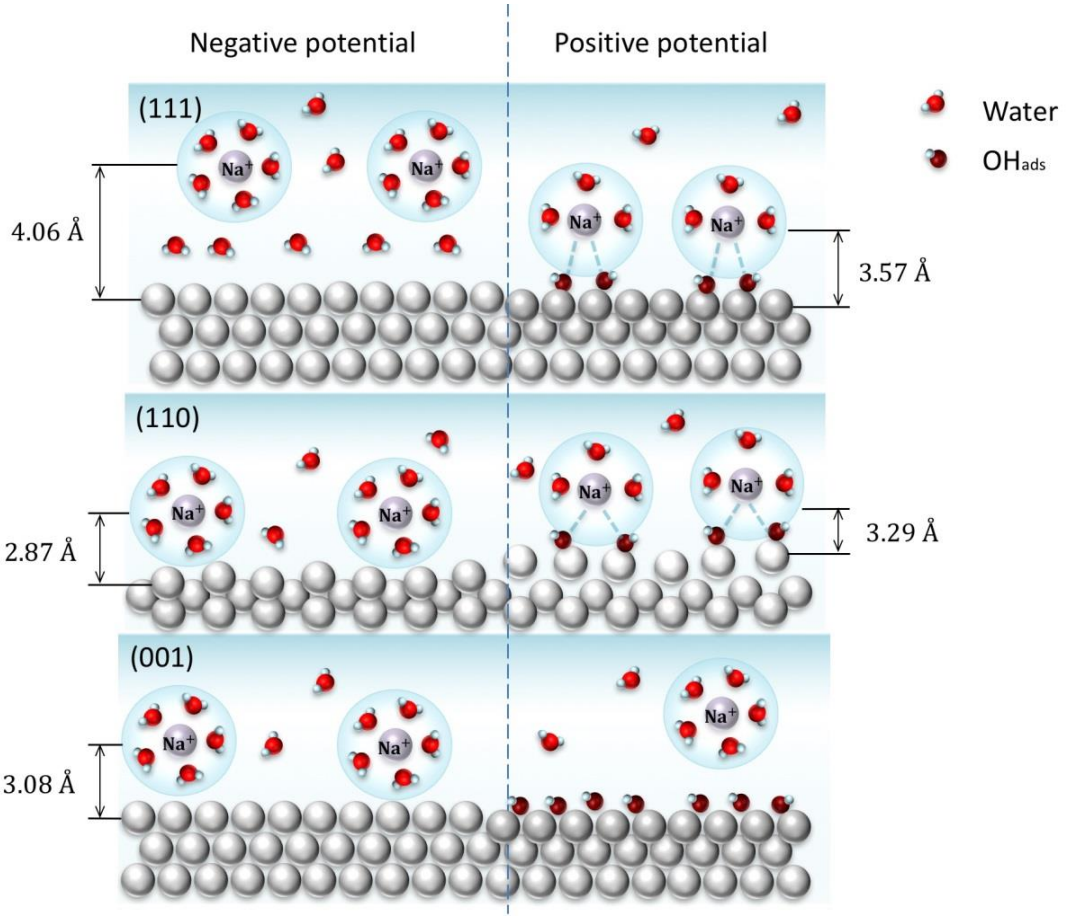

Figure 6.8 Schematic representation of the Ag(*hkl*)/Alkaline interface, highlighting the structural differences between the two potential limits. At negative potential the double layer structure is governed by a field effect attraction; positively charged Na^+ cations redistribute at the interface to maintain electroneutrality at the interface. At positive potential OH is adsorbed on the surface, maintaining a negative charge, the Na^+ are stabilised through non-covalent interactions forming a compact double layer at the Ag(111) and Ag(110) interface. At the Ag(001) interface, OH is adsorbed, but no evidence of Na^+ ordering was identified by the structural model.

Na^+ cations are not known to adsorb on the surface i.e. lose their solvation shell, as cations have much larger and stronger solvation shells than anions, they are much less likely to break up. This model is true for all 3 surfaces, and the height of the Na^+ layer above the electrode surface decreases, with decreasing coordination number, in the order (111)>(001)>(110). In the case of the Ag(111) surface, the best fit was

Parameter		Ag(111)		Ag(110)		Ag(001)	
		-1.0 V	-0.2 V	-1.0 V	-0.2 V	-0.8 V	-0.2 V
Metal layers	ε_{34} (Å)			0.007(2)	0.020(5)		
	ε_{23} (Å)			-0.023(2)	-0.038(5)	0	0.001(2)
	ε_{12} (Å)	-0.021(1)	-0.0417(2)	-0.023(1)	0.086(2)	-0.019(1)	-0.03(2)
	σ_3 (Å)			0.122(7)			
	σ_2 (Å)			0.193(7)	0.13(1)	0	0.040(6)
	σ_1 (Å)	0.124(2)	0.117(2)	0.328(4)	0.464(8)	0.111(4)	0.13(1)
O	θ (ML)	0.22(3)	0.78(2)		0.81(6)		0.83(6)
	d(Å)	2.74(8)	2.51(2)		2.20(4)		1.65(3)
	σ (Å)	0.15	0.15		0.15		0.32(5)
Na^+	θ (ML)	0.42(2)	0.14(2)	0.60(5)	0.58(6)	0.26(2)	
	d (Å)	4.06(1)	3.57(2)	2.87(4)	3.29(7)	3.08(7)	
	σ (Å)	0.15	0.15	0.15	0.15	0.2	
Err. func	dE (Å)			5.00(9)	5.15(1)		
	Red χ^2	1.75	1.40	1.60	1.98	1.76	1.82

Table 6.4 Summary of best fit parameters to the measured data on all three low-index Ag(*hkl*) surfaces in N_2 purged 0.01 M NaOH + 0.09 M NaF electrolyte.

obtained with a water layer between the cation layer and the surface. At positive potential OH adsorbs on the surface. OH has been proven to retain its negative charge on adsorption on Ag [22,133,134], as it is proposed to behave as an electron accepter acquiring negative charge [148]. To maintain electroneutrality at the interface Na^+ cations redistribute at the interface and are drawn into closer proximity through a non-covalent (van der Waal's) interaction and are stabilised by the OH_{ads} to form a compact double layer. The presence of Na^+ at both potentials is supported by an ex situ study of the Ag(111)/Alkaline double layer by Savinova *et al.* [22] where XPS measurements of an emersed electrode identified the presence of Na^+ both positive and negative of the E_{pzc}. This was the case for both the Ag(111) and the Ag(110) at negative potential, and is in agreement with a previous study on Ag(111) [23] and Pt(111) [139]. Strmcnik *et al.* [139] proposed a controversial model for the Pt(111)/Alkaline interface, from SXRD analysis, in which the cation is partially

hydrated forming a complex with the OH_{ads}, based on the interlayer spacings. Whilst it is a possible explanation for the interface structure further it is difficult to directly determine this without further investigation using other methods.

Whilst the model for the Ag(001)/alkaline interface does not include ordering from a Na^+ layer, scattering contribution to the specular CTR would only arise from an ordered layer and the presence of disordered Na^+ in the double layer cannot be ruled out. This is in contrast to a study on Ag(001) [133] in which Cs^+ forms an ordered layer on an adsorbed $c(2 \times 2)$-Br, stabilised by non-covalent interactions. This could be due to the difference in electrolyte used, and the Br structure adsorbed on the surface which would change the nature of bonding at the interface.

Although the main structural changes which occur with potential dependence are seen in the electrolyte side of the interface, the metal side of the interface does not go unaffected. All three surfaces undergo surface layer relaxations at both potentials. At negative potential the relaxations are not too dissimilar to those found on clean surfaces in UHV; all surfaces undergo an *inward* relaxation at this potential. The top metal layer of the Ag(111) surface undergoes small relaxation at negative potential, which increases at positive potential and the same is true for Ag(001). The Ag(110) surface is a more interesting case, in UHV the top metal layers have an oscillatory relaxation (as discussed in chapter 4) which is typically predicted (and observed) for metal surfaces. The structure in the electrochemical environment is quite different due to the presence of electrolyte and surface the top two layers are relaxed *inward* and the third layer is relaxed *outward*. The difference in relaxation is due to the electronic charge and screening effect of the electrolyte [149]. At positive potential, the top layer has an *outward* relaxation, the second layer is relaxed *inward*

and the third layer is relaxed *outward*. The adsorption of OH forms new metal-adsorbate bonds which weakens the internal metal-metal bonds and causes relaxation. The relaxations of the top layer are usually inwards, but this is not the case for Ag(110). The large expansion is consistent with oxygen adsorption of Ag(110) in UHV, however, in UHV the surface reconstructs [6], which is not in agreement with the analysis from this study. A reconstructed surface was considered in the model, however, it did not produce a good fit to the data.

6.2 Effects of Gases

Understanding the underpotential oxide region is important for electrocatalytic reactions such as the oxygen reduction reaction, ORR, and CO oxidation, which are dependent on the adsorbed oxygen species. There are two ways in which to increase the catalytic activity:

1) Development of the electrode material.
2) Selectively designing the electrochemical double layer.

In the following sections experiments are described in which the Ag(*hkl*) electrodes were investigated in the presence of different gases in the electrolyte, in order to probe effect of the saturating gas on the structure at the interface. A detailed knowledge of the interaction of these species with the surface of the near-interface ordering in the electrolyte is essential to develop a fundamental understanding of the driving forces behind important catalytic processes and stability of the electrodes under reaction conditions.

6.2.1 Experimental details

The measurements described in the following sections used the same alkaline electrolyte (0.01 M NaOH + 0.09 M NaF) used for the measurements presented in section 0. The electrolyte was saturated for 20 minutes with either O_2 or CO (BIP grade) in the electrolyte reservoir which was then pulled through to the X-ray electrochemical cell using a syringe. The polypropylene films on the cell were non-permeable, trapping the gas inside of the cell. The cyclic voltammetry data presented in this chapter was taken using the droplet cell setup. Unfortunately the droplet cell was not optimised, instead of using a longer flexi-ref reference electrode a shorter 'no-leak' solid reference electrode was used to minimise chloride contamination, and there was also an issue with keeping the cell gas tight. As a result of these issues, the cyclic voltammetry measured is not ideal, the reversible peaks in the CVs are not symmetrical over the potential axis due to the large iR drop caused by the large distance between the reference electrode to the counter and working electrodes. Despite this, the CVs still indicate some interesting features.

6.2.2 CO adsorption and electrooxidation

The oxidation of carbon monoxide, CO, to carbon dioxide, CO_2, is an important process in pollution control and fuel cell electrocatalysis. The removal of CO from exhaust fumes is done through catalytic converters. The oxidation of CO is also of paramount importance in fuel cells, where the CO from H_2 feed gas must be removed as alkaline fuel cells cannot tolerate CO and Proton Exchange Membrane (PEM) fuel cells can only cope with small amounts [150]. It is therefore essential to develop catalysts which are stable with a high efficiency. There have been many studies on CO oxidation on platinum and it has been shown that CO adsorption can promote electro-oxidation reactions on Au surfaces although the promotion is limited

to Au surfaces that exhibit reconstruction phenomena [138,139]. Study of Ag(*hkl*) surfaces that do not reconstruct may give some insight into the driving force for these surprising results.

There have been numerous experimental and theoretical studies of CO on Ag single crystal surfaces in the gas phase. DFT studies have shown that CO weakly adsorbs on silver, with adsorption energy -0.28 eV (Ag(111)) [153] and is most stable at atop sites for Ag(111) and Ag(001) [154]. Studies indicate some evidence of ordering on the Ag(111) surface; LEED indicates well-ordered incommensurate layers [155] and a low temperature study reports of islands of $\left(\sqrt{31} \times \sqrt{31}\right)R9°$ [156] above 17 K. Conversely, other reports do not find any evidence for ordering [153].

To date there are no studies reported in the literature for CO adsorption and oxidation on single crystal silver electrodes in an electrochemical environment, and only scarce studies on polycrystalline Ag. Infrared spectroscopy indicates relatively weak binding, similar to that observed on Au electrodes [157]. Marinkovic *et al.* [158] investigated CO oxidation on a Ag monolayer deposited on a Pt(111) electrode in acidic electrolyte of 0.05 M H_2SO_4 + 1 mM Ag^+ after investigations on Ag(111) electrodes revealed CO oxidation on a Ag(111) electrode 0.05 M H_2SO_4 could not be achieved due to the dissolution of the electrode at potentials negative of CO oxidation. In fact, subtractively normalised interfacial Fourier transform infrared spectroscopy (SNIFTIRS) spectra of the Ag(111) electrode showed no signs of CO adsorption or oxidation. However, for the Ag monolayer on Pt(111), a peak was observed in the CV which could be attributed to CO oxidation.

A study on polycrystalline silver investigated the effect of pH on the adsorption and oxidation of CO on silver [159] through CV measurements and Fourier Transform Infrared Spectroscopy (FTIRS) CO was found to adsorb over the pH range 0.3-13. The FTIRS measurements indicated bands corresponding to linearly chemisorbed CO and CO in the bridge position in the pH range 7-13, after holding the potential negative (corresponding to the region of CO adsorption) and exchanging the electrolyte for CO-free there was still a evidence of adsorbed CO in the CV and FTIRS. This indicates that at very alkaline pH CO is strongly adsorbed on the surface.

The mechanism for CO oxidation is described by the Langmuir-Hinshelwood mechanism in which CO continuously removes OH from the surface:

$$CO + OH = CO_2 + H^+ + e^-$$

Therefore it is important to understand the effect of CO in the double layer in the underpotential region for OH adsorption. The following sections presents the first reported cyclic voltammetry for CO adsorption and oxidation on the Ag(*hkl*) surfaces. The potential dependence of each surface were determined by XRV and a structural model is proposed from CTR analysis.

6.2.2.1 Ag(111)

Figure 6.9 shows the cyclic voltammogram of CO oxidation on Ag(111). In the anodic scan the there is a large increase in current in the CV measured in CO saturated electrolyte. This is due to the onset of CO oxidation, and is similar to that observed on polycrystalline silver [159]. The appearance of this peak tells us that CO must be adsorbed on the surface. Unfortunately there were no complete cycle XRV measured for the Ag(111) surface in the presence of CO during this experiment.

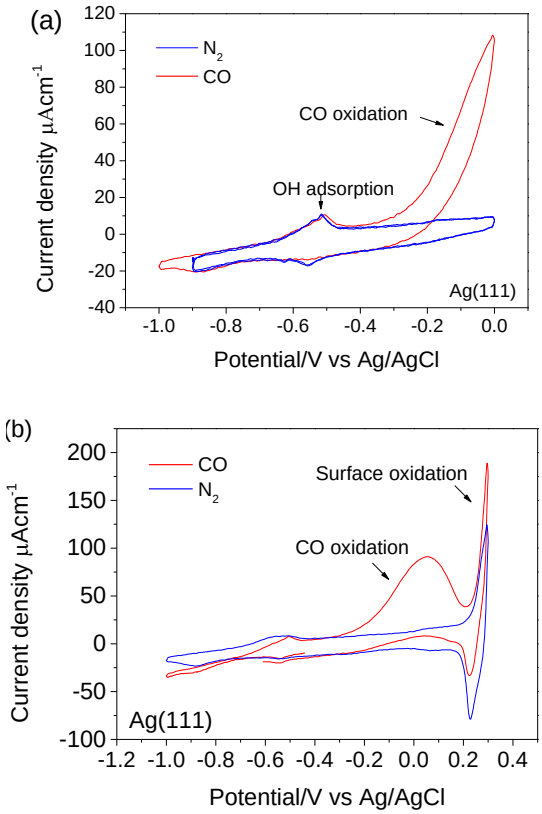

Figure 6.9 Cyclic voltammetry of Ag(111) in 0.09 M NaF + 0.01 M NaOH recorded at a sweep rate of 50 mVs^{-1} (a) region of hydroxide adsorption (b) extended potential region into oxidation.

There is a scan from -1.0 V to 0.2 V, shown in Figure 6.10, on the anti-Bragg position of the specular CTR (0, 0, 1.52), which gives some information about the potential dependence of the double layer. The XRV appears to be very similar to the one in section 6.1.1, in the absence of CO, with ~50 % change in scattered intensity, which suggests that the structure on the electrolyte side of the interface is very similar. The CTRs were taken at several potentials to obtain a structural model for this system. Measurements were taken at -1.0 V which should correspond to the region where CO is adsorbed, and -0.2 V which is in the region of CO oxidation. The data and calculated fits are shown in Figure 6.11 and Figure 6.12, and parameters are summarised in Table 6.5.

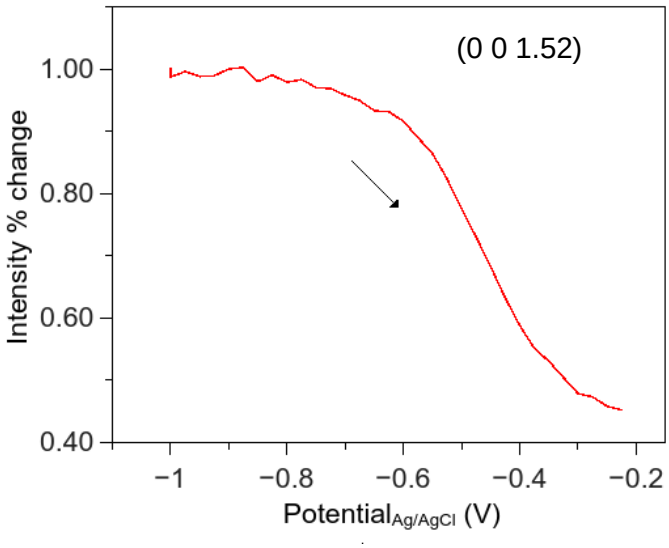

Figure 6.10 XRV at (0, 0, 1.52) in CO saturated electrolyte. Only the positive scan is shown.

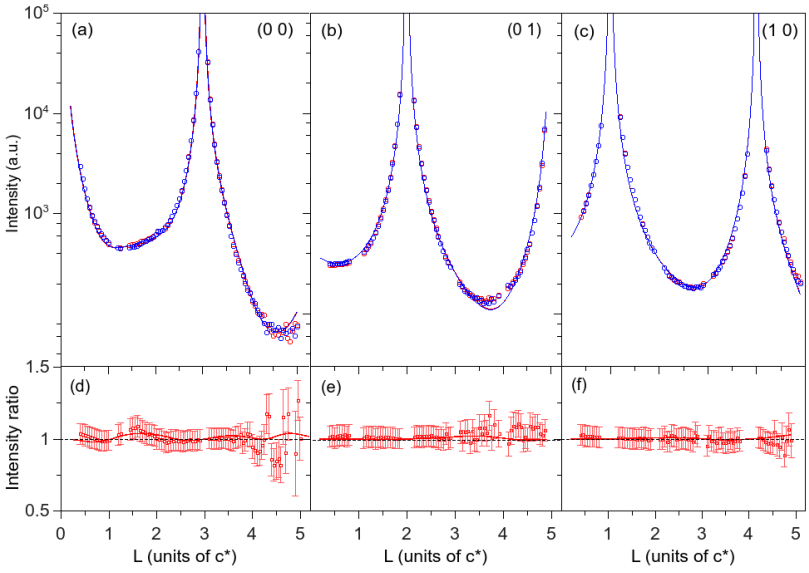

Figure 6.11 Ag(111) in 0.09 M NaF + 0.01 M NaF at -1.0 V in CO saturated electrolyte (red), and data in N_2 purged electrolyte (blue) (a) specular CTR (0, 0, L), (b) (0, 1, L) non-specular CTR (c) and (d) intensity ratios of the CO data normalised to the N_2 data. Solid lines are fits to the data given by the structural model described in the text.

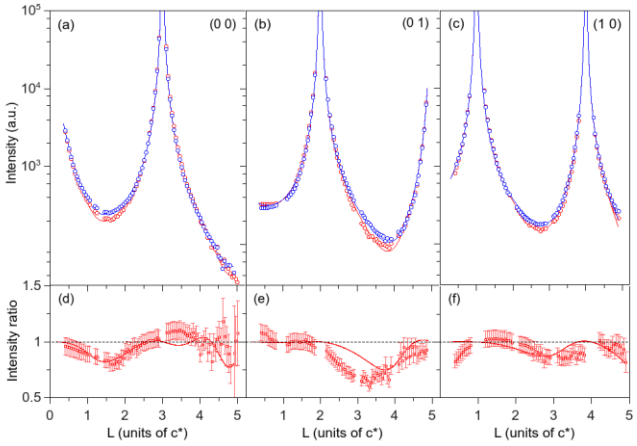

Figure 6.12 Ag(111) in 0.09 M NaF + 0.01 M NaF at -0.2 V in CO saturated electrolyte (red), and data in N_2 purged electrolyte (blue) (a) specular CTR (0, 0, L), (b) (0, 1, L) non-specular CTR (c) and (d) intensity ratios of the CO data normalised to the N_2 data. Solid lines are fits to the data given by the structural model described in the text.

Parameter		-1.0 V	-0.2 V
Metal layer	ε_1(Å)	-0.019(1)	-0.037(1)
	σ_{Ag1} (Å)	0.117(2)	0.147(2)
Oxygen layer	θ	0.23(3)	0.65(3)
	$d_{Ag\text{-}O}$ (Å)	2.75(7)	2.27(3)
	σ_O (Å)	0.15	0.15
Na^+ layer	θ	0.39(2)	0.36(2)
	$d_{Ag\text{-}Na}$ (Å)	4.08(2)	3.09(3)
	σ_{Na} (Å)	0.15	0.15
	Reduced χ^2	1.79	1.71

Table 6.5 Best fit parameters to the structural model for CTR measurements of the Ag(111)/0.09 M NaF + 0.01 M NaOH interface in the presence of CO at -1.0 V, and -0.2 V.

The differences between the structure in the presence of CO and in the absence are highlighted by the ratios in Figure 6.11 and Figure 6.12. The CO data is normalised to the data in N_2 purged electrolyte. Within error, the structure at negative potential in the presence of CO is the same as the structure without CO, this is consistent with the ratio of the datasets which is essentially a flat line. This indicates that the addition of CO in the electrolyte has no effect on the metal and double layer structure at this potential, despite the fact that CO should be adsorbed at this potential. This could suggest that CO is only weakly adsorbed as it does not seem to affect the metal.

The ratios at positive potential, -0.2 V, indicate some small changes. The non-specular CTRs were best modelled by an increase in the rms roughness, (σ_{Ag}). This implies that the electrooxidation, the removal of OH from the surface by CO, induces a slight roughening to the surface. The *inwards* relaxation of the metal layer is slightly less in the presence of CO 1.57 ± 0.04 % with CO, and 1.76 ± 0.04 % without CO, (a percentage of layer spacing $d_{(111)}$ = 2.36 Å), the difference in surface roughness is more significant 0.147 ± 0.002 Å, with CO, and 0.117 ± 0.002 Å without CO. The changes in electrolyte layering are more prominent. The first layer was modelled as an oxygen layer, although it is likely to be a mix of OH and CO. The layer has a reduced coverage of $\theta = 0.66 \pm 0.03$ ($\theta = 0.78 \pm 0.02$ without CO), which could be explained by the removal of OH from the surface by CO. It is closer to the surface at a height of 2.27 ± 0.03 Å (2.51 ± 0.02 Å in the absence of CO). The coverage of the Na^+ is greater in the presence of CO and in closer proximity to the electrode surface. A possible explanation of this is that the presence of CO changes

the nature of the bonding. Or if in fact, there cation is partially hydrated. The mechanism behind this is currently unknown.

6.2.2.2 Ag(110)

Figure 6.13 shows the voltammetry of the Ag(110) surface in 0.09 M NaF + 0.01 M NaOH in the presence and absence of CO. Unfortunately over the smaller potential range the voltammetry in CO saturated solution was not of sufficient quality to give any meaningful information. However, there are interesting features over the extended potential range into the region of oxidation. With the addition of

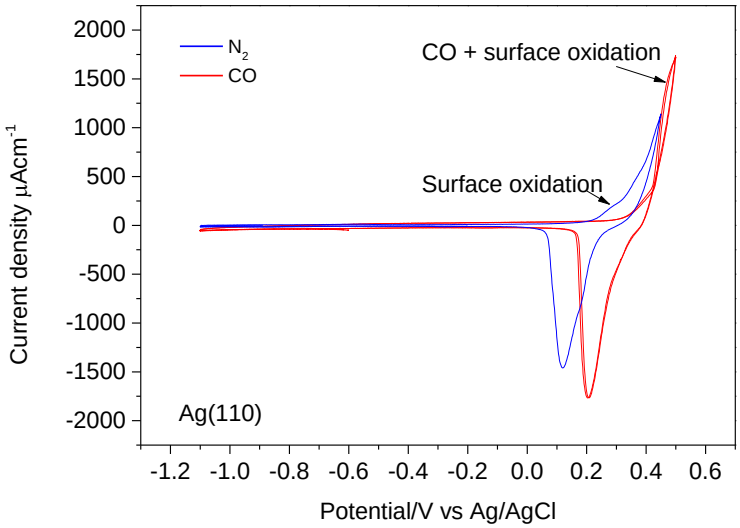

Figure 6.13 Cyclic voltammetery of Ag(110) in 0.09 M NaF + 0.01 M NaOH recorded at a sweep rate of 50mVs^{-1} in the presence of CO (red) and in the absence in N_2 purged electrolyte (blue).

CO in electrolyte the oxidation of silver is suppressed; onset of the anodic oxidation peak is shifted positive by approximately 0.1 V, which implies that CO must be adsorbed on the surface as it seems to protect the surface from oxidation.

To characterise the structural potential dependence of the Ag(110) surface in the presence of CO, XRV was measured at the anti-Bragg position on the specular CTR, and two non-specular CTRs (1, 0, 0.2) and (0, 1, 0.3) shown in Figure 6.14. The XRV is consistent with the those measured in the absence of CO, the intensity at the anti-Bragg position decreases which increased adsorption of OH during the anodic scan and increases with the desorption of OH during the cathodic scan. There are no obvious changes, to determine any structural differences in the electrolyte. There are some subtle changes observed in the XRVs at the two non-specular CTRs

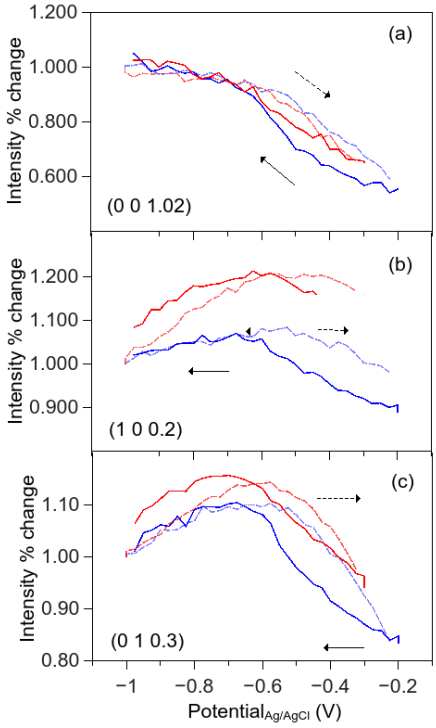

Figure 6.14 XRV of Ag(110) in 0.09 M NaF + 0.01 M NaOH taken in the presence of CO (red) and in the absence (blue) at (a) (0, 0, 1.02) on the specular CTR, (b) (1, 0, 0.2) and (c) (0, 1, 0.3) on the non-specular CTRs. The data is normalised to the first point in each scan to display the intensity as a percentage change for comparison. Negative sweep is indicated by the solid lines, and the positive sweep by the dashed lines.

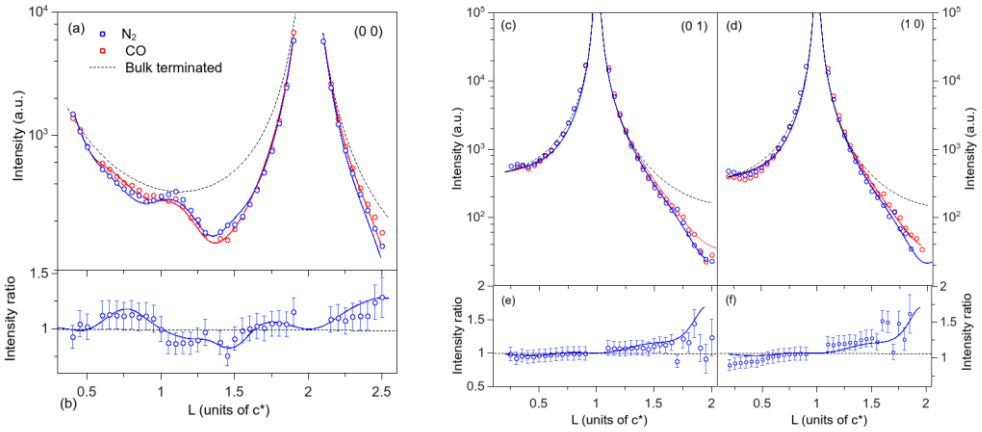

Figure 6.15 Ag(110) CTR data of the Ag(110)/0.09 NaF + 0.01 M NaOH interface measured at -1.0 V in N_2 purged electrolyte (blue), CO saturated electrolyte (red) (a) the specular CTR (0, 0, L) and the non-specular CTRs (c) (0, 1, L) and (d) (1, 0, L). The CTRs measured in the presence of CO were normalised to the data measured in N_2 purged electrolyte (b) (0, 0, L) (e) (0, 0, L) and (f) (1, 1, L). The solid lines are the fits to the data according to the structural model described in the text and parameters given in Table 6.6.

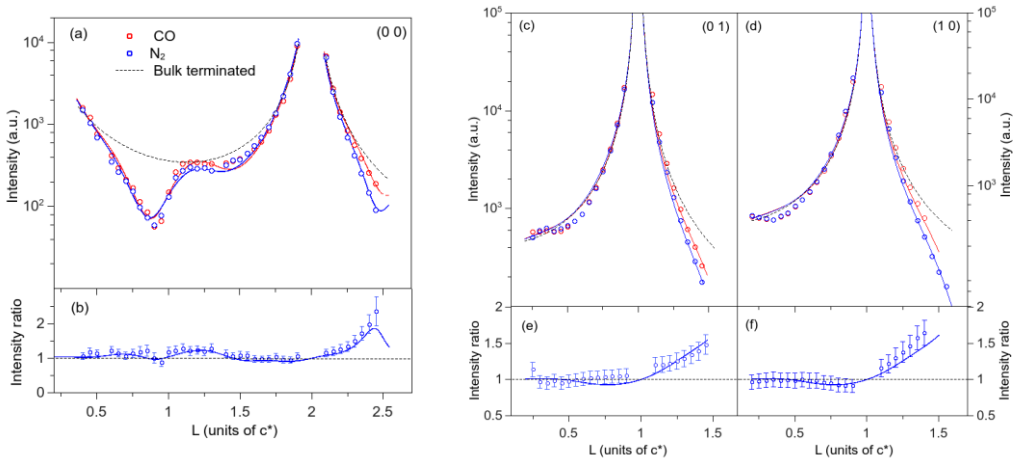

Figure 6.16 Ag(110) CTR data of the Ag(110)/0.09 NaF + 0.01 M NaOH interface measured at -0.2 V in N_2 purged electrolyte (blue) and CO saturated electrolyte (red) (a) the specular CTR (0, 0, L) and the non-specular CTRs (c) (0, 1, L) and (d) (1, 0, L). The CTRs measured in the presence of CO and O_2 were normalised to the data measured in N_2 purged electrolyte (b) (0, 0, L) (e) (0, 0, L) and (f) (1, 1, L). Solid lines are fits to the data.

Parameter		-1.0 V	-0.2 V
Metal layers	ε_3 (Å)	0.006(3)	0.020(5)
	σ_{Ag3} (Å)	0.08(7)	0
	ε_2(Å)	-0.014(2)	-0.037(6)
	σ_{Ag2} (Å)	0.17(1)	0
	ε_1(Å)	-0.043(2)	0.075 (5)
	σ_{Ag1} (Å)	0.312(5)	0.423(8)
Oxygen layer	θ_{01}	0.49(5)	0.76(6)
	d_{Ag-O1} (Å)	2.86(4)	2.17 (4)
	σ_{O1} (Å)	0.15	0.15
Oxygen layer	θ_{02}	-	0.50(6)
	d_{Ag-O2} (Å)	-	3.16(9)
	σ_{O2} (Å)	-	0.15
Error Function	σ_E	0.5	0.5
	d_E	5.0(1)	5.1(2)
	Reduced χ^2	1.60	2.30

Table 6.6 Best fit parameters to the structural model for CTR measurements of the Ag(110)/0.09 M NaF + 0.01 M NaOH interface in the presence of CO at -1.0 V, and -0.2 V. Numbers without errors correspond to parameters that were fixed during the fitting procedure.

indicating that the presence of CO in solution induces some structural changes in the metal side of the interface.

CTR measurements were taken at -1.0 V and -0.2 V to obtain a structural model for this system. The data and corresponding fits are shown in Figure 6.15 and Figure 6.16. The parameters for the structural model are summarised in Table 6.6. The data was fit using the same procedure outlined in section 6.1.2. At -1.0 V there are small differences in the structure of the metal compared to the data taken in the absence of CO. The *inwards* relaxation of the top metal layer increases, and the*inwards* relaxation of the 2nd layer decreases which results in a 2 % decrease in layer spacing d_{12}. In the electrolyte side of the interface there is very little difference between the structure with and without CO. In both cases the data was fit with an incommensurate adlayer at 2.86 Å above the surface. The difference in coverage of the adlayers is only marginal within error, with CO θ = 0.49 ± 0.05 ML, and without CO θ = 0.60 ± 0.05 ML. Although there is very little difference to the electrolyte side of the interface. It is possible that the presence of adsorbed CO in solution is responsible for the change in Ag surface relaxation. At positive potential (E = -0.2 V) potential there are only subtle differences between the CO and N_2. There is a very small decrease of the *outward* relaxation of the top metal layer with the presence of CO Δ_{12} = + 7.75 % compared to Δ_{12} = + 8.53 % in the absence of CO. On the electrolyte side of the interface, the biggest difference between the two datasets is the height of the 2nd adlayer above the top metal layer, in the presence of CO the height was determined to be 3.16 ± 0.04 Å, compared with 3.29 ± 0.07 Å. This is very similar to the results found on Ag(111), the presence of CO in electrolyte has an effect on the height on the cation layer – it seems to decrease the layer spacing, possibly through changing the nature of the bonding.

6.2.2.3 Ag(001)

Figure 6.17 shows the CV of CO oxidation on Ag(001). In the anodic scan there is a broad peak in the current at around 0 V in the CV measured in CO-saturated electrolyte. This is due to CO oxidation. The peak is much less pronounced than in the case of Ag(111), it is not visible over the extended potential range, which could suggest either CO is more strongly adsorbed on Ag(001), and therefore less prone to electrooxidation, or that the coverage is much less on Ag(001). The XRV

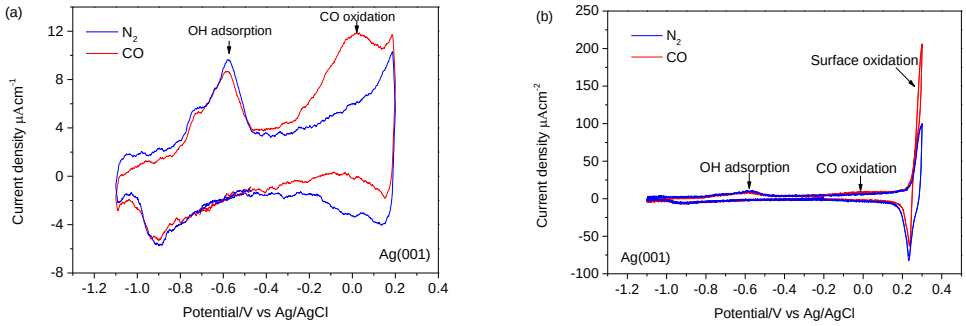

Figure 6.17 Cyclic voltammetry of the Ag(001) surface in 0.09 M NaF + 0.01 M NaOH in the presence of CO (red) and in the absence of CO (in N_2 purged electrolyte) (blue). (a) Over the potential range for OH adsorption and CO oxidation and (b) over the extended range into oxidation. Sweep rate 50 mVs^{-1}.

taken at (0 0 1.02) is shown in Figure 6.18. The shape of the XRV is very similar to the XRV measured in the absence of CO, implying that the addition of CO only causes subtle changes to the double layer structure. To obtain a structural model for the system CTR measurements were taken at E= -1.0 V and E= -0.2 V. There are noticeable differences in the data measured in the presence of CO and in the absence

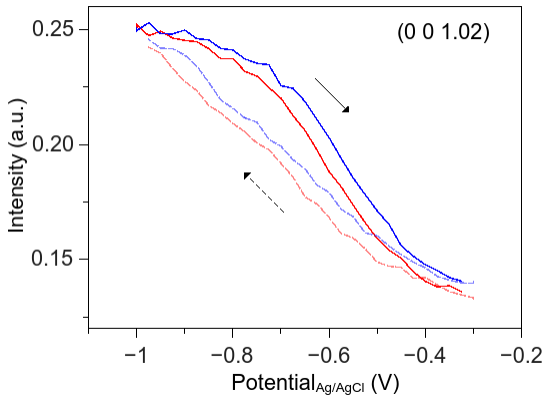

Figure 6.18 XRV of Ag(001) on the specular CTR position (0 0 1.02) in the presence of CO (red), in absence of CO (blue). Negative sweep is indicated by the dashed lines and the positive sweep is indicated by the solid lines. Sweep rate 20 mV/s.

of CO. At negative potential the effect is subtle; the electrolyte structure is similar to in N_2. The best fit was obtained when Na^+ cations were modelled in atop sites at a distance of 2.93 Å from the electrode surface with a coverage of θ_{Na+} = 0.21. At negative potential CO should be adsorbed on the surface although the inclusion of an additional adlayer to account for CO did not improve the fit suggesting that CO is not ordered on the surface.

At positive potential, -0.2 V, the changes between the data sets are more noticeable. Here the *outward* relaxation of the second layer is much larger ~0.8 % than in the absence of CO where it is ~0.04 %, and the top layer *inward* relaxation is reduced from 1.5 % in the absence of CO to 0.23 % in the presence of CO. The structure of the electrolyte is also significantly different. The 'oxygen' adlayer is much closer to the surface at 1.48 Å, than in the absence of CO where it is 1.65 Å. The coverage of the adlayer in the presence of CO is 1 ML compared with 0.8 ML in the absence of CO. The fits to the ratio of the data indicates that the specular CTR is

well represented by the structural model. However, the model does not give a good fit to the non-specular CTR data taken in the presence of CO at positive potential. This indicates something is missing from the model of the metal side of the interface. Modelling the adlayer in different adsorption sites, atop, bridge and hollow did not improve the fit. Further analysis is required in order to improve the structural model. The cyclic voltammetry indicates that -0.2 V is just at the onset of CO electrooxidation (onset of the oxidation peak) which suggests what the adlayer at this potential could be a mix of coadsorbed CO and OH.

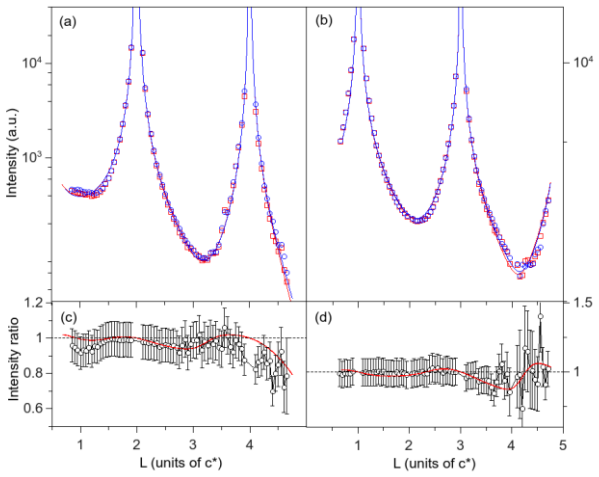

Figure 6.19 Crystal truncation rod (CTR) data of Ag(001) measured at -1.0 V in N_2 purged electrolyte (red squares) and CO saturated electrolyte (blue circles) (a) the specular CTR (0, ,0 L) and (b) the non-specular CTR (1, 1, L). The CTR measured in the presence of CO was normalised to the data measured in N_2 purged electrolyte (c) (0, 0, L) and (d) (1, 1, L).

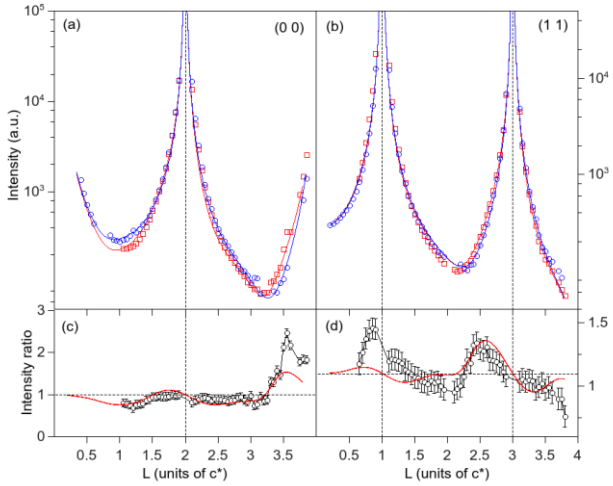

Figure 6.20 Crystal truncation rod (CTR) data of the Ag(001)/0.09 NaF + 0.01 M NaOH measured at -0.2 V in N_2 purged electrolyte (red squares) and CO saturated electrolyte (blue circles) (a) the specular CTR (0, 0, L) and (b) the non-specular CTR (1, 1 L). The CTR measured in the presence of CO was normalised to the data measured in N_2 purged electrolyte (c) (0, 0, L) and (d) (1, 1, L). The solid lines are the fits to the data.

Parameter		-1.0 V	-0.2 V
Metal layers	ε_2(Å.)	-	0.016(1)
	σ_{Ag2} (Å)	-	0
	ε_1(Å)	-0.019(1)	-0.006(1)
	σ_{Ag1} (Å)	0.118(2)	0.123(4)
Adlayer	θ	0.21(5)	1.0(1)
	d(Å)	2.939 (1)	1.48(3)
	σ(Å)	0.219(7)	0.3
	Reduced χ^2	2.02	1.82

Table 6.7 Best fit parameters to the structural model for CTR measurements of the Ag(001)/0.09 M NaF + 0.01 M NaOH interface in the presence of CO at -1.0 V and -0.2 V.

The layer spacing is very similar to a study by Lucas *et al.* [160] on Pt(001), where a platinum-carbon spacing is proposed to be $d_{Pt\text{-}C} = 1.4 \pm 0.4$ Å. The decrease of the Ag-OH interlayer spacing suggests an increase in bond strength or the OH could be located in a different site, although the mechanism for this is not currently determined.

6.2.3 Oxygen

The oxygen reduction reaction (ORR) is one of the most important reactions in electrochemistry. Understanding its mechanism is central to be able to tailor materials which can either catalyse it for use in energy conversion systems, or inhibit it, for corrosion resistant materials. Platinum is the best catalyst for the ORR due to its stability and high catalytic activity. For this reason it is the most widely studied catalyst. The first report by Zwetanova *et al.* [161] proposed that the ORR is not structure sensitive. In contrast, subsequent studies find that the kinetics of ORR *is* governed by the structure of the electrode and adsorbed species. Blizanac *et al.* [162] were the first to report the origin of the structure sensitivity. They determined the kinetics of the ORR to increase in the order (100) ≤ (111) ≤ (110). They found the kinetics were dependent upon a balance between the potential dependent adsorption of spectator ions (OH^-), and the variation in activation energies which are determined by the O_2 adsorption on Ag(*hkl*) surfaces covered by oxygenated species. More recently, studies have focussed on the double layer effects and role of cations on the ORR, these studies are again focussed on Pt, Au and Ir electrode. The studies reveal that the activity of the ORR can be inhibited by cation-OH_{ads} clusters in the compact double layer (as discussed in the previous section). It is therefore important to understand the structure of the double layer under reaction conditions.

Mechanism for ORR

There are many reaction pathways which have been proposed for the mechanism for the ORR. The one which is considered most appropriate for Ag is presented:

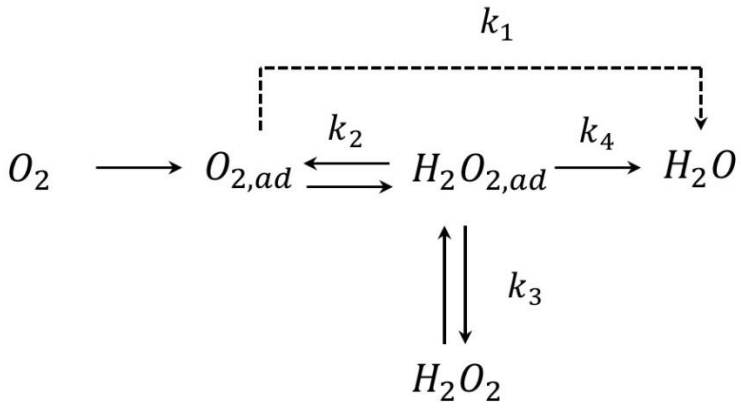

Figure 6.21 Serial pathway of oxygen reduction.

From this there are three possible reaction pathways. Blizanac *et al*. [162] proposed the reaction pathway on all Ag(*hkl*) is the direct four-electron O_2 reduction to water. In this section the structure of the Ag(*hkl*)/0.01 M NaOH and 0.09 M NaF interface was probed in the presence of O_2, and compared with the models determined in section 6.1 the absence of O_2 (i.e. N_2 purged electrolyte).

6.2.3.1 Ag(111)

XRV measured at the anti-Bragg position, (0, 0, 1.6), on the specular CTR is shown in Figure 6.22. The data was normalised to the first point of each scan, so that the percentage change in intensity of both systems could be compared. The figure highlights subtle differences between the two systems. The shape of the XRVs is very similar and the decrease in intensity on the positive sweep is consistent with OH adsorption. The change in intensity over the whole potential range is slightly greater

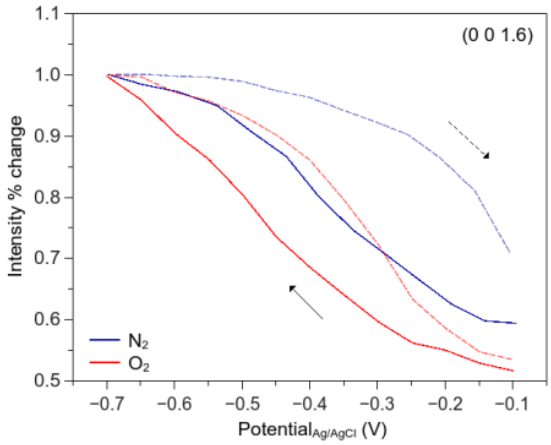

Figure 6.22 XRV on the (0 0 1.6) position in the presence of O_2 and in N_2 purged electrolyte. Negative sweep is indicated by the dashed lines and the positive sweep by the solid lines. Measured at a sweep rate of 20 mV/s.

in the presence of O2, which suggests that there some differences in the electrolyte side of the interface. The data in the presence of O_2 was taken during a different experiment to the data previously discussed in N_2 and CO and it was also taken at slightly different potentials. For this reason, the results have been normalised to a N_2 dataset taken during the same experiment and at the same potential. These results are summarised in Table 6.8 and the CTR data and calculated fits are presented in Figure 6.23-Figure 6.25. To fit the data at -0.7 V the relaxation of the top metal layer (ε), rms roughness (σ) and an inclusion of a commensurate Na^+ layer, in atop positions, gave a good fit to the data which is the same model used for both N_2 and CO. No additional oxygen layer was required to obtain a good fit to the data, in comparison to the data presented in section 6.1.1. This could be due to the slight difference in negative potential limit; the water layer could be disordered. There are only subtle differences between the data in the presence of O_2 and in the absence of O_2 which implies that there are no pronounced effects on the structure at the interface.

Parameter		N_2		O_2	
		-0.7 V	-0.1 V	-0.7 V	-0.1 V
Metal layer	ε_1(Å)	-0.001(3)	-0.038(3)	0.00	-0.039(4)
	σ_{Ag1} (Å)	0.128(5)	0.100(5)	0.114(4)	0.088(6)
Oxygen layer	θ	-	0.88(6)	-	0.9(1)
	$d_{Ag\text{-}O}$ (Å)	-	2.54(4)	-	2.45(7)
	σ_O (Å)	-	0.15	-	0.15
Na^+ layer	θ	0.38(3)	0.12(4)	0.35(3)	0.14(2)
	$d_{Ag\text{-}Na}$ (Å)	3.32(4)	3.3(2)	3.33(4)	3.16(2)
	σ_{Na} (Å)	0.15	0.15	0.15	0.15
	Reduced χ^2	1.97	1.64	2.1	1.65

Table 6.8 Best fit parameters to the structural model for CTR measurements of the Ag(111)/0.09 M NaF + 0.01 M NaOH interface in the presence and absence of O_2 at -0.7 V and -0.1 V.

There is small 0.4 % *inward* relaxation of the top metal layer in the absence of O_2, however, in the presence of O_2 there is no relaxation of the layer, a small rms roughness was sufficient to fit the data. At positive potential there is no change to the metal layers in the presence of O_2. However there are some small changes to the electrolyte layering. The height of the OH^- layer above the metal surface is slightly reduced 2.45 Å (compared to 2.54 ± 0.04 Å in the absence of O_2). The Na^+ layer is also closer at 3.16 (compared to 3.3 ± 0.2 Å), albeit within error they are not significant.

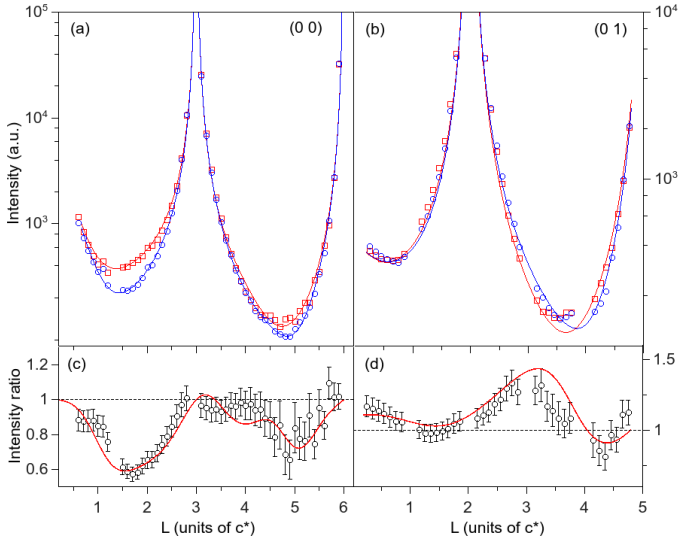

Figure 6.23 Potential dependence of Ag(111) in nitrogen purged electrolyte. Red squares (-0.7 V) and blue circles (-0.2 V) (a) specular CTR (0 0 L), (b) (0 1 L) non-specular CTR (c) and (d) intensity ratios of the -0.2 V data normalised to the -0.7 V data. Solid lines are fits to the data.

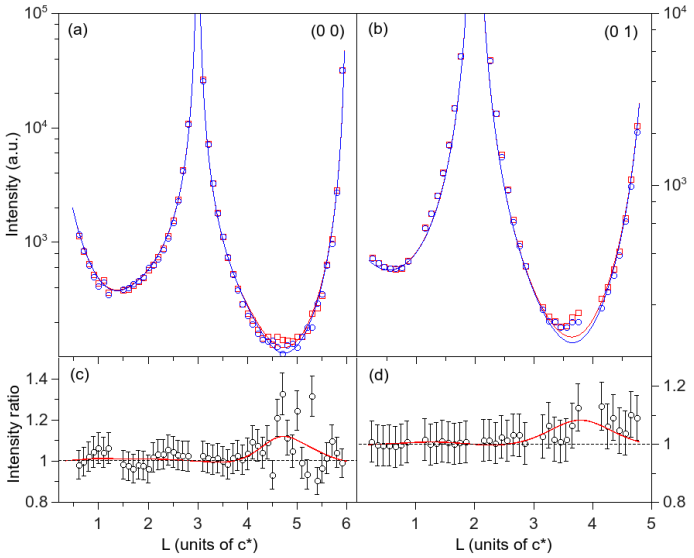

Figure 6.24 Ag(111) in 0.09 M NaF + 0.01 M NaF at -0.77 V in oxygen saturated electrolyte(red squares), and data in N2 purged electrolyte (blue circles) (a) specular CTR (0 0 L), (b) (0 1 L) non-specular CTR (c) and (d) intensity ratios of the O_2 data normalised to the N_2 data. Solid lines are fits to the data given by the structural model described in the text.

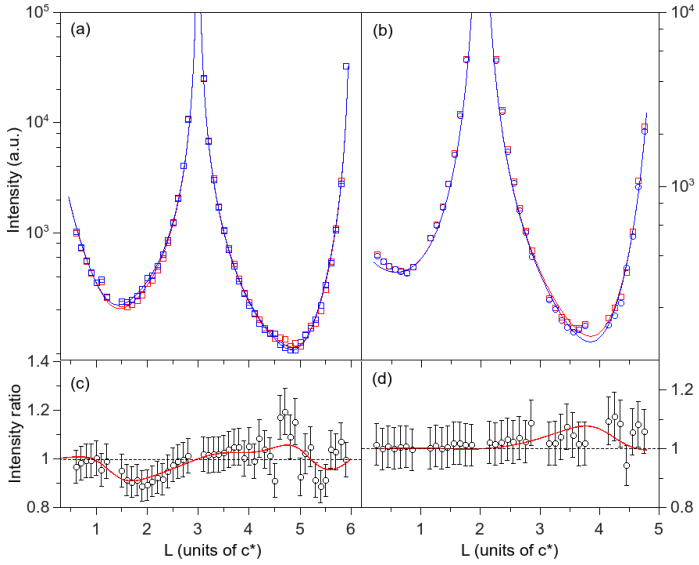

Figure 6.25 Ag(111) at -0.17 V Red circles, data in oxygen saturated electrolyte, and blue circles, data in N_2 purged electrolyte (a) specular CTR (0 0 L), (b) (0 1 L) non-specular CTR (c) and (d) intensity ratios of the O_2 data normalised to the N_2 data. Solid lines are fits to the data given by the structural model described in the text .

6.2.3.2 Ag(110)

The potential dependence of the Ag(110) surface in 0.09 M NaF + 0.01 M NaOH electrolyte measured in the presence of oxygen by XRV on the anti-Bragg position on the specular CTR as shown in Figure 6.26. The potential dependence is very similar to that found in the absence of O_2 (in N_2 purged electrolyte). With increasing potential the intensity decreases, which is attributed to the increased deposition of OH. On the reverse sweep, the intensity increases with the desorption of OH. CTR measurements were taken at -1.0 V, corresponding to the potential region where there is no adsorbed species, and -0.2 V the potential region for ORR. The data and corresponding fits are shown in Figure 6.27 and Figure 6.28. The parameters for the structural model are summarised in Table 6.9. The data was fit using the same procedure outlined in section 6.1.2. There are no significant changes

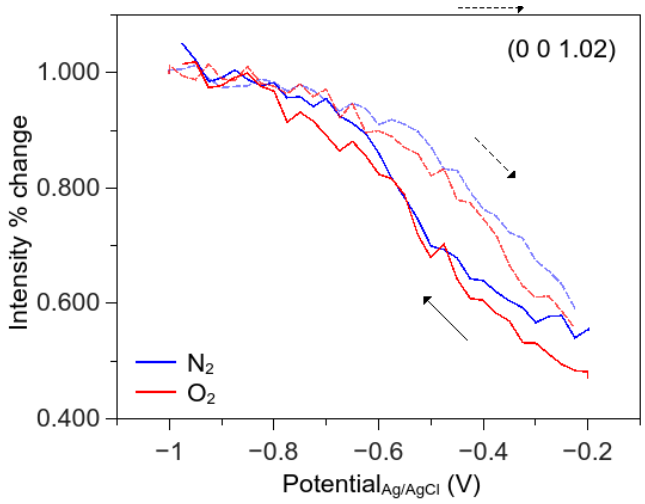

Figure 6.26 XRV of Ag(110) in 0.09 M NaF + 0.01 M NaOH taken in the presence of O_2 (red) and in the absence (blue) at (a) (0, 0, 1.02) on the specular CTR, (b) (1, 0, 0.2) and (c) (0, 1, 0.3) on the non-specular CTRs. Negative sweep is indicated by the solid lines, and the positive sweep by the dashed lines.

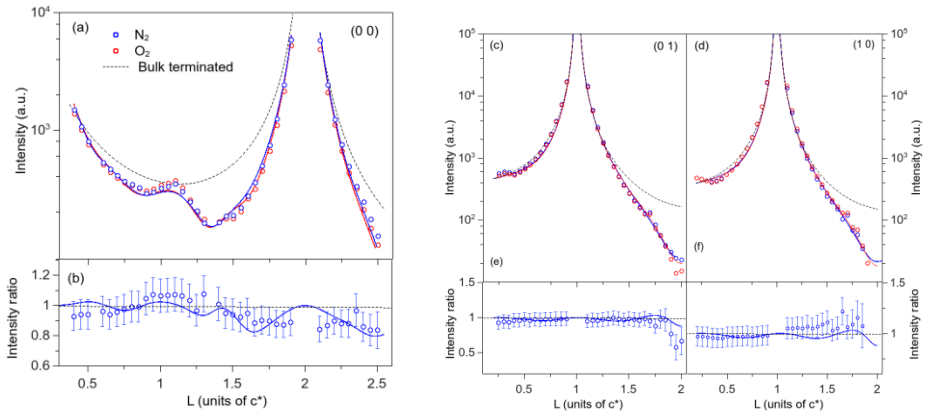

Figure 6.27 Ag(110) CTR data of the Ag(110)/0.09 NaF + 0.01 M NaOH interface measured at -1.0 V in N_2 purged electrolyte (blue), O_2 saturated electrolyte (red) (a) the specular CTR (0, 0, L) and the non-specular CTRs (c) (0, 1, L) and (d) (1, 0, L). The CTRs measured in the presence of O_2 were normalised to the data measured in N_2 purged electrolyte (b) (0, 0, L) (e) (0, 0, L) and (f) (1, 1, L). The solid lines are the fits to the data according to the structural model described in the text.

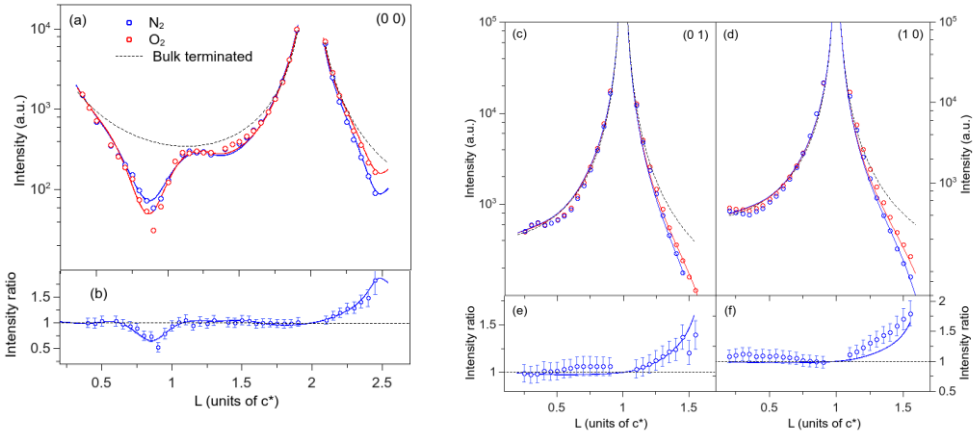

Figure 6.28 Ag(110) CTR data of the Ag(110)/0.09 NaF + 0.01 M NaOH interface measured at -0.2 V in N_2 purged electrolyte (blue) and O_2 saturated electrolyte (red) (a) the specular CTR (0, 0, L) and the non-specular CTRs (c) (0, 1, L) and (d) (1, 0, L). The CTRs measured in the presence of O_2 were normalised to the data measured in N_2 purged electrolyte (b) (0, 0, L) (e) (0, 0, L) and (f) (1, 1, L). The solid lines are the fits to the data according to the structural model described in the text.

between the structure with and without O_2 at this potential, which is not surprising as there is no adsorption at this potential. At positive potential the interface was modelled in the same way as in the absence of O_2. The data was best fit with 2 incommensurate adlayers and an error function. The structure of the electrolyte is very similar to the structure in the absence of O_2 within error. The main difference occurs in the metal side of the interface. The addition of O_2 changes effects the relaxation of the metal layers; the extent of the *outwards* relaxation of the first layer and the *inwards* relaxation of the second layer are both reduced. This decreases the change in layer spacing Δ_{12} = + 7.27 % from Δ_{12} = + 8.53 % in the absence of O_2.

Parameter		-1.0 V	-0.2 V
Metal layers	ε_3 (Å)	0.009(2)	0.021(3)
	σ_{Ag3} (Å)	0.145(5)	0
	ε_2(Å)	- 0.025(2)	-0.025(3)
	σ_{Ag2} (Å)	0.209	0
	ε_1(Å)	-0.029(2)	0.080(2)
	σ_{Ag1} (Å)	0.33	0.481(7)
Oxygen layer	θ_{01}	0.66(5)	0.87(6)
	d_{Ag-O1} (Å)	2.89(4)	2.25(3)
	σ_{O1} (Å)	0.15	0.15
Oxygen layer	θ_{02}	-	0.60(5)
	d_{Ag-O2} (Å)	-	3.29(6)
	σ_{O2} (Å)	-	0.15
Error Function	σ_E	0.5	0.5
	d_E	5.04(9)	5.23(1)
	Reduced χ^2	1.89	1.75

Table 6.9 Best fit parameters to the structural model for CTR measurements of the Ag(110)/0.09 M NaF + 0.01 M NaOH interface in the presence of CO and O_2 at -1.0 V, and -0.2 V. Numbers without errors correspond to parameters that were fixed during the fitting procedure.

6.3.3.3 Ag(001)

The XRV shown in Figure 6.29 indicates there is little difference between the data measured with and without O_2. To obtain a clearer picture of the differences

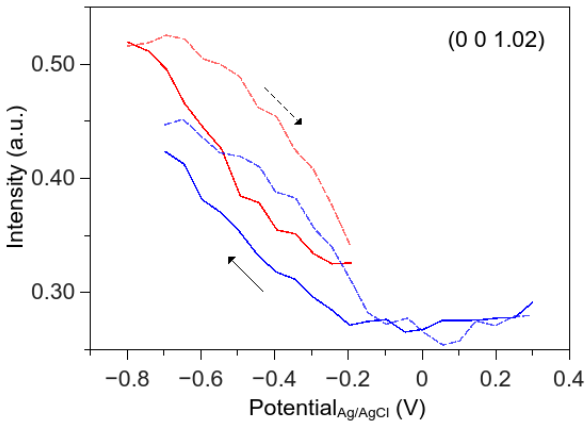

Figure 6.29 XRV of Ag(001) on the specular CTR position (0, 0, 1.02) in the presence of O_2 (red), in absence of O_2 (blue). Negative sweep is indicated by the dashed lines and the positive sweep is indicated by the solid lines.

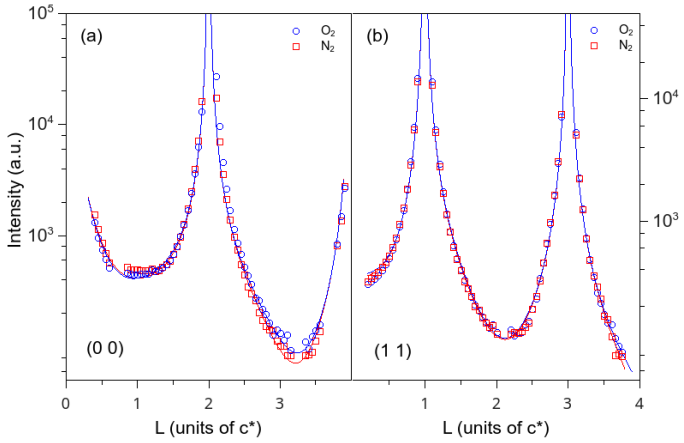

Figure 6.30 Crystal truncation rod (CTR) data Ag(001) measured at -0.8 V in N_2 purged electrolyte (red squares) and O_2 saturated electrolyte (blue circles) (a) the specular CTR (0, 0, L) and (b) the non-specular CTR (1, 1, L). The CTR measured in O_2 saturated electrolyte was normalised to the data measured in N_2 purged electrolyte (c) (0, 0, L) and (d) (1, 1, L). The solid lines are the fits to the data according to the structural model described in the text.

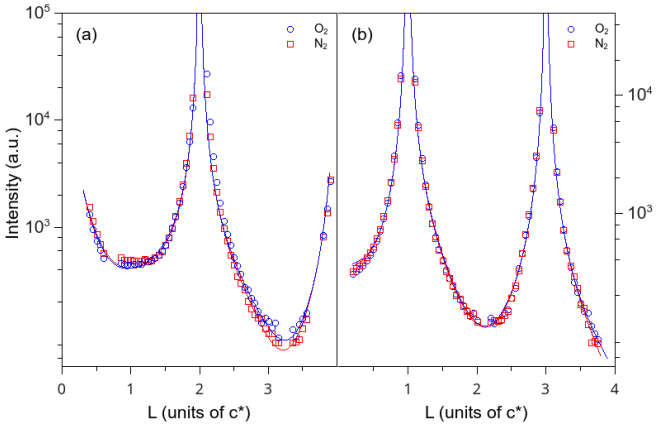

Figure 6.31 Crystal truncation rod (CTR) data of the Ag(001) measured at -0.2 V in N_2 purged electrolyte (red squares) and O_2 saturated electrolyte (blue circles) (a) the specular CTR (0, 0, L) and (b) the non-specular CTR (1, 1, L). The CTR measured in O_2 saturated electrolyte was normalised **t**o the data measured in N_2 purged electrolyte (c) (0, 0, L) and (d) (1, 1, L). The solid lines are the fits to the data.

between the two systems, CTR measurements of the specular CTR, (0, 0, L) and the first order non-specular CTR (1, 1, L) which are shown in Figure 6.30 and Figure 6.31 and best fit parameters are summarised in Table 6.10. At negative potential there is virtually no difference between the data measured with and without O_2. The *inward* relaxation of the metal layer in both cases was 0.9 % of the layer spacing. It was necessary to include in-plane ordering of the adlayer in order to model the non-specular CTR. The best fit indicated a Na^+ layer in atop sites, similarly to that found in the absence of O_2 and in the presence of CO. There are some subtle differences in the coverage of the adlayer with and without O_2, however, they are marginal. At positive potential there are some small differences in the data; the *inward* relaxation of the top metal layer is smaller in the presence of O_2 1.22 ± 0.05 % of the layer spacing compared to 1.5 ± 0.9 % without O_2. Within error there is no difference in the coverage of the oxygen layer, although the height of the adlayer is reduced in the

Parameter		-0.8 V	-0.2 V
	ε_2(Å)	-	0.001(1)
	σ_{Ag2} (Å)	-	0.051(5)
	ε_1 (Å)	-0.019(2)	-0.025(1)
	σ_{Ag1} (Å)	0.092(3)	0.14(1)
Adlayer	θ	0.32(3)	0.87(5)
	d (Å)	3.02(1)	1.53(3)
	Σ (Å)	0.2	0.3
	Reduced χ^2	1.9	1.88

Table 6.10 Best fit parameters to the structural model for CTR measurements of the Ag(001)/0.09 M NaF + 0.01 M NaOH interface in the presence of O_2 at -0.8 V and -0.2 V. Numbers without errors correspond to parameters that were fixed during the fitting procedure.

presence of O_2, 0.07 Å closer to the surface. Overall the presence of O_2 in electrolyte only slightly perturbs the double layer, which is not surprising considering the kinetics of the ORR are lowest on the Ag(001) [162].

6.2.4 Discussion

CO effect

Although there is no direct indication from the CTR modelling that CO is adsorbed on the surface, the presence of CO can be inferred from:

1) Voltammetry – there is clear evidence of CO adsorption on Ag(*hkl*) as there are peaks observed in the CV on Ag(111) and Ag(001) which must

be due to CO electroxidation, and CO appears to suppress oxidation on Ag(110).

2) Changes to the electrolyte structure.
3) Changes to the Ag(001) and Ag(110) metal layer relaxations.

From the cyclic voltammetry it is clear that CO must be adsorbed on the surface, as there are oxidation peaks observed in the CV measured on Ag(111) and Ag(001). On Ag(110) the oxidation peak is not visible over the extended potential range, despite this there is strong evidence for CO on the surface as the oxidation of the surface is suppressed. This implies that CO is strongly adsorbed on the Ag(110) surface as it seems to protect the surface from oxidation, and indicates that CO oxidation occurs at more positive potential which would result in a mix of current from both oxidation processes in the peak between 0.4-0.45 V, as the two charge transfer processes occur over the same potential region. This is supported by similar behaviour which has previously been reported [159] for polycrystalline silver where the electrooxidation of silver is inhibited by CO by 0.13 V. Orozco *et al.* report this is due to chemisorption of CO poisoning the Ag surface, which is supported by previous studies by Cuesta *et al*. on a number of other electrodes for Fe [157], Co [163] and Ni [164]. The effect of suppressing Ag oxidation was only observed for pH 13 indicating that the underpotential oxide formation (adsorption of OH^-) is key to the electrooxidation of CO. Unfortunately, due to the cell arrangement, we were unable to hold the electrode at negative potential whilst switching the CO-free electrolyte, and do not have the stripping voltammetry so we are unable to determine whether CO was still absorbed.

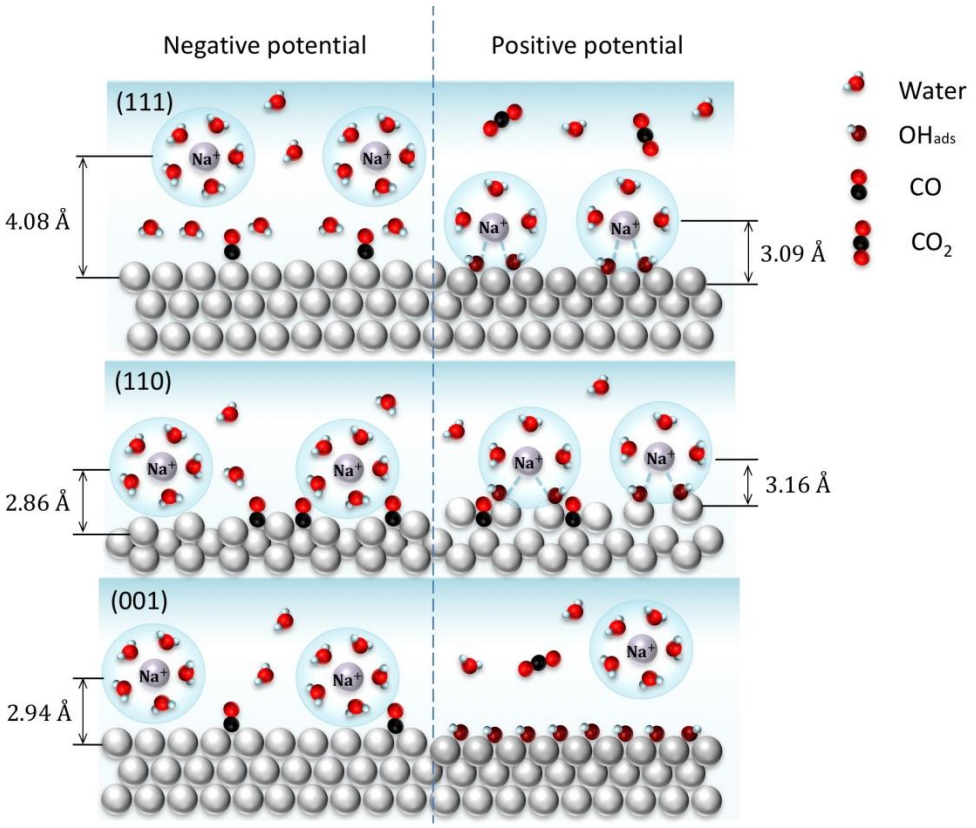

Figure 6.32 Schematic representation of the Ag(*hkl*)/alkaline interface in CO saturated solution, highlighting the structural differences between the two potential limits. At both potentials there is no evidence of any ordered CO structures – however the presence is inferred from changes to the interface structure. At negative potential CO is adsorbed on the surface. At positive potential CO oxidation occurs on Ag(111) and Ag(001), however on Ag(110) it is proposed that CO is still adsorbed on the surface – poisoning the surface from oxidation.

In a study by Oda *et al.* [165] on Ag(polycrystalline) and Ag layers on Pt(110), the coverage of CO on the surface could not be determined, suggesting that the coverage of adsorbed CO is very low. A low coverage of CO could be the reason why no ordered structure was determined in the CTR analysis. The effect of CO in electrolyte can be indirectly determined through changes to the relaxation of the

	Parameter	Ag(111) -1.0 V	Ag(111) -0.2 V	Ag(110) -1.0 V	Ag(110) -0.2 V	Ag(001) -1.0 V	Ag(001) -0.2 V
Metal layers	ε_{34} (Å)			0.006(3)	0.02(5)		
	ε_{23} (Å)			-0.014(2)	-0.037(6)		0.016(1)
	ε_{12} (Å)	-0.019(1)	-0.037(1)	-0.043(2)	0.075(5)	-0.019	-1.912
	σ_3 (Å)			0.08(7)			
	σ_2 (Å)			0.17(1)			0.016(1)
	σ_1 (Å)	0.117(2)	0.147(2)	0.312(5)	0.423(8)	0.118(2)	0.123(4)
O	θ (ML)	0.23(3)	0.65(3)		0.76(6)		1.0(1)
	d(Å)	2.75(7)	2.27(3)		2.17(4)		1.48(3)
	σ (Å)	0.15	0.15		0.15		0.3
Na^+	θ (ML)	0.39(2)	0.36(2)	0.49(5)	0.50(6)	0.21(5)	
	d (Å)	4.08(2)	3.09(3)	2.86(4)	3.16(9)	2.939(1)	
	σ (Å)	0.15	0.15	0.15	0.15	0.219(7)	
Error func	dE (Å)			5.0(1)	5.1(2)		
	Red χ^2	1.79	1.71	1.60	2.30	2.02	1.82

Table 6.11 Summary of best fit parameters to data on all three low-index Ag(*hkl*) surfaces in CO saturated 0.01 M NaOH + 0.09 M NaF electrolyte.

metal layers and of the electrolyte layering. A schematic representation of the interface structures is show in Figure 6.32 and a summary of the fit parameters is given in Table 6.11. The presence of CO has a significant effect on the relaxation of the metal layers on Ag(110). In comparison to the data in the absence of CO on Ag(110), at negative potential the presence of adsorbed CO induces a larger *inward* relaxation of the top metal layer, and at positive potential the *outwards* relaxation is slightly reduced. There are also small changes to the relaxation of the Ag(001) metal layers. The change in relaxation is due to the adsorption of CO at negative potential and at positive potential the difference in relaxation arises from the difference in the adsorbate metal bonding. A similar effect is reported on platinum surfaces, where the adsorption of CO on Pt(110) is inferred from the changes to the metal [166]. On Ag(111) there is no observed effect on the relaxation of the metal layers, although the roughness of the surface increases as the potential is scanned positive. CO seems

to have to have a larger effect on the electrolyte structure of Ag(111) and Ag(001) surfaces at positive potential. The most significant difference is the height of the adlayers at positive potential; in both cases the adlayers are much closer to the surface suggesting that CO is still adsorbed on the surface at this potential and has an effect on the nature of the bonding.

Oxygen

The effect of oxygen on the Ag(*hkl*)/alkaline interface was very subtle. At negative potentials on all three surfaces there was no effect due to the presence of oxygen. This is not surprising considering there is no adsorption of oxygen species at the negative limit. A schematic representation of the interface structures is presente in Figure 6.33 and a summary of the fit parameters to the structural models are given in Table 6.12. At positive potential there are some subtle changes to the interface structure. On Ag(001) and Ag(111) there are some changes to the electrolyte layering; the Ag-OH/O layer height is reduced and the cation layer is closer to the surface; although the relative distance between the OH and Na^+ layers remain the same. This implies that the OH^-/O layer is more strongly bound to the surface or that the adsorption sites are different. On Ag(110) there is almost no change to the electrolyte layering, only a slight increase in the OH^-/O layer which can be correlated to the bigger dip in intensity on the specular CTR. The presence of oxygen induces some small changes to the metal side of the interface on both Ag(001) and (110), small changes to the relaxation of the metal layers are observed, the relaxations of

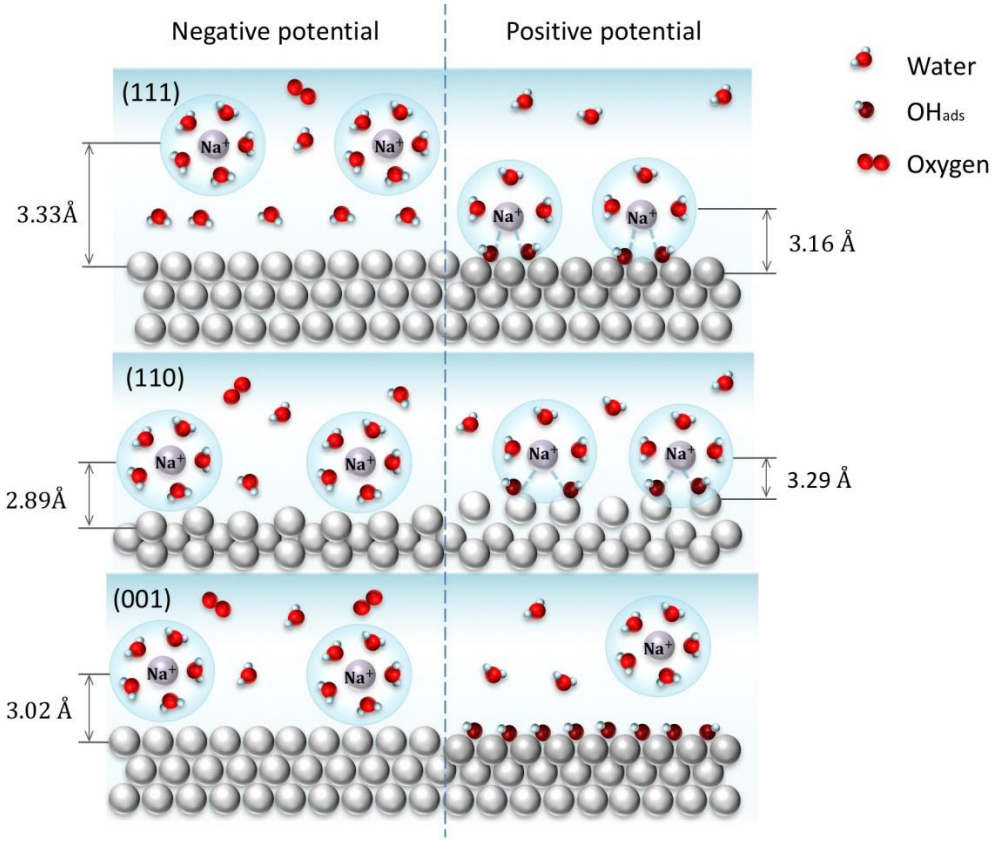

Figure 6.33 Schematic representation of the Ag(*hkl*)/alkaline interface in oxygen saturated solution, highlighting the structural differences between the two potential limits. At negative potential the double layer structure is governed by a field effect attraction; positively charged Na^+ cations redistribute at the interface to maintain electroneutrality at the interface. At positive potential OH is adsorbed on the surface, maintaining a negative charge, the Na^+ are stabilised through non-covalent interactions forming a compact double layer at the Ag(111) and Ag(110) interface. At the Ag(001) interface, OH is adsorbed, but no evidence of Na^+ ordering was identified by the structural model.

the top metal layers are reduced on both surfaces. On Ag(111) there is no disturbance to the metal, which is similar to the effect of CO. This is perhaps due to the close packed nature of the Ag(111) surface. Blizanac *et al.* find the kinetics of the ORR to increase in the order (001) ≤ (111) ≤ (110) [162], correlating this to the results presented in this chapter the presence of oxygen perturbs the (001) interface the most, both the metal and electrolyte layering, only the electrolyte layering changes in

	Parameter	Ag(111) -0.7 V	Ag(111) -0.1 V	Ag(110) -1.0 V	Ag(110) -0.2 V	Ag(001) -0.8 V	Ag(001) -0.2 V
Metal layers	ε_{34} (Å)			0.009(2)	0.021(3)		
	ε_{23} (Å)			-0.025(2)	-0.025(3)	-0.019(2)	0.001(1)
	ε_{12} (Å)	0.00	-0.039(4)	-0.029(2)	0.08(2)	-0.931	-0.025(1)
	σ_3 (Å)			0.145(5)	0.00		
	σ_2 (Å)			0.209(2)	0.00		0.051(5)
	σ_1 (Å)	0.114(4)	0.088(6)	0.33	0.48	0.092(3)	0.14(1)
O	θ (ML)		0.9(1)		0.87(6)		0.87(5)
	d(Å)		2.45(7)		2.25(3)		1.53(3)
	σ (Å)		0.15		0.15		0.3
Na^+	θ (ML)	0.35(3)	0.14(2)	0.66(5)	0.60(5)	0.32(3)	
	d (Å)	3.33(4)	3.16(2)	2.89(4)	3.29(6)	3.02(1)	
	σ (Å)	0.15	0.15	0.15	0.15	0.2	
Error func	dE (Å)			5.04(9)	5.29(1)		
	Red χ^2	2.1	1.65	1.89	1.75	1.9	1.88

Table 6.12 Summary of best fit parameters to data on all three low-index Ag(*hkl*) surfaces in O_2 saturated 0.01 M NaOH + 0.09 M NaF electrolyte.

the case of Ag(111) and on Ag(110) the changes are marginal. The largest effect of O_2 in solution corresponds to the surface with the least ORR activity, and interestingly the role of the cation does not appear to be significant in the structure of the Ag(001)/alkaline interface.This seemingly goes against the mechanism proposed by Stmcnik *et al*. [117] that the non-covalent interaction between cation and hydroxide leads to blocking of ORR active sites.

6.3 Conclusions

The double layer structure of the Ag(*hkl*) surfaces in alkaline electrolyte, in the underpotential oxide region, has been examined using SXRD measurements. The analysis has shown the layering in the electrolyte has a strong potential dependence; on all three surfaces there is a decrease in intensity on the specular CTR at potentials

where OH adsorption occurs. The effect is most pronounced on the Ag(110) surface where the specular CTR has a prominent oscillation. It is clear that scattering from electrolyte layering significant and it is necessary to include in the modelling of these systems in order to obtain a good fit and structural model. The results indicate that there is evidence of non-covalent bonding at the electrode/electrolyte interface on the Ag(111) and Ag(110) surfaces. This was not the case on the Ag(001) surface, the data was fit with one adlayer at both potentials indicating that the cations are not stabilised on this surface at positive potential, or the coverage is so small that the contribution to the scattering is negligible. Interestingly at negative potential on Ag(001) there is evidence of some in-plane ordering in the double layer which has not previously been observed, this shows the importance of *in situ* structural studies and in particular surface X-ray diffraction which does not disturb the double layer structure during measurements.

As the underpotential oxide region is where the ORR, CO adsorption and oxidation occur the study was extended to consider the effects of CO and O_2 on the interface structure. Although the effects of these gases were very subtle on all surfaces, especially in the presence of O_2, there were some interesting results to consider. Mainly, the presence of CO and O_2 in electrolyte affects the layering at the interface, and perturbs the relaxations of the metal surfaces. CO is adsorbed on all three (*hkl*) surfaces, although the only surface to exhibit the suppression of electrooxidation of Ag is the Ag(110) surface, indicates that adsorption of CO is also dependent upon the geometry of the surface and highlights the need for single crystals to determine the origin of this process.

To gain a thorough understanding of the interface it would be advantageous to apply other techniques which have a chemical sensitivity to give greater confidence to the models, and determine the nature of the changes identified by the structural models. For example, spectroscopic techniques such as FTIRS which could determine the element and the type of bond present at the interface. It would also be advantageous to repeat the CV measurements in a specially designed cell.

7 Dynamics of potential-driven structural changes at the electrochemical interface

7.1 Introduction

The dynamics of processes at the electrochemical interface are vitally important to a number of technologies such as energy conversion devices - fuel cells and batteries, and electrodeposition for nanotechnology and corrosion. Understanding the dynamics of an electrochemical system on a fundamental level allows for predictions scaling up to industrial applications. Single crystal electrodes, which have a well-defined atomic arrangement and specific adsorption sites, are ideal candidates for fundamental studies and the field of electrochemistry has greatly

profited from their study. Despite this progression the dynamics of potential-induced structural rearrangement are still not well understood.

The development of modern electrochemical methods to obtain a dynamic picture of events at the solid/liquid interface represents one of the most important contemporary frontiers of research in electrochemistry; *in situ* structural techniques must be employed to correlate electrochemical processes with structural changes at the electrochemical interface. *In situ* STM has been used to determine the kinetics of the Au surface reconstructions [150–153], electrodeposition [169], and desorption processes [50]. However STM is time resolution limited by the scan rate of the tip, and mass transport limited due to shielding effects from the tip which can affect the local growth rates in the scan area [51]. The problem of time resolution can be overcome by using high speed STM [170], however the interference of the tip is an integral problem with STM. These issues can be overcome by using SXRD techniques, as the probe does not interfere with the measurements – in this case (although for some systems the X-rays have been shown to interfere, such as in reference [52]). In the last few decades the improved brilliance of synchrotron sources has enabled such work and several time resolved studies of electrochemical systems have been reported [158-168]. In this technique the scattered intensity is monitored, at a specific reciprocal lattice point, as a function of time during a potential step measurement whilst simultaneously measuring the current response (current transients). The point in reciprocal space is chosen for its sensitivity to a particular surface property, such as relaxation of the surface, commensurate adlayer adsorption or the fact that new scattering arises due to the formation of a superstructure. From the change in intensity, so called ‘intensity transients’, the kinetics of specific structural changes can be determined. These can then be linked

with electrochemical processes determined from the current response. Initial studies which utilised this technique were carried out in the conventional X-ray electrochemical cell, which was later found to be limited due to the thin layer configuration which was rate limiting due to the RC drop [60]. Development of a 'droplet cell', in which all three electrodes are in close proximity, allowed greater potential response of 50 μs [57]. The focus of the studies has been metal deposition [161,165,166] and dissolution [13,163], and the results have demonstrated that the charge transfer process is much faster than the development of long range crystalline order.

Although the metal electrode side of the interface has been the focus of attention, recently there has been progress in understanding the electrolyte side of the interface [23,24,117,119,170], as discussed in chapter 6. Nakamura *et al.* [58] presented the first time resolved X-ray diffraction study to focus on the electrolyte side of the interface. The study determined the structural dynamics of the double layer during capacitive charging and discharging of Cs^+ at the Ag(001)/c(2x2)-Br interface. The double layer charging is specifically due to changes in the reorganisation of ionic species and reorientation of water molecules at the interface, i.e. no electron transfer between the electrode and electrolyte. The capacitive charging/discharging processes occurred on a millisecond timescale comparable to the complementary current transients.

SXRD measurements in chapter 6 showed sensitivity to the ordering in the electrolyte layers at the Ag(*hkl*)/0.01 M NaOH + 0.09 M NaF interface and confirmed the cation participation in the so-called 'double layer' structure, which is consistent with the study by Lucas *et al.* in 0.1 M KOH. In this chapter time dependent studies of the electrolyte layering process are presented, complimented by

metal reconstruction and metal deposition systems as a comparison of timescales for different structural processes. The Ag(111) electrode in alkaline electrolyte system offers a unique insight into the electrochemical interface as there is no significant restructuring of the metal surface (i.e. reconstruction), only a small *inward* relaxation, thus it is possible to separate structural changes in the metal from those that occur in the electrolyte. The Au(111) surface does, however, reconstruct; and so the kinetics of mass transport of the surface atoms and the subsequent structural ordering can be probed. In contrast to this, studying the underpotential deposition (UPD) process of Ag on Au(111) enables us to study the mass transport of ions through the electrolyte to the surface.

7.2 Experimental

The Ag(111), and Au(111) crystals (99.999%) obtained from Mateck (miscut < 0.1º) were prepared by Ar^+ sputtering and thermal annealing cycles in UHV until a sharp LEED pattern was obtained, Ag(111)-(1×1) and Au(111)-$\left(p \times \sqrt{3}\right)$. The Ag(111) sample was transferred from UHV to the electrochemical cell in a glove bag under inert atmosphere to protect the surface from oxidising. After UHV preparation, the Au(111) crystal was flame annealed prior to transfer to the electrochemical droplet cell. The electrochemical cell consists of a Teflon cross-piece and quartz capillary, a droplet of electrolyte is suspended from the capillary forming a droplet covering the sample surface (setup is discussed in detail in chapter 3). Platinum wire is used as the counter electrode for Ag(111) and Au wire for Au(111), which formed a ring around the droplet, this additionally acted to stabilise the droplet. The outer chamber was continuously purged with nitrogen to keep the electrolyte drop

deoxygenised and to protect the sample surface from oxidizing. The reference electrode is Ag/AgCl, to which all potentials are referenced. X-ray measurements were performed on the ID03 beamline at the European Synchrotron Radiation Facility, ESRF. Incident X-ray beam energy of 24 KeV was required to penetrate the electrolyte droplet. The Ag(111), and Au(111) surfaces were indexed to a conventional hexagonal unit cell for fcc(111) surface that is defined such that the surface normal is along the $(0, 0, L)_{hex}$ direction and the $(H, 0, 0)_{hex}$ and $(0, K, 0)_{hex}$ vectors lie in the plane of the surface and subtend 60°. The units for H, K and L are $a^* = b^* = 4\pi/\sqrt{3}a_{Ag}$ and $c^* = 2\pi/\sqrt{6}a$, where a is the nearest-neighbour distance.

MuSSTcard set up

Time dependent measurements were taken using a lock-in amplifier which is used to extract small signals from background to probe the structural ordering as a function of the frequency of the potential changes. The scattered X-ray beam is detected by a photodiode, working in photo-voltaic mode. The very small current produced by the diode is then amplified by a current to voltage amplifier and also filtered before being fed into the input of the lock-in amplifier. A signal generator provides the reference frequency for the lock-in amplifier and also controls the modulation of the surface, via the potentiostat. The output of both the potentiostat, and the lock-in can be fed into a Multipurpose Unit for Synchronisation Sequencing and Triggering (MUSST) card. The card can be integrated by SPEC [26], the beamline control system at the ESRF. A schematic of the set-up is shown in Figure 7.1.

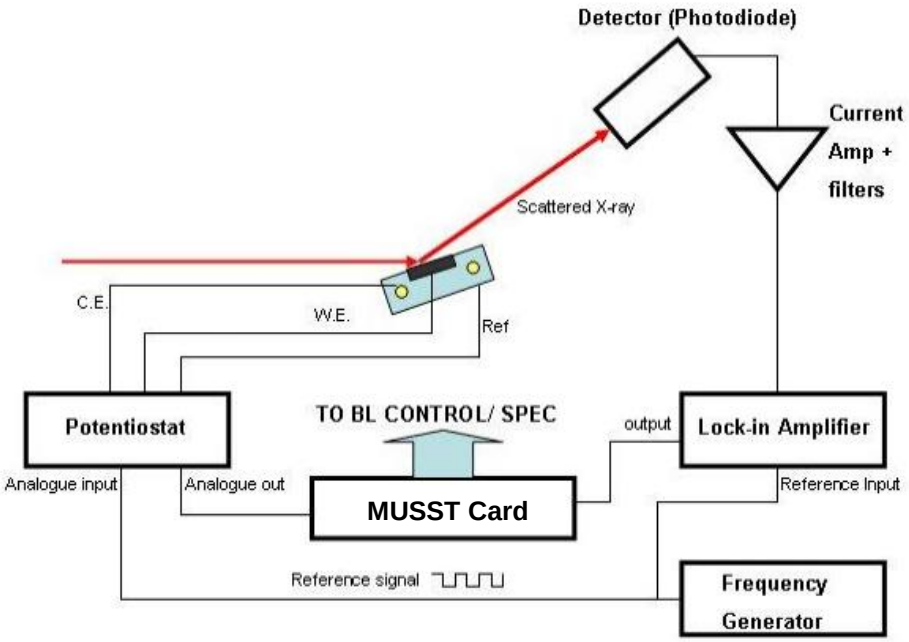

Figure 7.1 Schematic of the MUSST card setup. Working mode is discussed in the text.

Time-dependent measurements

The potential was stepped between limits at a reference frequency for numerous cycles. The intensity was monitored at a specific point in reciprocal space whilst simultaneously measuring the current response; this is shown schematically in Figure 7.2. After the experiment the first point of each potential step cycle was set to time t=0, and the cycles were binned and averaged for both potentials to improve the signal to noise ratio. This resulted in an intensity transient, and current transient of exponential forms for each potential. Appropriate exponential line shapes were fit to the data to obtain the time constants for the structural and electrochemical processes. Errors on the X-ray intensity data points were taken as $\sqrt{N}$. Exponential curves were fit using a Levenberg–Marquardt algorithm.

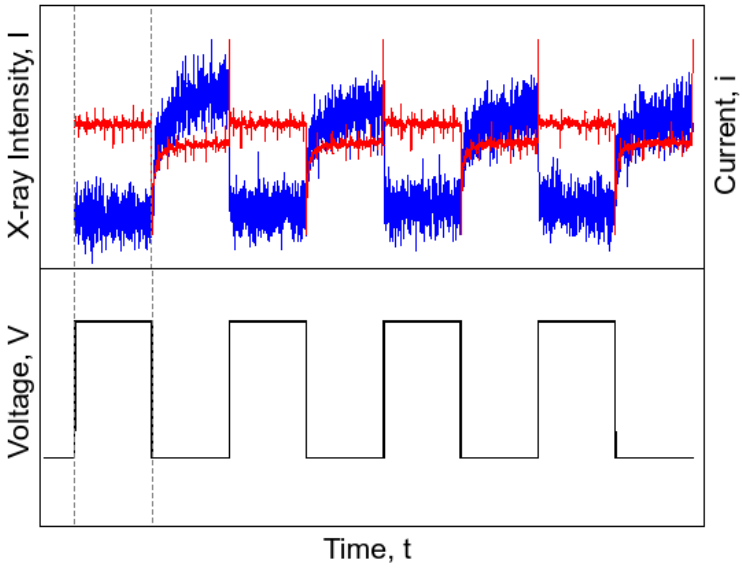

Figure 7.2 Applied voltage signal (shown in the lower section of the figure) to the electrode/electrolyte interface is stepped between two potential limits at a reference frequency. The change in scattered X-ray intensity, at some reciprocal lattice point, and change in current are measured simultaneously. The cycles are averaged to give better statistics for the resulting intensity and current transients.

7.3 Results and discussion

7.3.1 Ag(111)

The current model of Ag(111) in 0.1 M KOH electrolyte from SXRD, determined by Lucas *et al.* [23], indicates that at negative potential there is a presence of a hydrated K^+ cation layer located at a distance of 4.1 Å from the Ag surface. The applied potential induces a strong electric field at the interface which pulls the positively charged cations in close proximity to the surface to equalise the charge at the electrode at the OHP. At positive potential OH^- adsorbs on the surface and stabilises the hydrated K^+ cations through a non-covalent (van der Waals)

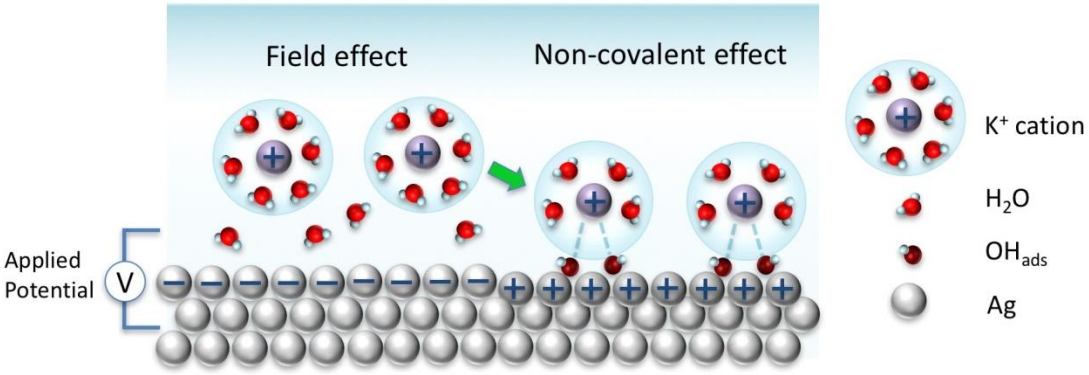

Figure 7.3 Structural changes in the electrochemical double layer at the Ag(111) electrode surface in 0.1 M KOH electrolyte. A hydrated K^+ cation layer at the negatively charged surface, and hydrated K^+ cations stabilised by OH_{ads} at positive potential.

interaction forming a compact double layer structure in which the Ag-K^+ distance is reduced to 3.6 Å, this is shown schematically in Figure 7.3. At the metal side of the interface, the top atomic layer has a small *inwards* relaxation at both potentials. At negative potential (E=-1.0 V) the relaxation is 0.7 % of the interatomic layer spacing ($d_{(111)}$ = 2.36 Å), which increases to 1.1 % at positive potential due to the adsorption of OH. The model indicates that scattering from electrolyte layering can be separated from the metal as there are no changes in the surface electron density of the metal; only a small *inward* relaxation of the top metal layer was needed to fit the data, indicating that the changes at the specular CTR position can be attributed primarily to ordering in the electrolyte. Any changes in the non-specular position are due to the response of the metal to changes in the electrolyte, such as relaxation of the surface atoms.

In this chapter, through time dependent measurements, the structural dynamics of the restructuring of the double layer at the Ag(111)/0.1 M KOH interface are determined. Intensity and current transients were measured

simultaneously by applying a square wave potential to the system, in which the potential is stepped between two limits (E=-0.2 V and E=-1.0 V) at a reference frequency of 0.05 Hz. The step to -0.2 V is associated with the adsorption of OH^- and non-covalent interaction between OH_{ads} and the K^+ cations. And the reverse step to -1.0 V is attributed to desorption of OH^-, and stabilisation of K^+ cations in the OHP. The intensity transients were measured at several reciprocal lattice points which are sensitive to specific structural features; these can be seen in Figure 7.4. The anti-Bragg position on the specular CTR, (0, 0, 1.5), which is sensitive to any layered ordering in the electrolyte and changes in electron density of the electrode surface, and the (0, 1, 0.5) a position on the non-specular (0, 1, L) CTR sensitive to adsorbed species commensurate with the crystal lattice, and (1, 0, 3.7) a position on the non-specular (1, 0, L) CTR sensitive to changes in the relaxation of the surface. Time constants obtained from the intensity transients and current are summarised in Table 7.1 and Table 7.2 respectively.

At (0, 0, 1.5) both of the intensity transients at -0.2 V and -1.0 V in figure 2 can be described by a simple first order exponential function given by equation (7.1):

$$f(x) = y_0 + Ae^{\left(\frac{-t-t_0}{\tau}\right)} \tag{7.1}$$

where y_0 is the background, A is the amplitude and τ is the time constant.

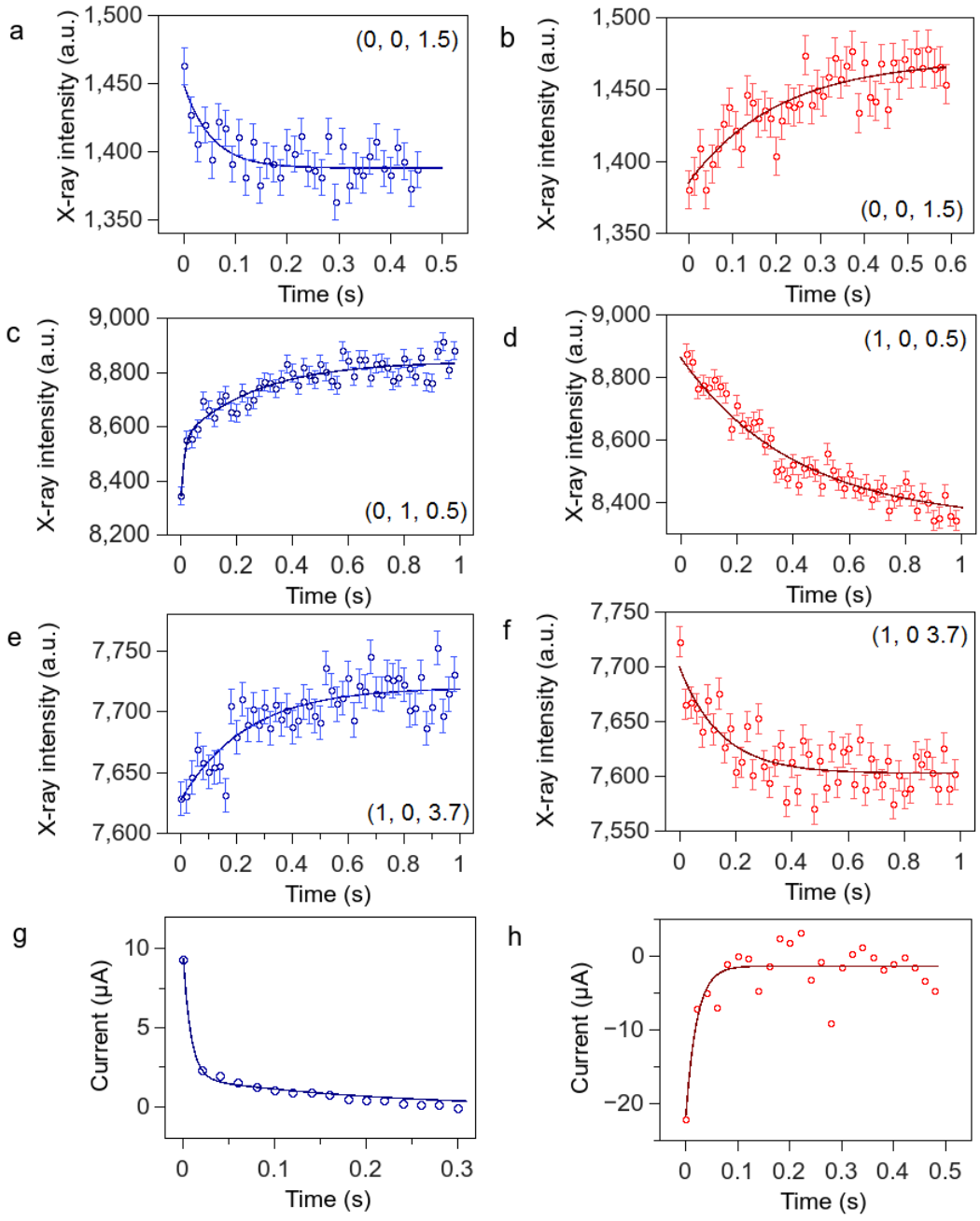

Figure 7.4 Intensity and current transients of the Ag(111)/0.1 M KOH interface measured after the step to -0.2 V (blue) -1.0 V (Red) (a) (b) Intensity transient at (0, 0, 1.5) position on the specular CTR. Only the first ~0.5 seconds at each potential is shown so that the growth and decay of intensity are clearly visible (c) (d) Intensity transients at the (0, 1, 0.5) position on the non-specular (0, 1, L) CTR. (e) and (f) (1, 0 3.7) (g) and (h) current transients.

On stepping to -0.2 V the time constant is 0.05 seconds for the structural changes. This is quite different to the time constants determined for the current transients. A two term exponential function, of the form

$$I(t) = y_0 + A_1 e^{\left(\frac{-t-t_0}{\tau_1}\right)} + A_2 e^{\left(\frac{-t-t_0}{\tau_2}\right)} \quad (7.2)$$

where y_0 is the background, $A_{1,2}$ are the amplitudes and $\tau_{1,2}$ are time constants.

gave the best fit to the current transient of the step to -0.2 V, a which requires two time constants where τ_1=0.008 s and τ_2=0.19 s. This suggests that the step to positive potential is a two-step process in terms of the charge transfer. This result indicates that there is an initial charge transfer at the interface which is quite fast, occurring on the millisecond time scale. This process can be attributed to the adsorption of OH on the surface. The second time constant is much slower, which can be assigned to the transfer of K^+ to the compact double layer in a non-covalent interaction with the OH. Interestingly though, the structural rearrangement of the electrolyte layer occurs on a much quicker timescale (τ=0.05 s) than for the current transients which suggest the slow kinetics of a charge transfer process at the interface. This could be explained by the cation-OH complexes formed at the interface. There appears to be no distinction between the adsorption of OH and the movement of cations through the double layer from the intensity transients, a two term exponential does not fit the data which implies that the structural kinetics is dominated by the mass transport of ions (the rate at which ions move from the bulk electrolyte to area near to the electrode) the surface.

Reciprocal lattice position	Potential (V)	τ_1 (s)	τ_2 (s)
(0, 0, 1.5)	-0.2 V	0.05 ± 0.01	
	-1.0 V	0.18 ± 0.02	
(0, 1, 0.5)	-0.2 V	0.009 ± 0.008	0.24 ± 0.04
	-1.0 V	0.37 ± 0.02	
(1, 0, 3.7)[1]	-0.2 V	0.24 ± 0.05	
	-0.7 V	0.19 ± 0.03	

Table 7.1 Time constants for different reciprocal lattice points at -0.2 V and -1.0 V.

Potential (V)	τ_1 (s)	τ_2 (s)
-0.2	0.008 ± 0.001	0.19
-1.0	0.004 ± 0.001	-

Table 7.2 Current transient time constants at steps to -0.2 V and -1.0 V

The intensity time constant determined for the reverse process, the step to -1.0 V, is 0.18 s which is in contrast to the current transient which occurs on a much shorter timescale of 4 ms. The current response is related to the desorption of OH, which is of a similar timescale to the discharging of the interface determined by Nakamura *et al.* [58] whereas the intensity transients are probing the restructuring of the double

[1] **There was an issue with data measured at (1, 0, 3.7) between the potential limits -0.2 V and -1.0 V, instead the data presented here is between -0.2 V and -0.7 V. The XRVs suggest there are no structural differences between -1.0 V and -0.7 V at this reciprocal lattice position.*

layer. This shows that the kinetics of the structural ordering of the layers is slower than the charge transfer process at this potential. The intensity time constant is much slower than the positive step. This implies that once the interaction between OH and K^+ is formed, it is more difficult to reverse the process i.e. transfer of the cation to the outer part of the double layer. This could be explained in terms of the driving forces of the double layer reconstruction at the interface; at negative potential the restructuring is driven by a field effect at the interface, whereas at positive potential there is an adsorption process and the cations are stabilised by non-covalent interactions.

The intensity transients at (0, 1, 0.5) and (1, 0, 3.7) are associated with the response of the metal. The XRVs at these positions in chapter 5, and reference [23] for the Ag(111)/alkaline interface indicate that the changes are very small, which was confirmed through the CTR models. The time constants at both -0.2 V and -0.7 V for the (1, 0, 3.7) position occur on a very similar time scale (~0.2 s). The change in intensity at this position is directly related to the relaxation of the surface. The kinetics of the relaxation appear to be unaffected by the direction of the potential step. The data at (0, 1, 0.5) is a bit more ambiguous. The scattered intensity at this position is primarily sensitive to commensurate ordering from adlayers; although there was no evidence of in-plane ordering of $OH_{ads,}$ and it was not required in the model to obtain a good fit to the data. This does not completely rule out the possibility of ordering, as scattering from OH is relatively weak and would only have a small contribution to the in-plane scattering. The intensity change could instead be due to relaxations in the metal; however, it is difficult to say for certain. Interestingly, the best fit to the data at -0.2 V was using a two-term exponential where τ_1 is on the same time scale as τ_1 for the current transient at this potential and

the second term has the same time constant (τ = 0.24 s) as the one determined for (1, 0, 3.7) . This implies that the first structural process identified could be due to adsorption of OH on the surface, and the second is due to the metal response i.e. relaxation of metal layers.

The response of the electrolyte layering is faster at both potentials than it is for the changes in the metal; indicating that the movement of metal atoms is a much slower process than structural rearrangement of the electrolyte. The study by Nakamura *et al.* [58], *which investigates the movement of* Cs^+ *cations at the Ag(001)*/c(2 × 2)-Br interface, indicates that the charging and discharging of the double layer occurs on very short timescales, milliseconds. Our study highlights the differences in kinetics with the introduction of adsorption processes as the electrochemical kinetics of the double layer at the Ag(111) interface are much slower than the Ag(001)/Alkaline system. The two time constants determined for the Ag(001)/Alkaline interface are related to the reorientation of water in the double layer and the movement of Cs^+ in the double layer. The transfer of Cs^+ is determined to be a slow kinetic process which is in agreement with our interpretation of the current transients.

7.3.2 Au(111)

The Au(111) surface is known to reconstruct in ultra-high vacuum under certain preparation conditions. The reconstruction survives transfer to the electrochemical environment, and can be controlled by the applied potential; the reconstruction can be lifted at positive potential or induced at negative potential. During the reconstruction process, the surface undergoes a uniaxial compression of the top layer of gold atoms which causes a lateral rearrangement of atoms to a

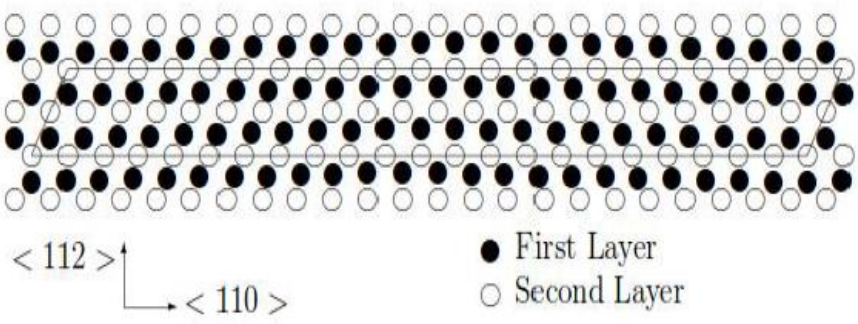

Figure 7.5 Schematic of the $(23 \times \sqrt{3})$ reconstruction of the Au(111) surface reprinted from reference [66] with permission.

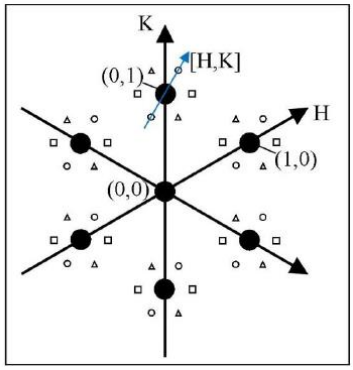

Figure 7.6 Schematic of in-plane diffraction pattern for the $(23 \times \sqrt{3})$ reconstruction. The solid circles correspond to the scattering from the bulk Au(111). The open symbols arise due to scattering from the $(23 \times \sqrt{3})$ reconstructed phase with three rotationally equivalent domains.

reconstructed $(p \times \sqrt{3})$ unit cell, shown schematically in Figure 7.5, such that every *pth* atom is in registry with an underlying bulk Au atom. This is characterised by additional diffraction spots in the surface plane of reciprocal space, in hexagonal arrangement around the CTR. This is shown schematically in Figure 7.6. Figure 7.7 shows the scattered intensity measured along the [1 1 0] direction through the (0, 1,

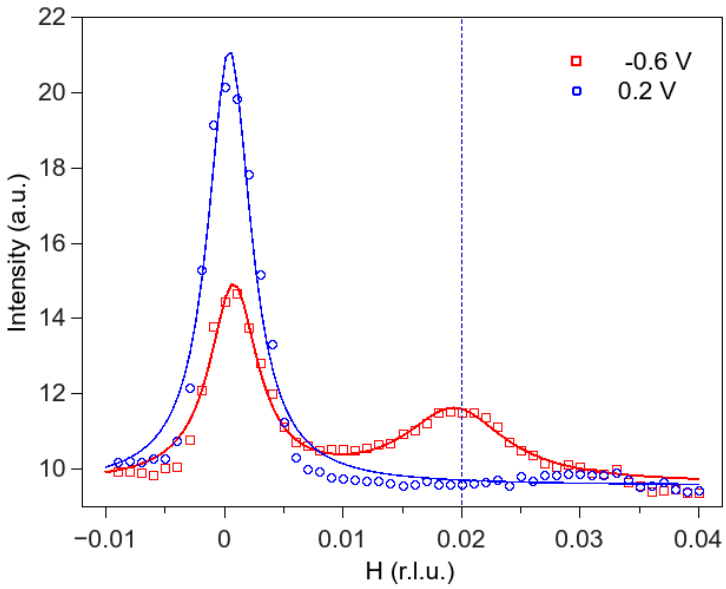

Figure 7.7 In-plane X-ray diffraction from the reconstructed Au (111) surface. The blue data corresponds to the unreconstructed (1x1) phase at 0.2 V. The red data is from the reconstructed surface, an additional peak is seen at (0.02, 1.02, 0.5).

0.15) reciprocal lattice position (the direction of the scan is indicated by the blue arrow in Figure 7.6. The blue data was taken at 0.2 V, only one peak is visible at H=0, K=1, this indicates that the surface structure is (1 x 1), the same symmetry as the bulk. At -0.6 V the peak at (0, 1, 0.5) is much smaller and there is an additional peak at H=0.02, this is consistent with the formation of the $(p \times \sqrt{3})$ surface at negative potential. The stripe separation, p, can be determined from the in-plane diffraction scans by p=1/(2ΔH) where ΔH is separation between the CTR peak at H=0 to the position of the reconstruction peak. In N_2 purged 0.1 M LiOH p=25.0 at -0.6 V. The correlation length can be determined by fitting a double Lorentzian lineshape to the curves.

To characterise the system the potential dependence of the reconstruction was determined by X-ray voltammetry shown in Figure 7.8. XRVs were taken at (0, 1, 0.5) an anti-Bragg position on the (0, 1, L) CTR which is sensitive to the in-plane

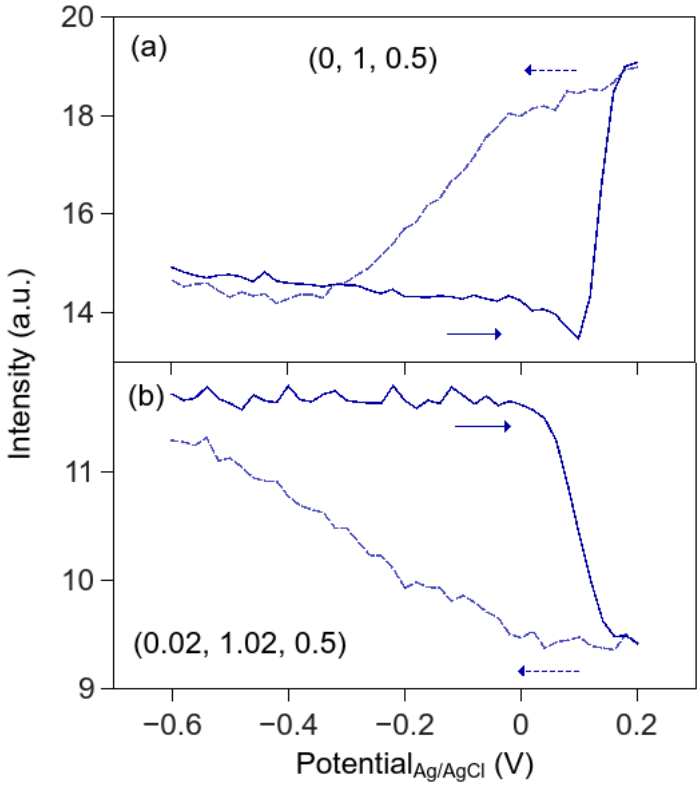

Figure 7.8 X-ray voltammetry at the non-specular CTR (0, 1, 0.5) and the reconstruction peak (0.02, 1.02, 0.5).

ordering of the (1×1) termination of the surface, and at (0.02, 1.02, 0.5) a position which is sensitive to scattering from the reconstruction. At (0, 1, 0.5) when the potential is scanned cathodically there is a decrease in scattered intensity at ~0 V which is due to the loss of the (1×1) structure and coincides with an increase in intensity at the reconstruction position at this potential, which is the potential where the reconstruction begins to form. When the potential is scanned anodically the lifting of the reconstruction does not occur until 0.1 V, where there is a sharp rise in intensity. The dip in intensity before this point was attributed to increased surface disorder during the phase transition by Wang *et al.* [174]. The measurement at (0.02, 1.02, 0.5) shows that at ~0 V the intensity begins to increase corresponding to the

formation of the reconstructed phase. This steadily increases until -0.6 V. On the reverse sweep, the reconstruction is stable until ~ 0 V where there is a sharp decrease in intensity corresponding to the lifting of the reconstruction. Between 0.2 V and 0 V the intensity at the reconstruction position is level, whereas the intensity is already decreasing at the (0, 1, 0.5) position, this is attributed to the initial nucleation, before the reconstruction begins to order. The XRVs have a large hysteresis indicating that the kinetics of the phase transformations are slow.

In order to determine the dynamics of the $(1 \times 1) \leftrightarrow \left(p \times \sqrt{3}\right)$ phase transition intensity and current transients were measured at several reciprocal lattice positions, shown in Figure 7.9. The reconstruction position (0.02, 1.02, 0.5) and (0, 1, 0.5) to determine the time constant for the ordering and lifting of the reconstruction and at the anti-Bragg on the specular (0, 0, 1.5), which is sensitive to changes in surface density along the surface normal. The changes in intensity at the two non-specular positions are correlated to the ordering of the two phases. The potential was modulated at a reference frequency of 5 mHz, between 0.2 V, corresponding to the (1×1) unreconstructed surface and -0.6 V where the surface is reconstructed.

The intensity, and current, was recorded simultaneously every 0.02 seconds over 8 cycles. The time constants from the intensity and current transients are summarised in Table 7.3 and Table 7.4, respectively. The step to positive potential, which corresponds to the lifting of the reconstruction, the intensity transients decay exponentially with time and were all fit with a first order exponential function in equation 7.1. The step to positive potential is faster than the reverse step at all three reciprocal lattice positions.

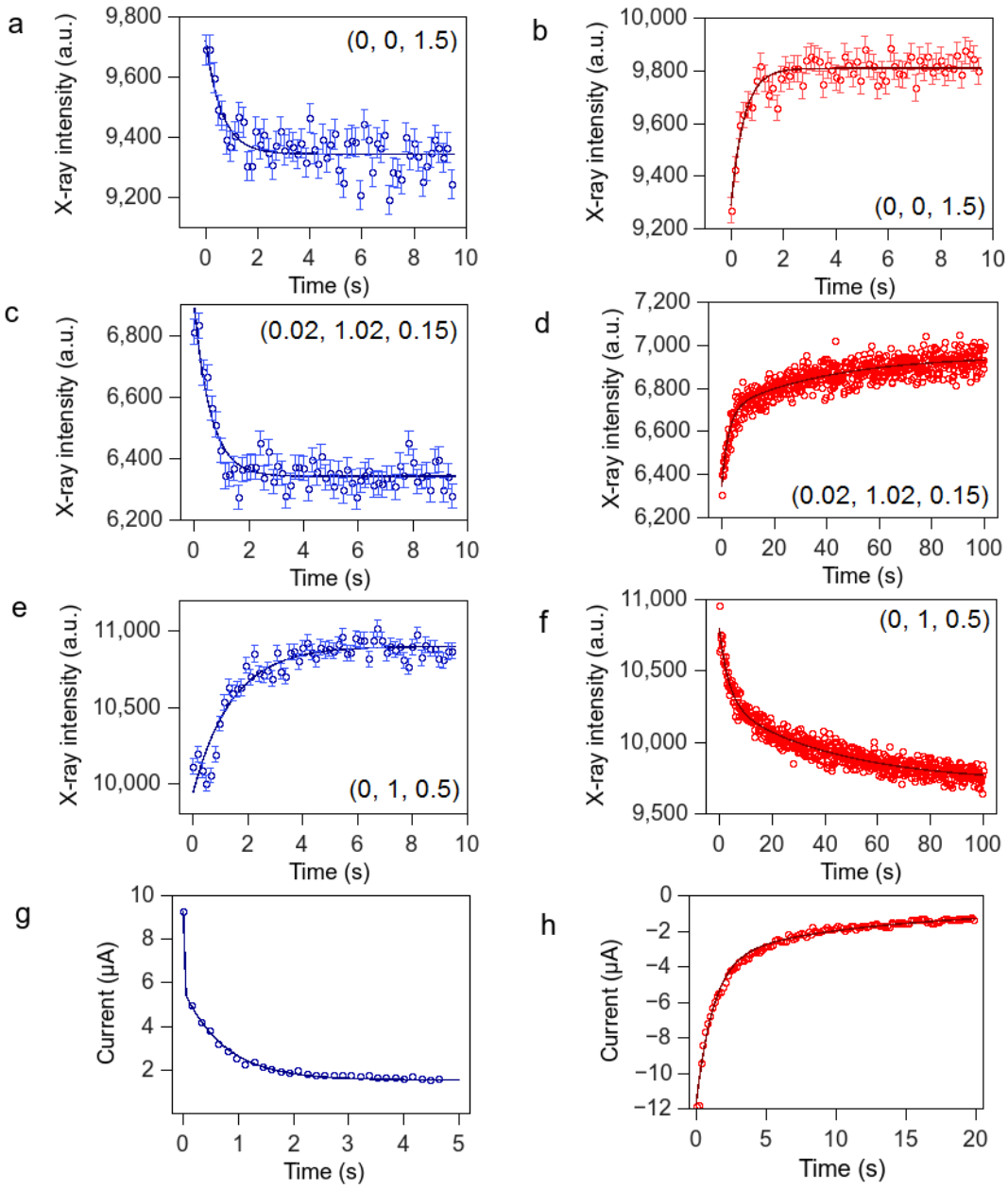

Figure 7.9 Intensity and current transients of Au(111) phase transition. Potential is stepped from 0.2 V (1 × 1) phase (blue), to -0.6 V reconstructed phase (red). (a) (b) (0, 0, 1.5) (c) (d) reconstruction position (0.02, 1.02, 0.15) (e) (f) (0, 1, 0.5) on the non-specular CTR sensitive to the bulk termination of the surface, (g) (h) current transients.

Reciprocal lattice position	Potential (V)	τ_1 (s)	τ_2(s)
(0, 0, 1.5)	0.2 V	0.58 ± 0.11	-
	-0.6 V	0.81 ± 0.11	-
(0.02, 1.02, 0.15)	0.2 V	0.64 ± 0.06	-
	-0.6 V	2.61 ± 0.32	39.59 ± 5.54
(0, 1, 0.5)	0.2 V	1.67 ± 0.09	-
	-0.6 V	3.75 ± 0.38	43.38 ± 4.26

Table 7.3 Time constants for different reciprocal lattice positions at 0.2 V and -0.6 V.

Potential (V)	τ_1 (s)	τ_2 (s)
0.2	0.07 ± 0.01	0.86 ± 0.04
-0.6	1.2 ± 0.03	11.3 ± 0.4

Table 7.4 Time constants determined by current transient. Steps to 0.2 V and -0.6 V.

The (0, 0, 1.5) position is sensitive to changes in surface density. The time constants at this point give the kinetics for the mass transport of excess surface gold atoms into the top surface layer, and is independent of ordering. The time constants are the same order of magnitude at both potentials, however, the time constant at 0.2 V is slightly faster indicating the kinetics of the mass transport of Au atoms out of the surface are faster than the reverse process. The time constant at (0.02, 1.02, 0.5) at 0.2 V describes the timescale that the $(p \times \sqrt{3})$ ordered surface is lost, which is

consistent with the time constant for (0, 0, 1.5); which is a measure of mass transport. This indicates that the reconstruction is lost with the mass transport of the surface atoms out of the plane. The time constant, 0.64 s, is much faster than found

in previous thin-layer cell measurements [174] of 2-3seconds, which proves the time limitation of the thin-layer cell configuration**.** The time constant at (0, 1, 0.5), sensitive to the (1×1) terminated surface, is slightly longer at 1.7s which means that although the reconstruction is lost, the surface requires an extended time to reorder into the (1×1) phase. The X-ray transients for the negative step to -0.6 V are more complicated requiring a second order exponential fit, of the form of equation (7.2), to the data which uses two time constants with the exception of the specular position which was fit by equation (7.1). This indicates that the reconstruction forms by a two-step process. The time constants determined for the first process at the two non-specular positions are between 2-4 seconds, which is much longer than the mass transport kinetics for the specular position. This is explained by the atoms organising into nucleation points. The nucleation of gold atoms is followed by a much slower ordering to the $(p \times \sqrt{3})$ occurring on the timescale of ~ 40 seconds. The intensity continues to change beyond this and does not reach saturation during the time of the measurement. This is consistent with previous measurements which find the reconstruction can take up to 120 seconds to complete [174].

The current transient for the negative step was also fit with equation (7.2), however the time constants are on a much shorter time sale τ_1=1.2 and τ_2=11 seconds than those determined from the intensity transients. The current transient at 0.2 V is of a similar order of magnitude to the kinetics of the mass transport. The results show

that although the charge transfer process is relatively fast, the structural rearrangement and ordering of the Au atoms requires a much longer timescale.

It would be interesting to compare the time constants in the presence of CO as it has been found to change the dynamics of the reconstruction [178]. Upon adsorption of CO there is found to be a partial lifting and a change in the lateral compression of the reconstructed surface.

7.3.3 Ag UPD on Au(111)

The deposition and dissolution of a metal on a foreign metal surface is important for many industrial applications such as manufacture of thin films, corrosion and electroplating. The control of deposition techniques is important for designing electrodes for integrated circuits and core-shell nanoparticles.

Underpotential deposition, (UPD), provides a way in which deposition of a metal can be finely controlled. UPD is a specific type of adsorption phenomena whereby a monolayer of a metal (M) is deposited on a foreign metal substrate (S) at potentials positive of the Nernst potential for bulk metal deposition. The violation of the Nernst equation 2.8 (the Nernst equation is discussed in section 2.2.1 Electrode Reactions) is permitted when the M-S interactions are stronger than the S-S bonds; which make the UPD process favourable [179]. The UPD process is self-limiting; once a monolayer has been formed deposition is terminated. However, there are some systems where M-S interactions are sufficiently strong enough to allow the formation of a bilayer at potentials positive of the onset of bulk deposition [180]. The UPD phenomena is of great interest as it allows precise control over the coverage and structure of a metal layer, and it is a fully reversible process. Understanding

these low growth rates is of vital importance for understanding the growth mechanisms and structure of the metal layer.

The processes involved in the formation of a UPD layer are represented by the schematic diagram shown in Figure 7.10. Solvated M_{Sol}^{n+} ions move from the bulk electrolyte to the double layer region where they lose their solvation shell and there is electron transfer from the substrate to the metal ions forming a S-M bond. UPD atoms form a strong bond i.e. adsorbed atoms are fully discharged. The UPD process is visible in CVs by characteristic deposition peaks in the cathodic scan, and corresponding stripping peaks in the reverse scan. The charge transfer during adsorption can be directly determined from integrating the area of the peak from which the coverage can be determined.

Apart from M-S interactions the structure and kinetics of the UPD layer is also dependent upon other factors such as coadsorbing anions, and the geometry of the metal surface. A more in depth discussion and theoretical considerations can be found in references [23–25].

Silver UPD on Au(111) is one of the few systems where the M-S interaction is strong enough to allow the deposition of up to a bilayer. It is a well-defined system and there have been several studies [174,176], the deposition of Ag can be finely tuned with potential control with regimes of monolayer, bilayer and bulk deposition [180]. The UPD process is fully reversible over the monolayer/bilayer range This ability to control the coverage provides a model system for fundamental studies of the UPD process; to investigate deposition and desorption dynamics. The system also has importance for Au-Ag core-shell nanoparticles [184]–[187]. The nanoparticles have shown enhanced antibacterial activity [183], and improved catalytic activity

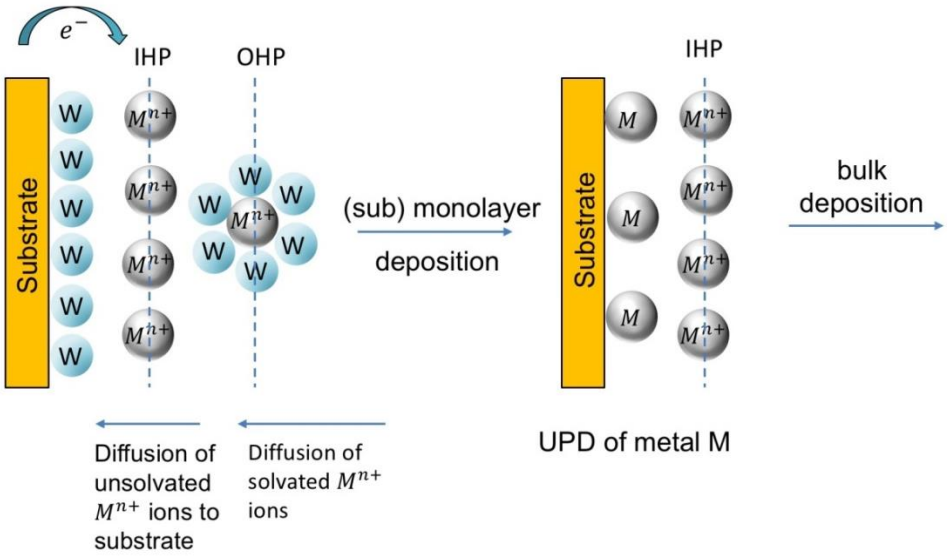

Figure 7.10 schematic representation of the UPD of a metal M^{n+} on to a foreign substrate. Figure is adapted from [181]. Water molecules are represented by the blue circles labelled 'W'.

[184] compared with mono-metal surfaces any alloy nanoparticles.

Figure 7.11 shows the cyclic voltammetry of the Au(111) electrode in 0.05 M H_2SO_4 + 1 mM Ag_2SO_4 at a sweep rate of 5mV/s. X-ray voltammetry was measured at 3 reciprocal lattice positions at (b) the anti-Bragg on the specular CTR (0, 0, 1.5), a position sensitive to any layered ordering at the interface (c) (1, 0, 3.7) a positionon the (1, 0, L) non-specular CTR which is sensitive to relaxation at the interface and (d) (0, 1, 0.5) an anti-Bragg position on the (0, 1, L) CTR sensitive to adsorbed structures commensurate with the Au(111) surface.

There are three cathodic peaks C1, C2 and C3 which are due to the deposition of Ag. These peaks can be related to structural changes highlighted by changes to the XRV. C1 is attributed to the deposition of a partial monolayer which corresponds to a decrease in intensity at all three reciprocal lattice positions. C2 is assigned to the further deposition of Ag, this is complemented by a further decrease in intensity on

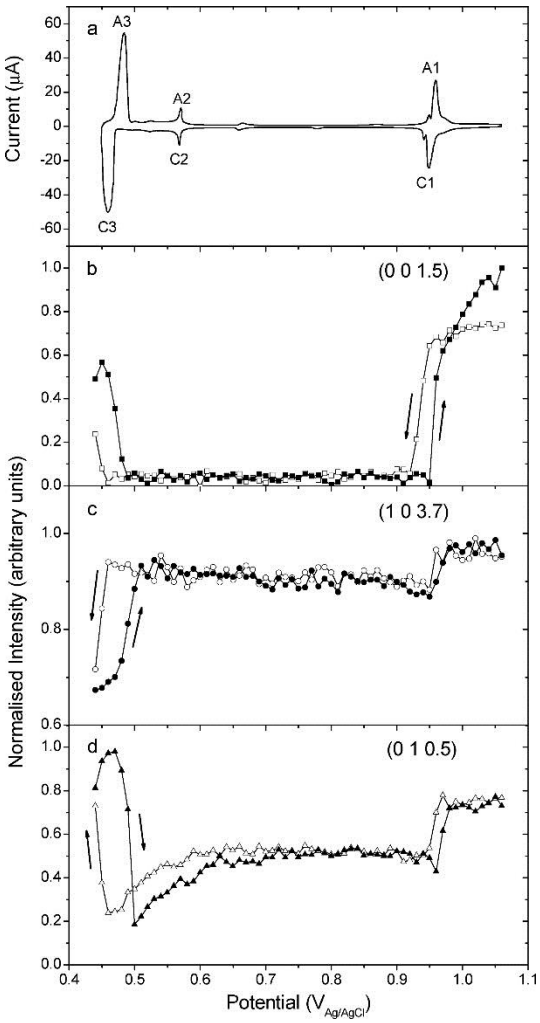

Figure 7.11 (a) Cyclic voltammetry of Au(111) in 0.05 M H_2SO_4 + 1 mM Ag_2SO_4 recorded at a sweep rate of 5 mV/s. X-ray voltammetry (XRV) measured at (b) (0, 0, 1.5), (c) (1, 0, 3.7), and (d) (0, 1, 0.5) at a sweep rate of 2 mV/s. All data is plotted vs a Ag/AgCl reference. Reprinted with permission from [182] Copyright (2016) American Chemical Society.

the (0, 1, 0.5). The intensity decreases until the completion of the monolayer just before C3. At this point the intensity begins to increase as the silver bilayer begins to form. This is consistent with changes to the CTR profile for a monolayer and bilayer as discussed in chapter 2 section 2.6.1. In this section the dynamics of the deposition/dissolution process of silver are studied in the sub-monolayer region. The potential was stepped between 1.05 V and 0.7 V. At 1.05 V the Au(111) surface

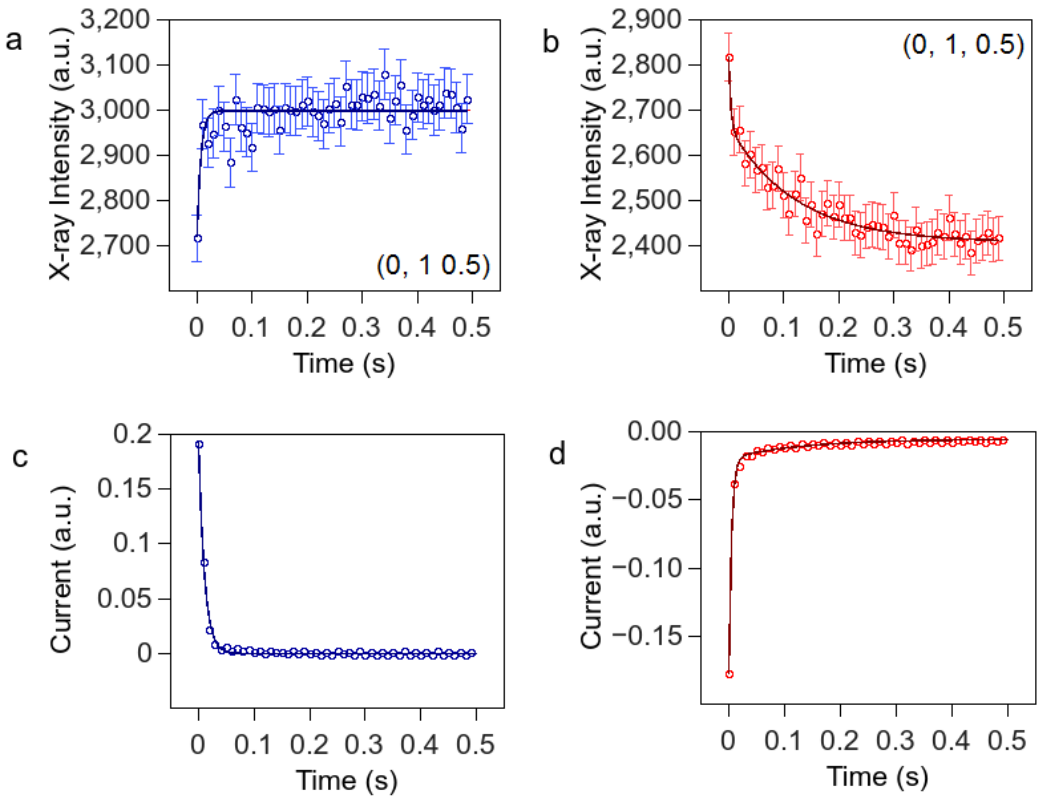

Figure 7.12 Ag UPD on Au(111) Intensity transients at (a) (0, 1, 0.5) at 1 V, (b) (0, 1, 0.5) at 0.7 V, (c) current transients at 1.05 V and (b) 0.7 V.

Transient	Potential (V)	τ_1 (s)	τ_2(s)
Intensity (0, 1, 0.5)	1.05	0.007 ± 0.002	-
	0.7	0.004 ± 0.004	0.12 ± 0.01
Current	1.05	0.0108 ± 0.0002	-
	0.7	0.0045 ± 0.0004	0.073 ± 0.09

Table 7.5 Time constants for intensity and current transients.

should be free of Ag atoms, 0.7 V corresponds to a partial monolayer of Ag. As this study is concerned with the deposition of the partial monolayer of silver the scattered

intensity measured during the potential step was monitored at (0, 1, 0.5), a position which is particularly sensitive to deposition of Ag. The intensity and current transients can be seen in Figure 7.12 and the time constants are summarised in Table 7.5. After the step to 1.05 V the intensity increases exponentially, and the reverse step to, 0.7 V, the intensity decreases with the deposition of Ag, this is consistent with the changes in scattered intensity observed in the XRV at (0, 1, 0.5) for monolayer deposition. The intensity transient of the step to 1.05 V was fit well with a one-term exponential equation (7.1) giving a time constant of 0.007 s which is similar to the current transient (τ=0.0108 s) which indicates that the charge transfer process occurs on the same timescale as the movement of Ag atoms from the Au(111) surface.

A good fit to the intensity transient following the step to 0.7 V could be obtained by a two-term exponential equation (7.2), and similarly with the current transient. The first term in the current transient is much quicker than the second term is associated with the transfer of metal ions to the double layer, and the second term is due to the charge transfer at the interface when the metal ion is adsorbed. The time constants for the intensity transients occur on very similar timescales the fast first term is attributed to the adsorption of Ag on the surface, and the second term is attributed to the ordering process.

A recent study by Nakamura *et al.* investigated the UPD process of different metal ions in real time through similar time-resolved surface X-ray diffraction (TRSXRD) and time resolved infrared spectroscopy (TRIRS). The dynamics of UPD of Ag on Au(111) was probed at (0, 0, 1.4) a position on the specular CTR which is

sensitive to changes in electron density. The time constant obtained was 9.6 ms which is of the same magnitude as the first time constant obtained

The formation of the Ag layer is relatively slow in comparison with the UPD of a (2 x 2)-Bi structure on Au(111) which occurs on the millisecond timescale [57], although the formation of a high coverage incommensurate Bi layer is 3 orders of magnitude slower. This suggests that the kinetics of the Ag/Au(111) system are slow due to the ordering process, and due to the coverage, although this cannot be said for sure as the coverage at 0.7 V was not determined.

7.4 Conclusion

In this chapter the study of three electrochemical systems were presented in order to separate the time-scales for different structural processes and link the structure to the charge transfer processes. The fastest process was the desorption of Ag atoms from the Au(111) surface which occurred over the millisecond timescale, and occurs on the same timescale as the charge transfer processes. The driving force for mass transport of metal ions through electrolyte is much stronger than the rearrangement of the electrochemical double layer, where the timescales are orders of magnitude slower. The time constant for the restructuring of the double layer in the negative step was an order of magnitude larger than the adsorption process, indicating a slower movement of the cations through electrolyte to form an ordered layer in the OHP. The mass transport of surface atoms is much slower than any movement of ions through electrolyte

The most sluggish of all of the systems is the kinetics of the in-plane reconstruction of Au(111), where it can take ~40 seconds to develop long-range

order. In contrast to this the relaxation of surface layers, out of plane, is a much faster structural process ~0.2 seconds. In terms of the current response, the charge transfer appears to be much faster than the structural rearrangements which is expect.

8 Conclusions and future work

Surface X-ray diffraction has been the principle technique in this thesis and has proved a powerful technique in determining the atomic structure of surfaces and interfaces in both UHV and an electrochemical environment.

The structure of the clean Ag(111) and Ag(110) surfaces were determined by SXRD. The oscillatory relaxation model of the Ag(110) surface was in agreement with previous experimental and theoretical works. The Ag(111) surface had much smaller surface relaxations, which is in agreement with theoretical models [2]; the more close packed a surface is surface is then the lesser extent the relaxations are felt. Both surfaces show an overall *inwards* relaxation of the surface layers. Studying the Ag(001) surface with SXRD would make for a complete set of the low index surfaces, given the model it is likely that the relaxation effect at the surface should be in between the Ag(110) and Ag(111) surfaces.

The growth conditions of silicene on Ag(111) were successfully optimised. Although a monolayer of silicene was formed, it exists as an exotic mix of structures, and it is has proven difficult to form a single phase on the surface. The average structure of the surface has been determined through analysis of the surface normal structure with the specular CTR, and shows interesting differences to the study by Curcella *et al.* [108], which only considered scattering from the FORs for the (4×4) silicene structure. The overall buckling of the surface determined by analysis of the specular CTR was 1.19 ± 0.02 Å, which was much greater than the value determined for the (4×4) structure by Curcella, 0.76 Å. This indicates that the (4×4) may not have been the most dominant structure on the surface under study. It is clear, that in order to obtain a complete analysis of the Ag(111)/Silicene interface the structure of the other silicene orientations needs to be addressed. The deposition of Si undoubtedly has an effect on the Ag(111) surface as it undergoes small, but non-negligible changes which results in the expansion of the top two surface metal layers. The interaction of Si with the Ag(111) surface could be probed further by resonant surface X-ray diffraction which could determine the charge transfer at the interface [129].

XRV and CTR measurements were used to build up a comprehensive picture of the Ag(*hkl*)/alkaline interface. CTR measurements have been used to determine the structure at both the electrode and electrolyte sides of the interface. The results reveal large structural changes on the electrolyte side of the interface on all three surfaces, with the response of relaxation of the surface layers in the metal. There was some evidence of in-plane ordering at the Ag(001) surface. Negative of the E_{pzc} the driving force behind the restructuring of the double layer is due to a Field effect. Cations are attracted from the bulk electrolyte to form a layer near the surface in

order to maintain electroneutrality at the interface. At potentials positive of the pzc, OH adsorbs on the surface, maintaining its negative charge. The OH_{ads} stabilises cations in a compact double layer through non-covalent interactions. These studies were extended to determine the effects of saturating the electrolyte gases, CO and O_2 on the double layer structure. The results indicate that double layer structure is subtly perturbed, and hints at a change in the nature of bonding at the interface. The mechanism behind this is currently unknown and additional experimental techniques with chemical sensitivity would be beneficial to elucidate this. It would be necessary to repeat the cyclic voltammetry measurements (presented chapter 6) in a specifically designed cell, to obtain data over the smaller potential region (before oxidation of the surface) in order to identify peaks corresponding to CO oxidation.

Time resolved SXRD measurements were utilised to determine the dynamics of the restructuring of the electrolyte layering at the Ag(111)/Alkaline interface. In order to gain a comprehensive picture of the structural dynamics, two other systems were also studied; the Au(111) reconstruction to determine the timescale of the $(4 \times 4) \leftrightarrow (p \times \sqrt{3})$ phase transition, and the underpotential deposition of Ag on Au(111). The results indicate that the mass transport of ions through electrolyte is on a timescale comparable to the charge transfer, whereas the ordering of ions and surface metal atoms occurs on much longer timescales. The kinetics of the restructuring of the double layer were slow in comparison with the work by Nakamura *et al.* [58], which is explained by the additional adsorption processes occurring at the interface. It would be interesting to extend the studies on Ag(111) to determine the how and if the kinetics change in the presence of CO and $O_{2;}$ this would fit in well with the work done in chapter 6.

A natural progression of this work, would be to bring together the work in chapters 5 and 6 to study the Ag(111)/Silicene interface in an electrochemical environment. There has been extensive studies of the electrochemistry of graphene and its derivatives [185], in particular it's use in energy storage systems – such as lithium ion batteries [186], and for sensing and biosensing systems [181–183]. More recently there has been interest into silicene as a prospective anode material for Na-ion [190] and Li-ion batteries [191]; theoretical investigations propose that silicene has a greater potential as an anode material than graphene due to better storage capability and greater energy density. As only theoretical studies exist, the stability of the silicene layer is unknown in an electrochemical environment making it an exciting new area to study. Growing the silicene in UHV on Ag(111) and transferring the sample into alkaline electrolyte of 0.01 M NaOH + 0.09 M NaF would allow direct comparison to the results in chapter 6 of this thesis. The electrochemical response of the system could be probed through XRV measurements with the possibility to extend the measurements to probe the surface behaviour during gas reactions, such as the ORR. Detailed structural analysis could be obtained from CTR measurements. Additionally, studying the system in an acidic electrolyte with halide anions would allow the study of adsorption and ordering. This would gain a good understanding of the surface structure in a fundamental range of electrochemical systems, providing the silicene layer is stable outside of UHV and in an electrochemical environment.

If the silicene is not stable on transfer to an electrochemical cell, an alternative method would be to electrochemically deposit silicon. Although is not possible to deposit silicon from aqueous electrolyte, as the potential window is only 1 V and the solution would break down before the potential for silicon deposition, it

is possible to deposit silicon from ionic liquids which have a much larger potential window of several volts. At present there are no reports of electrochemical deposition of silicene from ionic liquids, only amorphous structures have been formed [176–178].

References

[1] L. A. Kibler, “Preparation and Characterization of Noble Metal Single Crystal Electrode Surface.” Short Course Held 51st 53rd Annu. Mtg ISE., 2003.

[2] U. Landman, R. N. Hill, and M. Mostoller, “Lattice relaxation at metal surfaces: An electrostatic model,” *Phys. Rev. B*, vol. 21, no. 2, pp. 448–457, Jan. 1980.

[3] K. Kádas *et al.*, “Surface relaxation and surface stress of 4d transition metals,” *Surf. Sci.*, vol. 600, no. 2, pp. 395–402, Jan. 2006.

[4] T. Ning, Q. Yu, and Y. Ye, “Multilayer relaxation at the surface of fcc metals: Cu, Ag, Au, Ni, Pd, Pt, Al,” *Surf. Sci.*, vol. 206, no. 1, pp. L857–L863, Nov. 1988.

[5] H. L. Meyerheim, S. Pflanz, R. Schuster, and I. K. Robinson, “Surface X-ray diffraction on the potassium-induced reconstruction of the Ag(001) surface,” *Phys. B Condens. Matter*, vol. 221, no. 1, pp. 134–140, Apr. 1996.

[6] M. Pascal *et al.*, “Photoelectron diffraction study of the Ag(110)-(2×1)-O reconstruction,” *Surf. Sci.*, vol. 464, no. 2–3, pp. 83–90, Oct. 2000.

[7] M. Alff and W. Moritz, “Structure of the Ag(110) surface determined by using averaged leed intensities,” *Surf. Sci.*, vol. 80, pp. 24–31, Feb. 1979.

[8] M. Lindroos, C. J. Barnes, M. Valden, and D. A. King, “A re-examination of multilayer relaxation of Ag(110) by LEED structural analysis,” *Surf. Sci.*, vol. 218, no. 2, pp. 269–282, Aug. 1989.

[9] E. Holub-Krappe, K. Horn, J. W. M. Frenken, R. L. Krans, and J. F. V. D. Veen, “Multilayer relaxation at the Ag(110) surface,” *Surf. Sci.*, vol. 188, no.

3, pp. 335–349, Oct. 1987.

[10] Y. Kuk and L. C. Feldman, “Oscillatory relaxation of the Ag(110) surface,” *Phys. Rev. B*, vol. 30, no. 10, pp. 5811–5816, Nov. 1984.

[11] H. Li, J. Quinn, Y. S. Li, D. Tian, F. Jona, and P. M. Marcus, “Multilayer relaxation of clean Ag{001},” *Phys. Rev. B*, vol. 43, no. 9, pp. 7305–7307, Mar. 1991.

[12] E. A. Soares, G. S. Leatherman, R. D. Diehl, and M. A. Van Hove, “Low-energy electron diffraction study of the thermal expansion of Ag(111),” *Surf. Sci.*, vol. 468, no. 1–3, pp. 129–136, Nov. 2000.

[13] C. E. Botez, W. C. Elliott, P. F. Miceli, and P. W. Stephens, “X-ray Scattering Measurements of the Ag(111) Surface Thermal Expansion,” in *Symposia EE – Applications of Synchrotron Radiation Techniques…IV*, 2001, vol. 678, p. EE9.3.1 (5 pages).

[14] E. A. Soares *et al.*, “Structure determination of Ag(111) by low-energy electron diffraction,” *Surf. Sci.*, vol. 419, no. 2–3, pp. 89–96, Jan. 1999.

[15] M. Maglietta, E. Zanazzi, F. Jona, D. W. Jepsen, and P. M. Marcus, “Re-examination of the structure of the clean (110) surface of Ag,” *J. Phys. C Solid State Phys.*, vol. 10, no. 17, p. 3287, 1977.

[16] R. A. Van Santen and H. P. C. E. Kuipers, “The Mechanism of Ethylene Epoxidation,” in *Advances in Catalysis*, vol. 35, H. P. and P. B. W. D.D. Eley, Ed. Academic Press, 1987, pp. 265–321.

[17] C. I. Carlisle, D. A. King, M.-L. Bocquet, J. Cerdá, and P. Sautet, “Imaging the Surface and the Interface Atoms of an Oxide Film on {Ag}{111} by Scanning Tunneling Microscopy: Experiment and Theory,” *Phys. Rev. Lett.*, vol. 84, no. 17, pp. 3899–3902, Apr. 2000.

[18] W.-X. Li, C. Stampfl, and M. Scheffler, “Why is a Noble Metal Catalytically Active? The Role of the O-Ag Interaction in the Function of Silver as an Oxidation Catalyst,” *Phys. Rev. Lett.*, vol. 90, no. 25, p. 256102, Jun. 2003.

[19] D. Strmcnik, K. Kodama, D. van der Vliet, J. Greeley, V. R. Stamenkovic, and N. M. Marković, “The role of non-covalent interactions in electrocatalytic fuel-cell reactions on platinum,” *Nat. Chem.*, vol. 1, no. 6, pp. 466–472, Sep. 2009.

[20] S. L. Horswell *et al.*, “A comparative study of hydroxide adsorption on the

(111), (110), and (100) faces of silver with cyclic voltammetry, ex situ electron diffraction, and in situ second harmonic generation," *Langmuir*, vol. 20, no. 25, pp. 10970–10981, 2004.

[21] S. L. Horswell, A. L. N. Pinheiro, E. R. Savinova, B. Pettinger, M.-S. Zei, and G. Ertl, "Hydroxide Adsorption on Ag(110) Electrodes: An in Situ Second Harmonic Generation and ex Situ Electron Diffraction Study," *J. Phys. Chem. B*, vol. 108, no. 48, pp. 18640–18649, Dec. 2004.

[22] E. R. Savinova, D. Y. Zemlyanov, A. Scheybal, R. Schlögl, and K. Doblhofer, "Ex Situ X-ray Photoelectron Spectroscopy Study of the Interface between a Ag(111) Electrode and an Alkaline Electrolyte. 2. Structure of the Double Layer," *Langmuir*, vol. 15, no. 19, pp. 6552–6556, Sep. 1999.

[23] C. A. Lucas, P. Thompson, Y. Gründer, and N. M. Markovic, "The structure of the electrochemical double layer: Ag(111) in alkaline electrolyte," *Electrochem. Commun.*, vol. 13, no. 11, pp. 1205–1208, Nov. 2011.

[24] M. Nakamura, N. Sato, N. Hoshi, and O. Sakata, "Outer Helmholtz Plane of the Electrical Double Layer Formed at the Solid Electrode–Liquid Interface," *ChemPhysChem*, vol. 12, no. 8, pp. 1430–1434, Jun. 2011.

[25] A. Kara *et al.*, "A review on silicene — New candidate for electronics," *Surf. Sci. Rep.*, vol. 67, no. 1, pp. 1–18, Jan. 2012.

[26] H. L. Davis and J. R. Noonan, "Multilayer relaxation in metallic surfaces as demonstrated by LEED analysis," *Surf. Sci.*, vol. 126, no. 1, pp. 245–252, Mar. 1983.

[27] W. Schmickler and E. Santos, *Interfacial Electrochemistry*. Springer Science & Business Media, 2010.

[28] W. Schmickler, *Interfacial Electrochemistry*. Oxford University Press, 1996.

[29] E. Gileadi, *Physical Electrochemistry*. Wiley, 2011.

[30] A. J. Bard, *Electrochemical Methods: Fundamentals and Applications*, 2nd Edition. 2001.

[31] A. J. Bard *et al.*, "The electrode/electrolyte interface - a status report," *J. Phys. Chem.*, vol. 97, no. 28, pp. 7147–7173, Jul. 1993.

[32] W. Schmickler, "Electronic Effects in the Electric Double Layer," *Chem. Rev.*, vol. 96, no. 8, pp. 3177–3200, Jan. 1996.

[33] R. G. Compton, *Electrode Potentials*. Oxford Chemistry Primers, 1996.

[34] H. Helmholtz, “Studien über electrische Grenzschichten,” *Ann. Phys.*, vol. 243, no. 7, pp. 337–382, Jan. 1879.

[35] M. Gouy, “Sur la constitution de la charge électrique à la surface d’un électrolyte,” *J. Phys. Théorique Appliquée*, vol. 9, no. 1, pp. 457–468, 1910.

[36] D. L. Chapman, “LI. A contribution to the theory of electrocapillarity,” *Philos. Mag. Ser. 6*, vol. 25, no. 148, pp. 475–481, Apr. 1913.

[37] O. Stern, “The theory of the electrolytic double-layer,” *Z Fuer Elektrochem Angew Phys Chem*, no. 30, 1924.

[38] D. C. Grahame, “The Electrical Double Layer and the Theory of Electrocapillarity.,” *Chem. Rev.*, vol. 41, no. 3, pp. 441–501, Dec. 1947.

[39] W. Bragg, *The Reflection of X-rays by Crystals*. Royal Society of London, 1913.

[40] I. K. Robinson and D. J. Tweet, “Surface X-ray diffraction,” *Rep. Prog. Phys.*, vol. 55, no. 5, p. 599, May 1992.

[41] P. H. Fuoss and S. Brennan, “Surface Sensitive X-Ray Scattering,” *Annu. Rev. Mater. Sci.*, vol. 20, no. 1, pp. 365–390, 1990.

[42] R. Feidenhans’l, “Surface structure determination by X-ray diffraction,” *Surf. Sci. Rep.*, vol. 10, no. 3, pp. 105–188, May 1989.

[43] B. E. Warren, *X-ray Diffraction*. Courier Corporation, 1969.

[44] J. Als-Nielsen and D. McMorrow, *Elements of Modern X-ray Physics*. Wiley, 2001.

[45] E. Prince, “(International Tables) Volume C home page,” *urn:isbn:978-1-4020-1900-5*, 2006. [Online]. Available: http://it.iucr.org/Cb/. [Accessed: 24-Feb-2017].

[46] P. A. Fenter, “X-ray Reflectivity as a Probe of Mineral-Fluid Interfaces: A User Guide,” *Rev. Mineral. Geochem.*, vol. 49, no. 1, pp. 149–221, Jan. 2002.

[47] J. F. Moulder, *Handbook of X-ray Photoelectron Spectroscopy: A Reference Book of Standard Spectra for Identification and Interpretation of XPS Data*. Physical Electronics Division, Perkin-Elmer Corporation, 1992.

[48] X. Gao, G. J. Edens, A. Hamelin, and M. J. Weaver, “Real-space formation and dissipation mechanisms of hexagonal reconstruction on Au(100) in aqueous media as explored by potentiodynamic scanning tunneling microscopy,” *Surf. Sci.*, vol. 296, no. 3, pp. 333–351, Nov. 1993.

[49] X. Gao and M. J. Weaver, “Electrode potential-induced reconstruction of gold (100): effect of chemisorption on nanoscale dynamics as probed by in-situ scanning tunneling microscopy,” *J. Phys. Chem.*, vol. 97, no. 34, pp. 8685–8689, Aug. 1993.

[50] H. Wano and K. Uosaki, “In Situ, Real-Time Monitoring of the Reductive Desorption Process of Self-Assembled Monolayers of Hexanethiol on Au(111) Surfaces in Acidic and Alkaline Aqueous Solutions by Scanning Tunneling Microscopy,” *Langmuir*, vol. 17, no. 26, pp. 8224–8228, Dec. 2001.

[51] O. Sklyar, T. H. Treutler, N. Vlachopoulos, and G. Wittstock, “The geometry of nanometer-sized electrodes and its influence on electrolytic currents and metal deposition processes in scanning tunneling and scanning electrochemical microscopy,” *Surf. Sci.*, vol. 597, no. 1–3, pp. 181–195, Dec. 2005.

[52] R. Springell *et al.*, “Water corrosion of spent nuclear fuel: radiolysis driven dissolution at the UO2/water interface,” *Faraday Discuss.*, vol. 180, no. 0, pp. 301–311, Jul. 2015.

[53] M. F. Toney *et al.*, “Voltage-dependent ordering of water molecules at an electrode–electrolyte interface,” *Nature*, vol. 368, no. 6470, pp. 444–446, Mar. 1994.

[54] M. F. Toney *et al.*, “Distribution of water molecules at Ag(111)/electrolyte interface as studied with surface X-ray scattering,” *Surf. Sci.*, vol. 335, pp. 326–332, Jul. 1995.

[55] A. C. Finnefrock, L. J. Buller, K. L. Ringland, J. D. Brock, and H. D. Abruña, “Time-Resolved Surface X-ray Scattering Study of Surface Ordering of Electrodeposited Layers,” *J. Am. Chem. Soc.*, vol. 119, no. 48, pp. 11703–11704, Dec. 1997.

[56] A. C. Finnefrock, K. L. Ringland, J. D. Brock, L. J. Buller, and H. D. Abruña, “Nucleation and Ordering of an Electrodeposited Two-Dimensional Crystal: Real-Time X-Ray Scattering and Electronic Measurements,” *Phys. Rev. Lett.*, vol. 81, no. 16, pp. 3459–3462, Oct. 1998.

[57] K. Tamura, J. X. Wang, R. R. Adžic, and B. M. Ocko, “Kinetics of Monolayer Bi Electrodeposition on Au(111): Surface X-ray Scattering and Current Transients,” *J. Phys. Chem. B*, vol. 108, no. 6, pp. 1992–1998, Feb. 2004.

[58] M. Nakamura, H. Kaminaga, O. Endo, H. Tajiri, O. Sakata, and N. Hoshi, “Structural Dynamics of the Electrical Double Layer during Capacitive Charging/Discharging Processes,” *J. Phys. Chem. C*, vol. 118, no. 38, pp. 22136–22140, Sep. 2014.

[59] F. Golks, K. Krug, Y. Gründer, J. Zegenhagen, J. Stettner, and O. M. Magnussen, “High-Speed in situ Surface X-ray Diffraction Studies of the Electrochemical Dissolution of Au(001),” *J. Am. Chem. Soc.*, vol. 133, no. 11, pp. 3772–3775, Mar. 2011.

[60] J. E. DeVilbiss *et al.*, “Time response of the thin layer electrochemical cell used for in situ X-ray diffraction,” *Electrochimica Acta*, vol. 47, no. 19, pp. 3057–3064, Jul. 2002.

[61] I. K. Robinson, E. Vlieg, H. Hornis, and E. H. Conrad, “Surface morphology of Ag(110) close to its roughening transition,” *Phys. Rev. Lett.*, vol. 67, no. 14, pp. 1890–1893, Sep. 1991.

[62] D. M. Kolb, “An atomistic view of electrochemistry,” *Surf. Sci.*, vol. 500, no. 1–3, pp. 722–740, Mar. 2002.

[63] “OpenGDA Home Page.” [Online]. Available: http://www.opengda.org/. [Accessed: 23-Feb-2017].

[64] “Beamline Components.” [Online]. Available: http://www.esrf.eu/UsersAndScience/Experiments/MX/About_our_beamlines/Beamline_Components. [Accessed: 01-Mar-2017].

[65] C. Longo, M. Savaris, M. Zeni, R. N. Brandalise, and A. M. C. Grisa, “Degradation study of polypropylene (PP) and bioriented polypropylene (BOPP) in the environment,” *Mater. Res.*, vol. 14, no. 4, pp. 442–448, Dec. 2011.

[66] G. Harlow, “Surface X-ray Diffraction Studies of the Electrochemical Interface,” PhD Thesis, University of Liverpool, 2016.

[67] E. Vlieg, “A (2+3)-Type Surface Diffractometer: Mergence of the z-Axis and (2+2)-Type Geometries,” *J. Appl. Crystallogr.*, vol. 31, no. 2, pp. 198–203, Apr. 1998.

[68] C. Nicklin, T. Arnold, J. Rawle, and A. Warne, “Diamond beamline I07: a beamline for surface and interface diffraction,” *J. Synchrotron Radiat.*, vol. 23, no. 5, pp. 1245–1253, Sep. 2016.

[69] C. B. Duke, “Semiconductor Surface Reconstruction: The Structural Chemistry of Two-Dimensional Surface Compounds,” *Chem. Rev.*, vol. 96, no. 4, pp. 1237–1260, Jun. 1996.

[70] R. N. Barnett, U. Landman, and C. L. Cleveland, “Multilayer lattice relaxation at metal surfaces,” *Phys. Rev. B*, vol. 27, no. 10, pp. 6534–6537, May 1983.

[71] A. Franchini, C. Magherini, and G. Santoro, “Surface thermal expansion of Ag(1 1 0),” *Surf. Sci.*, vol. 502–503, pp. 443–448, Apr. 2002.

[72] D. P. Jackson, “Surface Relaxations in Cubic Metals,” *Can. J. Phys.*, vol. 49, no. 16, pp. 2093–2097, Aug. 1971.

[73] S. Kato, “Estimation on Surface Atomic Layer Spacing of Nickel and Iron Single Crystals,” *Jpn. J. Appl. Phys.*, vol. 13, no. 2, p. 218, Feb. 1974.

[74] J. W. Flocken, “Lattice-statics approach to surface calculations in a monatomic lattice,” *Phys. Rev. B*, vol. 9, no. 12, pp. 5133–5143, Jun. 1974.

[75] R. A. Johnson and P. J. White, “Calculations for surface energies and displacements using empirical interatomic forces,” *Phys. Rev. B*, vol. 13, no. 12, pp. 5293–5302, Jun. 1976.

[76] R. Benedek, “Lattice statics calculations of the surface relaxation in metals,” *J. Phys. F Met. Phys.*, vol. 8, no. 6, p. 1119, 1978.

[77] M. W. Finnis and V. Heine, “Theory of lattice contraction at aluminium surfaces,” *J. Phys. F Met. Phys.*, vol. 4, no. 3, p. L37, 1974.

[78] G. Attard and C. Barnes, *Surfaces*. Oxford, New York: Oxford University Press, 1998.

[79] H. B. Nielsen, J. N. Andersen, L. Petersen, and D. L. Adams, “Multilayer relaxation of the Al(110) surface,” *J. Phys. C Solid State Phys.*, vol. 15, no. 32, p. L1113, 1982.

[80] H. L. Davis, “Cu(100) multilayer relaxation,” *J. Vac. Sci. Technol.*, vol. 20, no. 3, pp. 842–845, Mar. 1982.

[81] D. L. Adams, H. B. Nielsen, and J. N. Andersen, “Oscillatory relaxation of the Cu(110) surface,” *Surf. Sci.*, vol. 128, no. 2, pp. 294–310, Jan. 1983.

[82] H. L. Meyerheim and W. Moritz, “Structure and dynamics of clean and adsorbate-covered crystal surfaces studied by surface X-ray diffraction,” *Appl. Phys. Mater. Sci. Process.*, vol. 67, no. 6, pp. 645–656, 1998.

[83] E. Zanazzi, F. Jona, D. W. Jepsen, and P. M. Marcus, “Structure of Ag (110)

and effect of surface roughness on LEED intensities," *J. Phys. C Solid State Phys.*, vol. 10, no. 3, p. 375, 1977.

[84] C.-M. Chan, S. L. Cunningham, M. A. van Hove, and W. H. Weinberg, "Surface relaxation of Ni(110), Al(110) and Ag(110) determined by the convolution-transform method," *Surf. Sci.*, vol. 67, no. 1, pp. 1–9, Oct. 1977.

[85] G. A. Held, J. L. Jordan-Sweet, P. M. Horn, A. Mak, and R. J. Birgeneau, "X-ray scattering study of the thermal roughening of Ag(110)," *Phys. Rev. Lett.*, vol. 59, no. 18, pp. 2075–2078, Nov. 1987.

[86] E. Holub-Krappe, K. Horn, J. W. M. Frenken, R. L. Krans, and J. F. V. D. Veen, "Multilayer relaxation at the Ag(110) surface," *Surf. Sci.*, vol. 188, no. 3, pp. 335–349, Oct. 1987.

[87] I. Y. Sklyadneva, G. G. Rusina, and E. V. Chulkov, "Vibrational states on vicinal surfaces of Al, Ag, Cu and Pd," *Surf. Sci.*, vol. 416, no. 1–2, pp. 17–36, Oct. 1998.

[88] S. M. Foiles, M. I. Baskes, and M. S. Daw, "Embedded-atom-method functions for the fcc metals Cu, Ag, Au, Ni, Pd, Pt, and their alloys," *Phys. Rev. B*, vol. 33, no. 12, pp. 7983–7991, Jun. 1986.

[89] M. Guillopé and B. Legrand, "(110) Surface stability in noble metals," *Surf. Sci.*, vol. 215, no. 3, pp. 577–595, May 1989.

[90] R. N. Barnett, U. Landman, and C. L. Cleveland, "Multilayer lattice relaxation at metal surfaces: A total-energy minimization," *Phys. Rev. B*, vol. 28, no. 4, pp. 1685–1695, Aug. 1983.

[91] D. Briggs, R. A. Marbrow, and R. M. Lambert, "Photoelectron spectroscopy and surface order: Some UPS and XPS observations on Ag(110)," *Solid State Commun.*, vol. 26, no. 1, pp. 1–2, Apr. 1978.

[92] K. S. Novoselov *et al.*, "Electric Field Effect in Atomically Thin Carbon Films," *Science*, vol. 306, no. 5696, pp. 666–669, Oct. 2004.

[93] S. Cahangirov, M. Topsakal, E. Aktürk, H. Şahin, and S. Ciraci, "Two- and One-Dimensional Honeycomb Structures of Silicon and Germanium," *Phys. Rev. Lett.*, vol. 102, no. 23, p. 236804, Jun. 2009.

[94] A. O'Hare, F. V. Kusmartsev, and K. I. Kugel, "A Stable "Flat" Form of Two-Dimensional Crystals: Could Graphene, Silicene, Germanene Be Minigap Semiconductors?," *Nano Lett.*, vol. 12, no. 2, pp. 1045–1052, Feb. 2012.

[95] K. Takeda and K. Shiraishi, “Theoretical possibility of stage corrugation in Si and Ge analogs of graphite,” *Phys. Rev. B*, vol. 50, no. 20, pp. 14916–14922, Nov. 1994.

[96] G. G. Guzmán-Verri and L. C. Lew Yan Voon, “Electronic structure of silicon-based nanostructures,” *Phys. Rev. B*, vol. 76, no. 7, p. 075131, Aug. 2007.

[97] N. Takagi *et al.*, “Silicene on Ag(1 1 1): Geometric and electronic structures of a new honeycomb material of Si,” *Prog. Surf. Sci.*, vol. 90, no. 1, pp. 1–20, Feb. 2015.

[98] E. Cinquanta *et al.*, “Getting through the Nature of Silicene: An sp2–sp3 Two-Dimensional Silicon Nanosheet,” *J. Phys. Chem. C*, vol. 117, no. 32, pp. 16719–16724, Aug. 2013.

[99] N. D. Drummond, V. Zólyomi, and V. I. Fal’ko, “Electrically tunable band gap in silicene,” *Phys. Rev. B*, vol. 85, no. 7, p. 075423, Feb. 2012.

[100] M. Tahir and U. Schwingenschlögl, “Valley polarized quantum Hall effect and topological insulator phase transitions in silicene,” *Sci. Rep.*, vol. 3, Jan. 2013.

[101] H. Liu, J. Gao, and J. Zhao, “Silicene on Substrates: A Way To Preserve or Tune Its Electronic Properties,” *J. Phys. Chem. C*, vol. 117, no. 20, pp. 10353–10359, May 2013.

[102] A. Fleurence, R. Friedlein, T. Ozaki, H. Kawai, Y. Wang, and Y. Yamada-Takamura, “Experimental Evidence for Epitaxial Silicene on Diboride Thin Films,” *Phys. Rev. Lett.*, vol. 108, no. 24, p. 245501, Jun. 2012.

[103] L. Meng *et al.*, “Buckled Silicene Formation on Ir(111),” *Nano Lett.*, vol. 13, no. 2, pp. 685–690, Feb. 2013.

[104] D. Chiappe *et al.*, “Two-Dimensional Si Nanosheets with Local Hexagonal Structure on a MoS2 Surface,” *Adv. Mater.*, vol. 26, no. 13, pp. 2096–2101, Apr. 2014.

[105] R. W. Olesinski and G. J. Abbaschian, “The B−Si (Boron-Silicon) system,” *Bull. Alloy Phase Diagr.*, vol. 5, no. 5, pp. 478–484, Oct. 1984.

[106] T. B. Massalski, “Binary Alloy Phase Diagrams–Second edition.,” *Adv. Mater.*, vol. 3, no. 12, pp. 628–629, Dec. 1991.

[107] G. Le Lay, “Physics and electronics of the noble-metal/elemental-semiconductor interface formation: A status report,” *Surf. Sci.*, vol. 132, no. 1, pp. 169–204, Sep. 1983.

[108] A. Curcella, R. Bernard, Y. Borensztein, A. Resta, M. Lazzeri, and G. Prévot, "Determining the atomic structure of the (4 x 4) silicene layer on Ag(111) by combined grazing-incidence x-ray diffraction measurements and first-principles calculations," *Phys. Rev. B*, vol. 94, no. 16, p. 165438, Oct. 2016.

[109] B. Lalmi *et al.*, "Epitaxial growth of a silicene sheet," *Appl. Phys. Lett.*, vol. 97, no. 22, p. 223109, Nov. 2010.

[110] P. De Padova *et al.*, "Evidence of graphene-like electronic signature in silicene nanoribbons," *Appl. Phys. Lett.*, vol. 96, no. 26, pp. 261905-261905–3, Jun. 2010.

[111] P. Vogt *et al.*, "Silicene: Compelling Experimental Evidence for Graphenelike Two-Dimensional Silicon," *Phys. Rev. Lett.*, vol. 108, no. 15, p. 155501, Apr. 2012.

[112] C.-L. Lin *et al.*, "Structure of Silicene Grown on Ag(111)," *Appl. Phys. Express*, vol. 5, no. 4, p. 045802, 2012.

[113] L. Chen *et al.*, "Evidence for Dirac Fermions in a Honeycomb Lattice Based on Silicon," *Phys. Rev. Lett.*, vol. 109, no. 5, p. 056804, Aug. 2012.

[114] H. Jamgotchian *et al.*, "Growth of silicene layers on Ag(111): unexpected effect of the substrate temperature," *J. Phys. Condens. Matter*, vol. 24, no. 17, p. 172001, May 2012.

[115] R. Arafune *et al.*, "Structural transition of silicene on Ag(111)," *Surf. Sci.*, vol. 608, pp. 297–300, Feb. 2013.

[116] Z. Majzik *et al.*, "Combined AFM and STM measurements of a silicene sheet grown on the Ag(111) surface," *J. Phys. Condens. Matter Inst. Phys. J.*, vol. 25, no. 22, p. 225301, Jun. 2013.

[117] A. Resta *et al.*, "Atomic Structures of Silicene Layers Grown on Ag(111): Scanning Tunneling Microscopy and Noncontact Atomic Force Microscopy Observations," *Sci. Rep.*, vol. 3, Aug. 2013.

[118] Y. Fukaya *et al.*, "Structure of silicene on a Ag(111) surface studied by reflection high-energy positron diffraction," *Phys. Rev. B*, vol. 88, no. 20, p. 205413, Nov. 2013.

[119] P. Moras, T. O. Mentes, P. M. Sheverdyaeva, A. Locatelli, and C. Carbone, "Coexistence of multiple silicene phases in silicon grown on Ag(1 1 1)," *J. Phys. Condens. Matter*, vol. 26, no. 18, p. 185001, May 2014.

[120] H. Jamgotchian *et al.*, “A comprehensive study of the (2√3 × 2√3)R30° structure of silicene on Ag(1 1 1),” *J. Phys. Condens. Matter*, vol. 27, no. 39, p. 395002, 2015.

[121] H. Enriquez *et al.*, “Atomic structure of the ()R30° of silicene on Ag(111) surface,” *J. Phys. Conf. Ser.*, vol. 491, no. 1, p. 012004, Mar. 2014.

[122] T. Shirai, T. Shirasawa, T. Hirahara, N. Fukui, T. Takahashi, and S. Hasegawa, “Structure determination of multilayer silicene grown on Ag(111) films by electron diffraction: Evidence for Ag segregation at the surface,” *Phys. Rev. B*, vol. 89, no. 24, p. 241403, Jun. 2014.

[123] K. Kawahara *et al.*, “Determination of atomic positions in silicene on Ag(111) by low-energy electron diffraction,” *Surf. Sci.*, vol. 623, pp. 25–28, May 2014.

[124] Z.-L. Liu *et al.*, “The fate of the 2√3 × 2√3R(30°) silicene phase on Ag(111),” *APL Mater.*, vol. 2, no. 9, p. 092513, Sep. 2014.

[125] M. S. Rahman, T. Nakagawa, and S. Mizuno, “Growth of Si on Ag(111) and determination of large commensurate unit cell of high-temperature phase,” *Jpn. J. Appl. Phys.*, vol. 54, no. 1, p. 015502, Dec. 2014.

[126] H. Enriquez, S. Vizzini, A. Kara, B. Lalmi, and H. Oughaddou, “Silicene structures on silver surfaces,” *J. Phys. Condens. Matter*, vol. 24, no. 31, p. 314211, Aug. 2012.

[127] R. Arafune *et al.*, “Structural transition of silicene on Ag(111),” *Surf. Sci.*, vol. 608, pp. 297–300, Feb. 2013.

[128] P. D. Padova, “Evidence of Dirac fermions in multilayer silicene,” *Appl. Phys. Lett.*, vol. 102, no. 16, p. 163106, Apr. 2013.

[129] C. Lucas and Y. Grunder, “Probing the Charge Distribution at the Electrochemical Interface,” *Phys. Chem. Chem. Phys.*, Feb. 2017.

[130] C. A. Lucas, P. Thompson, Y. Gründer, and N. M. Markovic, “The structure of the electrochemical double layer: Ag(111) in alkaline electrolyte,” *Electrochem. Commun.*, vol. 13, no. 11, pp. 1205–1208, Nov. 2011.

[131] M. Nakamura, N. Sato, N. Hoshi, and O. Sakata, “Outer Helmholtz Plane of the Electrical Double Layer Formed at the Solid Electrode–Liquid Interface,” *ChemPhysChem*, vol. 12, no. 8, pp. 1430–1434, Jun. 2011.

[132] D. Strmcnik *et al.*, “Effects of Li+, K+, and Ba2+ Cations on the ORR at Model and High Surface Area Pt and Au Surfaces in Alkaline Solutions,” *J.*

Phys. Chem. Lett., vol. 2, no. 21, pp. 2733–2736, Nov. 2011.

[133] M. Nakamura, Y. Nakajima, N. Sato, N. Hoshi, and O. Sakata, "Structure of the electrical double layer on Ag(100): Promotive effect of cationic species on Br adlayer formation," *Phys. Rev. B*, vol. 84, no. 16, p. 165433, Oct. 2011.

[134] H. Keller, M. Saracino, H. M. T. Nguyen, T. M. T. Huynh, and P. Broekmann, "Competitive anion/water and cation/water interactions at electrified copper/electrolyte interfaces probed by in situ X-ray diffraction," *J. Phys. Chem. C*, vol. 116, no. 20, pp. 11068–11076, 2012.

[135] J. N. Mills, I. T. McCrum, and M. J. Janik, "Alkali cation specific adsorption onto fcc(111) transition metal electrodes," *Phys. Chem. Chem. Phys.*, vol. 16, no. 27, pp. 13699–13707, Jun. 2014.

[136] M. Nakamura, Y. Nakajima, K. Kato, O. Sakata, and N. Hoshi, "Surface Oxidation of Au(111) Electrode in Alkaline Media Studied by Using X-ray Diffraction and Infrared Spectroscopy: Effect of Alkali Metal Cation on the Alcohol Oxidation Reactions," *J. Phys. Chem. C*, vol. 119, no. 41, pp. 23586–23591, Oct. 2015.

[137] C. Ding *et al.*, "Abnormal Effects of Cations (Li+, Na+, and K+) on Photoelectrochemical and Electrocatalytic Water Splitting," *J. Phys. Chem. B*, vol. 119, no. 8, pp. 3560–3566, Feb. 2015.

[138] O. Sklyar, T. H. Treutler, N. Vlachopoulos, and G. Wittstock, "The geometry of nanometer-sized electrodes and its influence on electrolytic currents and metal deposition processes in scanning tunneling and scanning electrochemical microscopy," *Surf. Sci.*, vol. 597, no. 1–3, pp. 181–195, Dec. 2005.

[139] D. Strmcnik, K. Kodama, D. van der Vliet, J. Greeley, V. R. Stamenkovic, and N. M. Marković, "The role of non-covalent interactions in electrocatalytic fuel-cell reactions on platinum," *Nat. Chem.*, vol. 1, no. 6, pp. 466–472, Sep. 2009.

[140] S. L. Horswell *et al.*, "A Comparative Study of Hydroxide Adsorption on the (111), (110), and (100) Faces of Silver with Cyclic Voltammetry, Ex Situ Electron Diffraction, and In Situ Second Harmonic Generation," *Langmuir*, vol. 20, no. 25, pp. 10970–10981, Dec. 2004.

[141] E. R. Savinova *et al.*, "Structure and dynamics of the interface between a Ag

single crystal electrode and an aqueous electrolyte," *Faraday Discuss.*, vol. 121, no. 0, pp. 181–198, Aug. 2002.

[142] B. M. Jovic, V. D. Jovic, and G. R. Stafford, "Cyclic voltammetry on Ag(111) and Ag(100) faces in sodium hydroxide solutions," *Electrochem. Commun.*, vol. 1, no. 6, pp. 247–251, Jun. 1999.

[143] J. Kunze, H.-H. Strehblow, and G. Staikov, "In situ STM study of the initial stages of electrochemical oxide formation at the Ag(111)/0.1 M NaOH(aq) interface," *Electrochem. Commun.*, vol. 6, no. 2, pp. 132–137, Feb. 2004.

[144] M. Klaua and T. E. Madey, "The adsorption of H2O on clean and oxygen-dosed silver single crystal surfaces," *Surf. Sci.*, vol. 136, no. 1, pp. L42–L50, Jan. 1984.

[145] C. Qin and J. L. Whitten, "Adsorption of O, H, OH, and H2O on Ag(100)," *J. Phys. Chem. B*, vol. 109, no. 18, pp. 8852–8856, May 2005.

[146] D. Hecht and H.-H. Strehblow, "XPS investigations of the electrochemical double layer on silver in alkaline chloride solutions," *J. Electroanal. Chem.*, vol. 440, no. 1, pp. 211–217, Dec. 1997.

[147] D. Lützenkirchen-Hecht and H.-H. Strehblow, "Bromide adsorption on silver in alkaline solution: A surface analytical study," *Berichte Bunsenges. Für Phys. Chem.*, vol. 102, no. 6, pp. 826–832, Jun. 1998.

[148] P. A. Thiel and T. E. Madey, "The interaction of water with solid surfaces: Fundamental aspects," *Surf. Sci. Rep.*, vol. 7, no. 6, pp. 211–385, Oct. 1987.

[149] D. Menzel, "Adsorbate-Induced Global and Local Expansions and Contractions of a Close-Packed Transition Metal Surface," *Surf. Rev. Lett.*, vol. 4, pp. 1283–1289, 1997.

[150] S. Royer and D. Duprez, "Catalytic Oxidation of Carbon Monoxide over Transition Metal Oxides," *ChemCatChem*, vol. 3, no. 1, pp. 24–65, Jan. 2011.

[151] P. Rodriguez, J. M. Feliu, and M. T. M. Koper, "Unusual adsorption state of carbon monoxide on single-crystalline gold electrodes in alkaline media," *Electrochem. Commun.*, vol. 11, no. 6, pp. 1105–1108, Jun. 2009.

[152] P. Rodriguez, Y. Kwon, and M. T. M. Koper, "The promoting effect of adsorbed carbon monoxide on the oxidation of alcohols on a gold catalyst," *Nat. Chem.*, vol. 4, no. 3, pp. 177–182, Mar. 2012.

[153] G. McElhiney, H. Papp, and J. Pritchard, "The adsorption of Xe and CO on

Ag(111),” *Surf. Sci.*, vol. 54, no. 3, pp. 617–634, Mar. 1976.

[154] C. Qin, L. S. Sremaniak, and J. L. Whitten, “CO Adsorption on Ag(100) and Ag/MgO(100),” *J. Phys. Chem. B*, vol. 110, no. 23, pp. 11272–11276, Jun. 2006.

[155] G. S. Leatherman and R. D. Diehl, “Thermal and Structural Properties of N2 or CO on Ag(111),” *Langmuir*, vol. 13, no. 26, pp. 7063–7067, Dec. 1997.

[156] M. Kulawik, H.-P. Rust, N. Nilius, M. Heyde, and H.-J. Freund, “STM studies of ordered (31×31)R9° CO islands on Ag(111),” *Phys. Rev. B*, vol. 71, no. 15, p. 153405, Apr. 2005.

[157] A. Cuesta and C. Gutiérrez, “Study by Fourier Transform Infrared Spectroscopy of the Electroadsorption of CO on the Ferrous Metals. 1. Iron,” *J. Phys. Chem.*, vol. 100, no. 30, pp. 12600–12608, Jan. 1996.

[158] N. S. Marinkovic, J. X. Wang, J. S. Marinkovic, and R. R. Adzic, “Unusual Adsorption Properties of Silver Adlayers on the Pt(111) Electrode Surface,” *J. Phys. Chem. B*, vol. 103, no. 1, pp. 139–144, Jan. 1999.

[159] G. Orozco, M. C. Pérez, A. Rincón, and C. Gutiérrez, “Adsorption and Electrooxidation of Carbon Monoxide on Silver,” *Langmuir*, vol. 14, no. 21, pp. 6297–6306, Oct. 1998.

[160] N. M. Marković, C. A. Lucas, B. N. Grgur, and P. N. Ross, “Surface Electrochemistry of CO and H2/CO Mixtures at Pt(100) Interface: Electrode Kinetics and Interfacial Structures,” *J. Phys. Chem. B*, vol. 103, no. 44, pp. 9616–9623, Nov. 1999.

[161] A. Zwetanova and K. Jüttner, “The electrocatalytical influence of underpotential lead and thallium adsorbates on the cathodic reduction of oxygen on (111), (100) and (110) silver single-crystal surfaces,” *J. Electroanal. Chem. Interfacial Electrochem.*, vol. 119, no. 1, pp. 149–164, Feb. 1981.

[162] B. B. Blizanac, P. N. Ross, and N. M. Marković, “Oxygen Reduction on Silver Low-Index Single-Crystal Surfaces in Alkaline Solution: Rotating Ring DiskAg(hkl) Studies,” *J. Phys. Chem. B*, vol. 110, no. 10, pp. 4735–4741, Mar. 2006.

[163] A. Cuesta and C. Gutiérrez, “Study by Fourier Transform Infrared Spectroscopy of the Adsorption of Carbon Monoxide on a Cobalt Electrode at

pH 3−14," *Langmuir*, vol. 14, no. 12, pp. 3390–3396, Jun. 1998.

[164] A. Cuesta and C. Gutiérrez, "Study by Fourier Transform Infrared Spectroscopy of the Adsorption of Carbon Monoxide on a Nickel Electrode at pH 3−14," *Langmuir*, vol. 14, no. 12, pp. 3397–3404, Jun. 1998.

[165] I. Oda, H. Ogasawara, and M. Ito, "Carbon Monoxide Adsorption on Copper and Silver Electrodes during Carbon Dioxide Electroreduction Studied by Infrared Reflection Absorption Spectroscopy and Surface-Enhanced Raman Spectroscopy," *Langmuir*, vol. 12, no. 4, pp. 1094–1097, Jan. 1996.

[166] N. M. Marković, B. N. Grgur, C. A. Lucas, and P. N. Ross, "Surface electrochemistry of CO on Pt(110)-(1 × 2) and Pt(110)-(1 × 1) surfaces," *Surf. Sci.*, vol. 384, no. 1, pp. L805–L814, Jul. 1997.

[167] G. J. Edens, X. Gao, M. J. Weaver, N. M. Markovic, and P. N. Ross, "Influence of adsorbed hydroxyl and carbon monoxide on potential-induced reconstruction of Au(100) as examined by scanning tunneling microscopy," *Surf. Sci.*, vol. 302, no. 1, pp. L275–L282, Jan. 1994.

[168] X. Gao, G. J. Edens, and M. J. Weaver, "Monocrystalline gold-aqueous interfaces as a model experimental link between macroscopic electrochemistry and in-situ electrochemical surface science," *J. Electroanal. Chem.*, vol. 376, no. 1, pp. 21–34, Oct. 1994.

[169] H. Naohara, S. Ye, and K. Uosaki, "Epitaxial growth of a palladium layer on an Au(100) electrode," *J. Electroanal. Chem.*, vol. 473, no. 1–2, pp. 2–9, Sep. 1999.

[170] W. Polewska, R. J. Behm, and O. M. Magnussen, "In-situ video-STM studies of Cu electrodeposition on Cu(100) in HCl solution," *Electrochimica Acta*, vol. 48, no. 20–22, pp. 2915–2921, Sep. 2003.

[171] X. H. Xia, L. Nagle, R. Schuster, O. M. Magnussen, and R. J. Behm, "The kinetics of phase transitions in underpotentially deposited Cu adlayers on Au(111)," *Phys. Chem. Chem. Phys.*, vol. 2, no. 19, pp. 4387–4392, Jan. 2000.

[172] J. Wang, A. J. Davenport, H. S. Isaacs, and B. M. Ocko, "Surface Charge—Induced Ordering of the Au(111) Surface," *Science*, vol. 255, no. 5050, pp. 1416–1418, Mar. 1992.

[173] K. Krug, D. Kaminski, F. Golks, J. Stettner, and O. M. Magnussen, "Real-Time Surface X-ray Scattering Study of Au(111) Electrochemical

Dissolution," *J. Phys. Chem. C*, vol. 114, no. 43, pp. 18634–18644, Nov. 2010.

[174] J. Wang, B. M. Ocko, A. J. Davenport, and H. S. Isaacs, "In situ x-ray-diffraction and -reflectivity studies of the Au(111)/electrolyte interface: Reconstruction and anion adsorption," *Phys. Rev. B*, vol. 46, no. 16, pp. 10321–10338, Oct. 1992.

[175] "Time response of the thin layer electrochemical cell used for in situ X-ray diffraction." [Online]. Available: http://www.sciencedirect.com.liverpool.idm.oclc.org/science/article/pii/S0013468602002244. [Accessed: 06-Jun-2016].

[176] F. Golks, Y. Gründer, J. Stettner, K. Krug, J. Zegenhagen, and O. M. Magnussen, "In situ surface x-ray diffraction studies of homoepitaxial growth on Cu(001) from aqueous acidic electrolyte," *Surf. Sci.*, vol. 631, pp. 112–122, Jan. 2015.

[177] D. Strmcnik *et al.*, "Effects of Li+, K+, and Ba2+ Cations on the ORR at Model and High Surface Area Pt and Au Surfaces in Alkaline Solutions," *J. Phys. Chem. Lett.*, vol. 2, no. 21, pp. 2733–2736, Nov. 2011.

[178] G. Harlow, "Atomic Structure at the Au(111) Electrode Surface in Alkaline Solution: The Origin of the CO-induced Increase in Electrocatalytic Activity," *Prep.*, 2017.

[179] E. Herrero, S. Glazier, L. J. Buller, and H. D. Abruña, "X-ray and electrochemical studies of Cu upd on single crystal electrodes in the presence of bromide: Comparison between Au(111) and Pt(111) electrodes," *J. Electroanal. Chem.*, vol. 461, no. 1–2, pp. 121–130, 1999.

[180] T. Kondo, J. Morita, M. Okamura, T. Saito, and K. Uosaki, "In situ structural study on underpotential deposition of Ag on Au(111) electrode using surface X-ray scattering technique," *J. Electroanal. Chem.*, vol. 532, no. 1–2, pp. 201–205, Sep. 2002.

[181] V. Sudha and M. V. Sangaranarayanan, "Underpotential Deposition of Metals: Structural and Thermodynamic Considerations," *J. Phys. Chem. B*, vol. 106, no. 10, pp. 2699–2707, Mar. 2002.

[182] N. Sisson, Y. Gründer, and C. A. Lucas, "Structure and Stability of Underpotentially Deposited Ag on Au(111) in Alkaline Electrolyte," *J. Phys. Chem. C*, vol. 120, no. 29, pp. 16100–16109, Jul. 2016.

[183] M. Banerjee, S. Sharma, A. Chattopadhyay, and S. S. Ghosh, “Enhanced antibacterial activity of bimetallic gold-silver core-shell nanoparticles at low silver concentration,” *Nanoscale*, vol. 3, no. 12, pp. 5120–5125, Dec. 2011.

[184] H.-L. Jiang and Q. Xu, “Synergistic Catalysis of Au@Ag Core−Shell Nanoparticles Stabilized on Metal−Organic Framework,” *J. Am. Chem. Soc. ACS Publ.*, vol. 133, no. 5, pp. 1304–1306, Jan. 2011.

[185] A. Ambrosi *et al.*, “Graphene and its electrochemistry – an update,” *Chem. Soc. Rev.*, vol. 45, no. 9, pp. 2458–2493, May 2016.

[186] J. Zhu, R. Duan, S. Zhang, N. Jiang, Y. Zhang, and J. Zhu, “The application of graphene in lithium ion battery electrode materials,” *SpringerPlus*, vol. 3, Oct. 2014.

[187] M. Pumera, “Graphene in biosensing,” *Mater. Today*, vol. 14, no. 7, pp. 308–315, Jul. 2011.

[188] C. S. Park, H. Yoon, and O. S. Kwon, “Graphene-based nanoelectronic biosensors,” *J. Ind. Eng. Chem.*, vol. 38, pp. 13–22, Jun. 2016.

[189] C. I. L. Justino, A. R. Gomes, A. C. Freitas, A. C. Duarte, and T. A. P. Rocha-Santos, “Graphene based sensors and biosensors,” *TrAC Trends Anal. Chem.*, vol. 91, pp. 53–66, Jun. 2017.

[190] J. Zhu and U. Schwingenschlögl, “Silicene for Na-ion battery applications,” *2D Mater.*, vol. 3, no. 3, p. 035012, 2016.

[191] J. Zhuang, X. Xu, G. Peleckis, W. Hao, S. X. Dou, and Y. Du, “Silicene: A Promising Anode for Lithium-Ion Batteries,” *Adv. Mater. Deerfield Beach Fla*, Mar. 2017.

[192] S. Zein El Abedin, N. Borissenko, and F. Endres, “Electrodeposition of nanoscale silicon in a room temperature ionic liquid,” *Electrochem. Commun.*, vol. 6, no. 5, pp. 510–514, May 2004.

[193] N. Borisenko, S. Zein El Abedin, and F. Endres, “In Situ STM Investigation of Gold Reconstruction and of Silicon Electrodeposition on Au(111) in the Room Temperature Ionic Liquid 1-Butyl-1-methylpyrrolidinium Bis(trifluoromethylsulfonyl)imide,” *J. Phys. Chem. B*, vol. 110, no. 12, pp. 6250–6256, Mar. 2006.

[194] G. Pulletikurthi, A. Lahiri, T. Carstens, N. Borisenko, S. Z. E. Abedin, and F. Endres, “Electrodeposition of silicon from three different ionic liquids:

possible influence of the anion on the deposition process," *J. Solid State Electrochem.*, vol. 17, no. 11, pp. 2823–2832, Nov. 2013.

Publications

- Water corrosion of spent nuclear fuel: radiolysis driven dissolution at the UO_2/water interface
  R. Springell, S. Rennie, L. Costelle, J. Darnbrough, C. Stitt, E. Cocklin, C. Lucas, R. Burrows, H. Sims, D. Wermeille, J. Rawle, C. Nicklin, W. Nuttall, T. Scott and G. Lander
  Faraday Discuss., 2015, 180, 301

- Atomic Structure at the Au(111) Electrode Surface in Alkaline Solution: The Origin of the CO-induced Increase in Electrocatalytic Activity
  G. Harlow, Y. Gründer , N. Sisson, P. Thompson, E. Cocklin and C. A. Lucas
  (*In preparation*)

- Structure of the Ag(*hkl*)/alkaline interface and the effect of O_2 and CO
  E. Cocklin, S. Horswell, Y. Gründer, J. Fogg and C. A. Lucas
  (*In preparation*)

- Dynamics of potential driven structural changes at the electrochemical interface
  E. Cocklin, Y. Gründer, J. Fogg, L. Rhodes-Martin, C. A. Lucas
  (*In preparation*)

Presentations

- Electrochemical Society Northwest Student Chapter Conference (2017)

Stephenson Institute for Renewable Energy, University of Liverpool

Poster presentation

Dynamics of potential-induced structural changes at the electrochemical interface

- XMaS user meeting (2014)

University of Warwick

Poster presentation

Surface X-ray Diffraction Studies of the Electrochemical Interface

- Nuclear Materials Research: The Role of Thin Films (2013)

Interface Analysis Centre part of the School of Physics, University of Bristol

Oral presentation

UO_2 Thin Film Electrochemistry